ISSN 1997-1397 (Print)
ISSN 2313-6022 (Online)

Журнал Сибирского федерального университета

Математика и физика

Journal of Siberian Federal University

Mathematics & Physics

2021 14 (2)

ISSN 1997-1997-1397 (Print)

ISSN 2313-6022 (Online)

ЖУРНАЛ СИБИРСКОГО ФЕДЕРАЛЬНОГО УНИВЕРСИТЕТА Математика и Физика

2021 14 (2)

JOURNAL OF SIBERIAN FEDERAL UNIVERSITY Mathematics & Physics

Издание индексируется Scopus (Elsevier), Emerging Sources Citation Index (WoS, Clarivate Analytics), Российским индексом научного цитирования (НЭБ), представлено в международных и российских информационных базах: Ulrich's periodicals directiory, ProQuest, EBSCO (США), Google Scholar, MathNet.ru, КиберЛенинке.

Включено в список Высшей аттестационной комиссии «Рецензируемые научные издания, входящие в международные реферативные базы данных и системы цитирования».

Все статьи представлены в открытом доступе http://journal.sfu-kras.ru/en/series/mathematics_physics.

Журнал Сибирского федерального университета. Математика и физика.
Journal of Siberian Federal University. Mathematics & Physics.

Учредитель: Федеральное государственное автономное образовательное учреждение высшего образования "Сибирский федеральный университет"(СФУ)
Главный редактор: А.М. Кытманов. Редакторы: В.Е. Зализняк, А.В. Щуплев.
Компьютерная верстка: Г.В. Хрусталева
№ 2. 26.04.2021. Индекс: 42327. Тираж: 1000 экз. Свободная цена
Адрес редакции и издательства: 660041 г. Красноярск, пр. Свободный, 79, оф. 32-03.
Отпечатано в типографии Издательства БИК СФУ
660041 г. Красноярск, пр. Свободный, 82а.
Свидетельство о регистрации СМИ ПИ № ФС 77-28724 от 27.06.2007 г., выданное Федеральной службой по надзору в сфере массовых коммуникаций, связи и охраны культурного наследия
http://journal.sfu-kras.ru
Подписано в печать 15.04.21. Формат 84×108/16. Усл.печ. л. 11,9.
Уч.-изд. л. 11,6. Бумага тип. Печать офсетная.
Тираж 1000 экз. Заказ 12926
Возрастная маркировка в соответствии с Федеральным законом № 436-ФЗ:16+

CONTENTS

СОДЕРЖАНИЕ

DOI: 10.17516/1997-1397-2021-14-2-133-143
УДК 517.956

Solvability of BVPs for the Parabolic-Hyperbolic Equation with Non-linear Loaded Term

Obidjon Kh. Abdullaev*
Romanovsky Institute of Mathematics
Tashkent, Uzbekistan
National University of Uzbekistan
Tashkent, Uzbekistan

Received 10.09.2020, received in revised form 10.11.2020, accepted 20.02.2021

Abstract. This work is devoted to prove the existence and uniqueness of solution of BVP with non-local assumptions on the boundary and integral gluing conditions for the parabolic-hyperbolic type equation involving Caputo derivatives. Using the method of integral energy, the uniqueness of solution have been proved. Existence of solution was proved by the method of integral equations.

Keywords: Caputo fractional derivatives, loaded equation, integral gluing condition, non-linear integral equation, non-local problem, existence and uniqueness of solution.

Citation: O.Kh. Abdullaev, Solvability of BVPs for the Parabolic-hyperbolic Equation with Non-linear Loaded Term, J. Sib. Fed. Univ. Math. Phys., 2021, 14(2), 133–143.
DOI: 10.17516/1997-1397-2021-14-2-133-143.

Boundary value problem (BVP) for the mixed type equation of fractional order is one of the intensively developing lines of study in the field of partial differential equations. Local and non-local problems for the parabolic-hyperbolic type equations involving several integro-differential operators of fractional order was investigated by many authors (see [1–3] and references therein).

BVPs for loaded partial differential equations arise in problems of optimal control of agro-economic systems, for example, in the problem of controlling the label of ground waters and soil moisture (see [4, 5] and references therein). Some results in the theory of BVPs for the loaded equations of parabolic, parabolic-hyperbolic and elliptic-hyperbolic types were presented in [6–8]. Integral boundary conditions have various applications in thermo-elasticity, chemical engineering, population dynamics, etc. Integral gluing conditions were used in [9, 10] and in related works.

In this paper we consider the following parabolic-hyperbolic type equation of fractional order with non-linear loaded term:

$$0=\begin{cases} u_{xx} - {}_C D_{oy}^{\alpha} u + f_1(x,y;u(x,0)) & \text{at } y>0 \\ u_{xx}-u_{yy}+f_2(x,y;u(x,0)) & \text{at } y<0 \end{cases}, \tag{1}$$

where ${}_C D_{oy}^{\alpha} u$ is the Caputo derivative with fractional order α $(0<\alpha<1)$ defined as (see [10], p. 92)

$$\left({}_C D_{ay}^{\alpha} f\right) y = \frac{1}{\Gamma(1-\alpha)} \int_a^y \frac{f'(t)}{(y-t)^{\alpha}} dt, \quad y>a. \tag{2}$$

*o.abdullaev@mathinst.ru, https://orcid.org/0000-0001-8503-1268

There are few works where local and non-local problems for the parabolic-hyperbolic type equation with Caputo operator and loaded terms were studied (see [11, 12] and references therein). Similar problems for the loaded parabolic-hyperbolic type equations that include several integro-differential operators of fractional order such as Riemann-Liouville, Erdelyi-Kober or, among others, Atangana-Baleano operators were considered (see [13–15]). We would like to note that the equations in the above mentioned woks have only linear loaded terms.

The main goal of this work is to prove the existence and uniqueness of solution of an analogue of the Gellerstedt problem with non-local assumptions on the boundary and integral gluing conditions for equation (1).

Let Ω^+ be a bounded domain with segments $A_1A_2=\{(x,y):\ \ x=1,\ 0<y<h\}$, $B_1B_2= =\{(x,y):\ \ x=0,\ 0<y<h\}$, $B_2A_2=\{(x,y):\ \ y=h,\ 0<x<1\}$ at $y>0$. $\Omega_1=\{A_1C_1E\}$ and $\Omega_2=\{B_1C_2E\}$ are characteristic triangles bounded with characteristics $A_1C_1: x-y=1$, $EC_1: x+y=l$ and $B_1C_2: x+y=0$, $EC_2: x-y=l$, $(0<l<1)$, respectively, of equation (1) at $y<0$, where $A_1\,(1;0)\,,\,A_2\,(1;h)\,,\,B_1\,(0;0)\,,\,B_2\,(0;h)\,,\,C_1\left(\frac{l+1}{2};\frac{l-1}{2}\right),\,C_2\left(\frac{l}{2};\frac{-l}{2}\right),\,E(l,0)$.

The following designations are used: $\Omega=\Omega^+\cup\Omega_1\cup\Omega_2\cup(A_1B_1)$, $I=\{y:0<y<h\}$, $I_1=\{x:\ 0<x<l\}$, $I_2=\left\{x: l<x<\frac{l+1}{2}\right\}$, $I_3=\{x:\ 0<x<1\}$.

The following two problems are considered in the domain Ω:

Problem I. To find a solution $u(x,y)$ of equation 1 in the following class of functions:

$$W=\left\{u(x,y):\ u(x,y)\in C(\bar{\Omega})\cap C^2(\Omega_1\cup\Omega_2)\quad u_{xx}\in C\left(\Omega^+\right),\ {}_CD^{\alpha}_{oy}u\in C\left(\Omega^+\right)\right\}.$$

The solution satisfies boundary conditions

$$u(x,y)\Big|_{A_1A_2}=\varphi_1(y),\quad u(x,y)\Big|_{B_1B_2}=\varphi_2(y),\quad 0\leqslant y\leqslant h, \tag{3}$$

$$u(x,y)\Big|_{EC_1}=\psi_1(x),\ l\leqslant x\leqslant\frac{l+1}{2}\ , \tag{4}$$

$$u(x,y)\Big|_{B_1C_2}=\psi_2(x),\ 0\leqslant x\leqslant\frac{l}{2}, \tag{5}$$

and gluing condition

$$\begin{aligned}\lim_{y\to+0}y^{1-\alpha}u_y(x,y)=&\lambda_1(x)u_y(x,-0)+\lambda_2(x)u_x(x,-0)+\\&+\lambda_3(x)\int_0^x r(t)u(t,0)dt+\lambda_4(x)u(x,0)+\lambda_5(x),\quad 0<x<1,\end{aligned} \tag{6}$$

where $\varphi_j(y)$, $\psi_j(x)$ $(j=1,2)$, $\lambda_k(x)$ $(k=\overline{1,5})$ are given functions such that $\sum\limits_{k=1}^{4}\lambda_k^2(x)\neq0$. The required class of functions is specified later.

Problem II. To determine a solution $u(x,y)$ of equation (1) in the class of functions W that satisfies all conditions of Problem I except condition (5) which is replaced by

$$\frac{d}{dx}u\left(\frac{x}{2},\frac{-x}{2}\right)=a_1(x)u_y(x,0)+a_2(x)u_x(x,0)+a_3(x)u(x,0)+a_4(x),\quad 0<x<l, \tag{7}$$

where $a_k(x)$ $(k=\overline{1,4})$ are given functions such that $\sum\limits_{k=1}^{3}a_k^2(x)\neq0$.

Condition (7) is called the non-local condition which connect linear combination of values of functions $u_y(x,0),u_x(x,0)$ and $u(x,0)$ at the points of the interval B_1E with the value of $\dfrac{d}{dx}u\left(\dfrac{x}{2},\dfrac{-x}{2}\right)$ at the points of the characteristic B_1C_2.

1. Main functional relations

It is well-known that solution of the Cauchy problem for equation

$$u_{xx} - u_{yy} + f_2(x, y; u(x, 0)) = 0, \quad \text{at } \ y < 0$$

with initial conditions $u(x, 0) = \tau(x)$, $0 \leqslant x \leqslant 1$; $u_y(x, -0) = \nu^-(x)$, $0 < x < 1$ can be represented as follows:

$$u(x,y) = \frac{\tau(x+y) + \tau(x-y)}{2} - \frac{1}{2}\int\limits_{x+y}^{x-y} \nu^-(t)dt - \frac{1}{4}\int\limits_{x+y}^{x-y} d\eta \int\limits_{x+y}^{\eta} f_2\left(\frac{\xi+\eta}{2}, \frac{\xi-\eta}{2}; \tau\left(\frac{\xi+\eta}{2}\right)\right) d\xi. \quad (8)$$

If we set $a_1(x) = a_2(x) = a_3(x) = 0$ and $a_4(x) = \psi_2'(x)$ then Problem I is a special case of Problem II. Then we will study the existence and uniqueness of solutions of Problem II.

Using condition (7) and relation (8), we obtain

$$(2a_1(x) + 1)\,\nu^-(x) = \frac{1}{2}\int_0^x f_2\left(\frac{\xi+x}{2}, \frac{\xi-x}{2}; \tau\left(\frac{\xi+x}{2}\right)\right) d\xi + \\ + (1 - 2a_2(x))\,\tau'(x) - 2a_3(x)\tau(x) - 2a_4(x), \ \ 0 < x \leqslant l. \quad (9)$$

Similarly, using condition (4) and relation (8), we obtain

$$\nu^-(x) = \tau'(x) - \frac{1}{2}\int_l^x f_2\left(\frac{\xi+x}{2}, \frac{\xi-x}{2}; \tau\left(\frac{\xi+x}{2}\right)\right) d\xi - \psi_1'\left(\frac{l+x}{2}\right), \quad l \leqslant x < 1 \quad (10)$$

Let $\lim\limits_{y\to+0} y^{1-\alpha}u_y(x,y) = \nu^+(x)$. Using gluing condition (6), we have

$$\nu^+(x) = \lambda_1(x)\nu^-(x) + \lambda_2(x)\tau'(x) + \lambda_3(x)\int_0^x r(t)\tau(t)dt + \lambda_4(x)\tau(x) + \lambda_5(x), \ \ 0 < x < 1. \quad (11)$$

On the other hand, taking into account (11) and to $\lim\limits_{y\to 0} D_{0y}^{\alpha-1} f(y) = \Gamma(\alpha) \lim\limits_{y\to 0} y^{1-\alpha} f(y)$, we obtain from equation (1) at $y \to +0$ that

$$\tau''(x) - \Gamma(\alpha)\lambda_1(x)\nu^-(x) - \Gamma(\alpha)\lambda_2(x)\tau'(x) - \Gamma(\alpha)\lambda_3(x)\int_0^x r(t)\tau(t)dt - \\ - \Gamma(\alpha)\lambda_4(x)\tau(x) + f_1(x, 0; \tau(x)) - \Gamma(\alpha)\lambda_5(x) = 0, \quad 0 < x < 1. \quad (12)$$

2. Uniqueness of solution of Problem II

Assuming $\lambda_5(x) \equiv 0$, we multiply equation (12) by $\tau(x)$ and then integrate it from 0 to 1:

$$\int_0^1 \tau''(x)\tau(x)dx - \Gamma(\alpha)\int_0^1 \lambda_2(x)\tau(x)\tau'(x)dx - \Gamma(\alpha)\int_0^1 \lambda_3(x)\tau(x)\left(\int_0^x r(t)\tau(t)dt\right)dx - \\ - \Gamma(\alpha)\int_0^1 \lambda_4(x)\tau^2(x)dx - \Gamma(\alpha)\int_0^1 \lambda_1(x)\tau(x)\nu^-(x)dx + \int_0^1 \tau(x)f_1(x, 0; \tau(x))dx = 0. \quad (13)$$

Obviously, if $\tau(0) = \tau(1) = 0$ then, integrating by parts, we obtain

$$\int_0^1 \tau''(x)\tau(x)dx = -\int_0^1 {\tau'}^2(x)dx \leqslant 0, \quad (14)$$

$$\Gamma(\alpha)\int_0^1 \lambda_2(x)\tau(x)\tau'(x)dx = -\frac{\Gamma(\alpha)}{2}\int_0^1 \lambda'_2(x)\tau^2(x)dx. \tag{15}$$

Taking into account that

$$2\Gamma(\alpha)\int_0^1 \lambda_3(x)\tau(x)\left(\int_0^x r(t)\tau(t)dt\right)dx = \Gamma(\alpha)\int_0^1 \frac{\lambda_3(x)}{r(x)}d\left(\int_0^x r(t)\tau(t)dt\right)^2 =$$

$$= \Gamma(\alpha)\frac{\lambda_3(1)}{r(1)}\left(\int_0^1 r(t)\tau(t)dt\right)^2 - \Gamma(\alpha)\int_0^1\left(\frac{\lambda_3(x)}{r(x)}\right)'\left(\int_0^x r(t)\tau(t)dt\right)^2 dx,$$

we obtain that inequality

$$\Gamma(\alpha)\int_0^1 \lambda_3(x)\tau(x)\left(\int_0^x r(t)\tau(t)dt\right)dx \geqslant 0$$

is satisfied provided that

$$\frac{\lambda_3(1)}{r(1)} \geqslant 0, \text{ and } \left(\frac{\lambda_3(x)}{r(x)}\right)' \leqslant 0. \tag{16}$$

Let us consider now the integral

$$J = \Gamma(\alpha)\int_0^1 \lambda_1(x)\tau(x)\nu^-(x)dx - \int_0^1 \tau(x)f_1(x,0;\tau(x))dx =$$

$$= \Gamma(\alpha)\int_0^l \lambda_1(x)\tau(x)\nu^-(x)dx + \Gamma(\alpha)\int_l^1 \lambda_1(x)\tau(x)\nu^-(x)dx - \int_0^1 \tau(x)f_1(x,0;\tau(x))dx.$$

Taking (9) and (10) into account when $\psi_1(x)\equiv a_4(x)\equiv 0$ and assuming $1+2a_1(x)\neq 0$, we obtain

$$J = -\Gamma(\alpha)\int_0^l \tau(x)A_1(x)dx\int_0^x f_2\left(\frac{\xi+x}{2},\frac{\xi-x}{2};\tau\left(\frac{\xi+x}{2}\right)\right)d\xi + \Gamma(\alpha)\int_0^l B(x)\tau(x)\tau'(x)dx -$$
$$-\int_0^1 \tau(x)f_1(x,0;\tau(x))dx - \Gamma(\alpha)\int_0^l C(x)\tau^2(x)dx + \Gamma(\alpha)\int_l^1 \lambda_1(x)\tau(x)\tau'(x)dx -$$
$$-\Gamma(\alpha)\int_l^1 \tau(x)A_2(x)dx\int_l^x f_2\left(\frac{\xi+x}{2},\frac{\xi-x}{2};\tau\left(\frac{\xi+x}{2}\right)\right)d\xi, \tag{17}$$

where $A_i(x) = \dfrac{(-1)^i\lambda_1(x)}{2(1+2a_1(x))^{2-i}}$ $(i=1,2)$, $B(x) = \dfrac{1-2a_2(x)}{1+2a_1(x)}\lambda_1(x)$, $C(x) = \dfrac{2a_3(x)\lambda_1(x)}{1+2a_1(x)}$.

Thus, assuming that

$$\Gamma(\alpha)\int_0^l B(x)\tau(x)\tau'(x)dx = \frac{\Gamma(\alpha)}{2}\int_0^l B(x)d\left(\tau^2(x)\right) = -\frac{\Gamma(\alpha)}{2}\int_0^l \tau^2(x)B'(x)dx\,,$$

$$\Gamma(\alpha)\int_l^1 \lambda_1(x)\tau(x)\tau'(x)dx = \frac{\Gamma(\alpha)}{2}\int_l^1 \lambda_1(x)d\left(\tau^2(x)\right) = -\frac{\Gamma(\alpha)}{2}\int_l^1 \tau^2(x)\lambda'_1(x)dx$$

and using (16), we have

$$J = \Gamma(\alpha)\int_0^1 \lambda_1(x)\tau(x)\nu^-(x)dx - \int_0^1 \tau(x)f_1(x,0;\tau(x))dx \geqslant 0 \tag{18}$$

if $A_i(x)\tau(x)f_2(s,s-x;\tau(s))\leqslant 0$, $\tau(x)f_1(x,0;\tau(x))\leqslant 0$, $B'(x)\leqslant 0$, $\lambda'_1(x)\leqslant 0$ and $C(x)\leqslant 0$.

Thus, considering (14), (15), (16), (17), (18) and assuming that $\frac{1}{2}\lambda_2'(x)-\lambda_4(x)\leqslant 0$, it follows from (13) that $\tau(x)\equiv 0$.

Hence, based on the solution of the first boundary problem (1) and (3) we obtain $u(x,y)\equiv 0$ in $\overline{\Omega}^+$. Further, taking into account that $\tau(x)\equiv 0$, we obtain from functional relations (9) and (10) that $\nu^-(x)\equiv 0$. Consequently, taking into account solution (8), we have $u(x,y)\equiv 0$ in closed domain $\overline{\Omega}_j$ $(j=1,2)$.

Let us assume that $f_i(x,y;\tau(x))=0$ at $\tau(x)=0$. Then the following theorem can be formulated

Theorem 2.1. *Let us assume that conditions*

$$A_i(x)\geqslant 0\ (\leqslant 0),\ \ (i=1,2),\quad \tau(x)f_2(s,s-x;\tau(s))\geqslant 0\ (\leqslant 0); \tag{19}$$

$$\tau(x)f_1(x,0;\tau(x))\leqslant 0,\quad B'(x)\leqslant 0,\ \ \lambda_1'(x)\leqslant 0,\quad C(x)\leqslant 0; \tag{20}$$

$$\frac{\lambda_3(1)}{r(1)}\geqslant 0,\quad \left(\frac{\lambda_3(x)}{r(x)}\right)'\leqslant 0,\quad \frac{1}{2}\lambda_2'(x)-\lambda_4(x)\leqslant 0, \tag{21}$$

are valid then the solution $u(x,y)$ of Problem II is unique if it exists.

3. Existence of solution of Problem I

Theorem 3.1. *If conditions (19), (20), (21) and*

$$f_1(x,y;\tau(x))\in C\left(\overline{\Omega^+}\right)\cap C^1\left(\Omega^+\right),\ \ f_2(x,y;\tau(x))\in C\left(\overline{\Omega_1}\cup\overline{\Omega_2}\right)\cap C^1\left(\Omega_1\cup\Omega_2\right); \tag{22}$$

$$|f_j(x,y;\tau_2(x))-f_j(x,y;\tau_2(x))|\leqslant L_j|\tau_2(x)-\tau_1(x)|,\ \ L_j=const>0\ (j=1,2); \tag{23}$$

$$\varphi_1(y),\ \varphi_2(y)\in C\left(\overline{I}\right)\cap C^1\left(I\right),\quad \psi_i(x)\in C\left(\overline{I_2}\right)\cap C^2\left(I_2\right); \tag{24}$$

$$a_i(x)\in C^1\left(\overline{I_1}\right)\cap C^2\left(I_1\right),\quad \lambda_k(x)\in C^1\left(\overline{I_3}\right)\cap C^2\left(I_3\right),\quad i=\overline{1,4},\ \ k=\overline{1,5} \tag{25}$$

are fulfilled then there exists a solution of Problem I.

Proof. Taking (9) and (10) into account, from (12) we obtain that

$$\tau''(x)=F_1(x),\quad 0<x<l, \tag{26}$$

$$\tau''(x)=F_2(x),\quad l<x<1, \tag{27}$$

where

$$F_1(x)=\Gamma(\alpha)\lambda_3(x)\int_0^x r(t)\tau(t)dt+\Gamma(\alpha)A_1(x)\int_0^x f_2\left(\frac{\xi+x}{2},\frac{\xi-x}{2};\tau\left(\frac{\xi+x}{2}\right)\right)d\xi-$$
$$-f_1(x,0;\tau(x))+\Gamma(\alpha)(B(x)+\lambda_2(x))\tau'(x)-\Gamma(\alpha)(C(x)-\lambda_4(x))\tau(x)+D(x), \tag{28}$$

$$F_2(x)=\Gamma(\alpha)\lambda_3(x)\int_l^x r(t)\tau(t)dt-\Gamma(\alpha)A_2(x)\int_l^x f_2\left(\frac{\xi+x}{2},\frac{\xi-x}{2};\tau\left(\frac{\xi+x}{2}\right)\right)d\xi-$$
$$-f_1(x,0;\tau(x))+\Gamma(\alpha)(\lambda_1(x)+\lambda_2(x))\tau'(x)+\Gamma(\alpha)\lambda_4(x)\tau(x)+$$
$$+\Gamma(\alpha)\left(\lambda_5(x)-\lambda_1(x)\psi_1'\left(\frac{l+x}{2}\right)\right) \tag{29}$$

and $D(x)=\Gamma(\alpha)\left(\lambda_5(x)-\dfrac{2\lambda_1(x)a_4(x)}{1+2a_1(x)}\right)$.

Solutions of equations (26) and (27) together with conditions

$$\tau(0)=\varphi_2(0),\quad \tau\left(l\right)=\psi_1\left(l\right)\ \text{ and, }\ \tau\left(l\right)=\psi_1\left(l\right),\quad \tau(1)=\varphi_1(0),$$

respectively, are

$$\tau(x)=\int_0^x(x-t)F_1(t)dt-\frac{x}{l}\int_0^l(l-t)F_1(t)dt+\left(1-\frac{x}{l}\right)\varphi_2(0)+\frac{x}{l}\psi_1\left(l\right) \tag{30}$$

and

$$\tau(x)=\int_l^x(x-t)F_2(t)dt+\frac{l-x}{1-l}\int_l^1(1-t)F_2(t)dt+\frac{1-x}{1-l}\psi_1\left(l\right)+\frac{x-l}{1-l}\varphi_1(0). \tag{31}$$

Further, substituting (28) and (29) into (30) and (31), respectively, we obtain

$$\begin{aligned}\tau(x)=\Gamma(\alpha)\int_0^x r(z)\tau(z)dz\int_z^x(x-t)\lambda_3(t)dt-\frac{\Gamma(\alpha)}{l}x\int_0^l r(z)\tau(z)dz\int_z^l(l-t)\lambda_3(t)dt-\\ -\Gamma(\alpha)\int_0^x\left[(x-t)(B(t)+\lambda_2(t))\right]'\tau(t)dt-\Gamma(\alpha)\int_0^x(x-t)(C(t)-\lambda_4(t))\tau(t)dt+\\ +\frac{\Gamma(\alpha)x}{l}\int_0^l\left[(l-t)(B(t)+\lambda_2(t))\right]'\tau(t)dt+\\ +\frac{\Gamma(\alpha)x}{l}\int_0^l(l-t)(C(t)-\lambda_4(t))\tau(t)dt+F_1^*(x)+\Phi_1(x,\tau(x)),\ \ 0\leqslant x\leqslant l\end{aligned} \tag{32}$$

where

$$\begin{aligned}&F_1^*(x)=\int_0^x(x-t)D(t)dt-\frac{x}{l}\int_0^l(l-t)D(t)dt+\left(1-\frac{x}{l}\right)\varphi_2(0)+\frac{x}{l}\psi_1(l),\\ &\Phi_1(x,\tau(x))=\frac{x}{l}\int_0^l(l-t)f_1(t,0;\tau(t))dt+\\ &\quad+\frac{\Gamma(\alpha)x}{l}\int_0^l(l-t)A_1(t)dt\int_0^t f_2\left(\frac{\xi+t}{2},\frac{\xi-t}{2};\tau\left(\frac{\xi+t}{2}\right)\right)d\xi-\\ &-\int_0^x(x-t)f_1(t,0;\tau(t))dt-\Gamma(\alpha)\int_0^x(x-t)A_1(t)dt\int_0^t f_2\left(\frac{\xi+t}{2},\frac{\xi-t}{2};\tau\left(\frac{\xi+t}{2}\right)\right)d\xi,\end{aligned}$$

and

$$\begin{aligned}\tau(x)=\Gamma(\alpha)\int_l^x r(z)\tau(z)dz\int_z^x(x-t)\lambda_3(t)dt+\frac{\Gamma(\alpha)(l-x)}{1-l}\int_l^1 r(z)\tau(z)dz\int_z^l(l-t)\lambda_3(t)dt-\\ -\Gamma(\alpha)\int_l^x\left[(x-t)(\lambda_1(t)+\lambda_2(t))\right]'\tau(t)dt+\Gamma(\alpha)\int_l^x(x-t)\lambda_4(t)\tau(t)dt+\\ \frac{\Gamma(\alpha)(l-x)}{1-l}\int_l^1\lambda_4(t)\tau(t)dt-\frac{\Gamma(\alpha)(l-x)}{1-l}\int_l^x\left[(1-t)(\lambda_1(t)+\lambda_2(t))\right]'\tau(t)dt+\\ +F_2^*(x)+\Phi_2(x,\tau(x)),\quad l\leqslant x\leqslant 1,\end{aligned} \tag{33}$$

where

$$\begin{aligned}&F_2^*(x)=\Gamma(\alpha)\int_0^x(1-t)\left(\lambda_5(t)-\lambda_1(t)\psi_1'\left(\frac{l+t}{2}\right)\right)dt-\\ &\quad-\frac{l-x}{l}\int_l^1\left(\lambda_5(t)-\lambda_1(t)\psi_1'\left(\frac{l+t}{2}\right)\right)dt+\frac{1-x}{1-l}\psi_1(l)+\frac{x-1}{1-l}\varphi_1(0)\end{aligned}$$

and

$$\Phi_2(x,\tau(x)) = \frac{(x-l)}{1-l}\int_l^1 (l-t)f_1(t,0;\tau(t))dt+$$
$$+\frac{\Gamma(\alpha)(x-l)}{1-l}\int_l^1 (l-t)A_2(t)dt\int_l^t f_2\left(\frac{\xi+t}{2},\frac{\xi-t}{2};\tau\left(\frac{\xi+t}{2}\right)\right)d\xi-$$
$$-\int_l^x (x-t)f_1(t,0;\tau(t))dt-\Gamma(\alpha)\int_l^x (x-t)A_2(t)dt\int_l^t f_2\left(\frac{\xi+t}{2},\frac{\xi-t}{2};\tau\left(\frac{\xi+t}{2}\right)\right)d\xi.$$

After some simplifications, equations (32) and (33) can be rewritten in the form of Fredholm integral equations of the second kind

$$\tau(x) = \int_0^l K_1(x,z)\tau(z)dz + \widetilde{F}_1(x,\tau(x)),\ \ 0\leqslant x\leqslant l \tag{34}$$

and

$$\tau(x) = \int_l^1 K_2(x,z)\tau(z)dz + \widetilde{F}_2(x,\tau(x)),\ \ l\leqslant x\leqslant 1. \tag{35}$$

Here $\widetilde{F}_j(x,\tau(x)) = F_j^*(x)+\Phi_j(x,\tau(x))$ $(j=1,2)$, and

$$K_1(x,z)=\begin{cases}K_{11}(x,z); & 0\leqslant z\leqslant x,\\ K_{12}(x,z); & x\leqslant z\leqslant l\end{cases};\ \ K_2(x,z)=\begin{cases}K_{21}(x,z); & l\leqslant z\leqslant x,\\ K_{22}(x,z); & x\leqslant z\leqslant 1,\end{cases}$$

with

$$K_{11}(x,z)=\Gamma(\alpha)r(z)\int_z^x (x-t)\lambda_3(t)dt-\frac{\Gamma(\alpha)}{l}xr(z)\int_z^l (l-t)\lambda_3(t)dt+$$
$$+\Gamma(\alpha)\frac{l-x}{l}(B(z)+\lambda_2(z))+\Gamma(\alpha)z\frac{l-x}{l}(B(z)+\lambda_2(z))'+\Gamma(\alpha)\frac{z(l-x)}{l}(C(z)-\lambda_4(z)),$$

$$K_{12}(x,z)=-\Gamma(\alpha)\frac{x}{l}r(z)\int_z^l (l-t)\lambda_3(t)dt+\frac{\Gamma(\alpha)}{l}x[(l-z)(B(z)+\lambda_2(z))]'+$$
$$+\Gamma(\alpha)\frac{x}{l}(l-z)(C(z)-\lambda_4(z)),$$

$$K_{21}(x,z)=\Gamma(\alpha)r(z)\int_z^x (x-t)\lambda_3(t)dt+\frac{\Gamma(\alpha)(l-x)}{1-l}r(z)\int_z^l (l-t)\lambda_3(t)dt+$$
$$+\Gamma(\alpha)\frac{l-x}{1-l}(\lambda_1(z)+\lambda_2(z))-\Gamma(\alpha)(z-l)\frac{x-1}{1-l}(\lambda_1(z)+\lambda_2(z))'+\Gamma(\alpha)\frac{(z-l)(x-1)}{1-l}\lambda_4(z),$$

and

$$K_{22}(x,z)=\Gamma(\alpha)\frac{l-x}{1-l}r(z)\int_z^l (l-t)\lambda_3(t)dt+\frac{\Gamma(\alpha)(x-l)}{1-l}[(1-z)(\lambda_1(z)+\lambda_2(z))]'+$$
$$+\Gamma(\alpha)\frac{l-x}{1-l}(l-z)\lambda_4(z).$$

Besides, due to regularity of functions in (22), (23), (24) and (25) it is not difficult to verify that $|K_j(x,t)|$ and $\left|\widetilde{F}_j(x)\right|$, $(j=1,2)$ are bounded. Moreover,

$$K_1(x,t)\in C\left([0,l]\times[0,l]\right)\cup C^{2,0}_{x,t}\left((0,l)\times(0,l)\right),$$

$$K_2(x,t)\in C\left([l,1]\times[l,1]\right)\cup C^{2,0}_{x,t}\left((l,1)\times(l,1)\right)$$

and $\widetilde{F}_1(x) \in C[0,l] \cup C^2(0,l)$, $\widetilde{F}_2(x) \in C[l,1] \cup C^2(l,1)$.

Since kernels $K_j(x,t)$ are continuous and functions $\widetilde{F}_j(x)$ are continuously differentiable, solutions of integral equations (34) and (35) can be derived in terms of resolvent-kernel as follows

$$\tau(x) = \int_0^l R_1(x,z)\widetilde{F}_1(z,\tau(z))dz + \widetilde{F}_1(x,\tau(x)), \ \ 0 \leqslant x \leqslant l \tag{36}$$

and

$$\tau(x) = \int_l^1 \widetilde{F}_2(z,\tau(z))R_2(x,z)dz + \widetilde{F}_2(x,\tau(x)), \ \ l \leqslant x \leqslant 1, \tag{37}$$

where $R_j(x,z)$ is the resolvent kernel of $K_j(x,z)$.

Considering functions $\Phi_j(x,\tau(x))$ $(j = 1,2)$ from (36) and (37), the Fredholm type nonlinear integral equations are constructed

$$\begin{gathered}\tau(x) = \int_0^l L_{12}(x,t)dt \int_0^t f_2\left(\frac{\xi+t}{2}, \frac{\xi-t}{2}; \tau\left(\frac{\xi+t}{2}\right)\right)d\xi + \\ + \int_0^l R_1(x,t)dt \int_0^l L_{12}(t,z)dz \int_0^z f_2\left(\frac{\xi+z}{2}, \frac{\xi-z}{2}; \tau\left(\frac{\xi+z}{2}\right)\right)d\xi + \\ + \int_0^l L_{11}(x,t)f_1(t,0;\tau(t))dt + \int_0^l R_1(x,t)dt \int_0^l L_{11}(t,z)dz f_1(z,0;\tau(z))dz + \\ + F_1^*(x) + \int_0^l F_1^*(t)R_1(x,t)dt, \ \ 0 \leqslant x \leqslant l,\end{gathered} \tag{38}$$

and

$$\begin{gathered}\tau(x) = \int_l^1 L_{22}(x,t)dt \int_l^t f_2\left(\frac{\xi+t}{2}, \frac{\xi-t}{2}; \tau\left(\frac{\xi+t}{2}\right)\right)d\xi + \\ + \int_l^1 R_2(x,t)dt \int_l^1 L_{22}(t,z)dz \int_l^z f_2\left(\frac{\xi+z}{2}, \frac{\xi-z}{2}; \tau\left(\frac{\xi+z}{2}\right)\right)d\xi + \\ + \int_l^1 L_{21}(x,t)f_1(t,0;\tau(t))dt + \int_l^1 R_2(x,t)dt \int_l^1 L_{21}(t,z)f_1(z,0;\tau(z))dz + \\ + F_2^*(x) + \int_l^1 F_2^*(t)R_2(x,t)dt, \ \ \ \ l \leqslant x \leqslant 1,\end{gathered} \tag{39}$$

where

$$L_{11}(x,t) = \begin{cases} \dfrac{t(l-x)}{l}; & 0 \leqslant t \leqslant x, \\ \dfrac{x(l-t)}{l}; & x \leqslant t \leqslant l \end{cases}; \ \ L_{12}(x,t) = \Gamma(\alpha)A_1(t)L_{11}(x,t);$$

$$L_{21}(x,t) = \begin{cases} \dfrac{(t-l)(1-x)}{1-l}; & l \leqslant t \leqslant x, \\ \dfrac{(1-t)(x-l)}{1-l}; & x \leqslant t \leqslant 1 \end{cases}; \ \ L_{22}(x,t) = \Gamma(\alpha)A_2(t)L_{21}(x,t).$$

It is not difficult to verify that

$$\left|\int_0^l L_{11}(x,t)dt\right| \leqslant \frac{2l^2}{27} = M_{11}; \ \ \left|\int_l^1 L_{21}(x,t)dt\right| \leqslant \frac{2(1-l)^2}{27} = M_{21}. \tag{40}$$

Now, assuming that $|\Gamma(\alpha)A_j(x)| \leqslant \beta_j$; $\left|\int_0^1 R_j(x,t)dt\right| \leqslant \delta_j$, $(j = 1,2)$ and taking into account (40), we obtain

$$\left|\int_0^l L_{12}(x,t)dt\right| \leqslant \beta_1 M_{11} = M_{12}; \ \ \left|\int_l^1 L_{22}(x,t)dt\right| \leqslant \beta_2 M_{21} = M_{22}, \tag{41}$$

$$\left|\int_0^l R_1(x,t)dt\int_0^l L_{1j}(x,z)dz\right| \leqslant \delta_1 M_{1j} = N_{1j}, \tag{42}$$

and

$$\left|\int_l^1 R_2(x,t)dt\int_l^1 L_{2j}(x,z)dz\right| \leqslant \delta_2 M_{2j} = N_{2j},\ (j=1,2). \tag{43}$$

Solvability of integral equation (38) can be established with the use of the method of successive approximations. Let us assume $\tau_0(x) = \widetilde{F_1^*}(x)$ and define the functional sequence $\{\tau_n(x)\}$ in the following form:

$$\begin{gathered}\tau_n(x) = \int_0^l L_{12}(x,t)dt\int_0^t f_2\left(\frac{\xi+t}{2},\frac{\xi-t}{2};\tau_{n-1}\left(\frac{\xi+t}{2}\right)\right)d\xi+\\ +\int_0^l R_1(x,t)dt\int_0^l L_{12}(t,z)dz\int_0^z f_2\left(\frac{\xi+z}{2},\frac{\xi-z}{2};\tau_{n-1}\left(\frac{\xi+z}{2}\right)\right)d\xi+\\ +\int_0^l L_{11}(x,t)f_1(t,0;\tau_{n-1}(t))dt+\int_0^l R_1(x,t)dt\int_0^l L_{11}(t,z)f_1(z,0;\tau_{n-1}(z))dz+\\ +F_1^*(x)+\int_0^l F_1^*(t)R_1(x,t)dt,\quad 0\leqslant x\leqslant l,\end{gathered} \tag{44}$$

where $\widetilde{F_1^*}(x) = F_1^*(x) + \int\limits_0^l F_1^*(t)R_1(x,t)dt$.

Let us assume that

$$|f_1(z,0,\tau(z))| \leqslant m_1,\quad \left|f_2\left(\frac{\xi+z}{2},\frac{\xi-z}{2},\tau\left(\frac{\xi+z}{2}\right)\right)\right| \leqslant m_2,\ \ (m_1,m_2>0).$$

Considering (22), (23) and taking into account (40)–(43), we obtain from (44) the following inequalities

$$|\tau_1(x)-\tau_0(x)| \leqslant M(m_1+m_2), \text{where}\ \ M=\max\{M_{11}+N_{11};M_{12}+N_{12}\},$$

$$\begin{gathered}|\tau_2(x)-\tau_1(x)| \leqslant |\tau_1(x)-\tau_0(x)|\cdot|L_1(M_{11}+N_{11})+L_2(M_{12}+N_{12})| \leqslant\\ \leqslant M(L_1+L_2)|\tau_1(x)-\tau_0(x)| \leqslant M^2(L_1+L_2)(m_1+m_2),\end{gathered} \tag{45}$$

$$|\tau_n(x)-\tau_{n-1}(x)| \leqslant M(L_1+L_2)|\tau_{n-1}(x)-\tau_{n-2}(x)| \leqslant M^n(L_1+L_2)^{n-1}(m_1+m_2).$$

Thus, we have contraction mapping. Let us note that solvability of the considered problem was reduced to integral equations (34) and (35). Based on the uniqueness of solution of the problem and due to equivalence of the problem to integral equations in the sense of solvability, we establish that integral equations (34) and (35) have a unique solution. Since, an integral equation does not have more than one solution and we have contraction mapping, one can conclude that functional sequence $\{\tau_n(x)\}$ has a unique limiting function $\tau(x)$.

With the arguments given above one can prove solvability of equation (37). Unknown function $\nu^-(x)$ can be found from (9). Solution of Problem II in the domain Ω^+ is the solution of the first BVP [2, 16]. Solution of Problem II in the domain Ω_j is given in (8). Hence, Theorem 3.1 is proved.

Remark. *Let us note that functions $f_i(x,y,u(x,0)) = u^{p_i}(x,0)$ satisfy our assumptions and all conditions on functions $f_i(x,y;u(x,0))$ at $p_i = const > 0$ $(i=1,2)$.*

References

[1] A.A.Kilbas., O.A.Repin, An analog of the Tricomi problem for a mixed type equation with a partial fractional derivative, *Fractional Calculus and Applied Analysis*, **13**(2010), no. 1, 69–84.

[2] A.S.Berdyshev, E.T.Karimov, N.Akhtayeva, Boundary Value problems with integral gluing conditions for fractional order mixed type equations, *Hindawi. IJDE*, (2011).

[3] B.J.Kadirkulov, Boundary problems for mixed parabolic-hyperbolic equations with two lines of changing type and fractional derivative, *EJDE*, **57**(2014), 1–7.

[4] A.M.Nakhushev, The loaded equations and their applications., Moscow, Nauka, 2012 (in Russian)

[5] A.M.Nakhushev, The Darboux problem for a certain degenerate second order loaded integral-differential equation, *Differential equations*, **12**(1976), no. 1, 103–108.

[6] K.B.Sabitov, Initial-boundary problem for parabolic-hyperbolic equation with loaded summands, *Russian Math. Iz. VUZ*, **59**(2015), no. 6, 23–33. DOI: 10.3103/S1066369X15060055

[7] E.P.Melisheva, Dirichlet problem for loaded equation of Lavrentiev-Bizadze, *Vestnik SamGU. Estestvenno Nauchnaya Ser*, **(80)**(2010), no. 6, 39–47 (in Russian).

[8] O.Kh.Abdullaev, A non-local problem for a loaded mixed-type equation with a integral operators, *J. Samara State Tech. Univ., Ser. Phys. and Math. Sci.*, **20**(2016), no.2, 220–240 (in Russian). DOI: 10.14498/vsgtu1485

[9] O.Kh.Abdullaev, K.Sadarangani, Non-local problems with integral gluing condition for loaded mixed type equations involving the Caputo fractional derivative, *Electronic Journal of Differential Equations (EJDE)*, **164**(2016), 1–10.

[10] A.A.Kilbas, H.M.Srivastava, J.J.Trujillo, Theory and Applications of Fractional Differential Equations, In: North-Holland Mathematics Studies, Vol. 204, Elsevier Science B.V., Amsterdam, 2006.

[11] M.S.Salakhitdinov, E.T.Karimov, On a nonlocal problem with gluing condition of integral form for parabolic-hyperbolic equation with Caputo operator, *Reports of the Academy of Sciences of the Republic of Uzbekistan. (DAN RUz)*, (2014), no. 4, 69–79 (in Russian).

[12] A.S.Berdyshev, A.Cabada, E.T.Karimov, On a non-local boundary problem for a parabolic-hyperbolic equation involving a Riemann-Liouville fractional differential operator, *Nonlinear Anal., Theory Methods Appl*, **75(6)**(2012), 3268–3273. DOI: 10.1016/j.na.2011.12.033

[13] K.Sadarangani, K.O.Kh.Abdullaev, A non-local problem with discontinuous matching condition for loaded mixed type equation involving the Caputo fractional derivative, *Advances in Difference Equations*, 2016, AIDE-D-16-00217R3. DOI: 10.1186/s13662-016-0969-1

[14] O.Kh.Abdullaev, Some Problems for the Degenerate Mixed Type Equation Involving Caputo and Atangana-Baleanu Operators Fractional Order, *Progr. Fract. Differ. Appl.*, **6**(2020), no. 2, 101–114. DOI: 10.18576/pfda/060203

[15] O.Kh.Abdullaev, About a problem for the degenerate mixed type equation involving Caputo and Erdelyi-Kober operators fractional order, *Ukr. math. jour*, **71**(2019), no. 6. 723–738. DOI: 10.1007/s11253-019-01682-z

[16] A.V.Pskhu, Partial differential equation of fractional order, Moscow, Nauka, 2000 (in Russian).

Разрешимость краевых задач для параболо-гиперболического уравнения с нелинейной нагруженной слагаемой

Обиджон Абдуллаев
Институт математики им. В. И. Романовского Академии наук Республики Узбекистан
Ташкент, Узбекистан
Национальный университет Узбекистана
Ташкент, Узбекистан

Аннотация. Данная работа посвящена доказательству существования и единственности краевой задачи с нелокальными краевыми и интегральными условиями склеивания для параболо-гиперболического уравнения с дробной производной Капуто. Применением метода интегралов энергии доказана единственность решения задачи. Существование решения было доказано методом интегральных уравнений.

Ключевые слова: дробная производная Капуто, нагруженное уравнение, интегральное условие склеивания, нелинейное интегральное уравнение, нелокальная задача, существование и единственность решения.

DOI: 10.17516/1997-1397-2021-14-2-144-149
УДК 621.373.826

Simulation of Broadening the Second Harmonic Spectrum in KDP by Chirp Pulse Pumping

Sergey V. Alekseev*
Valery F. Losev†
Institute of High Current Electronics SB RAS
Tomsk, Russian Federation
Yakov V. Grudtsyn‡
Andrey V. Koribut§
P. N. Lebedev Physical Institute of RAS
Moscow, Russian Federation
Vyacheslav A. Trofimov¶
South China University of Technology
Guangzhou, China

Received 10.08.2020, received in revised form 10.09.2020, accepted 20.11.2020

Abstract. The conditions of broadening the second harmonic spectrum in KDP upon pumping by a negatively chirped pulse of fundamental frequency with central wavelength of 950 nm are analyzed numerically. It is shown that broadening of the spectrum (K = 1.4) is mainly limited by difference in group velocities of radiation pulse between first and second harmonics. The article is based on materials of the report at the first All-Russian scientific conference with international participation "YENISEI PHOTONICS – 2020".

Keywords: femtosecond laser pulse, second harmonic, spectrum, efficiency, pulse duration.

Citation: S.V. Alekseev, V.F. Losev, Ya.V. Grudtsyn, A.V. Koribut, V.A. Trofimov, Simulation of Broadening the Second Harmonic Spectrum in KDP by Chirp Pulse Pumping, J. Sib. Fed. Univ. Math. Phys., 2021, 14(2), 144–149. DOI: 10.17516/1997-1397-2021-14-2-144-149.

Introduction

Currently, all powerful femtosecond laser systems operate in the infrared spectrum range (0.8–1 microns). The expansion of their spectral range will make it possible to push the boundaries of the application fields of these systems and, in some cases, will help to increase the interaction efficiency of femtosecond radiation pulses with matter. The way to advance into the visible region of the spectrum due to the generation of the second harmonic (SH) during the conversion of infrared (IR) radiation in a nonlinear crystal is known. However, the possibility of converting high peak power IR radiation into SH is limited by the technological difficulties of manufacturing thin (less than 1 mm thickness) nonlinear crystals with a sufficiently large diameter (20 cm or more), and the low quality of SH radiation due to phase self-modulation, cross-modulation, Kerr self-focusing, and deep spectrum modulation in a nonlinear crystal.

*sergey100@sibmail.com
†losev@ogl.hcei.tsc.ru
‡grudcynyv@lebedev.ru
§koributav@lebedev.ru
¶trofimov@scut.edu.cn

In the last decade, an alternative way of creating multi-terawatt laser systems has been developed in HCEI SB RAS, Tomsk. It is based on the use of a solid-state femtosecond laser complex and a photodissociation XeF(C-A) amplifier with a gas active medium [1,2]. The advantages of this hybrid scheme are the low optical nonlinearity of the gas active medium, the visible radiation range (475 nm), the ability to scale the gas amplifier, the achievement of high contrast due to the conversion of radiation in a nonlinear crystal and a low gain in the gas medium. In 2012, the THL-100 laser system produced a record peak power of 14 TW for the visible spectrum [1, 2]. In recent years, research has been conducted to increase this power.

An attractive method for increasing peak power is to reduce the duration of a transform limited radiation pulse without increasing its energy. To reduce the pulse duration, it is necessary to increase the width of its spectrum. For this purpose, phase modulation is usually used when a femtosecond pulse passes through gaseous or solid media. Since our system uses a non-linear crystal (KDP), it suggests organizing a broadening of the spectrum with a subsequent reduction in the duration of the SH pulse directly in the non-linear crystal itself [3]. Unfortunately, this method of broadening is poorly studied in the literature, and we have found only one work devoted to this [4], which showed the possibility of increasing the spectrum width in a nonlinear BBO crystal and reducing the duration of the SH pulse with a wavelength of 400 nm to two times.

In our opinion, additional theoretical and experimental studies are required to find optimal conditions for broadening the SH spectrum and obtaining information about the physical processes responsible for this.

In this regard the present work is devoted to study of conditions of SH generation upon pumping a nonlinear crystal at a wavelength of 950 nm with transform limited and chirped pulses in order to determine the processes that affect the broadening of the SH spectrum.

1. Instrumentation and techniques

The experiments were carried out on a Ti:Sa femtosecond complex, which is a front-end for THL-100 multi-terawatt laser system. The complex consists of a master oscillator, stretcher, regenerative and two multi-pass amplifiers, compressor on diffraction gratings, and a SH generator (2 mm, KDP crystal). The complex operates at a central wavelength of 950 nm with 50–70 fs pulse duration, the radiation pulse had 10 mJ energy. The transform limited radiation pulse with 60 fs duration or negatively chirped pulse with 700 fs duration were used. The pulse was chirped in the compressor by increasing the distance between the gratings. After compressor, the Gaussian fundamental frequency beam had 16 mm diameter at 1/e2 level. In front of the KDP the beam radius was reduced by factor of two in mirror telescope. The transform limited duration of SH chirped pulse was obtained using compression in glass block.

To measure the energy of laser radiation Gentec and OPHIR meters were used. The emission spectra were measured using ASP150C spectrometers (Avesta-project) and Ocean Optics HR4000 (200–1100 nm, 0.7 nm).

The simulation model allows analyzing the influence of such factors as: difference between group velocities of the first and second harmonics, self-phase modulation, and dispersive spreading of radiation pulses. The model was based on solving a system of nonlinear Schrodinger equations for the first and second harmonics in slowly varying wave approximation [5]. The system of equations describing the process of second harmonic generation in the approximation of slowly varying amplitudes has the following form:

$$\frac{\partial A_1}{\partial z} + iD_1 \frac{\partial^2 A_1}{\partial \eta^2} + iD_\perp \Delta_\perp A_1 + i\gamma A_1^* A_2 e^{-i\Delta kx} + i\alpha_1 A_1(|A_1|^2 + 2|A_2|^2) = 0, \quad 0 < z < L_z, \quad (1)$$

$$\frac{\partial A_2}{\partial z} + \nu \frac{\partial A_2}{\partial \eta} + iD_2 \frac{\partial^2 A_2}{\partial \eta^2} + iD_\perp \Delta_\perp A_2 + i\gamma A_1^2 e^{i\Delta kx} + i\alpha_2 A_1 (2|A_1|^2 + |A_2|^2) = 0, \quad \alpha_2 = 2\alpha_1 = 2\alpha, \tag{2}$$

$$\Delta_\perp = \frac{1}{r}\frac{\partial}{\partial r}(r\frac{\partial}{\partial r}), \tag{3}$$

where η is the dimensionless time in the main coordinate system accompanying the pulse, z is the longitudinal coordinate, $D_j \sim -0.5\dfrac{\partial^2 k}{\partial \omega^2}$ are the coefficients characterizing the second-order dispersion, γ is the coefficient of nonlinear coupling of the interacting waves, $\Delta k = k_2 - 2k_1$ is the detuning of the wave numbers. The complex amplitudes of the harmonics normalized to the maximum amplitude of the first harmonic are taken in the initial section of medium (z = 0). The parameter ν is proportional to the difference between the reciprocal values of the group velocities of the second harmonic waves and the fundamental frequency, L_z is the length of the nonlinear medium.

The initial distribution of first harmonic amplitude is modeled by a Gaussian pulse taking into account the normalization and chirp parameter C:

$$A(\eta, r) = exp(-(1+iC)((\eta - L_t/2)/\tau)^2/2 - (r/r_0)^2/2). \tag{4}$$

Such chirped pulse can be compressed to transform limited one with the duration $\sqrt{1+C^2}$ shorter than the original. The coefficient γ was determined from experimental data, ν and D_j were calculated using the Selmeyer formula by differentiating n with respect to the wavelength [6]:

$$n_0^2 = 2.259276 + \frac{13.00522\lambda^2}{\lambda^2 - 400} + \frac{0.01008956}{\lambda^2 - 0.0129426}; \tag{5}$$

$$n_e^2 = 2.132668 + \frac{3.2279924\lambda^2}{\lambda^2 - 400} + \frac{0.008637494}{\lambda^2 - 0.0122810}. \tag{6}$$

For the analysis, we took conditions close to the experimental ones, namely: wavelength of the first harmonic was 950 nm, duration of the transform limited pulse was 60 fs and 700 fs for chirped pulse, and 10 mJ energy. The conversion to the second harmonic was simulated in a KDP crystal of 1st phase-matching type with thickness of 2 mm.

The phase matching angle ($\theta = 41.6°$) was found from the dependence $n_o(950\ nm) = n_e(475\ nm)$, and the spectral phase matching width ($\Delta\lambda = 8.5\ nm$) from the condition $\sin c^2\left(\frac{\Delta k L}{2}\right) = 0.5$, where $\Delta k = k(950 + \Delta\lambda) - k(475 + \Delta\lambda/2)$. Since the total spectrum width is 18 nm, the narrowing effect due to the finite phase matching width can be neglected during conversion.

2. Results and discussion

To clarify our experimental data, Fig. 1 shows the spectral composition of second harmonic radiation for transform limited (1) and chirped (2) pulses. It can be seen that when a chirped pulse is used, approximately one and a half times, rather than a twofold broadening of the spectrum, as in [1], is observed.

The task of our calculations was to find the reasons for this behavior of SH spectrum and verify the analytical conclusion [1] taking into account all main processes accompanying the second harmonic generation process: dispersive spreading of pulses, runaway of pulses in the crystal thickness due to difference in group velocities, effect of Kerr nonlinearity, etc. Let us

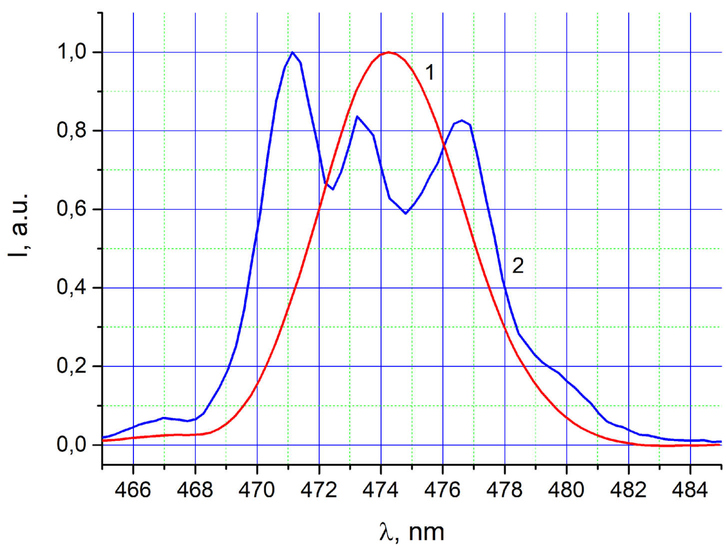

Fig. 1. Spectra of SH radiation pulses: 1 — transform limited pulse, 2 — negatively chirped pulse

begin with analysis of the results of [1], where the task of chirped pulse converting was carried out analytically neglecting the effects of dispersion and nonlinearity. In the case of transform limited pulse (the pump envelope has the form $\exp(-t^2)$) and with a low conversion efficiency in SH, its envelope will look like $\exp(-2t^2)$. This means that the pulse duration will be reduced by $\sqrt{2}$ times. Accordingly the spectral width should increase (up to 7.8 nm with pulse duration at the first harmonic of 60 fs). With increase of conversion efficiency the pulse at second harmonic approaches to the pulse of first harmonic $\exp(-t^2)$, that is, its duration increases and the spectrum narrows. If a chirped pulse $\exp(-(1+iC)t^2)$ is converted, then with low conversion efficiency for SH pulse the expression $\exp(-(1+iC)(\sqrt{2}t)^2)$ will be valid. With increasing of efficiency, this expression tends to $\exp(-(1+2iC)t^2)$. A chirped pulse $\exp(-(1+iC)t^2)$ with a chirp parameter C can be compressed to a transform limited one, while shortening the duration in $\sqrt{1+C^2}$ times.

From this it can be seen that the ratio of minimum pulse duration at first harmonic to second is for low conversion efficiency $\dfrac{1}{\sqrt{1+C^2}}\Big/\dfrac{1}{\sqrt{2}\sqrt{1+C^2}}=\sqrt{2}$, and for high efficiency it can reach 2, according to the relation $d\dfrac{1}{\sqrt{1+C^2}}\Big/\dfrac{1}{\sqrt{1+4C^2}}$. Thus, for a chirped pulse, the opposite process takes place — the spectrum width increases with an increase in the conversion efficiency.

Simulations showed that self-phase modulation and dispersive spreading of pulses insignificantly effect on SH emission spectrum broadening. In Fig. 2 shows the calculation results showing the dependence of SH radiation spectrum width on conversion efficiency for negatively chirped and transform limited pulses.

It can be seen that general trend remains with the results obtained in [1], where approximate consideration was used, namely: with increase of conversion efficiency the spectral width of second harmonic increases in case of first harmonic chirped pulse, and decreases for transform limited pulse. Analysis of the factors influencing broadening of SH spectrum in simulation showed that the main factor limiting the broadening of SH spectrum during the transformation of chirped pulse was the difference in group velocities. The dispersion of group velocities limited the broadening at level $K=\Delta\lambda_{ch}/\Delta\lambda=1.1$, where $\Delta\lambda_{ch}$ is the width of the second harmonic spectrum upon pumping with chirped pulse, and $\Delta\lambda$ — upon pumping by transform limited

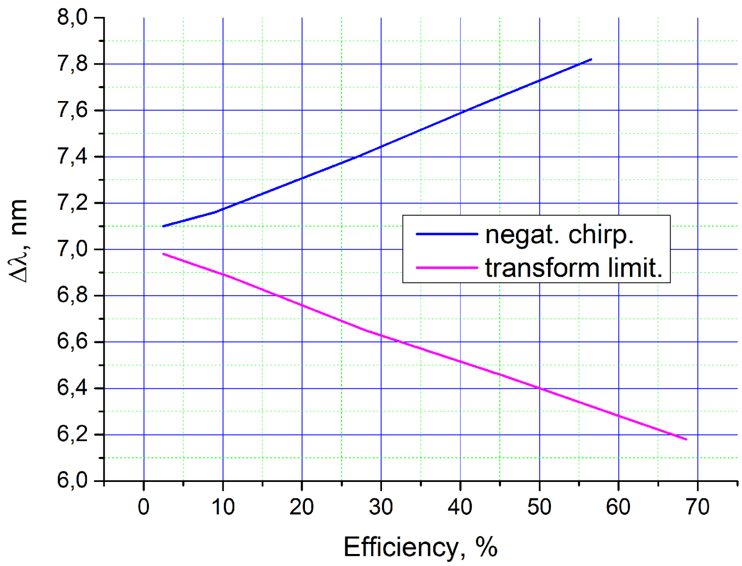

Fig. 2. Dependence of the width of SH radiation spectrum on conversion efficiency for 2 mm KDP crystal

pulse. This is less than theoretically possible $K = 1.4$, which can be obtained with low conversion efficiency. Nevertheless, taking into account the decrease of second harmonic spectrum width upon the transformation of transform limited first-harmonic pulse with increase of conversion efficiency, in the calculation, the spectral width for chirped pulse at high conversion efficiency was 1.3 times greater than conversion of transform limited pulse. This calculated value is close to that obtained experimentally (Fig. 1).

Conclusion

Thus, in result of numerical simulation of second harmonic spectrum broadening in KDP upon pumping by negatively chirped pulse of fundamental frequency with central wavelength of 950 nm and pulse duration of 700 fs, a fairly good agreement was obtained between the spectrum broadening ($K = 1.3$) and experimental result ($K = 1.4$). It was shown that SH spectrum broadening is mainly limited by the difference in group velocities of radiation pulse of first and second harmonics.

The experimental study was carried out with the financial support of Russian Foundation for Basic Research within the framework of scientific project no. 18-08-00383 and numerical calculations with financial support of Russian Science Foundation for no. 19-11-00113.

References

[1] S.V.Alekseev, A.I.Aristov, N.G.Ivanov, et all., Multi-terawatt femtosecond laser system of visible range based on a photochemical XeF(C-A) amplifier, *Laser and Particle Beams,* **31**(2013), 17–21. DOI: 10.1017/S0263034612000870

[2] S.V.Alekseev, A.I.Aristov, Ya.V.Grudtsyn, et all., Visible-range hybrid femtosecond systems based on a XeF(C-A) amplifier: state of the art and prospects, *Quantum Electronics,* **43**(2013), 190–200. DOI: 10.1070/QE2013v043n03ABEH015096

[3] S.V.Alekseev, M.V.Ivanov, N.G.Ivanov, V.F.Losev, Influence of chirp of the fundamental frequency pulse radiation on the spectral-time characteristics of second harmonic , *Izvestiya vuzov. Fizika*, **12**(2019), 151–155 (in Russian). DOI: 10.17223/00213411/62/12/151

[4] N.V.Didenko, A.V.Konyashchenko, L.L.Losev, et all., Femtosecond pulse compression based on second harmonic generation from a frequency chirped pulse, *Optics Communications*, **282**(2009), 997–999.

[5] V.A.Trofimov, T.M.Lysak, Highly efficient SHG of a sequence of laser pulses with a random peak intensity and duration, *Optics and Spectroscopy*, **107**(2009), 399–406. DOI: 10.1134/S0030400X0909015X

[6] V.G.Dmitriev, G.G.Gurzadyan, D.N.Nikogosyan, Handbook of Nonlinear Optical Crystals, *Third Revision, Springer series in optical sciences, Springer Berlin*, **64**(1999), 78–85.

Анализ условий уширения спектра второй гармоники в КДП при накачке чирпированным импульсом основной частоты

Сергей В. Алексеев
Валерий Ф. Лосев
Институт сильноточной электроники СО РАН
Томск, Российская Федерация
Яков В. Грудцын
Андрей В. Корибут
Физический институт имени П. Н. Лебедева
Москва, Российская Федерация
Вячеслав А. Трофимов
Южно-Китайский университет технологий
Гуанчжоу, Китай

Аннотация. Численно анализируются условия уширения спектра второй гармоники в КДП при накачке отрицательно чирпированным импульсом основной частоты с центральной длиной волны 950 нм. Показывается, что величина уширения спектра (K = 1.4) в основном ограничивается разностью групповых скоростей импульса излучения первой и второй гармоник. Статья подготовлена по материалам доклада на Первой Всероссийской научной конференции с международным участием «ЕНИСЕЙСКАЯ ФОТОНИКА — 2020».

Ключевые слова: фемтосекундный лазерный импульс, вторая гармоника, спектр, эффективность, длительность импульса.

DOI: 10.17516/1997-1397-2021-14-2-150-158
УДК 517.9

Fixed Points of Set-valued F-contraction Operators in Quasi-ordered Metric Spaces with an Application to Integral Equations

Ehsan Lotfali Ghasab*
Hamid Majani†
Department of Mathematics
Shahid Chamran University of Ahvaz
Ahvaz, Iran
Ghasem Soleimani Rad‡
Young Researchers and Elite club, West Tehran Branch
Islamic Azad University
Tehran, Iran

Received 01.01.2020, received in revised form 22.09.2020, accepted 20.11.2020

Abstract. In this paper, we prove some new fixed point theorems involving set-valued F-contractions in the setting of quasi-ordered metric spaces. Our results are significant since we present Banach contraction principle in a different manner from that which is known in the present literature. Some examples and an application to existence of solution of Volterra-type integral equation are given to support the obtained results.

Keywords: fixed point, sequentially complete metric spaces, F-contraction, ordered-close operator.

Citation: E.L. Ghasab, H. Majani, G.S.Rad, Fixed Points of Set-valued F-contraction Operators in Quasi-ordered Metric Spaces with an Application to Integral Equations, J. Sib. Fed. Univ. Math. Phys., 2021, 14(2), 150–158. DOI: 10.17516/1997-1397-2021-14-2-150-158.

1. Introduction and preliminaries

It is well known that the Banach contraction principle is a very useful and classical tool in nonlinear analysis [3]. After that, the generalization of this principle has been a heavily investigated. For example, in 1969, Nadler [10] extended the Banach contraction principle for set-valued mapping as follows:

Theorem 1.1. *Let (X,d) be a complete metric space and $T : X \to CB(X)$ be a set-valued operator. Also, let $H : N(X)^2 \to [0,+\infty]$ be the Hausdorff metric on $N(X)$ which defined by*

$$H(A,B) = \max\left\{\sup_{a\in A} D(a,B), \sup_{b\in B} D(b,A)\right\},$$

where $D(a,B) = D(B,a) = \inf_{b\in B} d(a,b)$. Assume that there exists $\alpha \in [0,1)$ such that $H(Tx,Ty) \leqslant \alpha d(x,y)$ for all $x,y \in X$. Then T has a fixed point in X.

*e-lotfali@stu.scu.ac.ir https://orcid.org/0000-0002-8418-9351
†Correspondent: h.majani@scu.ac.ir; majani.hamid@gmail.com https://orcid.org/0000-0001-7022-6513
‡gha.soleimani.sci@iauctb.ac.ir; gh.soleimani2008@gmail.com https://orcid.org/0000-0002-0758-2758

Then Ćirić [6] extended Nadler's result as follows:

Theorem 1.2. *Let (X,d) be a complete metric space and $T : X \to CB(X)$ be a set-valued operator. Assume that there exists $\alpha \in [0,1)$ such that $H(Tx,Ty) \leqslant \alpha M(x,y)$ for all $x,y \in X$, where*

$$M(x,y) = \max\left\{d(x,y), D(x,Tx), D(y,Ty), \frac{1}{2}[D(x,Ty) + D(y,Tx)]\right\}.$$

Then T has a fixed point in X.

In 2011, Amini-Harandi [2] considered some fixed point theorem for set-valued quasi-contraction mappings in metric spaces.

Theorem 1.3 ([2])**.** *Let (X,d) be a complete metric space and $T : X \to CB(X)$ be a k-set-valued quasi-contraction with $k \in \left[0, \frac{1}{2}\right)$; that is,*

$$H(Tx,Ty) \leqslant k \max\{d(x,y), D(x,Tx), D(y,Ty), D(x,Ty), D(y,Tx)\}$$

for all $x,y \in X$. Then T has a fixed point in X.

On the other hands, Ran and Reurings [12], and Nieto and Rodríguez-López [11] studied the Banach contraction principle distinctly from another point of view. They imposed a partial order to the metric space (X,d) and discussed on the existence and uniqueness of fixed points for contractive conditions and for the comparable elements of X (also, see [1, 4, 6–8, 13, 15]). Moreover, in 2012, Wardowski [14] obtained a new fixed point theorem concerning F-contraction for single-valued mapping.

Theorem 1.4 ([14])**.** *Let (X,d) be a complete metric space and $T : X \to X$ be an F-contraction. Then T has an unique fixed point $x^* \in X$ and for every $x_0 \in X$ a sequence $\{T^n x_0\}_{n\in\mathbb{N}}$ is convergent to x^*.*

In this paper, we obtain several fixed point results for set-valued F-contraction mappings in quasi-ordered metric spaces. Also, we prepare some examples and an application to the existence of a solution for Volterra-type integral equation. Throughout this paper, the family of all nonempty closed and bounded subsets of X is denoted by $CB(X)$, and the family of all nonempty subsets of X by $N(X)$.

Definition 1.1 ([9])**.** Let (X,d) be a metric space with a quasi-order " $\preceq$ " (pre-order or pseudo-order; that is, a reflexive and transitive relation). We say that X is sequentially complete if every Cauchy sequence whose consecutive terms are comparable in X converges.

Definition 1.2 ([9])**.** Let (X,d) be a metric space with a quasi-order " $\preceq$ ". For two subsets A, B of X, we say that $A \sqsubseteq B$ if each $a \in A$ and each $b \in B$ imply that $a \preceq b$.

Definition 1.3 ([9])**.** Let (X,d) be a metric space with a quasi-order " $\preceq$ ".

(i) A subset $D \subset X$ is said to be approximative, if the set-valued mapping $P_D(x) = \{p \in D : d(x,D) = d(p,x)\}$ for all $x \in X$ has nonempty value.

(ii) The set-valued mapping $G : X \longrightarrow N(X)$ is said to be have approximative values (for short, AV), if Gx is approximative for each $x \in X$.

(iii) The set-valued mapping $G : X \longrightarrow N(X)$ is said to be have comparable approximative values (for short, CAV), if Gx has approximative values for each $x \in X$ and for each $z \in X$, there exists $y \in P_{Gz}(x)$ such that y is comparable to z.

(iv) The set-valued mapping $G : X \longrightarrow N(X)$ is said to be have upper comparable approximative values (for short, UCAV), if Gx has approximative values and for each $z \in X$, there exists $y \in P_{Gz}(x)$ such that $y \succeq z$.

(v) The set-valued mapping $G : X \longrightarrow N(X)$ is said to be have lower comparable approximative values (for short, LCAV), if Gx has approximative values and for each $z \in X$, there exists $y \in P_{Gz}(x)$ such that $y \preceq z$.

Definition 1.4 ([9])**.** The set-valued mapping G is said to has a fixed point if there exists $x \in X$ such that $x \in Gx$.

2. Main result

From the idea of Wardowski [14], we consider a new type of F-contraction for set-valued operator in quasi-ordered metric spaces as follows.

Definition 2.1. Let $H : N(X)^2 \to [0, +\infty]$ be the Hausdorff metric on $N(X)$ and $F : \mathbb{R}^+ \longrightarrow \mathbb{R}$ be a mapping satisfying the following conditions:

(F1) F is increasing, i.e., for all $a, b \in \mathbb{R}^+$ such that $a \leqslant b$, then $F(a) \leqslant F(b)$;

(F2) for each sequence $\{a_n\}_{n\in\mathbb{N}}$ of positive numbers $\lim\limits_{n\to\infty} a_n = 0$ if and only if $\lim\limits_{n\to\infty} F(a_n) = -\infty$;

(F3) there exists $k \in (0, 1)$ such that $\lim\limits_{\alpha\to 0^+} \alpha^k F(\alpha) = 0$.

A mapping $G : X \longrightarrow CB(X)$ is said to be an F-contraction if there exists $\tau > 0$ such that

$$H(Gx, Gy) > 0 \Longrightarrow \tau + F(H(Gx, Gy)) \leqslant F(d(x, y)) \tag{1}$$

for all $x, y \in X$.

Example 2.1. If $F(a) = \ln a + a$ for all $a > 0$ and $H : N(X)^2 \to [0, +\infty]$ is the Hausdorff metric on $N(X)$, then F satisfies (F1)–(F3) and each mapping $G : X \longrightarrow CB(X)$ is an F-contraction such that $H(Gx, Gy)e^{H(Gx,Gy)-d(x,y)} \leqslant e^{-\tau} d(x, y)$ for all $x, y \in X$.

Example 2.2. If $F(a) = \ln a$ for all $a > 0$ and $H : N(X)^2 \to [0, +\infty]$ is the Hausdorff metric on $N(X)$, then F satisfies (F1)–(F3) and each mapping $G : X \longrightarrow CB(X)$ is an F-contraction such that $H(Gx, Gy) \leqslant e^{-\tau} d(x, y)$ for all $x, y \in X$.

Definition 2.2. Ordered-close operator is set-valued operator $G : X \to CB(X)$ if for two monotone sequences $\{x_n\}, \{y_n\} \subset X$ and $x_0, y_0 \in X$; $x_n \to x_0$, $y_n \to y_0$ and $y_n \in G(x_n)$ imply $y_0 \in G(x_0)$.

Theorem 2.1. *Let $(X, d, \preceq)$ be a sequentially complete metric space. Also, let the mapping $G : X \longrightarrow CB(X)$ be an ordered-close set-valued F-contraction and has UCAV. Then G has a fixed point $x^* \in X$.*

Proof. Let $x_0 \in X$. If $x_0 \in Gx_0$, then our proof is complete. Otherwise, since G has UCAV, there exists $x_1 \in Gx_0$ with $x_0 \neq x_1$ and $x_0 \preceq x_1$ such that $d(x_0, x_1) = \inf\limits_{x\in Gx_0} d(x_0, x) = D(x_0, Gx_0)$. Continue this procedure, we obtain a non-decreasing sequence $\{x_n\}$, where $x_n \in Gx_{n-1}$ with $x_{n-1} \preceq x_n$ and $x_{n-1} \neq x_n$ such that $d(x_n, x_{n+1}) = \inf\limits_{x\in Gx_n} d(x_n, x) = D(x_n, Gx_n)$. On the other hand,

$$D(x_n, Gx_n) \leqslant \sup_{x\in Gx_{n-1}} D(x, Gx_n) \leqslant H(Gx_n, Gx_{n-1}).$$

Therefore, $d(x_n, x_{n+1}) \leqslant H(Gx_n, Gx_{n-1})$. From (F1), we have $F(d(x_n, x_{n+1})) \leqslant F(H(Gx_n, Gx_{n-1}))$. In addition, G is F-contraction. Thus,

$$\begin{aligned} F(d(x_n, x_{n+1})) &\leqslant F(H(Gx_n, Gx_{n-1})) \\ &\leqslant F(d(x_n, x_{n-1})) - \tau \\ &\leqslant F(d(x_{n-2}, x_{n-1})) - 2\tau \\ &\leqslant \\ &\ \ \vdots \\ &\leqslant F(d(x_0, x_1)) - n\tau. \end{aligned} \tag{2}$$

We obtain $\lim\limits_{n\to\infty} F(d(x_n, x_{n+1})) = -\infty$ that together with (F2) gives

$$\lim_{n\to\infty} d(x_n, x_{n+1}) = 0. \tag{3}$$

Denote $\gamma_n = d(x_n, x_{n+1})$. By (F3), there exists $k \in (0, 1)$ such that

$$\lim_{n\to\infty} \gamma_n^k F(\gamma_n) = 0. \tag{4}$$

By (2), we have

$$\gamma_n^k F(\gamma_n) - \gamma_n^k F(\gamma_0) \leqslant \gamma_n^k (F(\gamma_0) - n\tau) - \gamma_n^k F(\gamma_0) = -\gamma_n^k n\tau \leqslant 0 \tag{5}$$

for all $n \in \mathbb{N}$. Letting $n \to \infty$ in (5), and applying (3) and (4), we obtain $\lim\limits_{n\to\infty} n\gamma_n^k = 0$. Hence, there exists $n_1 \in \mathbb{N}$ such that $n\gamma_n^k \leqslant 1$ for each $n \geqslant n_1$. Consequently, we have

$$\gamma_n \leqslant \frac{1}{\sqrt[k]{n}} < 1 \tag{6}$$

for all $n \geqslant n_1$. In order to show that $\{x_n\}$ is a Cauchy sequence, let $m, n \in \mathbb{N}$ with $m > n \geqslant n_1$. From the definition of the metric and (6), we obtain

$$d(x_n, x_m) \leqslant \gamma_{m-1} + \gamma_{m-2} + \cdots + \gamma_n < \sum_{i=n}^{\infty} \gamma_i \leqslant \sum_{i=n}^{\infty} \frac{1}{\sqrt[k]{i}}. \tag{7}$$

From (7) and the convergence of the series $\sum\limits_{i=n}^{\infty} \frac{1}{\sqrt[k]{i}}$, we conclude that $\{x_n\}$ is Cauchy sequence. From the completeness of X, there exists $x^* \in X$ such that $\lim\limits_{n\to\infty} x_n \to x^*$. Since G is ordered-close operator, $\{x_n\}$ is monotone and $x_{n+1} \in G(x_n)$, we deduce $x^* \in G(x^*)$ and x^* is a fixed point of G. □

Theorem 2.2. *Let $(X, d, \preceq)$ be a sequentially complete metric space. Also, let the mapping $G : X \to CB(X)$ be an ordered-close set-valued F-contraction and has LCAV. Then G has a fixed point $x^* \in X$.*

Proof. The proof is similar to Theorem 2.1. □

Example 2.3. Consider the sequence $\{S_n\}_{n\in\mathbb{N}}$ by $S_1 = 1$ and $S_n = 1 + 2 + \cdots + n = \dfrac{n(n+1)}{2}$ for all $n \in \mathbb{N}$. Let $X = \{S_n : n \in \mathbb{N}\}$ and $d(x, y) = |x - y|$ for all $x, y \in X$. Also, we define the relation " $\preceq$ " on X by $x \preceq y \Leftrightarrow S_p \leqslant S_q$ for all $x = S_p$, $y = S_q \in X$. Then $(X, d, \preceq)$ is a sequentially complete metric space. Also, let the mapping $G : X \to CB(X)$ be a ordered-close set-valued mapping and has LCAV defined by $G(S_1) = \{S_1\}$ and $G(S_n) = [1, S_{n-1}]$ for all $n > 1$. Then G is an F-contraction with F as in Example 2.1 and $\tau = 1$. To see this, let us consider the following calculations:

For each $m, n \in \mathbb{N}$ with $m > 2$ and $n = 1$, we have

$$H(G(S_m), G(S_1)) = \max\left\{ \sup_{a\in G(S_m)} D(a, G(S_1)), \sup_{b\in G(S_1)} D(b, G(S_m))\right\} = d(S_{m-1}, S_1)$$

and

$$\begin{aligned}\frac{H(G(S_m), G(S_1))}{d(S_m, S_1)} e^{H(G(S_m),G(S_1))-d(S_m,S_1)} &= \frac{d(S_{m-1}, S_1)}{d(S_m, S_1)} e^{d(S_{m-1},S_1)-d(S_m,S_1)} = \\ &= \frac{S_{m-1} - 1}{S_m - 1} e^{S_{m-1}-S_m} = \\ &= \frac{m^2 - m - 2}{m^2 + m - 2} e^{-m} < e^{-m} < e^{-1}.\end{aligned}$$

Now, for each $m, n \in \mathbb{N}$ with $m > n > 1$, we have

$$H(G(S_m), G(S_n)) = \max\left\{ \sup_{a\in G(S_m)} D(a, G(S_n)), \sup_{b\in G(S_n)} D(b, G(S_m))\right\} = d(S_{m-1}, S_{n-1})$$

and

$$\begin{aligned}\frac{H(G(S_m), G(S_n))}{d(S_m, S_n)} e^{H(G(S_m),G(S_n))-d(S_m,S_n)} &= \frac{d(S_{m-1}, S_{n-1})}{d(S_m, S_n)} e^{d(S_{m-1},S_{n-1})-d(S_m,S_n)} = \\ &= \frac{S_{m-1} - S_{n-1}}{S_m - S_n} e^{S_n-S_{n-1}+S_{m-1}-S_m} = \\ &= \frac{m + n - 1}{m + n + 1} e^{n-m} < e^{n-m} < e^{-1}.\end{aligned}$$

Therefore, by Theorem 2.2, S_1 is a fixed point of G.

Theorem 2.3. *Let $(X, d, \preceq)$ be a sequentially complete metric space. Suppose that the mapping $G : X \to CB(X)$ is an ordered-close set-valued F-contraction and has AV. If there exists $x_0 \in X$ such that $\{x_0\} \sqsubseteq Gx_0$, then G has a fixed point $x^* \in X$.*

Proof. If $x_0 \in Gx_0$, then the proof is finished. Otherwise, by Definition 1.2, we have $x \succeq x_0$ for any $x \in Gx_0$. Since G has approximative values, there exists $x_1 \in Gx_0$ with $x_1 \succeq x_0$ and $x_0 \neq x_1$ such that $d(x_0, x_1) = D(x_0, Gx_0)$. Continue this procedure, we have a non-decreasing sequence $\{x_n\}$ with $x_{n-1} \preceq x_n$, where $x_n \in Gx_{n-1}$ and $x_n \neq x_{n-1}$ such that $d(x_n, x_{n+1}) = = \inf_{x\in Gx_n} d(x_n, x) = D(x_n, Gx_n)$. The rest of this proof is the same as that of Theorem 2.1. □

Theorem 2.4. *Let $(X, d, \preceq)$ be a sequentially complete metric space. Suppose that the mapping $G : X \to CB(X)$ be an ordered-close set-valued F-contraction and has AV. If there exists $x_0 \in X$ such that $Gx_0 \sqsubseteq \{x_0\}$, then G has a fixed point $x^* \in X$.*

Proof. The proof is similar to Theorem 2.2. □

Theorem 2.5. *Let $(X, d, \preceq)$ be a sequentially complete metric space. Also, let the mapping $G : X \longrightarrow CB(X)$ be an ordered-close set-valued and has UCAV. If we have*

$$F(H(Gx, Gy)) \leqslant F(M(x, y)) - \tau \tag{8}$$

for all $x, y \in X$, where

$$M(x,y) = \max\left\{d(x,y), D(x,Gx), D(y,Gy), \frac{1}{2}[D(x,Gy)+D(y,Gx)]\right\},$$

then G has a fixed point $x^* \in X$.

Proof. Let $x_0 \in X$. If $x_0 \in Gx_0$, then the proof is complete. Otherwise, Since G has UCAV, there exists $x_1 \in Gx_0$ with $x_0 \neq x_1$ and $x_0 \preceq x_1$ such that $d(x_0,x_1) = \inf\limits_{x\in Gx_0} d(x_0,x) = D(x_0,Gx_0)$. Continue this procedure, we obtain a non-decreasing sequence $\{x_n\}$ with $x_{n-1} \preceq x_n$, where $x_n \in Gx_{n-1}$ and $x_n \neq x_{n-1}$ such that $d(x_n,x_{n+1}) = \inf\limits_{x\in Gx_n} d(x_n,x) = D(x_n,Gx_n)$. On the other hand,

$$D(x_n,Gx_n) \leqslant \sup_{x\in Gx_{n-1}} D(x,Gx_n) \leqslant H(Gx_n,Gx_{n-1}).$$

Therefore, $d(x_n,x_{n+1}) \leqslant H(Gx_n,Gx_{n-1})$. Now, from $(F1)$ and (8) we have

$$F(d(x_n,x_{n+1})) \leqslant F(H(Gx_n,Gx_{n-1})) \leqslant F(M(x_n,x_{n-1})) - \tau$$

for all $n \in \mathbb{N}$, where

$$\begin{aligned} &M(x_n,x_{n-1}) = \\ &\quad = \max\left\{d(x_n,x_{n-1}), D(x_n,Gx_n), D(x_{n-1},Gx_{n-1}), \frac{1}{2}[D(x_n,Gx_{n-1})+D(x_{n-1},Gx_n)]\right\}.\end{aligned}$$

Once more, note that $x_{n+1} \in Gx_n$ and $D(x_n,Gx_n) = d(x_n,x_{n+1})$. Hence, we have

$$\begin{aligned} M(x_n,x_{n-1}) &\leqslant \max\left\{d(x_n,x_{n-1}), d(x_n,x_{n+1}), d(x_{n-1},x_n), \frac{1}{2}[d(x_n,x_n)+d(x_{n-1},x_{n+1})]\right\} \leqslant \\ &\leqslant \max\left\{d(x_n,x_{n-1}), d(x_n,x_{n+1}), \frac{1}{2}[d(x_{n-1},x_n)+d(x_n,x_{n+1})]\right\} \leqslant \\ &\leqslant \max\{d(x_n,x_{n-1}), d(x_n,x_{n+1})\}.\end{aligned}$$

If $\max\{d(x_n,x_{n-1}), d(x_n,x_{n+1})\} = d(x_n,x_{n+1})$, then $F(d(x_n,x_{n+1})) \leqslant F(d(x_n,x_{n+1})) - \tau$, which contradicts with $\tau > 0$. Thus, we have $F(d(x_n,x_{n+1})) \leqslant F(d(x_n,x_{n-1})) - \tau$. The rest of the proof is in the similar manner given in Theorem 2.1. □

Theorem 2.6. *Let $(X,d,\preceq)$ be a sequentially complete metric space. Assume that the mapping $G : X \longrightarrow CB(X)$ is an ordered-close set-valued and has LCAV, and $F(H(Gx,Gy)) \leqslant F(M(x,y)) - \tau$ for all $x, y \in X$, where*

$$M(x,y) = \max\left\{d(x,y), D(x,Gx), D(y,Gy), \frac{1}{2}[D(x,Gy)+D(y,Gx)]\right\}.$$

Then G has a fixed point $x^* \in X$.

Proof. Let $x_0 \in X$. If $x_0 \in Gx_0$, then the proof is complete. Otherwise, Since G has LCAV, there exists $x_1 \in Gx_0$ with $x_0 \neq x_1$ and $x_1 \preceq x_0$ such that $d(x_0,x_1) = \inf\limits_{x\in Gx_0} d(x_0,x) = D(x_0,Gx_0)$. Continue this procedure, we obtain a non-increasing sequence $\{x_n\}$ with $x_n \preceq x_{n-1}$, where $x_n \in Gx_{n-1}$ and $x_n \neq x_{n-1}$ such that $d(x_n,x_{n+1}) = \inf\limits_{x\in Gx_n} d(x_n,x) = D(x_n,Gx_n)$. The rest of this proof is the same as that of Theorem 2.5. □

Theorem 2.7. *Let $(X, d, \preceq)$ be a sequentially complete metric space. Assume that the mapping $G : X \to CB(X)$ is an ordered-close set-valued and has AV, and $F(H(Gx, Gy)) \leqslant F(M(x, y)) - \tau$ for all $x, y \in X$, where*

$$M(x,y) = \max\left\{d(x,y), D(x,Gx), D(y,Gy), \frac{1}{2}[D(x,Gy) + D(y,Gx)]\right\}.$$

If there exists $x_0 \in X$ such that $\{x_0\} \sqsubseteq Gx_0$, then G has a fixed point $x^* \in X$.

Proof. If $x_0 \in Gx_0$, then the proof is finished. Otherwise, by Definition 1.2, we have $x \succeq x_0$ for any $x \in Gx_0$. Since G has approximative values, there exists $x_1 \in Gx_0$ with $x_1 \succeq x_0$ and $x_0 \neq x_1$ such that $d(x_0, x_1) = D(x_0, Gx_0)$. Continue this procedure, we have a non-decreasing sequence $\{x_n\}$ with $x_{n-1} \preceq x_n$, where $x_n \in Gx_{n-1}$ and $x_n \neq x_{n-1}$ such that $d(x_n, x_{n+1}) = = \inf_{x \in Gx_n} d(x_n, x) = D(x_n, Gx_n)$. The rest of this proof is the same as that of Theorem 2.5. □

Theorem 2.8. *Let $(X, d, \preceq)$ be a sequentially complete metric space. Assume that the mapping $G : X \to CB(X)$ is an ordered-close set-valued and has AV, and $F(H(Gx, Gy)) \leqslant F(M(x, y)) - \tau$ for all $x, y \in X$, where*

$$M(x,y) = \max\left\{d(x,y), D(x,Gx), D(y,Gy), \frac{1}{2}[D(x,Gy) + D(y,Gx)]\right\}.$$

If there exists $x_0 \in X$ such that $Gx_0 \sqsubseteq \{x_0\}$, then G has a fixed point $x^* \in X$.

Proof. If $x_0 \in Gx_0$, then the proof is finished. Otherwise, by Definition 1.2, we have $x_0 \succeq x$ for any $x \in Gx_0$. Since G has approximative values, there exists $x_1 \in Gx_0$ with $x_0 \succeq x_1$ and $x_0 \neq x_1$ such that $d(x_0, x_1) = D(x_0, Gx_0)$. Continue this procedure, we have a non-increasing sequence $\{x_n\}$ with $x_n \preceq x_{n-1}$, where $x_n \in Gx_{n-1}$ and $x_n \neq x_{n-1}$ such that $d(x_n, x_{n+1}) = = \inf_{x \in Gx_n} d(x_n, x) = D(x_n, Gx_n)$. The rest of this proof is the same as that of Theorem 2.5. □

3. Application to integral equation

As an application of our results, we will consider the following Volterra integral equation:

$$x(t) = \int_0^t K(t, s, x(s))ds + g(t), \tag{9}$$

where $I = [0, 1]$, $K \in C(I \times I \times \mathbb{R}, \mathbb{R})$ and $g \in C(I, \mathbb{R})$ for all $t \in I$.

Let $C(I, \mathbb{R})$ be the Banach space of all real continuous functions defined on I with the sup norm $||x||_\infty = \max_{t \in I} |x(t)|$ for all $x \in C(I, \mathbb{R})$ and $C(I \times I \times C(I, \mathbb{R}), \mathbb{R})$ be the space of all continuous functions defined on $I \times I \times C(I, \mathbb{R})$. Alternatively, the Banach space $C(I, \mathbb{R})$ can be endowed with Bielecki norm $||x||_B = \sup_{t \in I}\{|x(t)|e^{-\tau t}\}$ for all $x \in C(I, \mathbb{R})$ and $\tau > 0$, and the induced metric $d_B(x, y) = ||x - y||_B$ for all $x, y \in C(I, \mathbb{R})$ (see [5]). Also, let $f : C(I, \mathbb{R}) \to C(I, \mathbb{R})$ defined by $fx(t) = \int\limits_0^t K(t, s, x(s))ds + g(t)$ and $g \in C(I, \mathbb{R})$. Moreover, we define the relation "$\preceq$" on $C(I, \mathbb{R})$ by $x \preceq y \Leftrightarrow ||x||_\infty \leqslant ||y||_\infty$ for all $x, y \in C(I, \mathbb{R})$. Clearly the relation "$\preceq$" is a quasi-order relation.

Theorem 3.1. *Let $(C(I, \mathbb{R}), d_B, \preceq)$ be a sequentially complete metric space. Suppose that $G : C(I, \mathbb{R}) \to CB(C(I, \mathbb{R}))$ is a set-valued operator such that $G(x) = \{fx(t)\}$ and has UCAV. Let $K \in C(I \times I \times \mathbb{R}, \mathbb{R})$ be an operator satisfying the following conditions:*

(i) *K is continuous;*

(ii) $\int\limits_0^t K(t,s,.)$ *for all* $t,s \in I$ *is increasing;*

(iii) *there exists* $\tau > 0$ *such that* $|K(t,s,x(s)) - K(t,s,y(s))| \leqslant e^{-\tau}|x(s) - y(s)|$ *for all* $x, y \in C(I,\mathbb{R})$ *and all* $t, s \in I$.

Then, the Volterra-type integral equation (9) *has a solution in* $C(I,\mathbb{R})$.

Proof. By definition of G, we have $H(Gx, Gy) = d_B(f(x), f(y))$ for all $x, y \in C(I,\mathbb{R})$. Thus,

$$\begin{aligned} H(Gx,Gy) = d_B(f(x),f(y)) &= \sup_{t\in I}\left\{\Big|\int_0^t K(t,s,x(s))ds - \int_0^t K(t,s,y(s))ds\Big|e^{-\tau t}\right\} \\ &\leqslant \sup_{t\in I}\left\{\int_0^t |K(t,s,x(s)) - K(t,s,y(s))|e^{-\tau t}ds\right\} \\ &\leqslant \sup_{t\in I}\left\{\int_0^t e^{-\tau}|x(s)-y(s)|e^{-\tau t}ds\right\} \\ &\leqslant ||x-y||_B \sup_{t\in I}\left\{\int_0^t e^{-\tau}ds\right\} \\ &= e^{-\tau}d_B(x,y). \end{aligned}$$

Taking logarithms, we have $\ln(H(Gx,Gy)) \leqslant \ln(e^{-\tau}d_B(x,y))$, which implies that $(\tau + \ln(H(Gx,Gy))) \leqslant \ln(d_B(x,y))$. Now, consider the function $F(t) = \ln(t)$ for all $t \in C(I,\mathbb{R})$ and $\tau > 0$. Then, all conditions of Theorem 2.1 are satisfied. Consequently, Theorem 2.1 ensures the existence of fixed point of G that this fixed point is the solution of the integral equation. □

We are grateful to the Research Council of Shahid Chamran University of Ahvaz for financial support (Grant number: SCU.MM99.25894).

References

[1] R.P.Agarwal, M.A.El-Gebeily, D.O'Regan, Generalized contractions in partially ordered metric spaces, *Appl. Anal.*, **87**(2008), 1–8.

[2] A.Amini-Harandi, Fixed point theory for set-valued quasi-contraction maps in metric spaces, *Appl. Math. Lett.*, **24**(2011), 1791–1794. DOI: 10.1016/j.aml.2011.04.033

[3] S.Banach, Surles operations dans les ensembles abstraits et leurs application auxequations integrales, *Fund. Math.*, **3**(1922), 133–181.

[4] T.G.Bhaskar, V.Lakshmikantham, Fixed point theorems in partially ordered metric spaces and applications, *Nonlinear Anal.*, **65**(2006), 1379–1393.

[5] A.Bielecki, Une remarque sur la methode de Banach-Cacciopoli-Tikhonov dans la theorie des equations differentielles ordinaires, *Bull. Acad. Polon. Sci. Ser. Sci. Math. Astronom. Phys.*, **4**(1956), 261–264.

[6] Lj.Ćirić, Fixed points for generalized multi-valued contractions, *Math. Ves.*, **24**(1972), 265–272.

[7] E.L.Ghasab, H.Majani, E.Karapinar, G.Soleimani Rad, New fixed point results in F-quasi-metric spaces and an application, *Adv. Math. Phys.*, **2020**, 2020:9452350.
DOI: 10.1155/2020/9452350

[8] Z.Kadelburg, S.Radenović, Notes on some recent papers concerning F-contractions in b-metric spaces, *Construct. Math. Anal.*, **1**(2018), 108–112.

[9] H.P.Masiha, F.Sabetghadam, Fixed point results for multi-valued operators in quasi-ordered metric spaces, *Appl. Math. Lett.*, **25**(2012), 1856–1861.

[10] S.B.Nadler, Multi-valued contraction mappings, *Pacific J. Math.*, **30**(1969), 475–488.

[11] J.J.Nieto, R.Rodriguez-Lopez, Contractive mapping theorems in partially ordered sets and applications to ordinary differential equations, *Order.*, **22**(2005), 223–239.

[12] A.C.M.Ran, M.C.B.Reurings, A fixed point theorem in partially ordered sets and some applications to matrix equations, *Proc. Amer. Math. Soc.*, **132**(2004), 1435–1443.

[13] R.Saadati, S.M.Vaezpour, Monotone generalized weak contractions in partially ordered metric spaces, *Fixed Point Theory.*, **11**(2010), 375–382.

[14] D.Wardowski, Fixed points of a new type of contractive mappings in complete metric spaces, *Fixed Point Theory Appl.*, **2012**, 2012:94.

[15] D.Wardowski, Solving existence problems via F-contractions, *Proc. Amer. Math. Soc.*, **146**(2018), 1585–1598.

Неподвижные точки многозначных операторов F-сжатия в квазиупорядоченных метрических пространствах с приложением к интегральным уравнениям

Эхсан Л. Гасаб
Хамид Маджани
Университет Шахида Чамрана в Ахвазе
Ахваз, Иран
Гасем С. Рад
Исламский университет Азад
Тегеран, Иран

Аннотация. В этой статье мы докажем некоторые новые теоремы о неподвижных точках, включающие многозначные F-сжатия в условиях квазиупорядоченных метрических пространств. Наши результаты важны, поскольку мы представляем принцип банахового сжатия иначе, чем тот, который известен в настоящей литературе. Для подтверждения полученных результатов приведены некоторые примеры и приложение к существованию решения интегрального уравнения типа Вольтерра.

Ключевые слова: неподвижная точка, F-сжатие, секвенциально полные метрические пространства, оператор упорядоченного замыкания.

DOI: 10.17516/1997-1397-2021-14-2-159-175
УДК 517.9

On the Theory of ψ-Hilfer Nonlocal Cauchy Problem

Mohammed A. Almalahi*
Satish K. Panchal†
Department of Mathematics
Dr. Babasaheb Ambedkar Marathwada University
Aurangabad (M.S), India

Received 10.08.2020, received in revised form 10.09.2020, accepted 20.11.2020

Abstract. In this paper, we derive the representation formula of the solution for ψ-Hilfer fractional differential equation with constant coefficient in the form of Mittag-Leffler function by using Picard's successive approximation. Moreover, by using some properties of Mittag-Leffler function and fixed point theorems such as Banach and Schaefer, we introduce new results of some qualitative properties of solution such as existence and uniqueness. The generalized Gronwall inequality lemma is used in analyze E_α-Ulam-Hyers stability. Finally, one example to illustrate the obtained results.

Keywords: fractional differential equations, fractional derivatives, E_α-Ulam-Hyers stability, fixed point theorem.

Citation: M.A. Almalahi, S.K. Panchal, On the Theory of ψ-Hilfer Nonlocal Cauchy Problem, J. Sib. Fed. Univ. Math. Phys., 2021, 14(2), 159–175. DOI: 10.17516/1997-1397-2021-14-2-159-175.

Introduction

In recent years, the scientific community has been paying more attention to fractional calculus because it is an effective tool in modeling many phenomenaIn various fields of engineering and science, since its non-local properties are suitable for describing memory phenomena such as non-local elasticity, polymers, diffusion in complex medium, biological, electrochemical chemistry, porous media, viscosity, electromagnetism, etc. For more details, we refer the reader to monographs of Kilbas et al. [12], Samko et al. [21], Hilfer [10], Podlubny [19] and the papers [5, 9]. In the recently years, Kilbas et al. in [12] introduced the properties of fractional integrals and fractional derivatives of a function with respect to another function. Sousa and Oliveira [22] proposed a ψ-Hilfer fractional operator and extended few previous works dealing with the Hilfer [7, 10]. Moreover, they discussed some important qualitative properties of solutions such as existence, uniqueness, and stability results in the following papers [18, 22–24]. Over the last years, the stability results of fractional differential equations have been robustly developed. Very significant contributions about this topic were introduced by Ulam [28], Hyers [11] and this type of stability is called Ulam-Hyers stability. Thereafter, the Ulam-Hyers stability was extended by Rassias [20] in 1978 to a new type of stability which called Ulam-Hyers-Rassias stability. For some recent results of stability analysis, we refer the reader to a series of papers [2, 3, 14, 17, 18, 24, 26, 30, 31]. For the existence and uniqueness results of different classes of initial value problem for fractional differential equations involving ψ-Hilfer derivative operator, one can see [1–4, 15, 27]. More recently, Wang and Li in [32] introduced four new types of E_α-Ulam stabilities. Gao et al., in [8] established the existence and uniqueness of solutions to the Hilfer nonlocal boundary value problem by using some properties of Hilfer fractional calculus, Mittag-Leffler functions, and fixed

*aboosama736242107@gmail.com https://orcid.org/0000-0001-5719-086X
†drpanchalsk@gmail.com

point methods. Kucche et al., in [13] obtained representation formula for the solution of Cauchy problem in the form of Mittag–Leffler function.

Motivated by [8, 13, 32], in this paper, we use Picard's successive approximation technique to obtain representation formula for the solution of linear Cauchy problem with constant coefficient

$$ {}^{H}D_{a^+}^{\alpha,\beta;\psi}y(t) = \lambda y(t)+h(t),\ n-1<\alpha<n,\ \beta\in[0,1],\ t\in J:=(a,b], \tag{0.1} $$

$$ y_{\psi}^{[n-j]}I_{a^+}^{n-\gamma;\psi}y(a) = c_j,\ j=1,2,\dots,n, \qquad \alpha\leqslant\gamma=\alpha+n\beta-\alpha\beta. \tag{0.2} $$

in the form of Mittag–Leffler function, where $y_{\psi}^{[n-j]}y(t) = \left(\frac{1}{\psi'(t)}\frac{d}{dt}\right)^{n-j}y(t),\ j=1,2,\dots,n.$ Furthermore, we introduce new results of some qualitative properties of solution such as existence, uniqueness, and E_{α}-stability results of a nonlinear ψ-Hilfer fractional differential equation

$$ {}^{H}D_{a^+}^{\alpha,\beta;\psi}y(t)=\lambda y(t)+f(t,y(t)),\quad \alpha\in(1,2),\quad \beta\in[0,1],\quad t\in J:=(a,b], \tag{0.3} $$

$$ y(a)=0,\qquad y(b)=\sum_{i=1}^{m}\delta_i I_{a^+}^{\zeta;\psi}y(\tau_i),\quad \tau_i\in(a,b]\ , \tag{0.4} $$

where ${}^{H}D_{a^+}^{\alpha,\beta,\psi}$denotes the ψ-Hilfer fractional derivative of order $\alpha\in(1,2)$, type $\beta\in[0,1]$, $\gamma=\alpha+\beta(2-\alpha)$, $\lambda<0$, $m\in\mathbb{N}$, and $f:(a,b]\times\mathbb{R}\longrightarrow\mathbb{R}$ is given function satisfying some assumptions that will be specified later.

To the best of our knowledge, this is the first paper dealing with ψ-Hilfer fractional derivative with constant coefficient of order $\alpha\in(1,2)$. In consequence, our findings of the present work will be a useful contribution to the existing literature on the topic.

This paper is organized as follows: In Section 2, we recall the basic definitions and prove some lemmas which are used throughout this paper, also we present the concepts of some fixed point theorems. In Section 3 , we derive representation formula for the solution of the problem (0.1)–(0.2) in the form of Mittag-Leffler function. Furthermore, we derive an equivalent fractional integral equation to the nonlocal problem (0.3)–(0.4). In Section 4, we study the existence and uniqueness results of ψ-Hilfer nonlocal problem (0.3)–(0.4) by using some properties of Mittag-Leffler function and fixed point theorems. In Section 5, we discuss E_{α}-Ulam-Hyers stability of solution to a given problem. In Section 6 we give one example to illustrate our results. Concluding remarks about our results in the last section.

1. Preliminary

Let $[a,b]\subset\mathbb{R}^+$ with $0<a<b<\infty$. For $\gamma=\alpha+\beta(2-\alpha)$, $1<\alpha<2$, $0\leqslant\beta\leqslant1$. Then $1<\gamma\leqslant2$. Let $\psi\in C^1[a,b]$ be an increasing function with $\psi'\neq0$, for all $t\in[a,b]$, the weighted space $C_{2-\gamma;\psi}[a,b]$ of continuous function $f:[a,b]\to\mathbb{R}$ is defined by

$$ C_{2-\gamma;\psi}[a,b]=\left\{f:(a,b]\to\mathbb{R};(\psi(t)-\psi(a))^{2-\gamma}f(t)\in C[a,b]\right\},\quad 1<\gamma\leqslant2. $$

Obviously $C_{2-\gamma;\psi}[a,b]$ is the Banach spaces with the norm

$$ \|f\|_{C_{2-\gamma;\psi[a,b]}}=\max_{t\in[a,b]}\left|(\psi(t)-\psi(a))^{2-\gamma}f(t)\right|. $$

Next, define $L_p([a,b],\mathbb{R})$ the Banach space of all Lebesgue measurable functions $\mu:[a,b]\to\mathbb{R}$ with $\|\mu\|_{L_p[a,b]}<\infty$.

Definition 1.1 ([12]). *Let $\alpha>0$, $f\in L_1[a,b]$. Then, the ψ-Riemann–Liouville fractional integral of a function f with respect to ψ is defined by*

$$ I_{a^+}^{\alpha,\psi}f(t)=\frac{1}{\Gamma(\alpha)}\int_a^t\psi'(s)(\psi(t)-\psi(s))^{\alpha-1}f(s)ds. $$

Definition 1.2 ([22]). *Let $n-1<\alpha<n\in\mathbb{N}$, and $f,\psi\in C^n[a,b]$ $(-\infty<a<b<\infty)$ be two functions such that ψ is increasing and $\psi'(t)\neq 0$, for all $t\in[a,b]$. The left-sided ψ-Hilfer fractional derivative of a function f of order α and type $0\leqslant\beta\leqslant 1$ is defined by*

$$^{H}D_{a^+}^{\alpha,\beta,\psi}f(t)=I^{\beta(n-\alpha);\psi}\left(\frac{1}{\psi'(t)}\frac{d}{dt}\right)^n I_{a^+}^{(1-\beta)(n-\alpha),\psi}f(t).$$

Lemma 1.1 ([12]). *Let $\alpha,\gamma>0$. Then*

(1) $I_{a^+}^{\alpha,\psi}I_{a^+}^{\nu,\psi}f(t)=I_{a^+}^{\alpha+\nu,\psi}f(t)$

(2) $I_{a^+}^{\alpha,\psi}(\psi(t)-\psi(a))^{\gamma-1}=\dfrac{\Gamma(\gamma)}{\Gamma(\alpha+\gamma)}(\psi(t)-\psi(a))^{\alpha+\gamma-1}$

(3) $^{H}D_{a^+}^{\gamma,\psi}(\psi(t)-\psi(a))^{\gamma-1}=0.$

Lemma 1.2 ([22]). *If $f\in C^n[a,b]$, $n-1<\alpha<n$, and $0\leqslant\beta\leqslant 1$, then*

$$I_{a^+}^{\alpha;\psi}\ {}^{H}D_{a^+}^{\alpha,\beta,\psi}f(t)=f(t)-\sum_{k=1}^{n}\frac{(\psi(t)-\psi(a))^{\gamma-k}}{\Gamma(\gamma-k+1)}f_{\psi}^{[n-k]}I_{a^+}^{(1-\beta)(n-\alpha);\psi}f(a),$$

where $f_{\psi}^{[n-k]}f(t)=\left(\dfrac{1}{\psi'(t)}\frac{d}{dt}\right)^{n-k}f(t).$

Theorem 1.1 ([6]). *(Banach fixed point theorem) Let X be a Banach space, $K\subset X$ be closed, and $G:K\to K$ be a strict contraction, i.e., $\|G(x)-G(y)\|\leqslant L\|x-y\|$ for some $0<L<1$ and all $x,y\in K$. Then G has a fixed point in K.*

Remark 1.1. *To simplify the notation and the proof of some results, we will introduce the following notation*

$$Q_{\psi}^{\gamma-2}(t,a)=(\psi(t)-\psi(a))^{\gamma-2}\qquad\text{and}\qquad\mathcal{N}_{\psi}^{\alpha-1}(t,s)=\psi'(s)(\psi(t)-\psi(s))^{\alpha-1}.$$

Lemma 1.3 ([29]). *Let $\alpha\in(1,2]$ and $\beta>0$ be arbitrary. The function $E_\alpha(\cdot)$, $E_{\alpha,\alpha}(\cdot)$ and $E_{\alpha,\beta}(\cdot)$ are nonnegative, and for all $z<0$*

$$E_\alpha(z):=E_{\alpha,1}(z)\leqslant 1,\quad E_{\alpha,\alpha}(z)\leqslant\frac{1}{\Gamma(\alpha)},\quad E_{\alpha,\beta}(z)\leqslant\frac{1}{\Gamma(\beta)}.$$

Moreover, for any $\lambda<0$ and $t_1,t_2\in[0,1]$, we have

$$E_{\alpha,\alpha+\beta}(\lambda Q_{\psi}^{\alpha}(t_2,a))\to E_{\alpha,\alpha+\beta}(\lambda Q_{\psi}^{\alpha}(t_1,a))\quad\text{as } t_1\to t_2,\tag{1.1}$$

where $E_{\alpha,\beta}$ is the Mittag-Leffler function.

Proof. See [29], Lemma 2 and [33]. □

Lemma 1.4. *Let $\alpha>0$, $\beta>0$, $\gamma>0$ and $\lambda\in\mathbb{R}$. Then*

$$I_{a^+}^{\alpha,\psi}Q_{\psi}^{\beta-1}(t,a)E_{\gamma,\beta}(\lambda Q_{\psi}^{\gamma}(t,a))=Q_{\psi}^{\alpha+\beta-1}(t,a)E_{\gamma,\alpha+\beta}(\lambda Q_{\psi}^{\gamma}(t,a).$$

Proof. By Definition 1.1, we have

$$\begin{aligned}I_{a^+}^{\alpha,\psi}Q_{\psi}^{\beta-1}(t,a)E_{\gamma,\beta}(\lambda Q_{\psi}^{\gamma}(t,a)) &= \frac{1}{\Gamma(\alpha)}\int_a^t\mathcal{N}_{\psi}^{\alpha-1}(t,s)Q_{\psi}^{\beta-1}(s,a)E_{\gamma,\beta}(\lambda Q_{\psi}^{\gamma}(s,a))ds\\ &= \frac{1}{\Gamma(\alpha)}\int_a^t\mathcal{N}_{\psi}^{\alpha-1}(t,s)Q_{\psi}^{\beta-1}(s,a)\sum_{n=0}^{\infty}\frac{(\lambda Q_{\psi}^{\gamma}(s,a))^n}{\Gamma(\gamma n+\beta)}ds\end{aligned}$$

$$= \sum_{n=0}^{\infty} \frac{\lambda^n}{\Gamma(\gamma n+\beta)} \frac{1}{\Gamma(\alpha)} \int_a^t \mathcal{N}_\psi^{\alpha-1}(t,s) Q_\psi^{\gamma n+\beta-1}(s,a) ds.$$

Via Lemma 1.1, we get

$$I_{a^+}^{\alpha,\psi} Q_\psi^{\beta-1}(t,a) E_{\gamma,\beta}(\lambda Q_\psi^\gamma(t,a)) = Q_\psi^{\alpha+\beta-1}(t,a) E_{\gamma,\alpha+\beta}(\lambda Q_\psi^\gamma(t,a).$$

□

Lemma 1.5. *Let $\alpha > 0$, $\beta > 0$, $k > 0$, $\lambda \in \mathbb{R}$, $z \in \mathbb{R}$ and $f \in C[a,b]$. Then*

$$I_{a^+}^{k,\psi} \int_a^z \mathcal{N}_\psi^{\alpha-1}(z,t) E_{\alpha,\alpha}(\lambda Q_\psi^\alpha(z,t)) f(t) dt = \int_a^z (\mathcal{N}_\psi^{\alpha+k-1}(z,t) E_{\alpha,\alpha+k}(\lambda Q_\psi^\alpha(z,t)) f(t) dt.$$

Proof. According to Definition 1.1 and Lemma 1.4, we obtain

$$\begin{aligned}
& I_{a^+}^{k,\psi} \int_a^z \mathcal{N}_\psi^{\alpha-1}(z,t) E_{\alpha,\alpha}(\lambda Q_\psi^\alpha(z,t)) f(t) dt = \\
= {} & \frac{1}{\Gamma(k)} \int_a^z \mathcal{N}_\psi^{k-1}(z,u) \left\{ \int_a^u \mathcal{N}_\psi^{\alpha-1}(u,t) E_{\alpha,\alpha}(\lambda Q_\psi^\alpha(u,t)) f(t) dt \right\} du \\
= {} & \frac{1}{\Gamma(k)} \int_a^z \int_t^z \mathcal{N}_\psi^{\alpha-1}(u,t) E_{\alpha,\alpha}(\lambda Q_\psi^\alpha(u,t)) \mathcal{N}_\psi^{k-1}(z,u) f(t) du dt \\
= {} & \frac{1}{\Gamma(k)} \int_a^z f(t) \Gamma(k) \mathcal{N}_\psi^{\alpha+k-1}(z,t) E_{\alpha,\alpha+k}(\lambda Q_\psi^\alpha(z,t)) dt \\
= {} & \int_a^z (\mathcal{N}_\psi^{\alpha+k-1}(z,t) E_{\alpha,\alpha+k}(\lambda Q_\psi^\alpha(z,t)) f(t) dt.
\end{aligned}$$

□

2. Equivalent fractional integral equations

In this section, we present explicit solutions to ψ-Hilfer fractional differential equations 0.1, 0.2 in the form of Mittag–Leffler function. Moreover, we interduce equivalent fractional integral equation of the problem 0.3–0.4.

Lemma 2.1. *Let $h \in C_{n-\gamma;\psi}(J,\mathbb{R})$, $\lambda \in \mathbb{R}$, $n-1 < \alpha < n$ and $\beta \in [0,1]$. Then, the solution of Cauchy problem 0.1, 0.2 is given by*

$$y(t) = \sum_{j=1}^n c_j Q_\psi^{\gamma-j}(t,a) E_{\alpha,\gamma-j+1}\left[\lambda Q_\psi^\alpha(t,a)\right] + \int_a^t \mathcal{N}_\psi^{\alpha-1}(t,s) E_{\alpha,\alpha}\left[\lambda Q_\psi^\alpha(t,a)\right] h(s) ds. \tag{2.1}$$

Proof. The equivalent fractional integral of the linear Cauchy problem (0.1)–(0.2) is

$$y(t) = \sum_{j=1}^n \frac{Q_\psi^{\gamma-j}(t,a)}{\Gamma(\gamma-j+1)} c_j + \frac{\lambda}{\Gamma(\alpha)} \int_a^t \mathcal{N}_\psi^{\alpha-1}(t,s) y(s) ds + \frac{1}{\Gamma(\alpha)} \int_a^t \mathcal{N}_\psi^{\alpha-1}(t,s) h(s) ds. \tag{2.2}$$

For explicit solutions of Eq. (2.2), we use the method of successive approximations, that is,

$$y_0(t) = \sum_{j=1}^n \frac{Q_\psi^{\gamma-j}(t,a)}{\Gamma(\gamma-j+1)} c_j, \tag{2.3}$$

$$y_k(t) = y_0(t) + \frac{\lambda}{\Gamma(\alpha)} \int_a^t \mathcal{N}_\psi^{\alpha-1}(t,s) y_{k-1}(t) ds + \frac{1}{\Gamma(\alpha)} \int_a^t \mathcal{N}_\psi^{\alpha-1}(t,s) h(s) ds. \tag{2.4}$$

By Definition 1.1, Lemma 1.1 together with Eq. (2.3), we obtain

$$\begin{aligned} y_1(t) &= y_0(t) + \frac{\lambda}{\Gamma(\alpha)}\int_a^t \mathcal{N}_\psi^{\alpha-1}(t,s)y_0(s)ds + \int_a^t \mathcal{N}_\psi^{\alpha-1}(t,s)h(s)ds \\ &= \sum_{j=1}^n c_j \sum_{i=1}^2 \frac{\lambda^{i-1} Q_\psi^{\alpha i+\beta(n-\alpha)-j}(t,a)}{\Gamma(\alpha i+\beta(n-\alpha)-j+1)} + \frac{1}{\Gamma(\alpha)}\int_a^t \mathcal{N}_\psi^{\alpha-1}(t,s)h(s)ds. \end{aligned} \tag{2.5}$$

Similarly, using Eqs. (2.3)–(2.5), we get

$$y_2(t) = \sum_{j=1}^n c_j \sum_{i=1}^3 \frac{\lambda^{i-1} Q_\psi^{\alpha i+\beta(n-\alpha)-j}(t,a)}{\Gamma(\alpha i+\beta(n-\alpha)-j+1)} + \int_a^t \sum_{i=1}^2 \frac{\lambda^{i-1}}{\Gamma(\alpha i)}\psi'(s)Q_\psi^{\alpha i-1}(t,s)h(s)ds.$$

Continuing this process, the expression for $y_k(t)$ is given by

$$y_k(t) = \sum_{j=1}^n c_j \sum_{i=1}^{k+1} \frac{\lambda^{i-1} Q_\psi^{\alpha i+\beta(n-\alpha)-j}(t,a)}{\Gamma(\alpha i+\beta(n-\alpha)-j+1)} + \int_a^t \sum_{i=1}^k \frac{\lambda^{i-1}}{\Gamma(\alpha i)}\psi'(s)Q_\psi^{\alpha i-1}(t,s)h(s)ds.$$

Taking the limit $k\to\infty$, we obtain the expression for $y_k(t)$, that is

$$y(t) = \sum_{j=1}^n c_j \sum_{i=1}^{\infty} \frac{\lambda^{i-1} Q_\psi^{\alpha i+\beta(n-\alpha)-j}(t,a)}{\Gamma(\alpha i+\beta(n-\alpha)-j+1)} + \int_a^t \sum_{i=1}^\infty \frac{\lambda^{i-1}}{\Gamma(\alpha i)}\psi'(s)Q_\psi^{\alpha i-1}(t,s)h(s)ds.$$

Changing the summation index in the last expression, $i\to i+1$, we have

$$y(t) = \sum_{j=1}^n c_j \sum_{i=0}^{\infty} \frac{\lambda^{i} Q_\psi^{\alpha i+\gamma-j}(t,a)}{\Gamma(\alpha i+\gamma-j+1)} + \int_a^t \sum_{i=0}^\infty \frac{\lambda^{i}}{\Gamma(\alpha i+\alpha)}\psi'(s)Q_\psi^{\alpha i+\alpha-1}(t,s)h(s)ds.$$

Using the definition of Mittag–Leffler function, we can obtain (2.1). □

Lemma 2.2. *Let $\gamma=\alpha+2\beta-\alpha\beta$ such that $\alpha\in(1,2)$, $\beta\in[0,1]$ and $f:(a,b]\times\mathbb{R}\to\mathbb{R}$ be a continuous function. Then y is a solution of the problem (0.3)–(0.4) if and only if y is a solution of the follwing integral equation*

$$\begin{aligned} y(t) = \frac{Q_\psi^{\gamma-1}(t,a)E_{\alpha,\gamma}(\lambda Q_\psi^\alpha(t,a))}{K} \times \Bigg[\sum_{i=1}^m \delta_i \int_a^{\tau_i} \mathcal{N}_\psi^{\alpha+\zeta-1}(\tau_i,s)E_{\alpha,\alpha+\zeta}(\lambda Q_\psi^\alpha(\tau_i,s))f(s,y(s))ds - \\ - \int_a^b \mathcal{N}_\psi^{\alpha-1}(b,s)E_{\alpha,\alpha}(\lambda Q_\psi^\alpha(b,s))f(s,y(s))ds\Bigg] + \\ + \int_a^t \mathcal{N}_\psi^{\alpha-1}(t,s)E_{\alpha,\alpha}(\lambda Q_\psi^\alpha(t,s))f(s,y(s))ds, \end{aligned} \tag{2.6}$$

where

$$K := Q_\psi^{\gamma-1}(b,a)E_{\alpha,\gamma}(\lambda Q_\psi^\alpha(b,a)) - \sum_{i=1}^m \delta_i I_{a^+}^{\zeta,\psi} Q_\psi^{\gamma-1}(\tau_i,a)E_{\alpha,\gamma}(\lambda Q_\psi^\alpha(\tau_i,a)) \neq 0. \tag{2.7}$$

Proof. In view of Lemma 2.1, the problem (0.3)–(0.4) is equivalent to

$$\begin{aligned} y(t) &= Q_\psi^{\gamma-1}(t,a)E_{\alpha,\gamma}(\lambda Q_\psi^\alpha(t,a))c_1 + Q_\psi^{\gamma-2}(t,a)E_{\alpha,\gamma-1}(\lambda Q_\psi^\alpha(t,a))c_2 \\ &+ \int_a^t \mathcal{N}_\psi^{\alpha-1}(t,s)E_{\alpha,\alpha}(\lambda Q_\psi^\alpha(t,s))f(s,y(s))ds, \end{aligned} \tag{2.8}$$

where

$$c_1 = \left(\frac{1}{\psi'(t)}\frac{d}{dt}\right) I_{a^+}^{2-\gamma,\psi} y(a) = D_{a^+}^{\gamma-1,\psi} y(a) \quad \text{and} \quad c_2 = I_{a^+}^{2-\gamma,\psi} y(a).$$

By the first condition ($y(a) = 0$), $\lim_{t\to a} Q_\psi^{\gamma-2}(t,a) = \infty$, we get $c_2 = 0$ and hence, Eq. (2.8) reduce to

$$y(t) = Q_\psi^{\gamma-1}(t,a) E_{\alpha,\gamma}(\lambda Q_\psi^\alpha(t,a)) c_1 + \int_a^t \mathcal{N}_\psi^{\alpha-1}(t,s) E_{\alpha,\alpha}(\lambda Q_\psi^\alpha(t,s)) f(s,y(s)) ds. \tag{2.9}$$

Next, substitute $t = \tau_i$ into Eq. (2.9) and multiplying both side of Eq. (2.9) by δ_i, we derive that

$$\delta_i y(\tau_i) = \delta_i Q_\psi^{\gamma-1}(\tau_i,a) E_{\alpha,\gamma}(\lambda Q_\psi^\alpha(\tau_i,a)) c_1 + \delta_i \int_a^{\tau_i} \mathcal{N}_\psi^{\alpha-1}(\tau_i,s) E_{\alpha,\alpha}(\lambda Q_\psi^\alpha(\tau_i,s)) f(s,y(s)) ds.$$

Thus, we have

$$\begin{aligned} \sum_{i=1}^m \delta_i I_{a^+}^{\zeta,\psi} y(\tau_i) &= c_1 \sum_{i=1}^m \delta_i I_{a^+}^{\zeta,\psi} Q_\psi^{\gamma-1}(\tau_i,a) E_{\alpha,\gamma}(\lambda Q_\psi^\alpha(\tau_i,a)) \\ &\quad + \sum_{i=1}^m \delta_i I_{a^+}^{\zeta,\psi} \int_a^{\tau_i} \mathcal{N}_\psi^{\alpha-1}(\tau_i,s) E_{\alpha,\alpha}(\lambda Q_\psi^\alpha(\tau_i,s)) f(s,y(s)) ds. \end{aligned} \tag{2.10}$$

From Eqs. (2.9), (2.10) and second condition ($y(b) = \sum_{i=1}^m \delta_i I_{a^+}^{\zeta,\psi} y(\tau_i)$), we get

$$\begin{aligned} c_1 &= \frac{1}{K}\left[\sum_{i=1}^m \delta_i I_{a^+}^{\zeta,\psi} \int_a^{\tau_i} \mathcal{N}_\psi^{\alpha-1}(\tau_i,s) E_{\alpha,\alpha}(\lambda Q_\psi^\alpha(\tau_i,s)) f(s,y(s)) ds \right. \\ &\quad \left. - \int_a^b \mathcal{N}_\psi^{\alpha-1}(b,s) E_{\alpha,\alpha}(\lambda Q_\psi^\alpha(b,s)) f(s,y(s)) ds\right]. \end{aligned} \tag{2.11}$$

Substitute Eq. (2.11) into Eq. (2.9) and using Lemma 1.5, we obtain Eq. (2.6).

Conversely, applying $D_{0^+}^{\gamma,\psi}$ on both sides of Eq. (2.6) and using the fact $D_{a^+}^{\gamma,\psi} Q_\psi^{\gamma-1}(t,a) = 0$, we can easily prove that

$${}^H D_{a^+}^{\alpha,\beta;\psi} y(t) = \lambda y(t) + f(t,y(t)).$$

Next, take $t \to a$ in Eq. (2.6), we get $y(a) = 0$. On the other hand, applying $I_{a^+}^{\zeta,\psi}$ on both sides of Eq. (2.6) with taking $t \to \tau_i$, and multiply by δ_i, we get

$$\begin{aligned} \sum_{i=1}^m \delta_i I_{a^+}^{\zeta,\psi} y(\tau_i) &= \frac{\sum_{i=1}^m \delta_i I_{a^+}^{\zeta,\psi} Q_\psi^{\gamma-1}(\tau_i,a) E_{\alpha,\gamma}(\lambda Q_\psi^\alpha(\tau_i,a))}{K} \times \\ &\quad \times \left[\sum_{i=1}^m \delta_i \int_a^{\tau_i} \mathcal{N}_\psi^{\alpha+\zeta-1}(\tau_i,s) E_{\alpha,\alpha+\zeta}(\lambda Q_\psi^\alpha(\tau_i,s)) f(s,y(s)) ds - \right. \\ &\quad \left. - \int_a^b \mathcal{N}_\psi^{\alpha-1}(b,s) E_{\alpha,\alpha}(\lambda Q_\psi^\alpha(b,s)) f(s,y(s)) ds\right] + \\ &\quad + \sum_{i=1}^m \delta_i \int_a^{\tau_i} \mathcal{N}_\psi^{\alpha+\zeta-1}(\tau_i,s) E_{\alpha,\alpha+\zeta}(\lambda Q_\psi^\alpha(\tau_i,s)) f(s,y(s)) ds. \end{aligned} \tag{2.12}$$

Thus, from Eq. (2.7), we can reduces Eq. (2.12) to

$$\sum_{i=1}^{m}\delta_i I_{a^+}^{\zeta,\psi}y(\tau_i)=\frac{1}{K}\left(Q_\psi^{\gamma-1}(b,a)E_{\alpha,\gamma}(\lambda Q_\psi^{\alpha}(b,a))-K\right)\times$$
$$\times\left[\sum_{i=1}^{m}\delta_i\int_a^{\tau_i}\mathcal{N}_\psi^{\alpha+\zeta-1}(\tau_i,s)E_{\alpha,\alpha+\zeta}(\lambda Q_\psi^{\alpha}(\tau_i,s))f(s,y(s))ds-\right.$$
$$\left.-\int_a^{b}\mathcal{N}_\psi^{\alpha-1}(b,s)E_{\alpha,\alpha}(\lambda Q_\psi^{\alpha}(b,s))f(s,y(s))ds\right]+$$
$$+\sum_{i=1}^{m}\delta_i\int_a^{\tau_i}\mathcal{N}_\psi^{\alpha+\zeta-1}(\tau_i,s)E_{\alpha,\alpha+\zeta}(\lambda Q_\psi^{\alpha}(\tau_i,s))f(s,y(s))ds=y(b). \tag{2.13}$$

Thus, the nonlocal boundary conditions of the problem (0.3)–(0.4) are satisfied. □

3. Existence of solution

The existence and uniqueness theorems of solutions to problem (0.3)–(0.4) are presented in this section. For our analysis, the following assumptions should be valid.

(H_1) $f:(a,b]\times\mathbb{R}\to\mathbb{R}$ is jointly continuous.

(H_2) There exist $0<q<1$ and a real function $\mathcal{V}\in L_{\frac{1}{q}}([a,b],\mathbb{R}^+)$ such that $|f(t,y)|\leqslant\mathcal{V}(t)$ for all $t\in[a,b]$ and $y\in\mathbb{R}$.

(H_3) There exist $0<q'<1$ and a real function $\mathcal{W}\in L_{\frac{1}{q'}}([a,b],\mathbb{R}^+)$ such that $|f(t,x)-f(t,y)|\leqslant\mathcal{W}(t)\,|x-y|$ for all $t\in[a,b]$ and $x,y\in\mathbb{R}$.

For brevity, we set

$$\rho=\left(\mathcal{B}\left(\frac{\alpha+\zeta-q'}{1-q'},\frac{\gamma-q'-1}{1-q'}\right)\right)^{1-q'}\sum_{i=1}^{m}\delta_i Q_\psi^{\alpha+\zeta-q'+\gamma-2}(\tau_i,a),$$

$$\sigma=\left(\frac{Q_\psi(b,a)}{\Gamma(\gamma)K}+1\right)\left(\mathcal{B}\left(\frac{\alpha-q'}{1-q'},\frac{\gamma-q'-1}{1-q'}\right)\right)^{1-q'}.$$

Theorem 3.1. *Assume that $f:(a,b]\times\mathbb{R}\to\mathbb{R}$ is continuous and satisfies (H_1)–(H_2). Then the problem (0.3)–(0.4) has at least one solution in $C_{2-\gamma,\psi}[a,b]$.*

Proof. Consider the operator $\mathcal{U}:C_{2-\gamma,\psi}[a,b]\longrightarrow C_{2-\gamma,\psi}[a,b]$ defined as

$$\mathcal{U}y(t)=\frac{Q_\psi^{\gamma-1}(t,a)E_{\alpha,\gamma}(\lambda Q_\psi^{\alpha}(t,a))}{K}\left[\sum_{i=1}^{m}\delta_i\int_a^{\tau_i}\mathcal{N}_\psi^{\alpha+\zeta-1}(\tau_i,s)E_{\alpha,\alpha+\zeta}(\lambda Q_\psi^{\alpha}(\tau_i,s))f(s,y(s))ds-\right.$$
$$\left.-\int_a^{b}\mathcal{N}_\psi^{\alpha-1}(b,s)E_{\alpha,\alpha}(\lambda Q_\psi^{\alpha}(b,s))f(s,y(s))ds\right]+$$
$$+\int_a^{t}\mathcal{N}_\psi^{\alpha-1}(t,s)E_{\alpha,\alpha}(\lambda Q_\psi^{\alpha}(t,s))f(s,y(s))ds. \tag{3.1}$$

It is obvious that the operator $\mathcal{U}$ is well defined. Define a bounded, closed, convex and nonempty set

$$H_\xi=\left\{y\in C_{2-\gamma,\psi}[a,b]:\|y\|_{C_{2-\gamma,\psi}}\leqslant\xi\right\},$$

of Banach space $C_{2-\gamma,\psi}[a,b]$ with

$$\xi \geqslant \left\{ \frac{Q_\psi(b,a)}{\Gamma(\gamma)K}[A+B]+C \right\} \|\mathcal{V}\|_{L_{\frac{1}{q}}[a,b]},$$

where

$$A := \frac{1}{\Gamma(\alpha+\zeta)}\left(\frac{1-q}{\alpha+\zeta-q}\right)^{1-q}\sum_{i=1}^{m}|\delta_i|\,Q_\psi^{\alpha+\zeta-q}(\tau_i,a),$$

$$B := \frac{Q_\psi^{\alpha-q}(b,a)}{\Gamma(\alpha)}\left(\frac{1-q}{\alpha-q}\right)^{1-q},$$

$$C := \frac{Q_\psi^{2-\gamma+\alpha-q}(b,a)}{\Gamma(\alpha)}\left(\frac{1-q}{\alpha-q}\right)^{1-q}.$$

Claim(1). The operator $\mathcal{U}$ is continuous in H_ξ. Consider a sequence $\{y_n\}_{n=1}^{\infty}$ such that $y_n \longrightarrow y$ in $C_{2-\gamma,\psi}[a,b]$. In view of Lemmas 1.3 and 1.5, for $t\in(a,b]$, we have

$$\begin{aligned}
\left|Q_\psi^{2-\gamma}(t,a)\left[\mathcal{U}y_n(t)-\mathcal{U}y(t)\right]\right| &\leqslant \frac{Q_\psi(t,a)}{\Gamma(\gamma)K}\left[\sum_{i=1}^{m}\frac{|\delta_i|}{\Gamma(\alpha+\zeta)}\int_a^{\tau_i}\mathcal{N}_\psi^{\alpha+\zeta-1}(\tau_i,s)\,|f_{y_n}-f_y|\,ds+\right.\\
&\left.+\frac{1}{\Gamma(\alpha)}\int_a^b\mathcal{N}_\psi^{\alpha-1}(b,s)\,|f_{y_n}-f_y|\,ds\right]+\frac{Q_\psi^{2-\gamma}(t,a)}{\Gamma(\alpha)}\int_a^t\mathcal{N}_\psi^{\alpha-1}(t,s)\,|f(s,y_n(s))-f(s,y(s))|\,ds \leqslant\\
&\leqslant \frac{Q_\psi(t,a)}{\Gamma(\gamma)K}\left[\sum_{i=1}^{m}\frac{|\delta_i|\,\Gamma(\gamma-1)}{\Gamma(\alpha+\zeta+\gamma-1)}Q_\psi^{\alpha+\zeta+\gamma-2}(\tau_i,a)+\frac{\mathcal{B}(\alpha,\gamma-1)Q_\psi^{\alpha+\gamma-2}(b,a)}{\Gamma(\alpha)}\right]\times\\
&\quad\times\|f(\cdot,y_n(\cdot))-f(\cdot,y(\cdot))\|_{2-\gamma,\psi}+\frac{\mathcal{B}(\alpha,\gamma-1)Q_\psi^{\alpha}(b,a)}{\Gamma(\alpha)}\|f(\cdot,y_n(\cdot))-f(\cdot,y(\cdot))\|_{2-\gamma,\psi},
\end{aligned}$$

where $\mathcal{B}(\alpha,\gamma-1)$ is Beta function. As $1<\gamma<2$, then $\dfrac{Q_\psi^{\gamma}(\tau_i,a)}{Q_\psi^{2}(\tau_i,a)}<1$, it follows that

$$\begin{aligned}
&\|\mathcal{U}y-\mathcal{U}y_n\|_{C_{2-\gamma,\psi}} \leqslant\\
&\leqslant \left[\frac{Q_\psi(t,a)}{\Gamma(\gamma)K}\sum_{i=1}^{m}\frac{|\delta_i|\,\Gamma(\gamma-1)}{\Gamma(\alpha+\zeta+\gamma-1)}Q_\psi^{\alpha+\zeta}(\tau_i,a)+\left(\frac{Q_\psi(t,a)}{\Gamma(\gamma)K}+1\right)\frac{\mathcal{B}(\alpha,\gamma-1)Q_\psi^{\alpha}(b,a)}{\Gamma(\alpha)}\right]\times\\
&\quad\times\|f(\cdot,y_n(\cdot))-f(\cdot,y(\cdot))\|_{2-\gamma,\psi}.
\end{aligned}$$

Since f is continuous function and $y_n\to y$ as $n\to\infty$, we have

$$\|\mathcal{U}y-\mathcal{U}y_n\|_{C_{2-\gamma,\psi}}\to 0.$$

Thus, the operator $\mathcal{U}$ is continuous in H_ξ.

Claim(2). $\mathcal{U}$ maps bounded sets into bounded sets in $C_{2-\gamma,\psi}[a,b]$. For each $y\in H_\xi$, $t\in(a,b]$, by Lemmas 1.3, 1.5 and Hölder inequality, we have

$$\begin{aligned}
&\left|Q_\psi^{2-\gamma}(t,a)\mathcal{U}y(t)\right| \leqslant\\
\leqslant\ &\frac{Q_\psi(t,a)}{\Gamma(\gamma)K}\left[\sum_{i=1}^{m}\frac{|\delta_i|}{\Gamma(\alpha+\zeta)}\int_a^{\tau_i}\mathcal{N}_\psi^{\alpha+\zeta-1}(\tau_i,s)\,|f(s,y(s))|\,ds\right.\\
&\left.+\frac{1}{\Gamma(\alpha)}\int_a^b\mathcal{N}_\psi^{\alpha-1}(b,s)\,|f(s,y(s))|\,ds\right]+\frac{Q_\psi^{2-\gamma}(t,a)}{\Gamma(\alpha)}\int_a^t\mathcal{N}_\psi^{\alpha-1}(t,s)\,|f(s,y(s))|\,ds
\end{aligned}$$

$$
\begin{aligned}
&\leqslant \frac{Q_\psi(t,a)}{\Gamma(\gamma)K}\left[\sum_{i=1}^{m}\frac{|\delta_i|}{\Gamma(\alpha+\zeta)}\int_a^{\tau_i}\mathcal{N}_\psi^{\alpha+\zeta-1}(\tau_i,s)\mathcal{V}(s)ds+\frac{1}{\Gamma(\alpha)}\int_a^b\mathcal{N}_\psi^{\alpha-1}(b,s)\mathcal{V}(s)ds\right]\\
&\quad+\frac{Q_\psi^{2-\gamma}(t,a)}{\Gamma(\alpha)}\int_a^t\mathcal{N}_\psi^{\alpha-1}(t,s)\mathcal{V}(s)ds\\
&\leqslant \frac{Q_\psi(t,a)}{\Gamma(\gamma)K}\left[\sum_{i=1}^{m}\frac{|\delta_i|}{\Gamma(\alpha+\zeta)}\left(\int_a^{\tau_i}\left(\mathcal{N}_\psi^{\alpha+\zeta-1}(\tau_i,s)\right)^{\frac{1}{1-q}}ds\right)^{1-q}\left(\int_a^{\tau_i}(\mathcal{V}(s))^{\frac{1}{q}}ds\right)^q\right.\\
&\quad\left.+\frac{1}{\Gamma(\alpha)}\left(\int_a^b\left(\mathcal{N}_\psi^{\alpha-1}(b,s)\right)^{\frac{1}{1-q}}ds\right)^{1-q}\left(\int_a^b(\mathcal{V}(s))^{\frac{1}{q}}ds\right)^q\right]\\
&\quad+\frac{Q_\psi^{2-\gamma}(t,a)}{\Gamma(\alpha)}\left(\int_a^t\left(\mathcal{N}_\psi^{\alpha-1}(t,s)\right)^{\frac{1}{1-q}}ds\right)^{1-q}\left(\int_a^t(\mathcal{V}(s))^{\frac{1}{q}}ds\right)^q\\
&\leqslant \frac{Q_\psi(t,a)}{\Gamma(\gamma)K}\left[\sum_{i=1}^{m}\frac{|\delta_i|}{\Gamma(\alpha+\zeta)}\left(\int_a^{\tau_i}\mathcal{N}_\psi^{\frac{\alpha+\zeta-1}{1-q}}(\tau_i,s)ds\right)^{1-q}\left(\int_a^{\tau_i}(\mathcal{V}(s))^{\frac{1}{q}}ds\right)^q\right.\\
&\quad\left.+\frac{1}{\Gamma(\alpha)}\left(\int_a^b\mathcal{N}_\psi^{\frac{\alpha-1}{1-q}}(b,s)ds\right)^{1-q}\left(\int_a^b(\mathcal{V}(s))^{\frac{1}{q}}ds\right)^q\right]\\
&\quad+\frac{Q_\psi^{1-\gamma}(t,a)}{\Gamma(\alpha)}\left(\int_a^t\mathcal{N}_\psi^{\frac{\alpha-1}{1-q}}(t,s)ds\right)^{1-q}\left(\int_a^t(\mathcal{V}(s))^{\frac{1}{q}}ds\right)^q\\
&\leqslant \frac{Q_\psi(t,a)}{\Gamma(\gamma)K}\left[\sum_{i=1}^{m}\frac{|\delta_i|}{\Gamma(\alpha+\zeta)}\left(\int_a^{\tau_i}\mathcal{N}_\psi^{\frac{\alpha+\zeta-q}{1-q}-1}(\tau_i,s)ds\right)^{1-q}\left(\int_a^{\tau_i}(\mathcal{V}(s))^{\frac{1}{q}}ds\right)^q\right.\\
&\quad\left.+\frac{1}{\Gamma(\alpha)}\left(\int_a^b\mathcal{N}_\psi^{\frac{\alpha-q}{1-q}-1}(b,s)ds\right)^{1-q}\left(\int_a^b(\mathcal{V}(s))^{\frac{1}{q}}ds\right)^q\right]\\
&\quad+\frac{Q_\psi^{2-\gamma}(t,a)}{\Gamma(\alpha)}\left(\int_a^t\mathcal{N}_\psi^{\frac{\alpha-q}{1-q}-1}(t,s)ds\right)^{1-q}\left(\int_a^t(\mathcal{V}(s))^{\frac{1}{q}}ds\right)^q\\
&\leqslant \frac{Q_\psi(t,a)}{\Gamma(\gamma)K}\left[\frac{1}{\Gamma(\alpha+\zeta)}\left(\frac{1-q}{\alpha+\zeta-q}\right)^{1-q}\sum_{i=1}^{m}|\delta_i|\,Q_\psi^{\alpha+\zeta-q}(\tau_i,a)\right.\\
&\quad\left.+\frac{Q_\psi^{\alpha-q}(b,a)}{\Gamma(\alpha)}\left(\frac{1-q}{\alpha-q}\right)^{1-q}\right]\|\mathcal{V}\|_{L_{\frac{1}{q}}[a,b]}+\frac{Q_\psi^{2-\gamma+\alpha-q}(b,a)}{\Gamma(\alpha)}\left(\frac{1-q}{\alpha-q}\right)^{1-q}\|\mathcal{V}\|_{L_{\frac{1}{q}}[a,b]}\\
&\leqslant \left\{\frac{Q_\psi(b,a)}{\Gamma(\gamma)K}(A+B)+C\right\}\|\mathcal{V}\|_{L_{\frac{1}{q}}[a,b]}\leqslant\xi. \qquad (3.2)
\end{aligned}
$$

Thus, $\mathcal{U}: H_\xi \longrightarrow H_\xi$, that is $\mathcal{U}H_\xi$ is uniformly bounded.

Claim(3). $\mathcal{U}$ maps bounded sets into equicontinuous set of $C_{2-\gamma,\psi}[a,b]$. For any $y\in H_\xi$, $t_1,t_2\in[a,b]$ such that $t_1\leqslant t_2$, using Lemmas 1.5 and 1.3, we have

$$
\begin{aligned}
&\left|Q_\psi^{2-\gamma}(t_2,a)\mathcal{U}y(t_2)-Q_\psi^{2-\gamma}(t_1,a)\mathcal{U}y(t_1)\right|\leqslant\\
&\leqslant \|f_y\|_{C_{2-\gamma,\psi}}\left\{\frac{Q_\psi(t_2,a)E_{\alpha,\gamma}(\lambda Q_\psi^\alpha(t_2,a))-Q_\psi(t_1,a)E_{\alpha,\gamma}(\lambda Q_\psi^\alpha(t_1,a))}{|K|}\right\}\times\\
&\quad\times\left[\frac{\Gamma(\gamma-1)}{\Gamma(\alpha+\zeta+\gamma-1)}\sum_{i=1}^{m}\delta_iQ_\psi^{\alpha+\zeta+\gamma-1}(\tau_i,a)-\frac{\mathcal{B}(\alpha,\gamma-1)}{\Gamma(\alpha)}Q_\psi^\alpha(b,a)\right]+\\
&\quad+\frac{B(\alpha,\gamma-1)}{\Gamma(\alpha)}\left(Q_\psi^\alpha(t_2,a)-Q_\psi^\alpha(t_1,a)\right)\Big|.
\end{aligned}
$$

By Eq. (1.1) as $t_1 \longrightarrow t_2$, the right-hand side of the preceding inequality is not dependent on y and goes to zero. Hence

$$\left| Q_\psi^{2-\gamma}(t_2,a)\mathcal{U}y(t_2) - Q_\psi^{2-\gamma}(t_1,a)\mathcal{U}y(t_1) \right| \to 0, \ \forall \ |t_2-t_1| \to 0, \ y \in H_\xi. \tag{3.3}$$

From the above claims, together with Arzela–Ascoli theorem, we infer that the operator $\mathcal{U}$ is completely continuous. In the remaining part of the proof, we only need to prove that the set

$$\Delta = \left\{ y \in C_{2-\gamma}[a,b] : y = \varpi \mathcal{U}y, \text{ for some } \ \varpi \in (0,1) \right\},$$

is bounded set. For each $t \in (a,b]$, let $y \in \Delta$, and $y = \varpi\mathcal{U}y$ for some $\varpi \in (0,1)$. Then $\|y\|_{2-\gamma,\psi} \leqslant \|\mathcal{U}y\|_{2-\gamma,\psi}$. Hence, by virtue of claim (2), we obtain

$$\|y\|_{C_{2-\gamma,\psi}} \leqslant \xi.$$

Thus, the set Δ is bounded. According to Schaefer's fixed point theorem we deduce that $\mathcal{U}$ has a fixed point which is a solution of the problem (0.3)–(0.4). The proof is completed. $\square$

Theorem 3.2. *Assume that (H_1)–(H_3) hold. If*

$$\left[\frac{Q_\psi(b,a)}{\Gamma(\gamma)K} \frac{\rho}{\Gamma(\alpha+\zeta)} + \frac{Q_\psi^{\alpha-q'}(b,a)\sigma}{\Gamma(\alpha)} \right] \|\mathcal{W}\|_{L_{\frac{1}{q'}}[a,b]} < 1, \tag{3.4}$$

then the problem (0.3)–(0.4) has a unique solution in $C_{1-\gamma,\psi}[a,b]$.

Proof. In view of Theorem (3.1), we have known that the operator $\mathcal{U}$ defined by 3.1 is well defined and continuous. Now, we prove that $\mathcal{U}$ is a contraction map on $C_{2-\gamma,\psi}[a,b]$ with respect to the norm $\|\cdot\|_{C_{2-\gamma,\psi}}$. For each $y, y^* \in C_{2-\gamma,\psi}[a,b]$ and for all $t \in (a,b]$ with the help of Lemmas 1.3, 1.5 and Hölder inequality, we have

$$\begin{aligned}
&\left| Q_\psi^{2-\gamma}(t,a)\left[\mathcal{U}y(t) - \mathcal{U}y^*(t)\right] \right| \leqslant \left| \frac{Q_\psi(t,a)E_{\alpha,\gamma}(\lambda Q_\psi^\alpha(t,a))}{K} \times \right.\\
&\times \left[\sum_{i=1}^m \delta_i \int_a^{\tau_i} \mathcal{N}_\psi^{\alpha+\zeta-1}(\tau_i,s)E_{\alpha,\alpha+\zeta}(\lambda Q_\psi^\alpha(\tau_i,s))\left[f(s,y(s)) - f(s,y^*(s))\right] ds \right.\\
&\left. - \int_a^b \mathcal{N}_\psi^{\alpha-1}(b,s)E_{\alpha,\alpha}(\lambda Q_\psi^\alpha(b,s))\left[f(s,y(s)) - f(s,y^*(s))\right] ds \right]\\
&\left. + Q_\psi^{2-\gamma}(t,a)\int_a^t \mathcal{N}_\psi^{\alpha-1}(t,s)E_{\alpha,\alpha}(\lambda Q_\psi^\alpha(b,s))\left[f(s,y(s)) - f(s,y^*(s))\right] ds \right| \leqslant \frac{Q_\psi(t,a)}{\Gamma(\gamma)K} \times\\
&\times \left[\sum_{i=1}^m \frac{|\delta_i|}{\Gamma(\alpha+\zeta)} \left(\int_a^{\tau_i} \left(\mathcal{N}_\psi^{\alpha+\zeta-1}(\tau_i,s)Q_\psi^{\gamma-2}(s,a) \right)^{\frac{1}{1-q'}} ds \right)^{1-q'} \left(\int_a^{\tau_i} (\mathcal{W}(s))^{\frac{1}{q'}} ds \right)^{q'} \|y-y^*\|_{2-\gamma,\psi} \right.\\
&\left. + \frac{1}{\Gamma(\alpha)} \left(\int_a^b \left(\mathcal{N}_\psi^{\alpha-1}(b,s)Q_\psi^{\gamma-2}(s,a) \right)^{\frac{1}{1-q'}} ds \right)^{1-q'} \left(\int_a^b (\mathcal{W}(s))^{\frac{1}{q'}} ds \right)^{q'} \|y-y^*\|_{2-\gamma,\psi} \right]\\
&+ \frac{Q_\psi^{2-\gamma}(t,a)}{\Gamma(\alpha)} \left(\int_a^t \left(\mathcal{N}_\psi^{\alpha-1}(t,s)Q_\psi^{\gamma-2}(s,a) \right)^{\frac{1}{1-q'}} ds \right)^{1-q'} \left(\int_a^t (\mathcal{W}(s))^{\frac{1}{q'}} ds \right)^{q'} \|y-y^*\|_{2-\gamma,\psi} \leqslant\\
&\leqslant \left[\frac{Q_\psi(t,a)}{\Gamma(\gamma)K} \frac{1}{\Gamma(\alpha+\zeta)} \left(B\left(\frac{\alpha+\zeta-q'}{1-q'}, \frac{\gamma-q'-1}{1-q'} \right) \right)^{1-q'} \sum_{i=1}^m \delta_i Q_\psi^{\alpha+\zeta-q'+\gamma-2}(\tau_i,a) \times \right.
\end{aligned}$$

$$\times\left(\frac{Q_\psi(t,a)}{\Gamma(\gamma)K}+1\right)\frac{Q_\psi^{\alpha-q'}(b,a)}{\Gamma(\alpha)}\left(B\left(\frac{\alpha-q'}{1-q'},\frac{\gamma-q'-1}{1-q'}\right)\right)^{1-q'}\Bigg]\|\mathcal{W}\|_{L_{\frac{1}{q'}}[a,b]}\|y-y^*\|_{1-\gamma,\psi}\leqslant$$

$$\leqslant\left[\frac{Q_\psi(t,a)}{\Gamma(\gamma)K}\frac{\rho}{\Gamma(\alpha+\zeta)}+\frac{Q_\psi^{\alpha-q'}(b,a)\sigma}{\Gamma(\alpha)}\right]\|\mathcal{W}\|_{L_{\frac{1}{q'}}[a,b]}\|y-y^*\|_{2-\gamma,\psi} \qquad (3.5)$$

By (3.4), the operator $\mathcal{U}$ is a contraction map. According to Banach contraction principle, we conclude that the problem (0.3)–(0.4) has a unique solution in $C_{2-\gamma,\psi}[a,b]$ □

4. E_α-Ulam-Hyers stability

In this section, we discuss the E_α-Ulam-Hyers stability of the problem (0.3).

Lemma 4.1 ([23]). *Let $\alpha>0$ and x,y be two nonnegative function locally integrable on $[a,b]$. Assume that g is nonnegative and nondecreasing, and let $\psi\in C^1[a,b]$ an increasing function such that $\psi'(t)\neq 0$ for all $t\in[a,b]$. If*

$$x(t)\leqslant y(t)+g(t)\int_a^t\mathcal{N}_\psi^{\alpha-1}(t,s)x(s)ds,\quad t\in[a,b],$$

then

$$x(t)\leqslant y(t)+\int_a^t\sum_{n=1}^{\infty}\frac{[g(t)\Gamma(\alpha)]^n}{\Gamma(n\alpha)}\mathcal{N}_\psi^{n\alpha-1}(t,s)y(s)ds,\quad t\in[a,b].$$

If y be a nondecreasing function on $[a,b]$, then we have

$$x(t)\leqslant y(t)E_\alpha\left\{g(t)\Gamma(\alpha)Q_\psi^\alpha(t,a)\right\},\quad t\in[a,b].$$

Remark 4.1. *A function $z\in C_{2-\gamma,\psi}[a,b]$ satisfies the inequality*

$$\left|{}^HD_{a^+}^{\alpha,\beta,\psi}z(t)-\lambda z(t)-f(t,z(t))\right|\leqslant\varepsilon E_\alpha Q_\psi^\alpha(t,a),\ t\in(a,b], \qquad (4.1)$$

if and only if there exists a function $\eta\in C[a,b]$ such that

(i) $|\eta(t)|\leqslant\varepsilon E_\alpha Q_\psi^\alpha(t,a),\quad t\in[a,b]$;

(ii) ${}^HD_{a^+}^{\alpha,\beta,\psi}z(t)=\lambda z(t)+f\big(t,z(t)\big)\big)+\eta(t),\ t\in(a,b].$

Definition 4.1 ([32]). *The problem (0.3) is E_α-Ulam-Hyers stable with respect to $E_\alpha Q_\psi^\alpha(t,a)$ if there exists $C_{E_\alpha}>0$ such that, for each $\varepsilon>0$ and each $z\in C_{2-\gamma,\psi}[a,b]$ satisfies the inequality (4.1), there exists a solution $x\in C_{2-\gamma,\psi}[a,b]$ of the problem (0.3) with*

$$\|z-x\|_{2-\gamma,\psi}\leqslant C_{E_\alpha}\varepsilon E_\alpha(\kappa Q_\psi^\alpha(t,a)),\quad t\in[a,b],\ \kappa>0.$$

Lemma 4.2. *Let $1<\alpha<2$, $0\leqslant\beta\leqslant1$, if a function $z\in C_{2-\gamma,\psi}[a,b]$ satisfies the inequality (4.1), then z satisfies the following integral inequality*

$$\left|z(t)-\mathcal{A}_z-\int_a^t\mathcal{N}_\psi^{\alpha-1}(t,s)E_{\alpha,\alpha}(\lambda Q_\psi^\alpha(t,s))f(s,z(s))ds\right|\leqslant$$

$$\leqslant\varepsilon\left[\frac{1}{\Gamma(\gamma)K}\sum_{i=1}^m|\delta_i|\,Q_\psi^\zeta(\tau_i,a)E_{\alpha,\zeta+1}Q_\psi^\alpha(\tau_i,a)+\left(\frac{1}{\Gamma(\gamma)K}+1\right)E_\alpha Q_\psi^\alpha(b,a)\right],$$

where

$$\begin{aligned}\mathcal{A}_z &= \frac{Q_\psi^{\gamma-1}(t,a)E_{\alpha,\gamma}(\lambda Q_\psi^\alpha(t,a))}{K}\left[\sum_{i=1}^m \delta_i \int_a^{\tau_i} \mathcal{N}_\psi^{\alpha+\zeta-1}(\tau_i,s)E_{\alpha,\alpha+\zeta}(\lambda Q_\psi^\alpha(\tau_i,s))f(s,z(s))ds\right.\\ &\left.-\int_a^b \mathcal{N}_\psi^{\alpha-1}(b,s)E_{\alpha,\alpha}(\lambda Q_\psi^\alpha(b,s))f(s,z(s))ds\right].\end{aligned}$$

Proof. Indeed by Remark 4.1, we have

$$^H D_{a^+}^{\alpha,\beta,\psi} z(t) = \lambda z(t) + f(t,z(t)) + \eta(t), \qquad t \in (a,b].$$

By Lemma 2.2, we obtain

$$\begin{aligned}z(t) &= \mathcal{A}_z - \frac{Q_\psi^{\gamma-1}(t,a)E_{\alpha,\gamma}(\lambda Q_\psi^\alpha(t,a))}{K}\left[\sum_{i=1}^m \delta_i \int_a^{\tau_i} \mathcal{N}_\psi^{\alpha+\zeta-1}(\tau_i,s)E_{\alpha,\alpha+\zeta}(\lambda Q_\psi^\alpha(\tau_i,s))\eta(s)ds\right.\\ &\left.-\int_a^b \mathcal{N}_\psi^{\alpha-1}(b,s)E_{\alpha,\alpha}(\lambda Q_\psi^\alpha(b,s))\eta(s)ds\right] + \int_a^t \mathcal{N}_\psi^{\alpha-1}(t,s)E_{\alpha,\alpha}(\lambda Q_\psi^\alpha(t,s))f(s,z(s))ds\\ &+\int_a^t \mathcal{N}_\psi^{\alpha-1}(t,s)E_{\alpha,\alpha}(\lambda Q_\psi^\alpha(t,s))\eta(s)ds.\end{aligned}$$

It follows from Lemma 1.3 and the fact $Q_\psi^{\gamma-1}(t,a) = \dfrac{Q_\psi^\gamma(t,a)}{Q_\psi(t,a)} < 1$, that

$$\begin{aligned}&\left|z(t) - \mathcal{A}_z - \int_a^t \mathcal{N}_\psi^{\alpha-1}(t,s)E_{\alpha,\alpha}(\lambda Q_\psi^\alpha(t,s))f(s,z(s))ds\right| \leqslant\\ &\leqslant \frac{1}{\Gamma(\gamma)K}\left[\sum_{i=1}^m \frac{|\delta_i|}{\Gamma(\alpha+\zeta)}\int_a^{\tau_i} \mathcal{N}_\psi^{\alpha+\zeta-1}(\tau_i,s)\,|\eta(s)|\,ds + \frac{1}{\Gamma(\alpha)}\int_a^b \mathcal{N}_\psi^{\alpha-1}(b,s)\,|\eta(s)|\,ds\right]\\ &+\frac{1}{\Gamma(\alpha)}\int_a^t \mathcal{N}_\psi^{\alpha-1}(t,s)\,|\eta(s)|\,ds \leqslant\\ &\leqslant \frac{\varepsilon}{\Gamma(\gamma)K}\left[\sum_{i=1}^m \frac{|\delta_i|}{\Gamma(\alpha+\zeta)}\int_a^{\tau_i} \mathcal{N}_\psi^{\alpha+\zeta-1}(\tau_i,s)E_\alpha Q_\psi^\alpha(s,a)ds + \frac{1}{\Gamma(\alpha)}\int_a^b \mathcal{N}_\psi^{\alpha-1}(b,s)E_\alpha Q_\psi^\alpha(s,a)ds\right]\\ &+\frac{\varepsilon}{\Gamma(\alpha)}\int_a^t \mathcal{N}_\psi^{\alpha-1}(t,s)E_\alpha Q_\psi^\alpha(s,a)ds.\end{aligned}$$

By definition of Mittag-Leffler function and Theorem 1.1, we get

$$\begin{aligned}&\left|z(t) - \mathcal{A}_z - \int_a^t \mathcal{N}_\psi^{\alpha-1}(t,s)E_{\alpha,\alpha}(\lambda Q_\psi^\alpha(t,s))f(s,z(s))ds\right| \leqslant\\ &\leqslant \varepsilon\left[\frac{1}{\Gamma(\gamma)K}\sum_{i=1}^m |\delta_i|\, Q_\psi^\zeta(\tau_i,a)\sum_{n=0}^\infty \frac{Q_\psi^{\alpha(n+1)}(\tau_i,a)}{\Gamma((n+1)\alpha+\zeta+1)} + \left(\frac{1}{\Gamma(\gamma)K}+1\right)\sum_{n=0}^\infty \frac{Q_\psi^{\alpha(n+1)}(b,a)}{\Gamma((n+1)\alpha+1)}\right] \leqslant\\ &\leqslant \varepsilon\left[\frac{1}{\Gamma(\gamma)K}\sum_{i=1}^m |\delta_i|\, Q_\psi^\zeta(\tau_i,a)\sum_{n=0}^\infty \frac{Q_\psi^{\alpha n}(\tau_i,a)}{\Gamma(n\alpha+\zeta+1)} + \left(\frac{1}{\Gamma(\gamma)K}+1\right)\sum_{n=0}^\infty \frac{Q_\psi^{\alpha n}(b,a)}{\Gamma(n\alpha+1)}\right] =\\ &= \varepsilon\left[\frac{1}{\Gamma(\gamma)K}\sum_{i=1}^m |\delta_i|\, Q_\psi^\zeta(\tau_i,a)E_{\alpha,\zeta+1}Q_\psi^\alpha(\tau_i,a) + \left(\frac{1}{\Gamma(\gamma)K}+1\right)E_\alpha Q_\psi^\alpha(b,a)\right].\end{aligned}$$

$\square$

In the forthcoming theorem, we prove the E_α-Ulam-Hyers stability result for the problem (0.3). For that, the following assumption should be valid.

H_4 There exist $L_f > 0$ such that $|f(t,x) - f(t,y)| \leqslant L_f |x-y|$ for all $t \in [a,b]$ and $x, y \in \mathbb{R}$.

Theorem 4.1. *Assume that* (H_1) *and* (H_4), *are satisfied. Then Eq. (0.3) is* E_α*-Ulam-Hyers stable.*

Proof. Let $\varepsilon > 0$, $z \in C_{2-\gamma;\psi}[a,b]$ be a function satisfying the inequality 4.1 and let $x \in C_{2-\gamma;\psi}[a,b]$ be the unique solution of the following problem

$$\begin{cases} {}^H D_{a^+}^{\alpha,\beta;\psi} x(t) = \lambda x(t) + f(t, x(t)), & t \in (a,b], \\ x(a^+) = z(a^+), \quad x(b) = z(b). \end{cases}$$

Now, by using Lemma 2.2, we have

$$x(t) = \mathcal{A}_z + \int_a^t \mathcal{N}_\psi^{\alpha-1}(t,s) E_{\alpha,\alpha} Q_\psi^\alpha(t,s) f(s,x(s))ds, \quad t \in (a,b].$$

Hence, from (H_4) and Lemmas 4.2, 1.3, for each $t \in (a,b]$, we have

$$\begin{aligned} |z(t) - x(t)| &\leqslant \left| z(t) - \mathcal{A}_z - \int_a^t \mathcal{N}_\psi^{\alpha-1}(t,s) E_{\alpha,\alpha} Q_\psi^\alpha(t,s) f(s,z(s))ds \right| \\ &\quad + \left| \int_a^t \mathcal{N}_\psi^{\alpha-1}(t,s) E_{\alpha,\alpha} Q_\psi^\alpha(t,s) \left(f(s,z(s)) - f(s,x(s)) \right) ds \right| \leqslant \\ &\leqslant \varepsilon \left[\frac{1}{\Gamma(\gamma) K} \sum_{i=1}^m |\delta_i| Q_\psi^\zeta(\tau_i,a) E_{\alpha,\zeta+1} Q_\psi^\alpha(\tau_i,a) + \left(\frac{1}{\Gamma(\gamma)K} + 1 \right) E_\alpha Q_\psi^\alpha(b,a) \right] \\ &\quad + \frac{L_f}{\Gamma(\alpha)} \int_a^t \mathcal{N}_\psi^{\alpha-1}(t,s) |z(t) - x(t)| ds. \end{aligned} \tag{4.2}$$

Using Lemma 4.1, we obtain

$$\begin{aligned} &|z(t) - x(t)| \leqslant \\ &\leqslant \varepsilon \left[\frac{1}{\Gamma(\gamma) K} \sum_{i=1}^m |\delta_i| Q_\psi^\zeta(\tau_i,a) E_{\alpha,\zeta+1} Q_\psi^\alpha(\tau_i,a) + \left(\frac{1}{\Gamma(\gamma)K} + 1 \right) E_\alpha Q_\psi^\alpha(b,a) \right] E_\alpha(L_f Q_\psi^\alpha(t,a)). \end{aligned}$$

For all $t \in (a,b]$, we have

$$\begin{aligned} \|z - x\|_{2-\gamma,\psi} &\leqslant \varepsilon \left[\frac{1}{\Gamma(\gamma) K} \sum_{i=1}^m |\delta_i| Q_\psi^\zeta(\tau_i,a) E_{\alpha,\zeta+1} Q_\psi^\alpha(\tau_i,a) + \left(\frac{1}{\Gamma(\gamma)K} + 1 \right) E_\alpha Q_\psi^\alpha(b,a) \right] \times \\ &\quad \times Q_\psi^{\gamma-2}(t,a) E_\alpha(L_f Q_\psi^\alpha(t,a)) \\ &\leqslant \varepsilon \left[\frac{1}{\Gamma(\gamma) K} \sum_{i=1}^m |\delta_i| Q_\psi^\zeta(\tau_i,a) E_{\alpha,\zeta+1} Q_\psi^\alpha(\tau_i,a) + \left(\frac{1}{\Gamma(\gamma)K} + 1 \right) E_\alpha Q_\psi^\alpha(b,a) \right] \times \\ &\quad \times Q_\psi^{\gamma-2}(b,a) E_\alpha(L_f Q_\psi^\alpha(t,a)). \end{aligned}$$

Take $C_{E_\alpha} = \varepsilon \left[\frac{1}{\Gamma(\gamma) K} \sum_{i=1}^m |\delta_i| Q_\psi^\zeta(\tau_i,a) E_{\alpha,\zeta+1} Q_\psi^\alpha(\tau_i,a) + \left(\frac{1}{\Gamma(\gamma)K} + 1 \right) E_\alpha Q_\psi^\alpha(b,a) \right] Q_\psi^{\gamma-2}(b,a)$, we get

$$\|z - x\|_{2-\gamma,\psi} \leqslant C_{E_\alpha} \varepsilon E_\alpha(L_f Q_\psi^\alpha(t,a)).$$

Thus, Eq. (0.3) is E_α-Ulam-Hyers stable. □

5. An example

In this section, one example is given to illustrate our theory results

Example 6.1 Consider the following problem

$$\begin{cases} {}^{H}D_{0^+}^{\frac{3}{2},\frac{2}{3};e^t} y(t) = -\frac{1}{2}y(t) + \frac{e^{-rt}}{1+e^t}\sin y(t), \ r > 0 \ \ t \in J := (0,1], \\ y(0) = 0, \quad y(1) = \frac{2}{3} I_{0^+}^{\frac{1}{2}} y(\frac{1}{2}). \end{cases} \tag{5.1}$$

Here $\alpha = \frac{3}{2}$, $\beta = \frac{2}{3}$, $\gamma = \alpha + 2\beta - \alpha\beta = \frac{5}{6}$, $m = 1, \tau_1 = \frac{1}{2}$, $\delta_1 = \frac{2}{3}$, $\zeta = \frac{1}{2}$, $(a,b] = (0,1]$, $\psi(t) = e^{t\cdot}$, $\lambda = -\frac{1}{2}$ and $f(t,y(t)) = \frac{e^{-rt}}{1+e^t}\sin y(t)$. Then

$$|f(t,y(t))| = \left| \frac{e^{-rt}}{1+e^t} \sin y(t) \right| \leqslant \left| \frac{e^{-rt}}{1+e^t} \right| \leqslant \frac{e^{-rt}}{2}, \quad r > 0.$$

Let $z, y \in \mathbb{R}$ and $t \in [0,1]$. Then

$$|f(t,z(t)) - f(t,y(t))| \leqslant \left| \frac{e^{-rt}}{1+e^t} (\sin z(t) - \sin y(t)) \right| \leqslant \frac{e^{-rt}}{2} |z(t) - y(t)| .$$

We note that $\mathcal{V} = \mathcal{W} = \frac{e^{-rt}}{2} \in L_{\frac{1}{q'}}[0,1]$. Thus, for $t \in [0,1]$ and Choosing suitable $q' \in (0,1)$, we can arrive at the following inequality

$$\left[\frac{e-1}{\Gamma(\frac{5}{6})K} \frac{\rho}{\Gamma(2)} + \frac{(e-1)^{\frac{3}{2}-q'}\sigma}{\Gamma(\frac{3}{2})} \right] \|\mathcal{W}\|_{L_{\frac{1}{q'}}[0,1]} < 1.$$

Then all the assumptions in Theorem 3.2 are satisfied, the problem (5.1) has a unique solution in $C_{\frac{7}{6},e^t}[0,1]$. Also we see that the inequality

$$\left| {}^{H}D_{0^+}^{\frac{3}{2},\frac{2}{3};e^t} y(t) + \frac{1}{2}y(t) - \frac{e^{-at}}{1+e^t}\sin y(t) \right| \leqslant \varepsilon E_{\frac{3}{2}}(e^t-1)^{\frac{3}{2}}, \quad t \in [0,1] \tag{5.2}$$

is satisfied. For $z, x \in C_{\frac{7}{6}}[0,1]$, we have

$$\|z - x\|_{2-\gamma,\psi} \leqslant C_{E_{\frac{1}{3}}} \ \varepsilon E_{\frac{3}{2}} \left[\frac{1}{2}(e^t-1)^{\frac{1}{2}} \right], \quad t \in [0,1], \quad z, x \in C_{\frac{7}{6}}[0,1],$$

where

$$C_{E_{\frac{1}{3}}} = \left[\frac{1}{\Gamma(\frac{5}{6})|K|} \frac{2}{3} E_{\frac{3}{2},\frac{3}{2}}(e^{\frac{1}{2}}-1)^{\frac{3}{2}} + \left(\frac{1}{\Gamma(\frac{5}{6})K} + 1 \right) E_{\frac{3}{2}}((e-1)^{\frac{3}{2}}) \right] (e-1)^{\frac{5}{6}-2} > 0.$$

Thus the Eq. (5.1) is E_α-Ulam-Hyers stable.

6. Concluding remarks

We can conclude that the main results of this article have been successfully achieved, through some properties of Mittag-Leffler function and fixed point theorems such as Banach and Schaefer, we have investigated the existence and uniqueness of the solutions of nonlinear Cauchy problem for ψ-Hilfer fractional differential equation with constant coefficient. Further, we discussed E_α-Ulam-Hyers stability of solutions to such equations in the weighted space $C_{2-\gamma,\psi}[a,b]$.

References

[1] M.S.Abdo, S.K.Panchal, Fractional integro-differential equations involving ψ-Hilfer fractional derivative, *Advances in Applied Mathematics and Mechanics*, **11**(2019), 338–359 .

[2] M.A.Almalahi, S.K.Panchal, E_{α}-Ulam-Hyers stability result for ψ-Hilfer Nonlocal Fractional Differential Equation, *Discontinuity, Nonlinearity, and Complexity*, 2020. In press.

[3] M.A.Almalahi, M.S.Abdo, S.K.Panchal, Existence and Ulam–Hyers–Mittag-Leffler stability results of ψ-Hilfer nonlocal Cauchy problem, *Rend. Circ. Mat. Palermo, II. Ser*, (2020). DOI: 10.1007/s12215-020-00484-8

[4] M.A.Almalahi, M.S.Abdo, S.K.,Panchal, ψ-Hilfer Fractional functional differential equation by Picard operator method, *Journal of Applied Nonlinear Dynamics*, (2020). DOI: 10.5890/JAND.2020.12.011.

[5] A.Arara, M.Benchohra, N.Hamidi, J.J.Nieto, Fractional order differential equations on an unbounded domain, *Nonlinear Anal. Theory Methods Appl.*, **72**(2010), 580–586.

[6] K.Deimling, Nonlinear Functional Analysis, Springer, New York, 1985.

[7] K.M.Furati, M.D.Kassim, Existence and uniqueness for a problem involving Hilfer fractional derivative, *Comput. Math. Applic*, **64**(2012), 1616–1626.

[8] Z.Gao, X.Yu, Existence results for BVP of a class of Hilfer fractional differential equations, *Journal of Applied Mathematics and Computing*, **56**(2018), no. 1-2, 217–233.

[9] C.S.Goodrich, Existence of a positive solution to a class of fractional differential equations, *Appl. Math. Lett.*, **23**(2010), 1050–1055.

[10] R.Hilfer, Application of Fractional Calculus in Physics, World Scientific, Singapore, 1999.

[11] D.H.Hyers, G.Isac, Th.M.Rassias, *Stability of Functional Equations in Several Variables*, *Progr. Nonlinear Differential Equations Appl.*, Birkh 646user, Boston, **34**, 1998.

[12] A.A.Kilbas, H.M.Srivastava, J.J.Trujillo, Theory and Applications of Fractional Differential Equations, North-Holland Mathematics Studies, Vol. 207, Elsevier, Amsterdam, 2006.

[13] K.D.Kucche, A.D.Mali, J.Vanterler, C. da Sousa, On the Nonlinear ψ-Hilfer Fractional Differential Equations, *Computational and Applied Mathematics*, **38:73**(2019). DOI: 10.1007/s40314-019-0833-5.

[14] K.D.Kucche, A.D.Mali, Initial time difference quasilinearization method for fractional differential equations involving generalized Hilfer fractional derivative, *Computational and Applied Mathematics*, **39:31**(2020). DOI: 10.1007/s40314-019-1004-4

[15] J.P.Kharade, K.D.Kucche, On the impulsive implicit ψ-Hilfer fractional differential equations with delay, *Mathematical Methods in the Applied Sciences*, **43**(2020), no. 4, 1938–1952. DOI: 10.1002/mma.6017

[16] K.Liu, J.Wang, D.O'Regan, Ulam–Hyers–Mittag-Leffler stability for ψ-Hilfer fractional-order delay differential equations, *Advances in Difference Equations*, **50**(2019), no. 1. DOI: 10.1186/s13662-019-1997-4

[17] A.D.Mali, K.D.Kucche, Nonlocal Boundary Value Problem for Generalized Hilfer Implicit Fractional Differential Equations, arXiv preprint arXiv:2001.08479, 2020.

[18] E.C.Oliveira, J.V.D.C.Sousa, Ulam–Hyers–Rassias stability for a class of fractional integro-differential equations, *Results Math.*, **73**(2018), 111. DOI: 10.1007/s00025-018-0872-z

[19] I.Podlubny, Fractional Differential Equations: An Introduction to Fractional Derivatives, Fractional Differential Equations, to Methods of Their Solution and Some of Their Applications, *Math. Sci. Eng.*, **198**(1999), Elsevier, Amsterdam.

[20] T.M.Rassias, On the stability of the linear mapping in Banach spaces, *Proc. Amer. Math. Soc.*, **72**(1978), no. 2, 297–300.

[21] S.G.Samko, A.A.Kilbas, Marichev, O.I,:Fractional Integrals and Derivatives: Theory and Applications, Gordon and Breach, Yverdon, 1987.

[22] J.V.C.Sousa, E.C. de Oliveira, , On the ψ-Hilfer fractional derivative, *Commun. Nonlinear Sci. Numer. Simul.*, **60**(2018), 72–91. DOI: 10.1016/j.cnsns.2018.01.005

[23] J.Sousa, E.C. de Oliveira, A Gronwall inequality and the Cauchy-type problem by means of ψ-Hilfer operator, *Differential equations and applications*, **11**(2019), no. 1, 87–106.

[24] J.V.D.C.Sousa, K.D.Kucche, E.C. De Oliveira, Stability of ψ-Hilfer impulsive fractional differential equations, *Applied Mathematics Letters*, **88**(2019), 73–80.

[25] J.V.D.C.Sousa, E.C. de Oliveira, K.D.Kucche, On the fractional functional differential equation with abstract Volterra operator, *Bulletin of the Brazilian Mathematical Society. New Series*, **50**(2019), no. 4, 803–822.

[26] J.V.D.C.Sousa, E.C. de Oliveira, On the Ulam–Hyers–Rassias stability for nonlinear fractional differential equations using the ψ-Hilfer operator, *Journal of Fixed Point Theory and Applications*, **20**(2018), no. 3, 96.

[27] J.V.D.C.Sousa, K.D.Kucche, E.C. de Oliveira, On the Ulam-Hyers stabilities of the solutions of ψ-Hilfer fractional differential equation with abstract Volterra operator, *Mathematical Methods in the Applied Sciences*, **42**(2019), no. 9, 3021–3032.

[28] S.M.Ulam, A Collection of Mathematical Problems, Interscience Tracts in Pure and Applied Mathematics, Vol. 8, Inter-science, New York–London, 1960.

[29] J.R.Wang, M.Feckan, Y.Zhou, Presentation of solutions of impulsive fractional Langevin equations and existence results, *Eur. Phys. J. Spec. Top.*, **222**(2013), 1857–1874,

[30] H.Wang, Existence of solutions for fractional anti-periodic BVP, *Results Math.*, **88**(2015), 227–245. DOI: 10.1007/s00025-014-0431-1

[31] J.Wang, Y.Zhang, Nonlocal initial value problems for differential equations with Hilfer fractional derivative, *Appl. Math. Comput.*, **266**(2015), 850–859.
DOI: 10.1016/j.amc.2015.05.144

[32] J.Wang, X.Li, E_α-Ulam type stability of fractional order ordinary differential equations, *Journal of Applied Mathematics and Computing*, **45**(2014), no. 1-2, 449–459.

[33] M.A.Almalahi, S.K.Panchal, Some existence and stability results for ψ-Hilfer fractional implicit diferential equation with periodic conditions, *Journal of Mathematical Analysis and Modeling*, **1**(2020), no. 1, 1–19.

К теории ψ-гильферовской нелокальной задачи Коши

Мохаммед А. Альмалахи
Сатиш К. Панчал
Кафедра математики
Университет доктора Бабасахеба Амбедкара Маратвады
Аурангабад, Индия

Аннотация. В данной статье мы выводим формулу представления решения дробно-дифференциального уравнения ψ-Гильфера с постоянным коэффициентом в виде функции Миттаг-Леффлера с использованием последовательного приближения Пикара. Более того, используя некоторые свойства функции Миттаг-Леффлера и теоремы о неподвижной точке, такие как Банаха и Шефера, мы вводим новые результаты о некоторых качественных свойствах решения, таких как существование и единственность. Обобщенная лемма о неравенстве Гронуолла используется при анализе устойчивости E_α-Улама-Хайерса. Наконец, дан один пример, иллюстрирующий полученные результаты.

Ключевые слова: дробные дифференциальные уравнения, дробные производные, E_α-устойчивость Улама-Хайерса, теорема о неподвижной точке.

Journal of Siberian Federal University. Mathematics & Physics 2021, 14(2), 176–183

DOI: 10.17516/1997-1397-2021-14-2-176-183
УДК 537.9+539.216.2

Manufacturing of Opals from Polymethylmethacrylate Particles in Dispersion Media with Different Viscosities

Ivan V. Nemtsev*
Federal Research Center KSC SB RAS
Krasnoyarsk, Russian Federation
Kirensky Institute of Physics, Federal Research Center KSC SB RAS
Krasnoyarsk, Russian Federation
Siberian Federal University
Krasnoyarsk, Russian Federation

Olga V. Shabanova†
Special Designing and Technological Bureau "Nauka"
Krasnoyarsk, Russian Federation

Received 06.10.2020, received in revised form 23.10.2020, accepted 10.01.2021

Abstract. The article was prepared based on the materials of the report at the first All-Russian scientific conference with international participation "YENISEI PHOTONICS – 2020".
Photonic crystals are structures that have a spatial architecture with a periodically changing complex dielectric function at scales comparable to the wavelengths of light in the visible frequency range. The purpose of this study is to obtain three-dimensional photonic crystals by self-assembly from submicron spherical monodisperse particles of polymethylmethacrylate in dispersion media with different viscosities.

Keywords: emulsion-free polymerization, viscosity of dispersion medium, PMMA beads, submicrosphere, self-assembly, 2D and 3D colloidal crystals, photonic crystal, metamaterial, SEM micrographs, IR spectroscopy.

Citation: I.V. Nemtsev, O.V. Shabanova, Manufacturing of Opals from Polymethylmethacrylate Particles in Dispersion Media with Different Viscosities, J. Sib. Fed. Univ. Math. Phys., 2021, 14(2), 176–183. DOI: 10.17516/1997-1397-2021-14-2-176-183.

Introduction

Photonic crystals (PhCs) are considered promising optical materials for basic research and practical application in various fields of technology due to their outstanding properties, such as photonic bandgap (PBG), light wavelength selectivity, and high-performance photoluminescence [1–3]. Among PhCs, opals (artificial and natural) stand out as a special class. Opals are three-dimensional periodic structures of vivid interest [4–6]. This is due to the fact that such materials can be produced using relatively simple and inexpensive production methods, as well as the presence of a significant surface area of three-dimensional, high-precision, ordered opal patterns. It is obvious that the most suitable method for obtaining a colloidal crystal is the self-assembly approach [4], the most popular techniques of which are gravitational deposition, vertical deposition, meniscus deposition, etc. [7–9]. Artificial opals can be manufactured using polymer micro- and nanosized beads [10–12]. Based on these spheres it is possible to form perfectly ordered 2D [13] and 3D [14] mesoporous structures – PhCs or metamaterials. In its turn, polymethylmethacrylate (PMMA) is seemed to be the reassuring and advantageous polymer in the field

*ivan_nemtsev@mail.ru https://orcid.org/0000-0002-4222-3099
†ollach@yandex.ru

of using in biomedical practical implementation [15–17], applications in nanotechnology [18–21], sensor [22–24], optical [25, 26], solar cell technology [27–32]. A classical approach to synthesize PMMA spheres is emulsion-free polymerization. The physicochemical properties of such particles are well studied. Notwithstanding, using a more complex dispersion medium, it is possible to modify [33] the polymerization technique and obtain microparticles with variable properties [34]. In this work, the three-dimensional PhCs based on the submicron spherical monodisperse particles of PMMA obtained in dispersion media with different viscosities are fabricated by self-assembly approach. As a dispersion medium, distilled water with addition of dimethyl sulfoxide and acetone was used. The bead's sizes were in the range of 315–400 nm. The morphological, some physicochemical, and optical reflectance features of obtained samples were studied.

1. Experimental procedures

1.1. Synthesis of PMMA spheres

To synthesize PMMA emulsion methyl methacrylate (MMA), distilled water, dimethyl sulfoxide, distilled acetone, and an initiator. 2,2-azobis dihydrochloride (2-methylpropionamidine) were used without further purification. A necessary condition of a dispersion polymerization of polymer-based the submicrobeads with a narrow size distribution is a short phase of intensive multiple germ formation, followed by slow controlled growth of particles without changing their number. The process of chain radical polymerization of methyl methacrylate can be divided into three stages: activation of the initiator, the reaction of the monomer with the initiator radical, and growth of the molecule and breaking of the polymer chain. When heated, the initiator decomposes to form active radicals, which are the initiators of the polymerization reaction.

The emulsion polymerization procedure requires heating of methyl methacrylate emulsified in water to $70 \div 80\,^{\circ}$C. In this study, the emulsion temperature was maintained from 72.7 to $75\,^{\circ}$C. As a control sample, PMMA submicroparticles in an aqueous medium (100 ml of methyl methacrylate (MMA) and 620 ml of distilled water) were obtained by a classical emulsifier-free polymerization technique [35]. The speed of the mixer was fixed at 700 rpm. To synthesize the particles with variable properties, dispersion media were selected with the addition of dimethyl sulfoxide (DMSO) (100 ml MMA, 550 ml distilled water, 70 ml DMSO) and acetone (100 ml MMA, 550 ml distilled water, 70 ml acetone). Thus, the volume of MMA and the total volume of the emulsion were constant: 100 and 720 ml, respectively. The volume concentrations of acetone and DMSO were taken at random.

During the synthesis of submicroparticle dispersion, the IR spectra of the dispersion were recorded in situ by using the FT-801 IR Fourier spectrometer with a fiber probe [36]. Thus, the polymerization process is fully controlled with the IR spectra. Consequently, all the chemical reagents are assumed fully reacted.

1.2. Manufacturing of PMMA opal-like photonic crystal structures

In this work, the PMMA colloidal crystals were self-assembled [9, 37] on cover glasses by methods of natural sedimentation in a gravitational field, vertical deposition by evaporation, and meniscus. Humidity in a laboratory box was constantly kept at 70% and the temperature was constantly maintained at $24\,^{\circ}$C. Square pieces of 4x4 mm were cut from the cover glass and deposited with a thin film of 3 nm platinum in a sputter coater to provide electrical conductivity in the SEM chamber. To minimize the damage of the PMMA opal films, the coating modes were as follows: three cycles of 20 s with a set current of 10 mA. It also used argon gas to purge the chamber of the spray coating device.

1.3. Instrumentation

In situ measurements of disturbed total internal reflection were performed with an FT-801 IR Fourier spectrometer (Simex, Novosibirsk, Russia) to control the synthesis process. To ensure electrical conductivity a K575XD (Emitech, UK) magnetron sputtering coating system was used to cover the PMMA opal surface with a thin platinum film. Morphological features of the samples were obtained with a high-resolution field emission scanning electron microscope (FE-SEM) S-5500 (Hitachi, Japan) at an accelerating voltage of 3 kV a probe current of 10 nA. Steady-state attenuated total reflectance spectroscopy was performed with the FTIR-spectrometer Vertex 70 (Bruker, Germany).

2. Results and discussion

The bead's sizes by measuring diameters, their sphericity, shrinkage degree as well as polydispersity were estimated during SEM studies of the morphological features of the obtained particles.

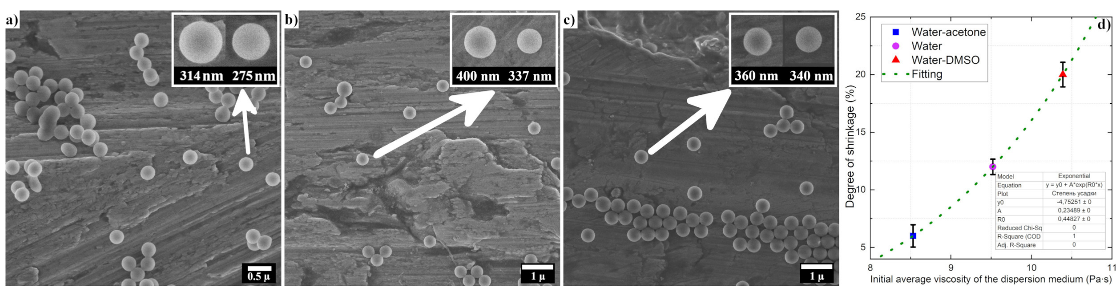

Fig. 1. SEM images of submicroparticles from PMMA obtained in (a) an aqueous medium; (b) an aqueous-DMSO dispersion medium; (c) an aqueous-acetone dispersion medium; (d) a dependence of shrinkage of PMMA submicroparticles on initial average viscosity of the dispersion medium

It was found that the additives significantly affect the size and degree of the shrinkage of the synthesized particles [38]. The bead's sizes of the control sample, "DMSO" sample, and "acetone" sample were 315, 400, and 360 nm, respectively. So, SEM revealed (Fig. 1) a different degree of the shrinkage of the PMMA submicrospheres under the influence [39] of the electron beam (3 kV, 10 nA) depending on the dispersion medium in which they were obtained. As shown, the "DMSO" sample has the maximum shrinkage of all the studied samples. It is 16 %. The smallest shrinkage is shown has the "acetone" sample. It is only 6 %. Moreover, beads obtained under different conditions were deformed in different degrees during sample preparation. Fig. 1a and 1b show that some of the submicroparticles are no longer spherical. The «acetone» spheres were the largest and the most spherical. The concentration of particles, for example, in the aqueous dispersion was estimated as 15 vol.% (6^{15} nanoparticles per liter). According to SEM, the polydispersity of nanoparticles was less than 5 %.

The various properties of spherical particles are primarily due to the viscosity of the dispersion medium. The classical Grunberg-Nissan [40] rule for a liquid mixture was used to estimate the average initial viscosity:

$$ln\mu_{\mathrm{mix}} = \sum x_i ln\mu_{\mathrm{i}}, \tag{1}$$

where μ_{mix} is the viscosity of the liquid mixture; μ_{i} is the viscosity of the liquid component i; x_i is the molar fraction of component i in the liquid mixture.

In the case of emulsifier-free emulsion polymerization, the reaction also begins in the medium phase with the formation of surface-active oligomeric forms resulting from the decomposition of the initiator. The diffusion of the formed primary particles can be described using the Stokes-Einstein relation:

$$D = (k_b T)/6\pi\eta r, \tag{2}$$

where T is the absolute temperature, k_b is the Boltzmann constant, η is the viscosity of the liquid, r is the radius of the particle.

The surface tension and the solubility index of the dispersion medium also play a significant role. The addition of DMSO and acetone to the dispersion medium increases the solubility of the monomer. Similarly, the additives benefit to increase the solubility of the resulting polymer. As a result, longer polymer chains are formed. From longer polymer chains, nanoglobules are formed that capture a larger amount of the dispersion medium (with an increased concentration of monomer). Thus, by the time of the gel effect, the particles in the acetone and DMSO dispersion medium contain more MMA and growing oligomers in comparison with «water» particles. Thus, by selecting a balance between the above parameters, it is possible to obtain PMMA submicrospheres with variable properties.

In this work, three-dimensional opal templates are obtained (Fig. 2) based on the submicron monodisperse [41] spherical PMMA particles in various dispersion media [42] and investigated by SEM and IR spectroscopy.

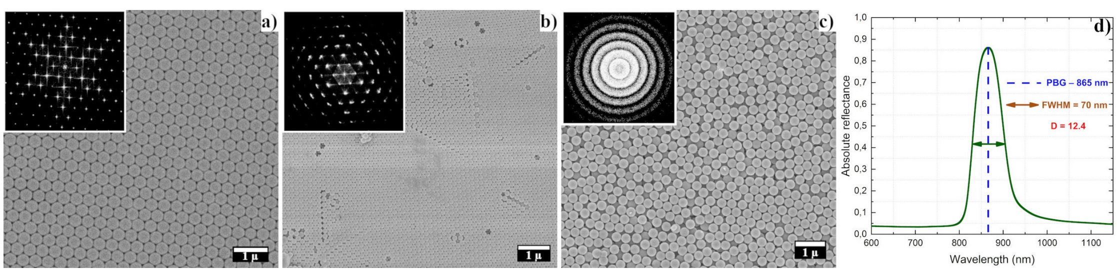

Fig. 2. SEM images of the (111) opal's surfaces based on PMMA submicrospheres obtained in a) an aqueous medium (the inset shows the Fourier transform, demonstrating monocrystalline structure); b) an aqueous medium with the addition of 70 ml of DMSO; c) an aqueous-acetone medium (70 ml of acetone). d) Absolute reflection spectrum obtained from the (111) surface shown in Fig. 2a

Figs. 2a–2c demonstrate the surfaces (111) of the PMMA photonic crystals manufactured by self-assembly in aqueous, aqueous-DMSO, and aqueous-acetone dispersion media, respectively. A non-defected long-range order of perfectly-ordered submicrospheres was discovered only in the aqueous sample. Fourier transform, demonstrating a single crystal structure, was performed using ImageJ open-source software. SEM micrograph of the surfaces (111) of the aqueous-DMSO sample in Fig. 2b shows multiple defects: domains, twinning, extra planes, vacancies, spheres of larger and smaller sizes. But nevertheless, these defects are very quickly "healed", the structure is restored. The inset demonstrates a quasi-crystalline structure. Finally, the aqueous-acetone sample showed the most disordered structure. The Fourier transform illustrates a polycrystalline structure.

To verify the long-range order in the most ordered opal a reflectance spectrum from the (111) surface was obtained with IR spectrometer Vertex 70 V (Fig. 2d). The absolute reflection of the sample was 86 % at an angle of incidence of 12° relative to normal. According to Bragg's Law, the maximum reflectivity is observed in a normal fall [41]. Thus, it can be argued that the reflectivity of the best opal photonic crystal structure obtained in an aqueous dispersion medium is significantly higher than 86 %. Moreover, from the reflectance spectrum, full width at half maximum and a quality factor at the PBG center of $\lambda = 865$ nm were determined as 70 nm and 12.4, respectively.

Conclusion

In this study, the submicron spherical monodisperse PMMA particles are synthesized in the dispersion media with different viscosities. On their basis, the method of self-assembly is used to manufacture the various PhC opal templates with different hierarchy (from polycrystalline to monocrystalline with high degree of ordering).

Morphological features of the obtained beads and opals were carefully investigated by FE-SEM. The particle sizes, their sphericity, polydispersity, shrinkage degree as well as crystalline order were estimated. It was experimentally found that the impurities significantly affect the size and degree of the shrinkage of the synthesized spheres. Thus, SEM revealed the decreasing of the diameters from 400 to 314 nm and the increasing of the shrinkage degree with the increasing of the initial average viscosity of the dispersion medium.

The reflectance spectrum from the (111) surface was obtained by IR spectroscopy. The non-defected long-range order of perfectly-ordered submicrospheres was discovered. The absolute reflection of the bests sample was 86 % at an angle of incidence of 12° relative to normal. The quality factor of that sample was calculated as 12.4.

The study was carried out with the support of the Krasnoyarsk Regional Center of Research Equipment of Federal Research Center "Krasnoyarsk Science Center SB RAS". The work was supported by the framework of the state assignment of the Ministry of Science and Higher Education of the Russian Federation (topic no. AAAA-A18-118041990041-8).

References

[1] J.Zhou, et al., Large-area crack-free single-crystal photonic crystals via combined effects of polymerization-assisted assembly and flexible substrate, *NPG Asia Mater*, **4**(2012), e21. DOI: 10.1038/am.2012.38

[2] P.Lova, G.Manfredi, D.Comoretto, Advances in Functional Solution Processed Planar 1D Photonic Crystals, *Adv. Opt. Mater*, **6**(2018), 1800730–1800756. DOI: 10.1002/adom.201800730

[3] M.Bellingeri, A.Chiasera, I.Kriegel, F.Scotognella, Optical properties of periodic, quasi-periodic, and disordered one-dimensional photonic structures, *Opt. Mater. (Amst)*, **72**(2017), 403–421. DOI: 10.1016/j.optmat.2017.06.033

[4] J.Zhang, Z.Sun, B.Yang, Self-assembly of photonic crystals from polymer colloids, *Curr. Opin. Colloid. Interface Sci.*, **14**(2009), 103–114.

[5] G.I.N.Waterhouse, M.R.Waterland, Opal and inverse opal photonic crystals: Fabrication and characterization, *Polyhedron*, **26**(2007), 356–368.

[6] E.Armstrong, C.O'Dwyer, Artificial opal photonic crystals and inverse opal structures – fundamentals and applications from optics to energy storage, *J. Mater. Chem. C*, **3**(2015), 6109–6143.

[7] Q.Zhao, et al., Large-scale ordering of nanoparticles using viscoelastic shear processing, *Nat. Commun*, **7**(2016), 11661. DOI: 10.1038/ncomms11661

[8] Q.Zhao, et al., Nanoassembly of Polydisperse Photonic Crystals Based on Binary and Ternary Polymer Opal, *Alloys, Adv. Opt. Mater*, **4**(2016), 1494–1500. DOI: 10.1002/adom.201600328

[9] G.Shang, et al., Transparency induced in opals via nanometer thick conformal coating, *Sci. Rep.* **9**(2019), 1–7. DOI: 10.1038/s41598-019-47963-2

[10] Z.Z.Gu, et al., Self-assembly of monodisperse spheres on substrates with different wettability, *Appl. Phys. A Mater. Sci. Process.*, **81**(2005), 47–49.

[11] J.-H.Lee, et al., 25th Anniversary Article: Ordered Polymer Structures for the Engineering of Photons and Phonons, *Adv. Mater.*, **26**(2014), 532–569. DOI: 10.1002/adma.201303456

[12] G.I.N.Waterhouse, W.T.Chen, A.Chan, D.Sun-Waterhouse, Achieving Color and Function with Structure: Optical and Catalytic Support Properties of ZrO2 Inverse Opal Thin Films, *ACS Omega*, **3**(2018), 9658–9674. DOI: 10.1021/acsomega.8b01334

[13] J.F.Galisteo, et al., Self-assembly approach to optical metamaterials, *J. Opt. A Pure Appl. Opt*, **7**(2005), S244–S254.

[14] A.Baron, A.Aradian, V.Ponsinet, P.Barois, Self-assembled optical metamaterials, *Opt. Laser Technol*, **82**(2016), 94–100. DOI: 10.1016/j.optlastec.2016.02.024

[15] Y.Chen, L.Zhang, G.Chen, Fabrication, modification, and application of poly(methyl methacrylate) microfluidic chips, *Electrophoresis*, **15**(2008).

[16] C.Bouzigues, T.Gacoin, A.Alexandrou, Biological Applications of Rare-Earth Based Nanoparticles, *ACS Nano*, **5**(2011), 8488–8505. DOI: 10.1021/nn202378b

[17] S.Lazzari, et al., Colloidal stability of polymeric nanoparticles in biological fluids, *J. Nanoparticle Res.*, **65**(2012). DOI: 10.1007/s11051-012-0920-7

[18] M.Perween, D.B.Parmar, G.R.Bhadu, D.N.Srivastava, Polymer–graphite composite: A versatile use and throw plastic chip electrode, *Analyst*, **139**(2014), no. 22, 5919–5926. DOI: 10.1039/c4an01405g

[19] X.Wang, P.Wang, Y.Jiang, Q.Su, J.Zheng, Facile surface modification of silica nanoparticles with a combination of noncovalent and covalent methods for composites application, *Compos. Sci. Technol*, **104**(2014), 1–8.

[20] J.H.Sung, H.S.Kim, H.J.Jin, H.J.Choi, I.J.Chin, Nanofibrous membranes prepared by multiwalled carbon nanotube/poly(methyl methacrylate) composites, *Macromolecules*, **37**(2004), 9899–9902.

[21] L.Zhang, et al., Core-shell nanospheres to achieve ultralow friction polymer nanocomposites with superior mechanical properties, *Nanoscale*, **254**(2019).

[22] W.-K.Kuo, H.-P.Weng, J.-J.Hsu, H.Yu, Photonic Crystal-Based Sensors for Detecting Alcohol Concentration, *Appl. Sci.*, **6**(2016), 67. DOI: 10.3390/app6030067

[23] S.Y.Lin, et al., A three-dimensional photonic crystal operating at infrared wavelengths, *Nature*, **394**(1998), 251–253.

[24] A.Bearzotti, et al., Alcohol vapor sensory properties of nanostructured conjugated polymers, *J. Phys. Condens. Matter*, **65**(2008).

[25] K.Gipson, K.Stevens, P.Brown, J.Ballato, Infrared spectroscopic characterization of photoluminescent polymer nanocomposites, *J. Spectrosc*, **11**(2015), 9. DOI: 10.1155/2015/489162

[26] I.Venditti, Gold nanoparticles in photonic crystals applications: A review, *Materials (Basel)*, **10**(2017), 97.

[27] H.-Q.Wang, M.Batentschuk, A.Osvet, L.Pinna, C.J.Brabec, Rare-Earth Ion Doped Up-Conversion Materials for Photovoltaic Applications, *Adv. Mater.*, **23**(2011), 2675–2680. DOI: 10.1002/adma.201100511

[28] B.Shao, et al., Coupling of Ag Nanoparticle with Inverse Opal Photonic Crystals as a Novel Strategy for Upconversion Emission Enhancement of NaYF 4?: Yb 3+ , Er 3+ Nanoparticles, *ACS Appl. Mater. Interfaces*, **7**(2015), 25211–25218.

[29] D.Bi, et al., Polymer-templated nucleation and crystal growth of perovskite films for solar cells with efficiency greater than 21%, *Nat. Energy*, **9**(2016).

[30] M.K.Assadi, et al., Enhancing the efficiency of luminescent solar concentrators (LSCs), *Appl. Phys. A Mater. Sci. Process*, **28**(2016).

[31] L.Xu, et al., Increasing the Efficiency of Organic Dye-Sensitized Solar Cells over 10.3% Using Locally Ordered Inverse Opal Nanostructures in the Photoelectrode, *Adv. Funct. Mater.*, **28**(2018), 1706291. DOI: 0.1002/adfm.201706291

[32] X.Huang, S.Han, W.Huang, X.Liu, Enhancing solar cell efficiency: the search for luminescent materials as spectral converters., *Chem. Soc. Rev*, **42**(2013), 173–201.

[33] R.D'Amato, V I.enditti, M.V.Russo, M.Falconieri, Growth control and long-range self-assembly of poly(methyl methacrylate) nanospheres, *J. Appl. Polym. Sci.*, **102**(2006), 4493–4499.

[34] R.De Angelis, et al., From nanospheres to microribbons: Self-assembled Eosin Y doped PMMA nanoparticles as photonic crystals, *J. Colloid Interface Sci.* **414**(2014), 24–32. DOI: 10.1016/j.jcis.2013.09.045

[35] I.V.Nemtsev, O.V.Shabanova, A.V.Shabanov, Electron microscopy investigation of polymethylmethacrylate spherical particles & artificial opals based on it, *Sib. J. Sci. Technol.*, **1**(2012), 126–129.

[36] O.V.Shabanova, M.A.Korshunov, I.V.Nemtsev, A.V.Shabanov, Features of self-assembly of opal-like structures based on poly(methyl methacrylate) submicron dispersions, *Nanotechnologies Russ.*, **11**(2016), 633–639. DOI: 10.1134/S1995078016050153

[37] T.A.Taton, D.J.Norris, Defective promise in photonics, *Nature*, **416**(2002), 685–686.

[38] T.Y.Kwon, J.Y.Ha, J.N.Chun, J.S.Son, K.H.Kim, Effects of prepolymerized particle size and polymerization kinetics on volumetric shrinkage of dental modeling resins, *Biomed Res. Int.*, **14**(2014), 6. DOI: 10.1155/2014/914739

[39] O.V.Shabanova, A.V.Shabanov, I.V.Nemtsev, Research of conditions of synthesis of nanoscale monodisperse spherical particles of poly-methylmethacrylate, *Siberian journal of science and technology*, **4**(2011), 201–205.

[40] A.Dukhin, S.Parlia, P.Somasundaran, Rheology of non-Newtonian liquid mixtures and the role of molecular chain length, *J. Colloid Interface Sci.*, **560**(2020), 492–501. DOI: 10.1016/j.jcis.2019.10.044

[41] I.V.Nemtsev, I.A.Tambasov, A.A.Ivanenko, V.Y.Zyryanov, Angle-resolved reflection spectroscopy of high-quality PMMA opal crystal, *Photonics Nanostructures – Fundam. Appl.*, **28**(2018), 37–44. DOI: 10.1016/j.photonics.2017.11.007

[42] I.V.Nemtsev, O.V.Shabanova, N.P.Shestakov, A.V.Cherepakhin, Y.Y.Zyryanov, Morphology stability of polymethylmethacrylate nanospheres formed in water–acetone dispersion medium, *Appl. Phys. A*, **125**(2019), 738–750.

Синтез опалов из частиц полиметилметакрилата в дисперсионных средах с различной вязкостью

Иван В. Немцев
Федеральный исследовательский центр КНЦ СО РАН
Красноярск, Российская Федерация
Институт физики им. Л. В. Киренского
Красноярск, Российская Федерация
Сибирский федеральный университет
Красноярск, Российская Федерация

Ольга В. Шабанова
Специальное Конструкторско-Технологическое Бюро «Наука»
Красноярск, Российская Федерация

Аннотация. Фотонные кристаллы — это структуры, которые имеют пространственную архитектуру с периодически изменяющейся сложной диэлектрической функцией в масштабах, сопоставимых с длинами волн света в видимом диапазоне частот. Целью данной работы является получение трёхмерных фотонных кристаллов путём самосборки из субмикронных сферических монодисперсных частиц полиметилметакрилата в дисперсных средах с различной вязкостью.

Ключевые слова: безэмульсионная полимеризация, вязкость дисперсионной среды, гранулы ПММА, субмикросфера, самосборка, 2D и 3D коллоидные кристаллы, фотонный кристалл, метаматериал, СЭМ-микрофотографии, ИК-спектроскопия.

Journal of Siberian Federal University. Mathematics & Physics 2021, 14(2), 184–192

DOI: 10.17516/1997-1397-2021-14-2-184-192
УДК 517.9

Supercritical Convection of Water in an Elongated Cavity at a Given Vertical Heat Flux

Vadim A. Sharifulin*
Perm National Research Polytechnic University
Perm, Russian Federation
Tatyana P. Lyubimova†
Institute of Continuous Media Mechanics Ural Branch of RAS
Perm, Russian Federation

Received 14.06.2020, received in revised form 11.10.2020, accepted 22.11.2020

Abstract. The supercritical modes of water convection are investigated at room temperature in an elongated horizontal cavityes, with a width-to-height ratios of 2 : 1 and 3 : 1. The Prandtl number is assumed to be equal to seven. A constant heat flux is set at the upper free and lower solid boundaries, and the lateral solid boundaries are assumed to be thermally insulated. Calculations carried out by the finite-difference method for values of the Rayleigh number exceeding the critical one by up to thirty times have shown that in the indicated interval of Rayleigh numbers in both cavities in the supercritical region, a single-vortex steady state is realized.

Keywords: thermal convection, bifurcations, fixed heat flux.

Citation: V.A. Sharifulin, T.P. Lyubimova, Supercritical Convection of Water in an Elongated Cavity at a Given Vertical Heat Flux, J. Sib. Fed. Univ. Math. Phys., 2021, 14(2), 184–192.
DOI: 10.17516/1997-1397-2021-14-2-184-192.

To optimize technological processes with the participation of fluidsystems, it is desirable to develop methods for controlling the structure of the movement of water heated from below, as the most common liquid. A technical reservoir or a natural reservoir can have a free upper boundary, which in a wide range of heating conditions can remain flat and horizontal. With a weak uniform heating from below, when the Rayleigh number Ra does not exceed the critical value Ra_c, the liquid can remain at rest. An increase in the intensity of heating $Ra > Ra_c$ leads to Rayleigh-Benard convection, which covers the entire cavity. The form of critical disturbances, the nonlinear development of which leads to a supercritical regime, depends on the conditions of heating (cooling) at the boundaries of the layer. The critical value of the Rayleigh number and the shape of the critical disturbance are determined by the boundary conditions for temperature. So, for isothermal boundaries, the most dangerous disturbance is in the form of cells with a horizontal scale of the order of the layer thickness, and in the case of a given heat flux, long-wave disturbances are the most dangerous [1]. The infinity of the layer is a good approximation of an elongated cavity and allows one to determine the threshold for the onset of convection. To study the nonlinear regime arising in the supercritical region, it is necessary to take into account the finiteness of the layer length. Such studies were carried out mainly for the case of isothermal boundaries but, as a rule, in the presence of various complicating factors that

*vadsharif@bk.ru https://orcid.org/0000-0001-9932-6622
†lubimova@icmm.ru https://orcid.org/0000-0002-8212-2890

were important from the point of view of applications.The role of thermal boundary conditions, namely, a given heat flux, remained outside the attention of most researchers. Although with relation to geophysical and technical applications, it is more natural to set not the temperature, but the heat flux at the boundaries [2–4].

In this work, we analyze the influence of the finiteness of the cavity length on the onset of instability and the arising plane supercritical regimes. On the horizontal boundaries (solid bottom and free top), a constant heat flux is set, cavities with length-to-height ratios of 2 : 1 and 3 : 1 are considered. The average temperature in the layer is close to room temperature, the dependence of the density of water on temperature is linear and the Prandtl number $Pr = 7$. Calculations of supercritical flows were carried out in the range of Grashof numbers up to forty supercriticalities $r = Ra/Ra_c$.

1. Problem formulation

Consider a horizontally elongated cavity with height h and width L, located in an uniform gravity field g. The origin of the cartesian coordinate system (x, z) is located at the lower boundary, the z axis is directed vertically upward. The cavity is filled with a viscous incompressible fluid, the lateral and lower boundaries are assumed to be solid, and the upper boundary is free. On both horizontal boundaries $z = 0, h$, a fixed vertical heat flux is set $q_z = q$, lateral boundaries $x = 0, L$ are assumed to be thermally insulated, i.e. the heat flux q_x through them is zero.

If the liquid is at rest, then in accordance with the Fourier law, a stationary linear vertical distribution of temperature is established in the cavity, which can be written in the form:

$$T = T_0 + Ah - Az, \tag{1}$$

where $A = -q/\kappa$ is the value of a given constant temperature gradient generated by a given heat flux q, $A > 0$ corresponds to heating from below, then it will be used as a given external parameter of the problem. We introduce into consideration the temperature T' measured from the temperature T_0, then relation (1) will be rewritten as

$$T = Ah - Az. \tag{2}$$

Hereinafter, the prime at the temperature is omitted.

The temperature dependence of the density is assumed to be linear, and its changes due to thermal expansion are sufficiently small. It allows one to use the equations of thermal convection in the Boussinesq approximation.

The linear temperature distribution specified in accordance with (2) will change when an instability of the state of mechanical equilibrium arises and the development of a supercritical flow takes place.

The amount of heat entering the layer through the lower boundary per unit time is equal to the heat flux through the upper boundary, as a result of which the average temperature in the layer does not depend on the convection intensity and is determined only by the initial temperature distribution:

$$T_{av} = \frac{Ah}{2}\,. \tag{3}$$

We restrict ourselves to considering plane supercritical motions. Let us introduce the stream function ψ and vorticity φ into consideration:

$$\mathrm{v}_x = -\frac{\partial\psi}{\partial z}, \quad \mathrm{v}_z = \frac{\partial\psi}{\partial x}, \quad \varphi = \frac{\partial \mathrm{v}_x}{\partial z} - \frac{\partial \mathrm{v}_z}{\partial x}. \tag{4}$$

The equations of free thermal convection of a liquid in the Bussinesq approximation taking into account (4) for variables (ψ, φ, T) can be written in dimensionless form [5]:

$$\frac{\partial \varphi}{\partial t} + \frac{\partial \psi}{\partial x}\frac{\partial \varphi}{\partial z} - \frac{\partial \psi}{\partial z}\frac{\partial \varphi}{\partial x} = \Delta\varphi - \mathrm{Gr}\frac{\partial T}{\partial x}, \tag{5}$$

$$\frac{\partial T}{\partial t} + \frac{\partial \psi}{\partial x}\frac{\partial T}{\partial z} - \frac{\partial \psi}{\partial z}\frac{\partial T}{\partial x} = \frac{1}{\mathrm{Pr}}\Delta T, \tag{6}$$

$$\Delta\psi + \varphi = 0. \tag{7}$$

The following units of measurement are introduced: time — h^2/ν, distance — h, temperature — Ah, velocity — ν/h, stream function — ν and vorticity — ν/h^2. Parameter $\mathrm{Pr} = \nu/\chi$ is the Prandtl number. The dimensionless similarity criterion is an analogue of the Grashof number Gr, and it is determined through the physical constants of the problem by the relation:

$$\mathrm{Gr} = \frac{g\beta A h^4}{\nu^2}. \tag{8}$$

The Rayleigh number is related to Gr and Pr by the ratio:

$$\mathrm{Ra} = \mathrm{Gr}\cdot\mathrm{Pr} = \frac{g\beta A h^4}{\nu\chi}. \tag{9}$$

The coefficients of volumetric expansion β, kinematic viscosity ν and thermal diffusivity χ are assumed to be constant.

The thermocapillary effect, the effects of evaporation and radiation at the upper free boundary are neglected. Then the boundary conditions will be written in the form :

$$\begin{aligned} z = 0: &\quad \psi = \frac{\partial \psi}{\partial z} = 0, \quad \frac{\partial T}{\partial z} = -1,\\ z = 1: &\quad \psi = \varphi = 0, \quad \frac{\partial T}{\partial z} = -1. \end{aligned} \tag{10}$$

The boundary conditions at solid and thermally insulated side boundaries are written as:

$$\begin{aligned} x = 0: &\quad \psi = \frac{\partial \psi}{\partial x} = 0, \quad \frac{\partial T}{\partial x} = 0,\\ x = L: &\quad \psi = \frac{\partial \psi}{\partial x} = 0, \quad \frac{\partial T}{\partial x} = 0. \end{aligned} \tag{11}$$

The state of mechanical equilibrium (2) will be written as:

$$\psi^0 = \varphi^0 = 0, \quad T^0 = 1 - z. \tag{12}$$

Thus, the solution to problem (5)–(7), (10)–(11) is determined by the Prandtl number Pr, Grashof number Gr and aspect ratio L.

In the dimensionless form condition for the constancy of the average temperature (3) can be written as follows:

$$T_{av} = \frac{1}{2}. \tag{13}$$

Problem (5)–(7), (10)–(11) was solved numerically by the finite-difference method, all spatial derivatives were approximated by central differences on a uniform grid. In most calculations, the grid step was assumed to be equal $\Delta = 1/64$. Cavities with $L = 2$, $L = 3$ are considered. An explicit scheme with a constant time step $\Delta^2/10$ was used. The Poisson equation (7) for the stream function was solved on every time step by the succesive over-relaxation method. The vorticity φ values on left, right and bottom boundaries were obtained using Thom's formula [6]. The method used is described in more detail in [5].

The boundary conditions for the temperature at the boundaries of the cavity ensure the conservation of the internal energy of the liquid, i.e. average temperature in the cavity. Therefore, the maintenance of the average temperature was strictly controlled, i.e. implementation of relation (13) in the process of calculating was monitored.

2. Numerical results

The calculations were performed for the value of the Prandtl number $Pr = 7$. Based on the results of calculations, for each of the given values, the critical Grashof number was determined and the nonlinear supercritical regime was investigated in the region of up to several tens of supercriticalities. For the case of an infinitely elongated layer, i.e. for $L = \infty$, the quiescent state of the fluid (12) becomes unstable with respect to small normal disturbances when the Rayleigh number exceeds the critical value $Ra_{cr}(\infty) = 320$ defined in [1] and confirmed in [7,8]. Hence, it follows that the critical Grashof number is equal to $Gr_{cr}(\infty) = 45.7$ for an infinitely elongated cavity $L = \infty$ and the value of the Prandtl number considered in this paper.

Let us consider the effect of a smooth increase in the Grashof number on the stability of solution (12) corresponding to mechanical equilibrium. The finite horizontal size of the cavity, due to the presence of solid vertical walls that inhibit the development of disturbances, as a rule, leads to an increase in the critical numbers of the onset of convective instability. Therefore, the first series of calculations was carried out for the Grashof number $Gr = 70$ in the hope that it exceeds the as yet unknown critical number Gr_{cr} for $L = 2$. Let us describe in more detail the methodology for this calculation. The following distributions were set as the initial state:

$$\psi^0_{i,k} = 0, \quad T^0_{i,k} = 1 - h \cdot k, \quad \varphi^0_{i,k} = \varphi^c \ . \tag{14}$$

The initial value of the vorticity φ^c at all grid nodes was assumed to be 10. Calculations at lower absolute values φ^c, for example, at $\varphi^c = 1$, led to the attenuation of the disturbance (14) and the establishment of an equilibrium state (12).

Fig. 1a shows the stationary solution obtained as a result of the numerical calculation of the evolution of the initial state (14) with $\varphi^c = 10$. In subsequent calculations, to obtain a solution for other values of the Grashof number, the parameter continuation method was used, i.e. the stationary state obtained earlier for a certain Grashof number Gr_1 was taken as the initial state, the Grashof number was changed per step ΔGr, and by numerically solving the problem with this state taken as the initial one, a new stationary state for the Grashof number $Gr_2 = Gr_1 + \Delta Gr$ was obtained. The step size for the Grashof number ΔGr varied from $\Delta Gr = 10$ to $\Delta Gr = 500$. Calculations have shown that such a step-by-step increase in the Grashof number from $Gr = 70$ to $Gr = 3000$ does not lead to a qualitative change in the structure of the supercritical flow, it remains single-vortex (see Fig. 1), although the intensity of movement increases many times. The temperature field changes so that a temperature gradient is formed along the horizontal boundaries, and the temperature gradient in the center of the cavity rotates clockwise by more than 90°.

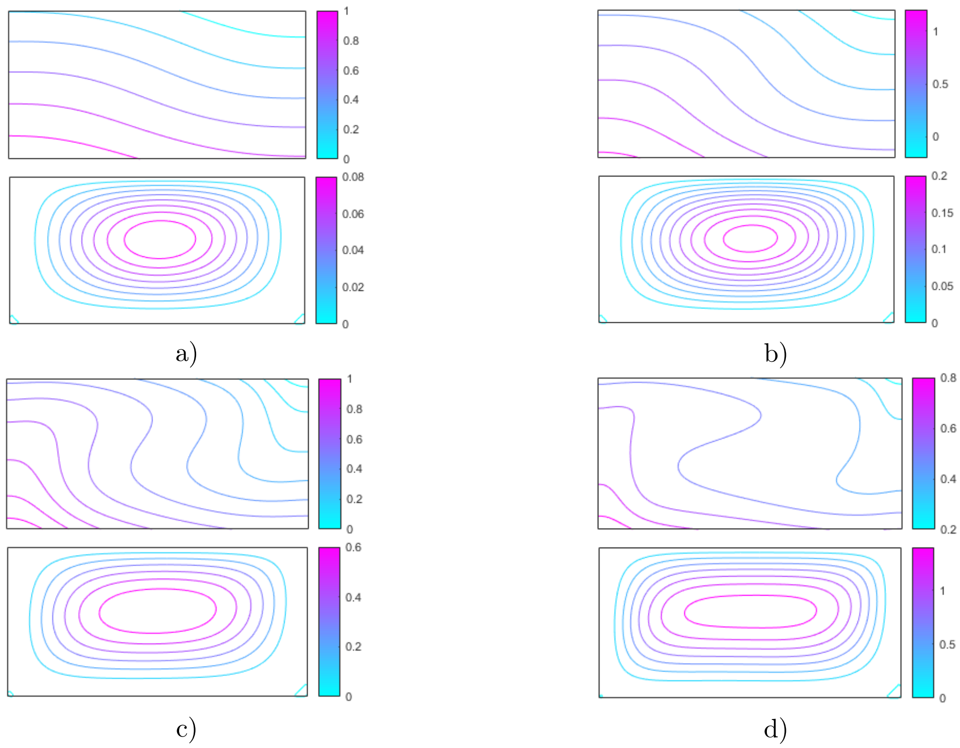

Fig. 1. Isotherms and streamlines of the supercritical convective flow in the cavity $L = 2$ for different values of the Grashof number: a) — $Gr = 70$, b) — $Gr = 100$, c) — $Gr = 500$, d) — $Gr = 3000$

To quantitatively characterize the change in the intensity of supercritical movements with an increase in the Grashof number, we will use the dependences of the average value of the stream function in the cavity $\psi_s(Gr)$ and the kinetic energy of convective motion $E(Gr)$ on Gr:

$$\psi_s(Gr) = \frac{1}{L}\int_0^1\int_0^L \psi dzdx, \tag{15}$$

$$E(Gr) = \frac{1}{2L}\int_0^1\int_0^L v^2 dzdx = \frac{1}{2L}\int_0^1\int_0^L \psi\varphi dzdx. \tag{16}$$

The dependences $\psi_s(Gr)$ and $E(Gr)$ obtained in the calculations and for the interval of Grashof numbers $0 \leqslant Gr \leqslant 3000$ for the flow in the cavity $L = 2$ are presented in Fig. 2. In the region of Grashof numbers $70 \leqslant Gr \leqslant 1000$, the kinetic energy of stationary solutions depends on the Grashof number linearly (the dependence is obtained by the least squares method):

$$E = 1.74 \cdot 10^{-3} \cdot (Gr - 64.5). \tag{17}$$

Extrapolating linearly dependence (17) to zero $E = 0$, we obtain the critical value of the Grashof number $Gr_{cr}(2) = 64.5$. In the area of Grashof numbers $70 \leqslant Gr \leqslant 500$, the root law for the mean stream function is satisfied:

$$\psi_s = 1.17 \cdot 10^{-2} \cdot \sqrt{Gr - 64.5}. \tag{18}$$

Dependencies (17) and (18) are shown by dashed lines in Fig.2.

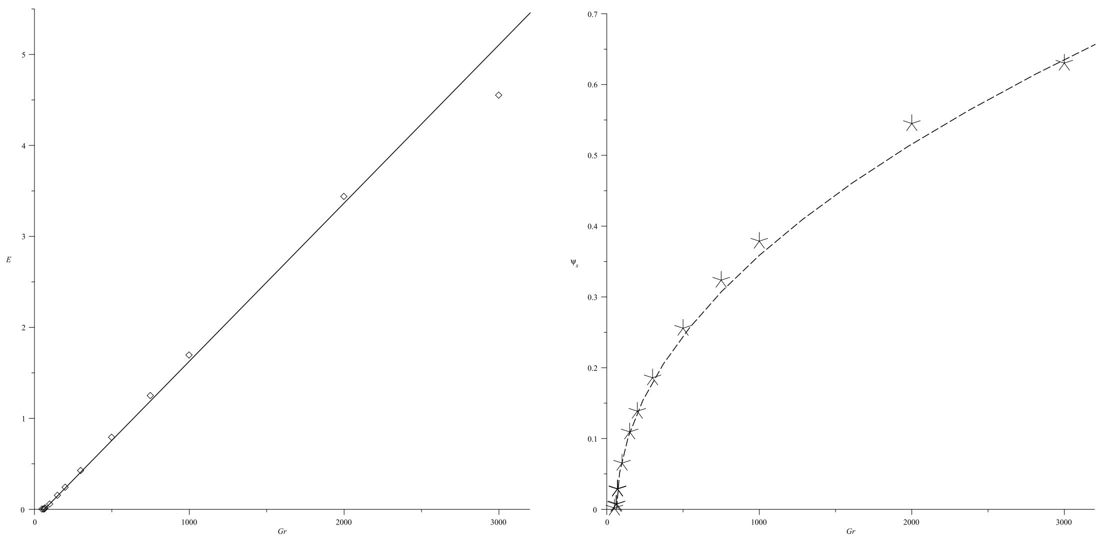

a) b)

Fig. 2. Dependences of kinetic energy $E(Gr)$ (a) and average stream function $\psi_s(Gr)$ (b) of stationary supercritical convective motion in the cavity $L = 2$

Fig. 3a shows the stationary solution obtained as a result of the numerical calculation of the evolution of the initial state (14) with $\varphi_c = 10$ for the case of a more elongated cavity ($L = 3$) than the one considered above. An increase in the elongation of the cavity on 50% does not lead to a qualitative change in the effect of an increase in the Grashof number on the structure of the supercritical flow (see Fig. 3).

The dependences $\psi_s(Gr)$ and $E(Gr)$ obtained in the calculations and for the interval of Grashof numbers $0 \leqslant Gr \leqslant 5000$ for the motion shown in Fig. 3 are presented in Fig. 4. In the region of Grashof numbers $70 \leqslant Gr \leqslant 1000$, the kinetic energy of stationary motions depends on the Grashof number linearly:

$$E = 2.07 \cdot 10^{-3} \cdot (Gr - 61.1). \tag{19}$$

Extrapolating this dependence linearly to zero, we obtain the critical value of the Grashof number $Gr_{cr} = 61.1$. In the area of Grashof numbers $70 \leqslant Gr \leqslant 1000$, the root law for the stream function is satisfied:

$$\psi_s = 1.43 \cdot 10^{-2} \cdot \sqrt{Gr - 61.1}. \tag{20}$$

Dependencies (19) and (20) are shown by dashed lines in Fig. 4. The single-vortex flows obtained in the calculations are a manifestation of long-wave instability, since they can be interpreted as a result of the nonlinear development of the most horizontally extended perturbation. From the streamlines shown in Fig. 3d, it can be seen that for the case of a more elongated cavity, the development of this analogue of a two-wave disturbance leads to the formation of a plane-parallel advective flow in the central part of the cavity, on the upper and lower boundaries of which a constant horizontal temperature gradient is formed.

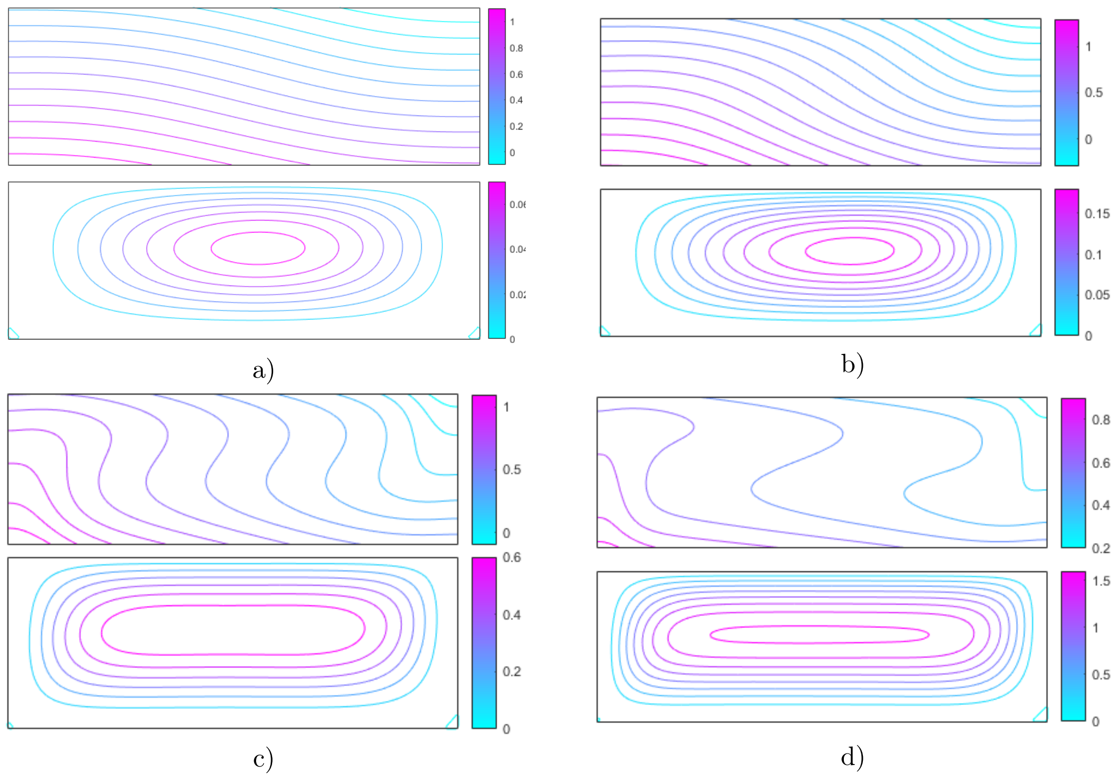

Fig. 3. Isotherms and streamlines of the supercritical convective flow in the cavity $L = 3$ for different values of the Grashof number: a) — $Gr = 70$, b) — $Gr = 100$, c) — $Gr = 500$, d) — $Gr = 3000$

Conclusion

Calculations have shown that even in moderately elongated cavities, the long-wave nature of convective instability manifests itself similarly to this in an infinite horizontal layer at a given vertical heat flux at the boundaries. A manifestation of the long-wave nature of the supercritical convection is that the supercritical convective flow in the entire considered interval of supercriticality has a large-scale one-vortex structure occupying the entire cavity. Note that with an increase in the intensity of heat transfer through the layer, the central part of the vortex is stretched, forming a plane-parallel flow. Such a plane-parallel flow in an infinite layer (i.e. at $L = \infty$), for the case of both rigid boundaries, can lose stability with respect to plane cellular disturbances [9, 10]. Therefore, in future studies, the case when the horizontal size of the plane-parallel flow will be sufficient for the appearance of cellular instability there will be calculated. It is also planned to take into account the thermocapillary effect at the free boundary, which can also lead to the appearance of cellular instability.

Calculations for $L = 2$ were made within the framework of the state assignment. This study was funded by the Ministry of Science and High Education of Russian Federation (Grant No. FSNM-2020-0026). Calculations for $L = 3$ were carried out with the support of the Russian Foundation for Basic Research (project 20-51-12010 NNIO_a) and NNIO (DFG: Projekt ZA 658 / 3-1).

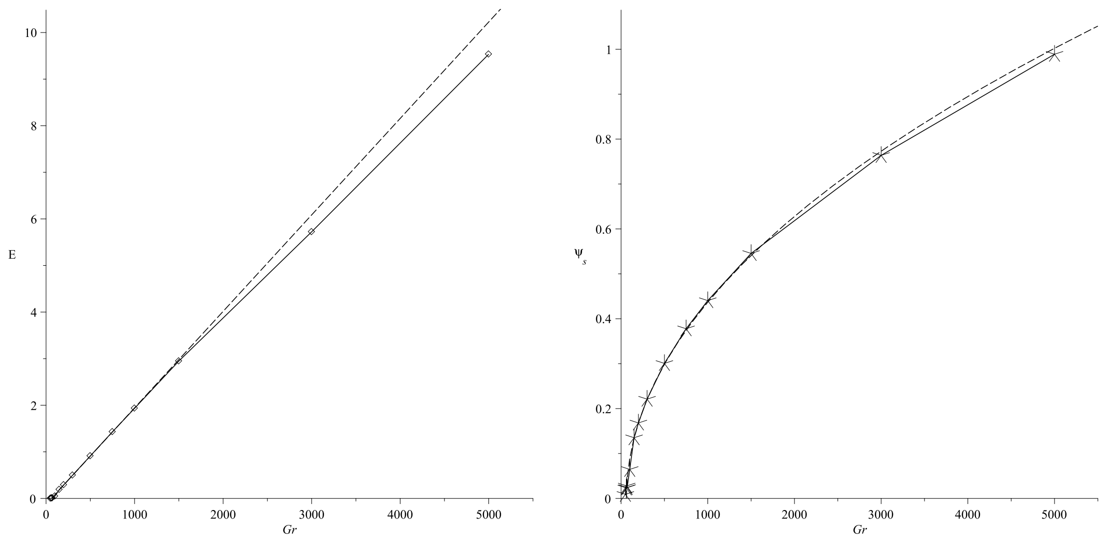

Fig. 4. Dependences of the kinetic energy $E(Gr)$ (a) and the average stream function $\psi_s(Gr)$ (b) of the supercritical stationary convective flow in the cavity $L = 3$

References

[1] E.M.Sparrow, R.J.Goldstein, V.K.Jonsson, Thermal instability in a horizontal fluid layer: effect of boundary conditions and non-linear temperature proille, *Journal of Fluid Mechanics*, **18**(1964), no. 4. 513–528.

[2] L.Kh.Ingel, On the theory of slope flows, *Journal of Engineering Physics and Thermophysics*, 91(2018), no. 3, 641–647. DOI: 10.1007/s10891-018-1785-0

[3] V.B.Bekezhanova, Stability of the equilibrium state in a convection model with nonlinear temperature and pressure dependences of density, *Journal of applied mechanics and technical physics*, **48**(2007), no. 2, 200–207

[4] T.P.Lyubimova, S.A.Prokopev, Nonlinear regimes of Soret-driven convection of ternary fluid with fixed vertical heat flux at the boundaries, *The European Physical Journal E*, **42**(2019), no. 6, 76. DOI: 10.1140/epje/i2019-11837-4

[5] A.N.Sharifulin, Poludnitsin Anatoliy N. The borders of existence of anomalous convection flow in the inclined square cylinder: Numerical determination, *St. Petersburg Polytechnical University Journal: Physics and Mathematics*, **2**(2016), no. 2, 150–156.
DOI: 10.1016/j.spjpm.2016.05.013

[6] A.Thom, C.J.Apelt, Field computations in engineering and physics, 1961.

[7] D.V.Lyubimov, T.P.Lyubimova, V.A.Sharifulin, Onset of convection in a horizontal fluid layer in the presence of density inversion under given heat fluxes at its boundaries, *Fluid Dynamics*, **47**(2012), no. 4, 448–453. DOI: 10.1134/S0015462812040035

[8] V.A.Sharifulin, T.P.Lyubimova, Structure of critical perturbations in a horizontal layer of melted water with the prescribed heat flux at the boundaries, IOP Conf. Series: Materials Science and Engineering, Vol. 208, 2017, 012025.

[9] R.V.Sagitov, A.N.Sharifulin, Stability of advective flow in an inclined plane fluid layer bounded by solid planes with a longitudinal temperature gradient. 1. Unstable stratification, *Journal of Applied Mechanics and Technical Physics*, **58**(2017), no. 2, 264–270. DOI: 10.1134/S0021894417020092

[10] R.V.Sagitov, A.N.Sharifulin, Stability of advective flow in an inclined plane fluid layer bounded by solid planes with a longitudinal temperature gradient 2. Stable stratification, *Journal of Applied Mechanics and Technical Physics*, **58**(2017), no. 4, 687–692. DOI: 10.1134/S0021894417040137

Надкритическая конвекция воды в вытянутой полости при заданном вертикальном тепловом потоке

Вадим А. Шарифулин
Пермский национальный исследовательский политехнический университет
Пермь, Российская Федерация
Татьяна П. Любимова
Институт механики сплошных сред УрО РАН
Пермь, Российская Федерация

Аннотация. Исследуются надкритические режимы конвекции воды при комнатной температуре в вытянутых горизонтальных полостях, с отношением ширины к высоте 2 : 1 и 3 : 1. Число Прандтля полагается равным семи. На верхней свободной и нижней твердой границах задан постоянный тепловой поток, а боковые твердые границы полагаются теплоиз олированными. Расчеты, проведенные конечно-разностным методом для значений числа Релея, превышающих критическое до тридцати раз, показали, что в указанном интервале чисел Релея в обоих полостях в надкритической области реализуется одновихревое стационарное состояние.

Ключевые слова: тепловая конвекция, бифуркации, постоянный тепловой поток.

DOI: 10.17516/1997-1397-2021-14-2-193-203
УДК 622.691.4:622.279.72

Method for Determining the Mass Flow for Pressure Measurements of Gas Hydrates Formation in the Well

Natalya N. Borisova*
North-Eastern Federal University named after M. K. Ammosov
Yakutsk, Russian Federation
Igor I. Rozhin†
Institute of Oil and Gas Problems SB RAS
Federal Research Center "Yakut Scientific Center SB RAS"
Yakutsk, Russian Federation

Received 02.09.2020, received in revised form 25.10.2020, accepted 10.01.2021

Abstract. The work focuses on the inverse problem of determining differential equation coefficients for additional information on the behavior of solution. Furthermore, the algorithm for determining parameters of systems of ordinary differential equations on the basis of stomatal pressure measurements is generalized for the model of hydrate formation when the internal well section of changes with time and also has to be determined during the solution of the general problem. The computational experiment has been conducted for wells of Otradninsky gas condensate deposits of the Republic Sakha (Yakutia), the exploitation of which indicates that the complications are most likely caused by formation of gas hydrates both in the bottom-hole and in the well and its plumes. It has been established that the most important influence on the dynamics of hydrate plugs formation in wells is the gas production mode, its equation of state, reservoir and geocryological conditions. Time dependency of mass flow has been determined, which knowledge will make it possible to control the change of flow area of the entire well and, if necessary, to prevent and remove formation of natural gas hydrates.

Keywords: conjugated problems of heat exchange, production and transport of natural gas, natural gas hydrates, mathematical modeling.

Citation: N.N. Borisova, I.I. Rozhin, Method for Determining the Mass Flow for Pressure Measurements of Gas Hydrates Formation in the Well, J. Sib. Fed. Univ. Math. Phys., 2021, 14(2), 193–203.
DOI: 10.17516/1997-1397-2021-14-2-193-203.

When studying physical phenomena or objects by means of empirical methods, there are often circumstances in which no possible direct observation and measurement of any characteristics of object are noted. The experiment may be associated with technical and material difficulties, considered as a dangerous or simply not feasible process. It is almost possible to obtain any additional information about the object for making appropriate conclusions. In such situations for diagnostics of objects (for example, their internal structure) mathematical processing and interpretation of observation are required. These tasks are required to determine the reasons if the consequences obtained are known as a result of the observation. Such kinds of tasks are called the inverse problems [1]. The inverse problem is the problem of determining model parameters based on available observations of model states.

*kaf_teplofiz@mail.ru
†i_rozhin@mail.ru https://orcid.org/0000-0002-9998-6425

The inverse problems are critical in the modeling, control and operation on technologic processes in complex systems. In particular, this applies to oil and gas production processes related to the filtration and flow through pipes of structured multi-component multi-phase liquids having complex rheological properties (oil with paraffin and tarry asphaltene inclusions, oil-water-gas mixtures, drilling solutions of polymers and surface-active substances, etc.). In accordance with the analysis of experimental information raising and solution of the inverse problem allows to select an adequate model, evaluate its parameters and determine if necessary, missing initial and boundary conditions [2].

Solution of practical problems of gas production and transportation is impossible without use of the most modern achievements of mechanics of liquid and gas and applied mathematics. In the monography [3] solutions of the inverse problems for hydraulic models are considered described by the ordinary differential equations. Such models in hydraulics always correspond to the established flow modes. In this case, the characteristic of the process is not time-dependent.

The established modes are convenient for the solution of identification problems. This is due, first, to the fact that it is quite simple to measure time-independent values in practice, and, second, to the fact that the inverse problems are much easier to solve in the case of ordinary differential equations than in the case of partial differential equations. The identifiable parameters must be effectively incorporated into ordinary differential equations or boundary conditions after the non-stationary terms have been discarded. Among the various numerical methods of solving boundary problems, the most effective are the different modifications of the sweep method (for linear problems) and the combination of Newton methods (quasi-linearization) and sweep method. The characteristic feature of these methods is the reduction of the resolution of boundary problems to the solution of Cauchy problems [3].

An analysis of the methods used to calculate the parameters of gas pipelines and wells by M. A. Kanibolotsky showed that they were very approximate character. For direct gas flow calculations, when all design parameters are known by setting boundary conditions, the pressure and temperature distribution can be found [4].

The coefficient of hydraulic resistance and the coefficient of heat exchange are considered the main phenomenological parameters of the mathematical model of the non-isothermal flow of real gas in the well. These values can be found in three ways: 1) through empirical and semi-empirical relationships that are based on small, and sometimes misunderstood, experimental data, so that they are not devoid of elements of randomness and limitation; 2) description of the non-isothermal flow of gas in pipes within the theory of boundary layer; 3) identification of the well model using additional information on the behavior of the model on pressure and temperature measurements in the well and wellhead; which will serve as boundary conditions for the definite system [3].

The use of additional measurements to determine the coefficient of hydraulic resistance and the coefficient of heat exchange has been used before [5]. However, to process the results of these measurements, simplified models were chosen that neglected the real properties of gas, non-isothermal flow, etc. It was not feasible to calculate directly on more accurate models with such inaccurate identification. The identification method proposed in the monograph [3] makes it possible to find parameters without simplifying the model chosen in such a way as to ensure the required accuracy of the direct calculations.

The natural gas production process is the most important solution of the inverse problems among the complex systems. Gas hydrates may form at this process.

Gas hydrates are divided into natural and technogenic (artificial). The natural gas hydrates may form clusters with a foreseeable industrial significance and may also be scattered. Gas hydrates are currently found in the natural precipitation of the oceans and seas, in the subsoil of the mainland and islands, in the ice of Antarctica and Greenland [4].

Technogenic hydrates are formed in oil and gas production systems: in the bottom-hole, gas and oil wells, plumes and in gas pipelines. In the process of oil and gas production, artificial hydrates are undesirable and methods for preventing and eliminating hydrates have been developed and improved.

The main factors determining the possibility of natural gas hydrates formation under reservoir conditions are: gas composition, reservoir pressure and temperature, the degree of mineralization of pore water. The conditions of hydrate formation are mainly determined experimentally, although these experiments are difficult to perform due to the non-stoichiometry and instability of hydrates. A large number of methods are noted for calculating equilibrium conditions of hydrate formation [4].

In the well gas is intensively cooled by throttling at reduced pressure (isoenthalpic process for gas production and transport [6]) and by means of heat exchange caused by surrounding permafrost rocks. Since many deposits in the northern regions have fairly high reservoir pressures, there is a risk of gas hydrates formation. The formation of hydrates in the bottom-hole results in less productivity and lower capacity in the wells or in their total blockage. The risk of gas hydrates blocking the wells also occurs when they stop due to the low temperature of the surrounding rocks [7].

To describe the formation and deposition of hydrates in the well, a quasi-stationary mathematical model [4, 6–9] is applied, in which movement of the real gas in the pipes is described within the tube hydraulics, while the dynamics of hydrate formation presented within the generalized Stefan problem, in which the temperature of the phase transition «gas+water=hydrate» depends on the pressure in the gas flow. Based on the laws of mass and energy conservation for the gas flow, the equations of continuity, motion and energy of gas is reduced to a system of two ordinary differential equations concerning pressure and temperature [10]. This model is closed by some phenomenological ratios corresponding to a level of description of physical phenomena, so that in the equations there are inevitably some constants revealed by additional information on the basis of the chosen model [11] which can be used, for example, the measurements of gas pressure and temperature. In addition to the phenomenological constants, the model includes technological parameters that can also be characterized by these measurements, such as the gas mass flow, noted as a constant in the stationary mode.

This inverse problem of determining differential equation coefficients is considered in some additional information on the behavior of the solution [7], furthermore, the algorithms for determining parameters of the systems of ordinary differential equations on additional measurements are presented in the works [3, 7, 12], and generalized for the hydrate formation model demonstrated in [4, 6–9].

1. Formulation of the problem

An essential feature of the model studied is the determination of the time-changing well section area, together with the calculation of gas temperature and pressure distribution from the solution of the Cauchy problem for the equation, describing the variation of the dimensionless area of the well section in the course of time

$$\frac{dS}{d\tau} = b_2 \frac{T_e - T_{ph}(p)}{1 - b_2 \ln S} - b_1 \sqrt{S}(T_{ph}(p) - T), \qquad (1)$$

where $b_1 = \dfrac{\alpha_1 d_0}{4\lambda_h}$, $b_2 = \dfrac{\alpha_2 d_0}{4\lambda_h}$, α_1 is the coefficient of heat exchange between the gas and the hydrate layer; α_2 is the coefficient of heat exchange between the hydrate layer and the rock; d_0 is the well diameter before hydrate formation; λ_h the coefficient of hydrate heat conductivity; dimensionless time $\tau = \dfrac{\lambda_h T_c}{\rho_h q_h d_0^2}$; p is the gas pressure, S the dimensional cross section, T the gas temperature, T_e the temperature of the surrounding rocks, T_c is the gas critical temperature; ρ_h the density of hydrate; q_h the specific heat of the phase transition "gas+water=hydrate"; t is the time; $T_{ph}(p) = a\ln(p) + b$ the is equilibrium temperature of hydrate formation, where the empirical coefficients a and b depend on the gas composition. In the equation (1), all temperature values are assigned to the critical gas temperature T_c, the coefficient α_1 depends on the time-changing area of the well section S as follows:

$$\frac{\alpha_1 d_0}{\lambda_g} = 0.023 Pr^{0,43} \left(\frac{M}{d_0 \eta_g}\right)^{0.8} \left(\frac{4}{\pi}\right)^{0.8} \frac{1}{S^{0.9}}, \tag{2}$$

where Pr is the Prandtl number, M is the gas mass flow, η_g and λ_g are the coefficients of gas dynamic viscosity and its heat conductivity

In the equation (1), the coefficient of heat exchange in the well sections is calculated by the formula (2), where the hydrate layer is formed, i.e., where the dimensionless value of the section S is less than 1, and the temperature of the rocks T_e is replaced by the temperature of the phase transition «gas+water = hydrate» T_{ph}.

The algorithm for solving the inverse problem of determining the gas mass flow at variable length and time of the well section according to pressure measurements, which will make it possible to identify signs of hydrates formation in it, varying pressure and temperature distribution over its length.

Following the method described in the work [3], and using the mathematical model proposed in [7, 8], we can set the zero approximation M^0 and compute $p^0(x)$ and $T^0(x)$, presenting the equations of this model in the form of quasi-stationary equations of tube hydraulics [4, 6–9]:

$$\frac{dp}{dx} = -\rho g - \frac{\sqrt{\pi}\psi M^2}{4\rho S^{2.5} S_0^{2.5}}, \tag{3}$$

$$\frac{dT}{dx} - \varepsilon \frac{dp}{dx} = \frac{\pi d\alpha}{c_p M}(T_e - T) - \frac{g}{c_p}, \tag{4}$$

where c_p is the specific heat capacity of gas at constant pressure, d_w is the well diameter, g is the acceleration of gravity, $M = \rho v S S_0$ is the mass gas flow, S_0 is the dimensional section before the formation of hydrates, x is the coordinate along the well axis, α is the total coefficient of heat transfer, $\varepsilon = \dfrac{RT^2}{c_p p}\left(\dfrac{\partial Z}{\partial T}\right)_p$ — throttling factor, ρ — gas density; v — gas flow velocity, ψ — hydraulic resistance coefficient, R is the gas constant. The compressibility coefficient of gas in contrast to the work [4, 7] instead of the Bertlo equation is determined by the Latonov–Gurevich equation [13] , which corresponds appropriately with the reference data [14]:

$$z = \left(0.17376 \ln \frac{T}{T_c} + 0.73\right)^{\frac{p}{p_c}} + 0.1 \frac{p}{p_c},$$

where p_c, T_c are the critical values of natural gas pressure and temperature, which are determined by the critical value sum of each component per gas content.

To the linearized approximation system (3–4) referring $(s + 1)$:

$$\frac{dp^{s+1}}{dx} = f_1^s + \left(\frac{\partial f_1}{\partial p}\right)^s (p^{s+1} - p^s) + \left(\frac{\partial f_1}{\partial T}\right)^s (T^{s+1} - T^s) + \left(\frac{\partial f_1}{\partial M}\right)^s (M^{s+1} - M^s), \quad (5)$$

$$\frac{dT^{s+1}}{dx} = f_2^s + \left(\frac{\partial f_2}{\partial p}\right)^s (p^{s+1} - p^s) + \left(\frac{\partial f_2}{\partial T}\right)^s (T^{s+1} - T^s) + \left(\frac{\partial f_2}{\partial M}\right)^s (M^{s+1} - M^s), \quad (6)$$

we can set $p^{s+1}(x)$ and $T^{s+1}(x)$, expressed through the sweeping coefficients C and D

$$p^{s+1} = C_1 M^{s+1} + D_1, \quad (7)$$

$$T^{s+1} = C_2 M^{s+1} + D_2. \quad (8)$$

As the result of these coefficients we obtain the following equations:

$$\frac{dC_1}{dx} = \left(\frac{\partial f_1}{\partial p}\right)^s C_1 + \left(\frac{\partial f_1}{\partial T}\right)^s C_2 + \left(\frac{\partial f_1}{\partial M}\right)^s, \quad (9)$$

$$\frac{dC_2}{dx} = \left(\frac{\partial f_2}{\partial p}\right)^s C_1 + \left(\frac{\partial f_2}{\partial T}\right)^s C_2 + \left(\frac{\partial f_2}{\partial M}\right)^s, \quad (10)$$

$$\frac{dD_1}{dx} = \left(\frac{\partial f_1}{\partial p}\right)^s (D_1 - p^s) + \left(\frac{\partial f_1}{\partial T}\right)^s (D_2 - T^s) + f_1^s - \left(\frac{\partial f_1}{\partial M}\right)^s M^s, \quad (11)$$

$$\frac{dD_2}{dx} = \left(\frac{\partial f_2}{\partial p}\right)^s (D_1 - p^s) + \left(\frac{\partial f_2}{\partial T}\right)^s (D_2 - T^s) + f_2^s - \left(\frac{\partial f_2}{\partial M}\right)^s M^s, \quad (12)$$

and initial states

$$C_1(0) = C_2(0) = 0, \quad D_1(0) = p_0, \quad D_2(0) = T_0. \quad (13)$$

After numerical solution of these problems Cauchy, using the exit condition $p(L) = p_y$ and the ratio (7), we detect

$$M^{s+1} = \frac{p_y - D_1(L)}{C_1(L)}, \quad (14)$$

where L is the length of the well, p_y is the pressure on the wellhead.

The algorithm for the numerical solution of the conjugate problem of the well heat exchange with frozen rocks can now be described as follows:

1. Set the zero approximation of the flow rate M^0, which is formed by a simplified model of the isothermal flow of ideal gas without the formation of hydrate ($S = 1$):

$$M^0 = \left(\frac{4}{\sqrt{\pi}}\frac{gS_0^{2.5}}{\psi R^2 T_0^2}\left(\frac{p_0^2 e^{-\frac{2gL}{RT_0}} - p_y^2}{1 - e^{-\frac{2gL}{RT_0}}}\right)\right)^{\frac{1}{2}}. \quad (15)$$

2. Compute from equation (15):

$$p_y^0(x) = \left(p_0^2 e^{-\frac{2gL}{RT_0}} - \frac{\sqrt{\pi}\psi R^2 T_0^2 (M^0)^2}{4gS_0^{2.5}}\left(1 - e^{-\frac{2gL}{RT_0}}\right)\right)^{\frac{1}{2}}.$$

3. Define the initial values of the sweeping coefficients on the equations (13) by means of them the following solutions (7) and (8) are expressed.

4. Solving the Cauchy problem for the system (9)–(12) by the Runge-Kutta method of the order 4, find $C_1(x)$ and $D_1(x)$.

5. In the equation (14) determine the flow rate M^{s+1}.

6. By setting in the ratio (7) to (8), find $p^{s+1}(x)$ and $T^{s+1}(x)$.

7. Repeat the items 3 to 6 until the necessary precision is achieved. This parameter is determined by nature of the object on which measurements are made, where the accuracy of the measurement equipment (i.e. input data) is of great importance. Calculations have shown that the necessary accuracy of determining the model parameters with an error determined by modern measuring equipment is achieved with 3–8 measurement points. In all cases, the convergence of successive approximations with a relative accuracy of 1% required 2–4 iterations.

8. From the equation (1), taking the time step, using the Runge–Kutta method, find a new value of the section area. In this case, the x-coordinate is included as a parameter in this equation.

9. Determinate the temperature distribution in the rock mass, that is to say, solve the initial-boundary problem for the thermal conductivity equation by the pass-through method with smoothing the breaking coefficients by temperature in the surroundings of the phase transition according to the approach described in the work [8]. Since the smoothed coefficients depend on temperature, the resulting difference problem is nonlinear and its solution is detected by the method of simple iteration using the sweeping algorithms. The algorithm phase is performed only when the task is conjugated.

At each time step, items 3 to 9 are repeated.

To evaluate the accuracy of the finite-difference scheme developed on the basis of the Samarsky-Moiseenko method [15], the results of numerical calculation were compared with the exact self-similar solution of thawing problem an unlimited rock mass at a constant temperature of exposure at the boundary [16]. Based on the dynamics of the phase front movement of thawing rocks, it is found that the speed of the phase front decreases over time due to the low thermal inertia of the thawed zone of rocks. The insignificant difference between the results of calculating the thawing of rocks is explained by the fact that in the exact self-similar solution, in contrast to the numerical solution, the rock is considered unlimited, that is, due to the lack of a heat-insulated boundary, favorable conditions are created. For the numerical solution of this one-dimensional problem, a boundary condition of the 1st kind is assumed for the radius of thermal influence. The results of comparing the exact self-similar and numerical solutions allow us to conclude that the developed finite-difference scheme and computational algorithm are correct.

2. Results of the computational experiment

The calculations were carried out at the following parameter values corresponding to the Otradninsky gas condensate deposit of the Sakha Republic (Yakutia) [9]: $\alpha = 5.82$ W/(m^2·K), $R = 438.271$ J/(kg·K), $d_w = 0.146$ m, $\varphi = 90°$, $\psi = 0.02$, $\rho_h = 920$ kg/m^3, $q_h = 510000$ J/kg, $\lambda_h = 1.88$ W/(m·K), $\lambda_g = 0.0307$ W/(m·K), $c_p = 2300$ J/(kg·K), $\eta_g = 1.3\cdot 10^{-5}$ Pa·s, $p_0 = 188.352\cdot 10^5$ Pa, $T_0 = 286.35$ K, $p_c = 44.679\cdot 10^5$ Pa, $T_c = 195.376$ K, $a = 6.635$ K, $b = 182.951$ K,

$$T_e = \begin{cases} T_{e0} - \Gamma x, & 0 < x < L - H; \\ 272.15K, & L - H < x < L. \end{cases}$$

$L = 2480$ m, $H = 680$ m, $T_{e0} = 286.48$ K, $\Gamma = 0.0074$ K/m, gas content (об.%): CH_4 – 83.15, C_2H_6 – 4.16, C_3H_8 – 1.48, iC_4H_{10} – 0.17, nC_4H_{10} – 0.50, iC_5H_{12} – 0.12, nC_5H_{12} – 0.17, C_6H_{14} – 0.17, C_7H_{16+} – 0.28, CO_2 – 0.07, N_2 – 9.50, H_2 – 0.02, He – 0.21. The pressure at the wellhead ranged from 11 MPa to 14 MPa.

Comparing to experimental data is very difficult and always requires the expenses of facilities and time. Therefore, only theoretical numeral calculations are performed. There are practically no model tests or studies on these processes. In process fact sheets are not considered about hydrate formation on the indicated deposit. During the operation of wells in the Otradninsky deposit, due to the low reservoir temperature, even with small depressions on the formation, intensive hydrate formation occurs in the wellbore and a sharp decrease in gas inflow. For this reason, the bottom-hole zone of wells is pre-treated with methanol. Further operation of gas wells has shown that one of the main causes of complications is the formation of hydrate plugs in the pump and compressor pipes and wellhead equipment. This is understandable, since the wellhead temperature of operating wells is 1°C below zero. Therefore, testing the capabilities of mathematical modeling of the Otradninsky deposit development at this stage is reduced to predicting the presence of gas hydrates before the start of gas production and the possibility of their formation in the bottom-hole zone and the wellbore.

To test an algorithm of the numerical solution, a preliminary comparison of the calculation results with the results presented in [7] and carried out in the case of a main gas pipeline was carried out.

The analysis of the calculation results shows that in the Otradninsky deposit the formation of hydrates can be noted in the absence of inhibitors throughout the well, but more intensively this process takes place in its upper part, approximately corresponding to the permafrost capacity. The complete plugging of the wellhead can be observed approximately in $1 \div 2.5$ hours depending on the pressure drop. At the same time, 25–40 % per cent of the well section will be covered on the bottom-hole (Fig. 1 and Fig. 2).The results of the computational experiment showed that the calculation results of the well section coincide for the conjugate and non-conjugate (at a constant temperature of the rocks) problems. This is due to the relatively rapid formation of hydrates,

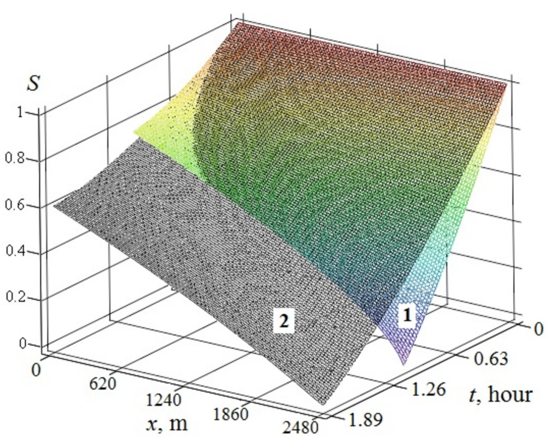

Fig. 1. Dynamics of change in the dimensionless flow area along the well depth at $p_y = 11$ MPa: 1 — real gas, 2 — ideal gas

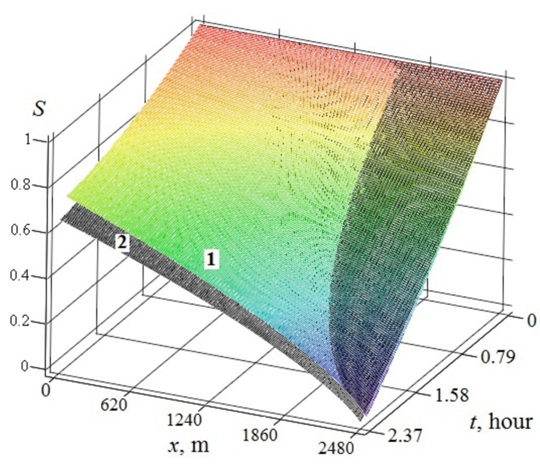

Fig. 2. Dynamics of change in the dimensionless area flow area along the well depth at $p_y = 14$ MPa: 1 — real gas, 2 — ideal gas

i.e. the heat exposure time of the rocks is insignificant: at $p_y = 11$ MPa pressure for the real gas is 1.08 hours, for the ideal gas it is 1.89 hours; at $p_y = 14$ MPa for the real gas it is 2.28 hours; for the ideal gas it is 2.37 hours (Fig. 1 and Fig. 2). You can see that the well plugging time for the real gas is shorter, that testifies to the significant role of throttling at relatively small pressure ratio. As the depression decreases, the length of the complete hydrate blocking process is almost doubled in the well. In the case of real gas there is less intensive increase of the hydrate layer, than in the case of ideal gas especially at the well bottom . At the same time, the growth dynamics of this layer is more dependent on the pressure in the output section than on the temperature of the rocks [7].

Consequently, in the equal reservoir and geocryological conditions the gas production mode and its state equation have the greatest influence on the dynamics of hydrate cork formation in the wells. As you can see from the Fig. 3, the gas temperature throughout the depth of the well is

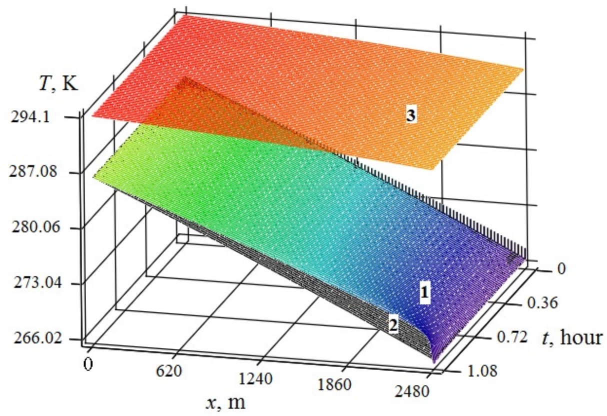

Fig. 3. Gas temperature variation on the well depth and time for Otradninsky deposit at $p_y = 11$ MPa: 1 — conjugate statement, 2 — non-conjugate statement, 3 — equilibrium temperature of hydrate formation

lower than the hydrate formation temperature, which proves the rapid plugging of the gas well. The gas temperatures are slightly higher in the conjugate statement than in the unchanging temporal temperature of the surrounding rocks. The case of the temperature change at the well-head pressure 14 MPa is not presented, as the gas temperature values at the conjugate and non-conjugate statement are practically the same.

Fig. 4 and Fig. 5 present the dynamics of changes in the radii of thawing of frozen rocks near the well in the case of real and ideal gas at the wellhead 11 MPa and 14 MPa. It can be seen that if in calculating gas is considered to be ideal, the radius of thawing will be about 10 cm on the permafrost bottom. Due to the shorter time for gas to heat the rocks, the depth of thawing at the wellhead $p_y = 11$ MPa is lower than for $p_y = 14$ MPa. This is also confirmed by the temperature variation at the well surface (see Fig. 6 and Fig. 7).

Fig. 8 illustrates the effect of the pressure drop, the gas state and hydrate formation equations on the gas mass flow rate, that is, the capacity of the well. For all variants of calculation no increase of the mass flow is noted at the beginning as it was obtained for the pipeline [7]. This is due to the minor thermal interaction of gas in the well with the surrounding rocks. For gas in the presence of hydrate formation inhibitor, the mass flow rate remains almost constant and, while in the case of hydrates formation it decreases to zero in relatively short time. The rate of decline depends on the gas state equation (compare pairs of lines 3 and 7, 4 and 8). At the same time, it depends on the pressure difference (compare the pairs of lines for the real gas 1, 2 and 3, 4, for the ideal gas 5, 6 and 7, 8), although this effect can also be explained by the fact that a higher rate of the pressure drop corresponds to the increase in the initial mass flow.

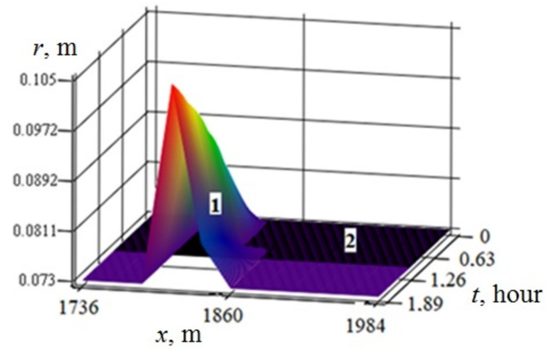

Fig. 4. Variation of the radius at thawing frozen rocks around the well in its depth and time if $p_y = 11$ MPa: 1 — ideal gas; 2 — real gas

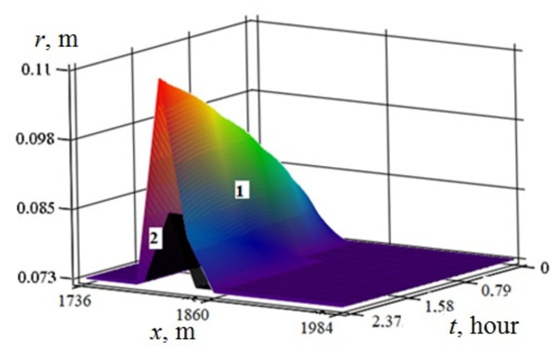

Fig. 5. Variation of the radius at thawing frozen rocks around the well in its depth and time if $p_y = 14$ MPa: 1 — ideal gas; 2 — real gas

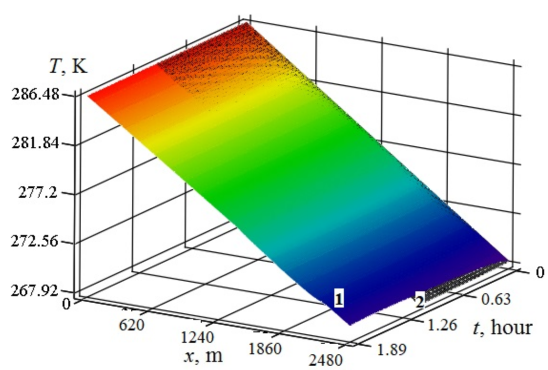

Fig. 6. Variation of temperature on the well surface in its depth and time at $p_y = 11$ MPa: 1 — real gas, 2 — ideal gas

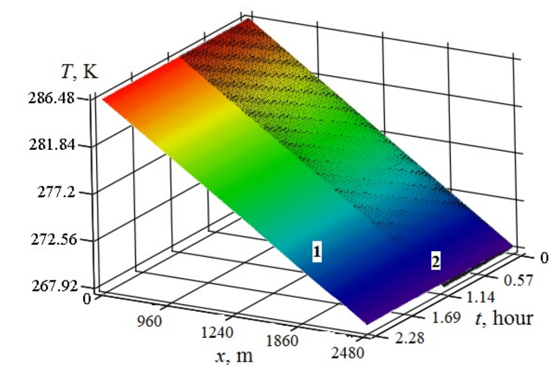

Fig. 7. Variation of temperature on the well surface in its depth and time at: 1 — $p_y = 14$ MPa, 2 — $p_y = 11$ MPa

For lower depression, the initial flow rate for the real gas is lower than for the ideal gas (see curves 1 and 5), and for larger depression it is higher (see curves 2 and 6). But as this initial flow increases, the length of the complete plugging of the wellhead area by hydrates is reduced (see curves 4 and 8). It can be seen that due to throttling in the case of real gas this time is less than in the case of ideal gas.

Conclusion

Variations in pressure and temperature distribution over the length of the well are the main signs of hydrate formation, the inventive generalized algorithm for solving the inverse problem of determining a mass gas flow at a well cross-section which is variable in time according to the wellhead pressure measurements is disclosed. Knowing the dynamics of changes in the mass flow rate over time, it is possible to control the change in the flow section throughout the well and, if necessary, measures should be taken to prevent and remove natural gas hydrates.

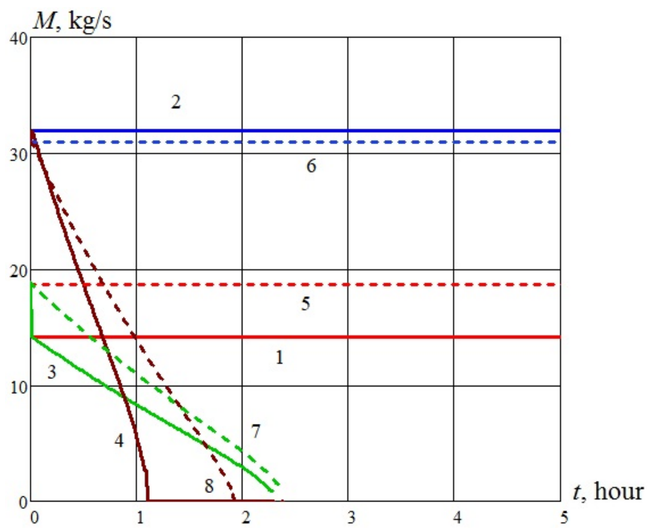

Fig. 8. Mass flow rate dynamics: 1–4 for real gas (solid lines); 5–8 for ideal gas (dotted lines); 1, 3, 5 and 7 for $p_y = 14$ MPa; 2, 4, 6 and 8 for $p_y = 11$ MPa; 1, 2, 5 and 6 — a hydrate free mode; 3, 4, 7 and 8 — a hydrate mode

References

[1] A.I.Korotkiy, Yu.V.Starodubtsev, Modeling of direct and inverse boundary problems for stationary heat and mass transfer models: monography, Ekaterinburg, Ural federal university, EBS ASV, 2015 (in Russian).

[2] A.H.Mirzadzhanzade, M.M.Hasanov, R.N.Bahtizin, Modeling of oil and gas production processes. Nonlinearity, non-equilibrium, uncertainty, Moscow–Izhevsk, Institute of computer researches, 2004 (in Russian).

[3] E.A.Bondarev, A.F.Voevodin, V.S.Nikiforovskaya, Methods of identification of hydraulics mathematical models, Yakutsk, Publishing house NEFU, 2014 (in Russian).

[4] E.A.Bondarev, A.F.Voevodin, Solution of problems of trumpet hydraulics in systems of natural gas production and transport, Novosibirsk, Publishing house of the Siberian Branch of the Russian Academy of Science, 2017 (in Russian).

[5] I.A.Charny, Basis of gas dynamics, Moscow, Gostoptechizdat, 1961 (in Russian).

[6] E.A.Bondarev, V.I.Vasilev, A.F.Voevodin, N.N.Pavlov, A.P.Shadrina, Thermohydrodynamics of gas production and transport system, Novosibirsk, Nauka, Sib. Branch, 1988 (in Russian).

[7] E.A.Bondarev, I.I.Rozhin, K.K.Argunova, A new algorithm of mass flow rate determination in gas production and transport systems via pressure measurement, *J. of Applied Mechanics and Technical Physics*, **58**(2017), no. 5, 853–861. DOI: 10.1134/S002189441705011X

[8] E.A.Bondarev, I.I.Rozhin, K.K.Argunova, Modeling of hydrate formation in gas wells at their thermal interaction with rocks, *J. of Engineering Physics and Thermophysics*, **87**(2014), no. 4, 900–907. DOI: 10.1007/s10891-014-1087-0

[9] E.A.Bondarev, I.I.Rozhin, K.K.Argunova, Features of mathematical modeling of natural gas production and transport systems in the Russia's arctic zone, *J. of Mining Institute*, **228**(2017), 705–716.

[10] O.F.Vasilev, E.A.Bondarev, A.F.Voevodin, M.A.Kanibolotskiy, Non-isothermal gas current in pipes, Novosibirsk, Nauka, 1978 (in Russian).

[11] I.I.Blehman, A.D.Myshkis, J.G.Panovko, Applied mathematics. Subject, logic, sensitive approaches, Kiev, Naukova Dumka, 1976 (in Russian).

[12] E.A.Bondarev, A.F.Voevodin, M.A.Kanibolotsky, E.A.Metljaeva, Inverse problems of stationary non-isothermal gas current in pipes, *Bulletin of the USSR Academy of Sciences. Energy and transport*, (1977), no. 1, 143–145 (in Russian).

[13] V.V.Latonov, G.R.Gurevich, Calculation of compressibility factor of natural gases, *Gas industry*, (1969), no. 2, 7-9 (in Russian).

[14] K.K.Argunova, E.A.Bondarev, I.I.Rozhin, Properties of real gas and their analytical representation, *Gas chemistry*, **16**(2010), no. 6, 52–54 (in Russian).

[15] A.A.Samarsky, B.D.Moiseenko, An economic continuous calculation scheme for the Stefan multidimensional problems, *J. Computational Mathematics and Mathematical Physics*, **5**(1965), no. 5, 816–827 (in Russian).

[16] H.S.Carslow, J.C.Jaeger, Heat conduction of solids, Moscow, Nauka, 1964 (in Russian).

Метод определения массового расхода по замерам давления при образовании газовых гидратов в скважине

Н.Н. Борисова
Северо-Восточный федеральный университет им. М. К. Аммосова,
Якутск, Российская Федерация
И.И. Рожин
Институт проблем нефти и газа СО РАН
Федеральный исследовательский центр «Якутский научный центр СО РАН»
Якутск, Российская Федерация

Аннотация. Работа посвящена обратной задаче определения коэффициентов дифференциальных уравнений по дополнительной информации о поведении решения. При этом алгоритм определения параметров систем обыкновенных дифференциальных уравнений по замерам устьевого давления обобщается для модели гидратообразования, когда внутреннее сечение скважины изменяется во времени и также подлежит определению в ходе решения общей задачи. Вычислительный эксперимент проведен для скважин Отраднинского газоконденсатного месторождения Республики Саха (Якутия), эксплуатация которых свидетельствует о том, что наиболее вероятной причиной осложнений является образование газовых гидратов как в призабойной зоне, так и в стволе скважин и их шлейфах. Установлено, что наибольшее влияние на динамику образования гидратных пробок в скважинах оказывают режим отбора газа, его уравнение состояния, пластовые и геокриологические условия. Определена зависимость массового расхода по времени, знание которой позволит контролировать изменение проходного сечения по всей скважине и в случае необходимости проводить мероприятия по предотвращению образования и удалению гидратов природного газа.

Ключевые слова: сопряженные задачи теплообмена, добыча и транспорт природного газа, гидраты природного газа, математическое моделирование.

Journal of Siberian Federal University. Mathematics & Physics 2021, 14(2), 204–212

DOI: 10.17516/1997-1397-2021-14-2-204-212
УДК 517.977.55:536.25

Asymptotic Behavior of Small Perturbations for Unsteady Motion an Ideal Fluid Jet

Viktor K. Andreev*
Institute of Computational Modelling SB RAS
Krasnoyarsk, Russian Federation
Siberian Federal University
Krasnoyarsk, Russian Federation

Received 14.11.2020, received in revised form 05.01.2021, accepted 15.02.2021

Abstract. The stability problem of unsteady rotating circular jet motion of an ideal fluid is reduced to solving an initial-boundary value problem for Poincare–Sobolev type equation with an evolutionary condition on the jet free initial boundary. The solution of this problem is constructed by the method of variables separation. The asymptotic amplitudes behavior perturbations of the free jet boundary at $t \to \infty$ is found. The results obtained are compared with the known results on the stability of the potential jet motion.

Keywords: unsteady motion, free boundary, small perturbations, equations of the Poincare–Sobolev type, instability.

Citation: V.K. Andreev, Asymptotic Behavior of Small Perturbations for Unsteady Motion an Ideal Fluid Jet, J. Sib. Fed. Univ. Math. Phys., 2021, 14(2), 204–212.
DOI: 10.17516/1997-1397-2021-14-2-204-212.

Introduction

There are numeros works devoted to the study small disturbances of rest or uniform fluid rotation (see [1, 2] and the literature available there). Let $\boldsymbol{e}_3$ is unit vector of the rotation axis z. Homogeneous gravity field of intensity $-g\boldsymbol{e}_3$ acts on an ideal fluid. Fluid rotates with constant angular velocity $\omega_0 \boldsymbol{e}_3$ ($\omega_0 > 0$). The equations of small oscillations of such a fluid were derived by A. Poincare in 1885 [3]. In a rotating Euler coordinate system, they have the form

$$\boldsymbol{U}_t - \omega_0 \boldsymbol{e}_3 \times \boldsymbol{U} + \frac{1}{\rho_0}\nabla P = 0, \quad \operatorname{div} \boldsymbol{U} = 0, \tag{0.1}$$

where $\boldsymbol{U}, P$ are speed and pressure disturbances, $\rho_0 > 0$ is constant fluid density. In this case, the main state is $(0, 0, 0, -gz + \omega_0^2(x^2 + y^2)/2)$. Poincare showed that any component of the vector $\boldsymbol{U}$ and the function P are the solution of the equation

$$\frac{\partial^2}{\partial t^2}\triangle\Psi + 4\omega_0^2\frac{\partial^2\Psi}{\partial z^2} = 0, \tag{0.2}$$

where $\triangle$ is Laplace operator in variables x, y, z. A survey of the results of A. Poincare and some other authors can be found in the classical monograph [4] (see chapter XII "Rotating masses of liquid").

*andr@icm.krasn.ru

The solvability of some initial-boundary value problems for system (0.1) was established by S. L. Sobolev in [5]. He also introduced the state function $\Phi(x, y, z, t)$ in terms of which the solution of system (0.1) is expressed in the form [6]:

$$\begin{gathered} \boldsymbol{U} = \frac{\partial^2}{\partial t^2}\nabla\Phi + 2\omega_0\frac{\partial}{\partial t}\nabla\Phi \times \boldsymbol{e}_3 + 4\omega_0^2(\nabla\Phi \cdot \boldsymbol{e}_3)\boldsymbol{e}_3, \\ \frac{1}{\rho_0}P = -\frac{\partial^3\Phi}{\partial t^3} - 4\omega_0^2\frac{\partial^2\Phi}{\partial t^2}, \end{gathered} \tag{0.3}$$

and the function Φ satisfies (0.2). Representation (0.3) makes it possible to more simply establish the properties of solutions of capillary hydrodynamics problems [2]. Equation (0.2) does not satisfy the Cauchy–Kovalevskaya conditions. Its nonclassicality significantly affects the formulation of boundary value problems, the asymptotic properties of solutions, and the properties of the spectrum [7, 8]. In connection with the above, equation (0.2) is usually called the Poincare–Sobolev equation. More general differential equations that are not resolved with respect to the highest time derivative are studied in [8]. These include the equations of small perturbations in the atmosphere and ocean [9–11] in particular. In contrast to (0.2), here the coefficients of differential operators can depend on spatial variables.

In the present work, we study the asymptotic behavior of small perturbations of unsteady tension and rotation of a circular jet of an ideal fluid. In this case, the equation coefficients of the Poincare–Sobolev type already depend on the time variable. Using the Lagrange coordinates, it is possible to separate the variables and obtain the amplitude equations. They are ODEs of the second order in the time variable. The asymptotic behavior of the perturbation of the jet free boundary is found. A comparison with a similar behavior of perturbations for a non-rotating jet is made.

1. Basic motion

System of equations for an ideal incompressible fluid in Lagrangian coordinates $\boldsymbol{\xi} = (\xi, \eta, \zeta)$ has the form [12, 13]

$$M^*\left(\mathbf{x}_t - \mathbf{g}(\mathbf{x}, t)\right) + \frac{1}{\rho_0}\nabla p = 0, \tag{1.1}$$

$$\operatorname{div} M^{-1}\mathbf{x}_t = 0, \tag{1.2}$$

where M is Jacobi matrix of the mapping $\mathbf{x}(\boldsymbol{\xi}, t)$ the initial area Ω to the region of motion Ω_t at the time t; M^*, M^{-1} are transposed and inverse to M matrices; $\mathbf{g}(\mathbf{x}, t)$ is known vector mass forces; $p(\boldsymbol{\xi}, t)$ is fluid pressure; ρ_0 is constant density; all differential operations are performed by variables ξ, η, ζ. Mass conservation equation (1.2) is equivalent to the equality $\det M = 1$ for all $t \geqslant 0$ [12].

Solution of systems (1.1), (1.2) is sought in a fixed region Ω with initial data a $t = 0$

$$\mathbf{x} = \boldsymbol{\xi}, \quad \mathbf{x}_t = \mathbf{u}_0(\boldsymbol{\xi}), \quad \operatorname{div}\mathbf{u}_0(\boldsymbol{\xi}) = 0, \quad \boldsymbol{\xi} \in \Omega. \tag{1.3}$$

It is easy to check that formulas

$$\mathbf{x} = M\boldsymbol{\xi}, \quad \frac{1}{\rho_0}\,p = \frac{1}{2}\left(\omega_0^2\tau - \frac{3}{4}\frac{k^2}{\tau^3}\right)(\xi^2 + \eta^2) + f(t), \tag{1.4}$$

where

$$M = \begin{pmatrix} \frac{1}{\sqrt{\tau}}\cos\theta & -\frac{1}{\sqrt{\tau}}\sin\theta & 0 \\ \frac{1}{\sqrt{\tau}}\sin\theta & \frac{1}{\sqrt{\tau}}\cos\theta & 0 \\ 0 & 0 & \tau \end{pmatrix}, \quad \tau = 1 + kt, \tag{1.5}$$

$$k = \mathrm{const} > 0, \quad \omega_0 = \mathrm{const} > 0, \quad \theta = \omega_0 \int_0^{\mathrm{t}} \tau(\mathrm{t})\,\mathrm{dt},$$

$f(t)$ is an arbitrary function, represent an exact solution of the system (1.1), (1.2) in the absence of mass forces, that is $\mathbf{g}(\mathbf{x}, t) = 0$.

If in (1.4) we choose the function $f(t)$ in the form

$$f(t) = -\frac{1}{2}\left(\omega_0^2\tau - \frac{3}{4}\frac{k^2}{\tau^3}\right) r_0^2 + \frac{\sigma\sqrt{\tau}}{r_0}, \tag{1.6}$$

$r_0 > 0$, $\sigma \geqslant 0$ are constants, then we can give the solution (1.4)–(1.6) next physical interpretation.

At the initial moment of time $t = 0$ circular jet of ideal fluid of length h_0 rotates around the z axis, and vorticity $\boldsymbol{\omega}_0 = (\mathrm{rot}\,\mathbf{u}_0)/2 = (0, 0, \omega_0)$, see Fig. 1, $\mathbf{u}_0 = (-k\xi/2 - \omega_0\eta, \omega_0\xi - k\eta/2, k\zeta)$.

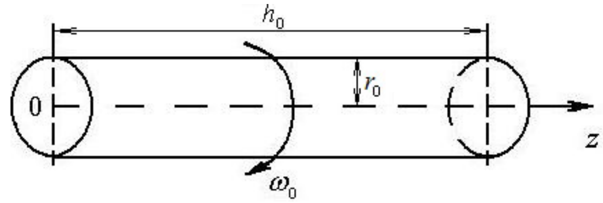

Fig. 1. Motion field scheme

The jet surface $\xi^2 + \eta^2 = r_0^2$ is free and on it capillary forces act (σ is surface coefficient tension). At $t > 0$ the jet begins to stretch along the z axis and continues to rotate around this axis. Vorticity in Euler coordinates is $\boldsymbol{\omega} = \mathrm{rot}_x\mathbf{u} = (0, 0, \omega_0\tau)$ and the velocity vector is

$$\mathbf{u} = \left(-\frac{k}{2\tau}\,x - \omega_0\tau y, \omega_0\tau x - \frac{k}{2\tau}\,y, \frac{k}{\tau}\,z\right). \tag{1.7}$$

The walls $\zeta = 0$ and $\zeta = h_0$ can be considered impenetrable, and the second of them at $t = 0$ starts to move with the speed $\omega_0 = \mathrm{const}$. The first wall remains stationary. The moving wall law is $z = (1 + kt)h_0$, then the constant $k = \omega_0/h_0$. Free border in all times remain cylindrical, and its radius decreases according to the formula $R(t) = r_0/\sqrt{\tau}$.

Remark 1. A solution of the form (1.4) for $\omega_0 = 0$ and $\sigma = 0$ was indicated in paper [12] as an example of unsteady motion of an ideal fluid with a free boundary with a linear velocity field. In this case, the matrix M is diagonal, and the movement will be potential.

In Euler coordinates, the pressure is in the form (equality (1.6) taken into account)

$$\frac{1}{\rho_0}\,p = -\frac{1}{2}\left(\omega_0^2\tau^2 - \frac{3}{4}\frac{k^2}{\tau^2}\right)[R^2(t) - (x^2 + y^2)] + \frac{\sigma}{R(t)}. \tag{1.8}$$

It is clear that the simplest solution (1.7), (1.8) is written in the cylindrical coordinate system (r, φ, z), such as,

$$\mathbf{u} = \left(-\frac{k}{2\tau}\,r, \omega_0\tau r, \frac{k}{\tau}\,z\right), \quad \frac{1}{\rho_0}\,p = -\frac{1}{2}\left(\omega_0^2\tau^2 - \frac{3}{4}\frac{k^2}{\tau^2}\right)[R^2(t) - r^2] + \frac{\sigma}{R(t)}. \tag{1.9}$$

2. Small perturbation equations

Since the jet motion described by the formulas (1.4)–(1.6) is vortex, then we will use equations for perturbations in Lagrangian coordinates, obtained in [13]

$$\operatorname{div}\left[M^{-1}W\int_0^t W^{-1}M^{*-1}(\nabla\Phi+\mathbf{U}_0)\,dt_1\right]=0,\quad \boldsymbol{\xi}\in\Omega,\quad t>0, \tag{2.1}$$

$$\Phi_t+aN-\sigma\overline{\Delta}_\Gamma(t)N=0, \tag{2.2}$$

$$N=b\mathbf{n}\cdot M^{-1}W\int_0^t W^{-1}M^{*-1}(\nabla\Phi+\mathbf{U}_0)\,dt_1,\quad \boldsymbol{\xi}\in\Gamma, \tag{2.3}$$

$$\Phi=0,\quad t=0,\quad \boldsymbol{\xi}\in\Omega\cup\Gamma. \tag{2.4}$$

We introduced the following notation in expressions (2.1)–(2.3): M is Jacobi matrix of basic motion; $W(\boldsymbol{\xi},t)$ is solution of matrix equation

$$W_t=\left(\frac{\partial(\mathbf{u})}{\partial(\mathbf{x})}\right)^*W,\quad W\big|_{t=0}=\operatorname{diag}(1,1,1), \tag{2.5}$$

$\mathbf{U}_0(\boldsymbol{\xi})$ is the initial disturbance velocity vector; $\Phi(\boldsymbol{\xi},t)$ is the disturbance of the Weber's potential [13] and the pressure disturbance is

$$P(\boldsymbol{\xi},t)=-\Phi_t(\boldsymbol{\xi},t). \tag{2.6}$$

The quantity $a(\boldsymbol{\xi},t)$ is given by the equality

$$a=-\frac{1}{\rho_0}\frac{\partial p}{\partial n_{\Gamma_t}}-\sigma\left(\frac{1}{R_1^2}+\frac{1}{R_2^2}\right), \tag{2.7}$$

where $\mathbf{n}_{\Gamma_t}$ is the extarnal normal to the boundary of the region of motion Ω_t, R_1, R_2 are the principal radii curvatures of normal sections Γ_t; $\overline{\Delta}_\Gamma(t)$ is the surface transformation result to the Lagrangian coordinates of the Laplace–Beltrami operator Γ_t [13, c.25],

$$\begin{gathered}\overline{\Delta}_\Gamma(t)=\frac{1}{q}\left\{\frac{\partial}{\partial\alpha_1}\left[\left(G\frac{\partial}{\partial\alpha_1}-F\frac{\partial}{\partial\alpha_2}\right)q^{-1}\right]+\frac{\partial}{\partial\alpha_2}\left[\left(E\frac{\partial}{\partial\alpha_2}-F\frac{\partial}{\partial\alpha_1}\right)q^{-1}\right]\right\},\\ E=|M\boldsymbol{\xi}_{\alpha_1}|^2,\quad G=|M\boldsymbol{\xi}_{\alpha_2}|^2,\quad F=M\boldsymbol{\xi}_{\alpha_1}\cdot M\boldsymbol{\xi}_{\alpha_2},\quad q=(EG-F^2)^{1/2},\end{gathered} \tag{2.8}$$

$(\alpha_1,\alpha_2)\to\boldsymbol{\xi}(\alpha_1,\alpha_2)$ is the parameterization of the initial free boundary Γ; the function $b(\boldsymbol{\xi},t)$, $\boldsymbol{\xi}\in\Gamma$ is defined by the equality

$$b(\boldsymbol{\xi},t)=\frac{|\nabla f_0|}{|M^{*-1}\nabla f_0|}, \tag{2.9}$$

$f_0(\boldsymbol{\xi})=0$ is the implicit equation on Γ; $\mathbf{n}$ is the external normal to Γ: $\mathbf{n}=\nabla f_0/|\nabla f_0|$.

The function $N(\boldsymbol{\xi},t)$ characterizes the deviation of the perturbed boundary from its unperturbed state Γ along the normal. Often in stability problems of the fluid motion with a free boundary, this function is the main required quantity [12, 13].

The perturbation of the velocity vector by the known Φ is given by the formula

$$\mathbf{U}=M\left[M^{-1}W\int_0^t W^{-1}M^{*-1}(\nabla\Phi+\mathbf{U}_0)\,dt_1\right]_t, \tag{2.10}$$

and vector of perturbations (vector of displacement of liquid particles) is

$$\mathbf{X} = W \int_0^t W^{-1} M^{*-1} (\nabla \Phi + \mathbf{U}_0)\, dt_1. \tag{2.11}$$

We calculate all auxiliary quantities included in the problem (2.1)–(2.4). In fact it is problem to define a function $\Phi(\boldsymbol{\xi}, t)$.

Using the formulas (1.5) and (1.7), we make sure that the solution of the Cauchy problem (2.5) is the matrix $W \equiv M^*$. Further, since the equation Γ is $\xi^2 + \eta^2 - r_0^2 = 0$, and Γ_t is the equation $x^2 + y^2 - r_0^2/\tau = 0$, then $\mathbf{n} = (\xi, \eta, 0)/r_0$, $\mathbf{n}_{\Gamma_t} = \tau(x, y, 0)/r_0$, $R_1 = r_0/\sqrt{\tau}$, $R_2 = \infty$ and function $a(\boldsymbol{\xi}, t)$, $\boldsymbol{\xi} \in \Gamma$, from formula (2.7) is

$$a = \frac{r_0^2}{\rho_0} \left(\frac{3}{4} \frac{k^2}{\tau^2} - \omega_0^2 \tau \right) - \frac{\sigma \tau}{r_0^2}\,. \tag{2.12}$$

To transform $\overline{\Delta}_\Gamma(t)$ from the expression (2.8) we introduce cylindrical Lagrangian coordinates ρ, φ, ζ, so that $\xi = \rho \cos\varphi$, $\eta = \rho \sin\varphi$, $\zeta = \zeta$. Then for the jet surface Γ at the initial moment of time $\alpha_1 = \varphi$, $\alpha_2 = \zeta$, $0 \leqslant \varphi \leqslant 2\pi$, $0 \leqslant \zeta \leqslant h_0$, a $\rho = r_0$. Moreover, the coefficients of the first quadratic form is $E = r_0^2/\tau$, $G = \tau^2$, $F = 0$ and $q = r_0\sqrt{\tau}$, so

$$\overline{\Delta}_\Gamma(t) = \frac{1}{r_0^2 \tau} \left(\tau^2 \frac{\partial^2}{\partial \varphi^2} + \frac{r_0^2}{\tau} \frac{\partial^2}{\partial \zeta^2} \right). \tag{2.13}$$

Because $f_0(\xi, \eta, \zeta) = \xi^2 + \eta^2 - r_0^2 = 0$, then from the formulas (2.9) and (1.5) we get $b = 1/\sqrt{\tau}$.

Since the matrix $W \equiv M^*$, then the equation (2.1) is simplified to the following

$$\begin{aligned} &\int_0^t \left[\tau(t_1) \cos 2\left(\theta(t) - \theta(t_1)\right) (\Phi_{\xi\xi} + \Phi_{\eta\eta}) + \frac{1}{\tau^2(t_1)}\, \Phi_{\zeta\zeta} \right] dt_1 = \\ &= -\int_0^t \left[\left(\frac{1}{\tau^2(t_1)} - \tau(t_1) \cos 2\left(\theta(t) - \theta(t_1)\right) \right) U_{03\zeta} + \tau(t_1) \sin 2\left(\theta(t) - \theta(t_1)\right) \Omega_{03} \right] dt_1, \end{aligned} \tag{2.14}$$

where equality $U_{01\xi} + U_{02\eta} + U_{03\zeta} = 0$ was used for initial velocity vector $\mathbf{U}_0 = (U_{01}, U_{02}, U_{03})$; the value $\Omega_{03} = U_{02\xi} - U_{01\eta}$ is twice the third component of the initial vortex vector.

Differentiating the equation (2.14) with respect to t three times and introducing the variable $\gamma = \tau^2(t) = (1 + kt)^2$ instead of t we arrive at the equation ($\mu = \omega_0/k$)

$$\frac{\partial^2}{\partial \gamma^2} \left(\Phi_{\xi\xi} + \Phi_{\eta\eta} + \frac{1}{\gamma^{3/2}}\, \Phi_{\zeta\zeta} \right) + \frac{\mu^2}{\gamma^{3/2}}\, \Phi_{\zeta\zeta} = -\left(\frac{15}{4\gamma^{7/2}} + \frac{\mu^2}{\gamma^{3/2}} \right) U_{03\zeta}.$$

The resulting equation must be solved in the initial cylinder $\xi^2 + \eta^2 < r_0^2$, $0 \leqslant \varphi \leqslant 2\pi$, $0 < \zeta < h_0$. In cylindrical coordinates ρ, φ, ζ the equation will be written like this

$$\frac{\partial^2}{\partial \gamma^2} \left(\Phi_{\rho\rho} + \frac{1}{\rho}\, \Phi_\rho + \frac{1}{\rho^2}\, \Phi_{\varphi\varphi} + \frac{1}{\gamma^{3/2}}\, \Phi_{\zeta\zeta} \right) + \frac{\mu^2}{\gamma^{3/2}}\, \Phi_{\zeta\zeta} = -\left(\frac{15}{4\gamma^{7/2}} + \frac{\mu^2}{\gamma^{3/2}} \right) U_{03\zeta}. \tag{2.15}$$

Equation (2.15) is an equation of Poincare–Sobolev type (0.2) with variable coefficients and a nonzero right-hand side.

The value $N(\boldsymbol{\xi}, t)$ from the expression (2.3) is converted to the form

$$\begin{aligned} N = \frac{1}{r_0 \sqrt{\tau}} \int_0^t \tau(t_1) \Big[&\cos 2\left(\theta(t) - \theta(t_1)\right) (\xi \Phi_\xi + \eta \Phi_\eta + \xi U_{01} + \eta U_{02}) + \\ &+ \sin 2\left(\theta(t) - \theta(t_1)\right) (\xi \Phi_\eta - \eta \Phi_\xi + \xi U_{02} - \eta U_{01}) \Big] dt_1. \end{aligned} \tag{2.16}$$

Based on the obtained representation, we write down the equation for the N. Differentiating the expression (2.16) twice in t and after some transformations we arrive at the equation

$$\frac{\partial^2 \bar{N}}{\partial \gamma^2} + \mu^2 \bar{N} = \frac{1}{2k}\,\Phi_{\rho\gamma} + \frac{\mu}{2k}\,\Phi_{\varphi} + \frac{\mu}{2k}\,V_0, \tag{2.17}$$

where the right-hand side is calculated at $\rho = r_0$, $\bar{N} = \sqrt{\tau}\,N = \gamma^{1/4}N$; $V_0(r_0,\varphi,\zeta)$ is the azimuthal component of the initial velocity vector in cylindrical coordinates ($V_0 = \cos\varphi U_{02} - \sin\varphi U_{01}$).

As for the boundary condition (2.2) it can be written like this

$$\Phi_\gamma + \frac{1}{2\gamma^{1/4}}\left[\frac{r_0^2 k}{\rho_0}\left(\frac{3}{4\gamma^{3/2}} - \mu^2\right) - \frac{\sigma}{r_0^2 k}\right]\bar{N} - \frac{\sigma}{2r_0 k\gamma^{1/4}}\left(\bar{N}_{\varphi\varphi} + \frac{r_0^2}{\gamma^{3/2}}\,\bar{N}_{\zeta\zeta}\right) = 0 \tag{2.18}$$

at $\rho = r_0,\ 0 < \varphi < 2\pi,\ 0 < \zeta < h_0$.

The initial data at $\gamma = 1$ are

$$\Phi = 0, \quad \boldsymbol{\xi} \in \Omega \cup \Gamma,$$
$$\frac{\partial}{\partial \gamma}\left(\Phi_{\rho\rho} + \frac{1}{\rho}\,\Phi_\rho + \frac{1}{\rho^2}\,\Phi_{\varphi\varphi} + \Phi_{\zeta\zeta}\right) = \frac{3}{2}\,U_{03\zeta} - \frac{\mu}{2}\,\Omega_{03}, \quad \boldsymbol{\xi} \in \Omega, \tag{2.19}$$
$$\bar{N} = 0, \quad \boldsymbol{\xi} \in \Gamma, \quad \bar{N}_\gamma = U_0(r_0,\varphi,\zeta),$$

where $U_0(\rho,\varphi,\zeta) = \cos\varphi U_{01} + \sin\varphi U_{02}$ is radial component of the velocity vector at the initial moment of time.

The conditions for the impermeability of solid walls $\zeta = 0$ and $\zeta = h_0$ are reduced to the fact that the component Z of the perturbation vector $\mathbf{X} = (X, Y, Z)$ (2.11) is equal to zero. Using the equality (2.11), we get

$$\Phi_\zeta + U_{03} = 0, \quad \zeta = 0; h_0, \quad t \geqslant 0. \tag{2.20}$$

3. Solution of Small Perturbation Equations

We are looking for a solution to the problem (2.15)–(2.20) in the form of a Fourier series

$$\Phi(\rho,\varphi,\zeta,\gamma) = \sum_{n=1}^{\infty}\sum_{m=1}^{\infty} A_{nm}(\gamma) I_m\left(\frac{\rho}{r_0}\right)\exp(im\varphi)\cos\left(\frac{n\pi\zeta}{h_0}\right) + B(\gamma). \tag{3.1}$$

From formula (2.19), we get

$$A_{nm}(1) = 0, \quad B(1) = 0. \tag{3.2}$$

In expression (3.1) $I_m(x)$ is the Bessel function of the 2nd kind.

Substitution of the solution form (3.1) into the formula (2.15) leads to the equations for the amplitudes $A_{nm}(\gamma)$:

$$\left[\left(1 - \frac{æ^2}{\gamma^{3/2}}\right)A_{nm}\right]_{\gamma\gamma} - \frac{\mu^2 æ^2}{\gamma^{3/2}}\,A_{nm} = f(\gamma)\bar{U}_{0nm}, \tag{3.3}$$

where

$$æ^2 = \frac{n^2\pi^2 r_0^2}{h_0^2}, \quad f(\gamma) = -r_0^2\left(\frac{15}{4\gamma^{7/2}} + \frac{\mu^2}{\gamma^{3/2}}\right), \quad \bar{U}_{0nm} = -\frac{n\pi}{h_0}\,U_{0nm}, \tag{3.4}$$

and U_{0nm} are the coefficients of the Fourier series of the function $U_{03}(\rho,\varphi,\zeta)$:

$$U_{03}(\rho,\varphi,\zeta) = \sum_{n=0}^{\infty}\sum_{m=0}^{\infty} U_{0nm} I_m\left(\frac{\rho}{r_0}\right)\exp(im\varphi)\sin\left(\frac{n\pi\zeta}{h_0}\right). \tag{3.5}$$

Remark 2. The expressions (3.1) and (3.5) satisfy conditions for the flow around the walls (2.20) at $\zeta = 0$, $\zeta = h_0$.

If $\bar{N}_{nm}(\gamma)$ are the coefficients of the Fourier series of the form (3.1) of the function $\bar{N}(\varphi,\zeta,\gamma)$, then from (3.1) and (2.18) we get

$$B_\gamma + a(\gamma)D(\gamma) + \sum_{n=1}^{\infty}\sum_{m=1}^{\infty}\{[a(\gamma)+b_{nm}(\gamma)]\,\bar{N}_{nm}(\gamma) + \\ + A_{nm\gamma}(\gamma)I_m(1)\}\exp(im\varphi)\cos\left(\frac{n\pi\zeta}{h_0}\right) = 0, \tag{3.6}$$

where $D(\gamma)$ is the free term in expansion $\bar{N}(\varphi,\zeta,\gamma)$,

$$a(\gamma) = \frac{1}{2\gamma^{1/4}}\left[\frac{r_0^2 k}{\rho_0}\left(\frac{3}{4\gamma^{3/2}} - \mu^2\right) - \frac{\sigma}{r_0^2 k}\right], \\ b_{nm} = \frac{\sigma}{2r_0 k\gamma^{1/4}}\left(m^2 + \frac{æ^2}{\gamma^{3/2}}\right). \tag{3.7}$$

Hence,

$$B_\gamma = -a(\gamma)D(\gamma), \quad \bar{N}_{nm}(\gamma) = -\frac{I_m(1)}{a(\gamma)+b_{nm}(\gamma)}\,\frac{dA_{nm}(\gamma)}{d\gamma}\,. \tag{3.8}$$

The function $D(\gamma)$ is found from formula (2.17) as a solution of the equation

$$\frac{d^2D}{d\gamma^2} + \mu^2 D = \frac{\mu}{2k}\,V_{00}. \tag{3.9}$$

Let's turn to the equation (3.3), in which we will make the replacement

$$H = \left(1 - \frac{æ^2}{\gamma^{3/2}}\right)A_{nm} \tag{3.10}$$

with n and m are fixed. Then the function H is a solution of the equation

$$\frac{d^2H}{d\gamma^2} - \frac{\mu^2 æ^2}{\gamma^{3/2} - æ^2}\,H = f(\gamma)\bar{U}_{0nm}. \tag{3.11}$$

The fundamental system $H_1(\gamma)$, $H_2(\gamma)$ of the homogeneous equation (3.11) at $\gamma \gg 1$ has the form [14]

$$H_{1,2} = \gamma^{3/8}\exp(\pm 4\mu æ\gamma^{1/4})(1+\mathcal{E}_{1,2}(\gamma)), \quad \lim_{\gamma\to\infty}\mathcal{E}_{1,2}(\gamma) = 0. \tag{3.12}$$

These asymptotics can be differentiated twice (see [14, p. 58])

$$H_{1,2}^{(j)} \sim \left(\pm\frac{1}{\gamma^{3/4}}\right)^{(j)}\gamma^{3/8}\exp(\pm 4\mu æ\gamma^{1/4}) \tag{3.13}$$

at $\gamma \to \infty$.

From formula (3.4) function $f(\gamma)$ and relations (3.12), (3.13) we obtain the asymptotic representation of the solution of the equation for large γ (3.11):

$$H \sim \gamma^{3/8}[C_1\exp(4\mu æ\gamma^{1/4}) + C_2\exp(-4\mu æ\gamma^{1/4})] + \frac{r_0^2}{æ^2}\,. \tag{3.14}$$

According to the replacement (3.10) we have $A_{nm} \sim H$ at $\gamma \to \infty$. Then from expressions (3.8), (3.13) and (3.14) we will find

$$\bar{N}_{nm}(\gamma) \sim \gamma^{-9/8} \exp(4\mu æ\gamma^{1/4}), \quad \gamma \to \infty. \tag{3.15}$$

Moreover, the asymptotics does not depend on the surface tension coefficient at $\mu \neq 0$. Since $\bar{N}_{nm}(\gamma) = \gamma^{1/4} N_{nm}$, then for the amplitudes of perturbations of the free boundary we obtain from the formula (3.15)

$$N_{nm} \sim \gamma^{-11/8} \exp(4\mu æ\gamma^{1/4}), \quad \gamma \to \infty. \tag{3.16}$$

The function $D(\gamma)$ is found from the equation (3.9):

$$D = C_3 \cos \mu\gamma + C_4 \sin \mu\gamma + \frac{V_{00}}{2k\mu}, \tag{3.17}$$

then from formula (3.8)

$$B(\gamma) = -\int_1^\gamma a(\tau) \left[C_3 \cos \mu\tau + C_4 \sin \mu\tau + \frac{V_{00}}{2k\mu} \right] d\tau.$$

Thus, there is an instability.

Conclusion

The problem on the behavior of small perturbations of an expanding and rotating jet of an ideal fluid is reduced to a problem for equations of the Poincare–Sobolev type with variable coefficients depending on time. Due to the specifics of complex boundary conditions and the equation itself, the solution was found by the method of variables separation. For the obtained amplitude equations, the asymptotic of the solutions is found for $t \to \infty$. Since $\gamma \sim (kt)^2$, then from (3.16) we get $N_{nm} \sim (kt)^{-11/4} \exp[4\mu æ(kt)^{1/2}]$ at $t \to \infty$. Notice, that $\mu æ = (n\omega_0 \pi r_0)/(kh_0)$. Therefore, the growth of perturbations of the free boundary does not depend on the influence of capillarity (parameter σ), as well as on the parameter m. For "pure" stretching of the jet ($\omega_0 = 0$), the results differ significantly. Namely, [13], at $\sigma = 0$ $N_{n0} \sim (kt)^{-1/2}$, $N_{nm} \sim (kt)^{1/2}$, $m \geqslant 1$, and at $\sigma \neq 0$ $N_{n0} \sim (kt)^{-5/8} \exp[2\pi n h_0 r_0^{-1} \sqrt{\mathrm{We}} (kt)^{1/4}]$, $N_{nm} \sim (kt)^{-1/8}$ $(m \geqslant 1)$, where $\mathrm{We} = \sigma/(\rho r_0^3 k^2)$ is the Weber number. Thus, here the surface tension has very strong effects on the perturbations behavior, especially for axisymmetric perturbations with $m = 0$.

This research was supported by the Krasnoyarsk Mathematical Center and financed by the Ministry of Science and Higher Education of the Russian Federation in the framework of the establishment and development of regional Centers for Mathematics Research and Education (Agreement no. 075-02-2020-1631).

References

[1] N.N.Moiseev, V.V.Rumyantsev, Dinamika tela s polostyami, soderzhachshimi zhidkost' (Dynamics of Bodies with Fluid-Filled Cavities), Moscow, Nauka, 1965 (in Russian).

[2] V.G.Babskii, N.D.Kopachevskii, A.D.Myshkis, L.A.Slobozhanin, A.D.Tyuptsov, Low-Gravity Fluid Mechanics, Moscow, Nauka, 1976 (in Russian).

[3] A.Poincaré, Sur l'équilibre d'une masee fluide animée d'un mouvement de rotation, *Acta Math.*, **7**(1985), 259–380.

[4] H.Lamb, Hydrodynamics, Moscow, Leningrad, Gostekhizdat, 1947 (in Russian).

[5] S.L.Sobolev, On a new problem of mathematical physics, *Izv. Akad. Nauk SSSR Ser. Mat.*, **18**(1954), no. 1, 3–50.

[6] S.L.Sobolev, On Symmetric Top Motion with a Fluid-Filled Cavity, *Prikl. Mekh. Tekh. Fiz.*, **3**(1960), 20–55 (in Russian).

[7] T.I. Zelenyak, Selected Problems of the Qualitative Theory of Partial Differential Equations, Novosibirsk Univ., Novosibirsk, 1970 (in Russian).

[8] S.V.Uspenskij, G.V.Demidenko, V.G.Perepelkin, Imbedding theorems and applications to differential equations, Nauka, Novosibirsk, 1984 (in Russian).

[9] V.M.Kamenkovich, A.S.Monin, Ocean Physics, Moscow, Nauka, 1978 (in Russian).

[10] M.J.Lighthill, On waves generated in dispersive systems by travelling forcing effects, with applications to the dynamics of rotating fluids, *Jour. Fluid Mech.*, **27**(1967), no. 4, 725–752.

[11] H.P.Greenspan, On the transient motion of a contained rotatinh fluid, *Jour. Fluid Mech.*, **20**(1964), no. 4, 673–696.

[12] L.V.Ovsyannikov, General equations and examples, *Problems of Unsteady Free-Boundary Fluid Flows*, Nauka, Novosibirsk, 1967, 5–75 (in Russian).

[13] V.K.Andreev, Stability of unsteady fluid motions with a free boundary, Novosibirsk, Nauka, 1992 (in Russian).

[14] M.V.Fedoryuk, Asymptotic Methods for Linear Ordinary Differential Equations, Moscow, Nauka, 1983 (in Russian).

Асимптотическое поведение малых возмущений нестационарного движения струи идеальной жидкости

Виктор К. Андреев
Институт вычислительного моделирования СО РАН
Красноярск, Российская Федерация
Сибирский федеральный университет
Красноярск, Российская Федерация

Аннотация. Задача об устойчивости нестационарного движения вращающейся круглой струи идеальной жидкости сведена к решению начально-краевой задачи для уравнения типа Пуанкаре–Соболева с эволюционным условием на свободной начальной границе струи. Решение поставленной задачи построено методом разделения переменных. Найдено асимптотическое поведение амплитуд возмущения свободной границы струи при $t \to \infty$. Произведено сравнение полученных результатов с известными результатами об устойчивости потенциального движения струи.

Ключевые слова: нестационарное движение, свободная граница, малые возмущения, уравнения типа Пуанкаре–Соболева, неустойчивость.

Journal of Siberian Federal University. Mathematics & Physics 2021, 14(2), 213–223

DOI: 10.17516/1997-1397-2021-14-2-213-223
УДК 517.958:531.32

Numerical and Analytical Modeling of Centrifugal Pump

Viktor A. Ivanov*
Siberian Federal University
Krasnoyarsk, Russian Federation
Nikolay V. Erkaev†
Institute of Computational Modeling SB RAS
Krasnoyarsk, Russian Federation

Received 10.08.2020, received in revised form 10.12.2020, accepted 21.01.2021

Abstract. A mathematical model of non-stationary rotation modes of the rotor of a centrifugal pump is constructed. It is based on preliminary calculation in ANSYS Fluent package with subsequent analytical calculation taking into account the specified parameters.

Keywords: mathematical modeling, hydrostatic bearing, centrifugal pump.

Citation: V.A. Ivanov, N.V. Erkaev, Numerical and Analytical Modeling of Centrifugal Pump, J. Sib. Fed. Univ. Math. Phys., 2021, 14(2), 213–223. DOI: 10.17516/1997-1397-2021-14-2-213-223.

Introduction

Low-flow centrifugal pumps are widely used in technology. They are especially often used in various cooling systems. The design and calculation of centrifugal pumps are fairly well studied and described in the literature [1–9]. When calculating such a pump and the hydrostatic bearing included in it (Fig. 1), simplified formulas are often used, containing rather vague empirical coefficients of nozzle flow and oil flow through the bearing ends. In principle, self-consistent determination of these coefficients is possible with a full simulation of hydrostatic bearings in the ANSYS Fluent package. However, in this case, a complete calculation would require a powerful computational resources. In this case, the best option seems to be the limited use of a computing package such as ANSYS Fluent in conjunction with an analytical model, which allows one to simulate the device operation with minimal computational costs. We call further this approach as "hybrid modeling". This work is devoted to hybrid simulation of the nonstationary dynamics of the centrifugal pump rotor during its rotational acceleration from the initial steady position to a final stationary rotational regime.

A schematic diagram of a centrifugal pump is shown in Fig. 1 with the following designations: 1 — impeller; 2 — hydraulic bearing; 3 — a pair of thrust bearings; 4 — inlet pipe; 5 — outlet branch pipe; 6 — auxiliary pump; 7 — the rotor of the electric motor; 8 — electric motor stator; 9 — motor housing; 10 — housing of one of the pumps of the electric pump unit; 11 — dashed lines indicate the direction of movement of the working fluid; 12 — throttle space; 13 — throttle; 14 — pocket; 15 — a system of holes in the shaft, providing a return of the working fluid back to the entrance to the impeller.

*vintextrim@yandex.ru
†erkaev@icm.krasn.ru https://orcid.org/0000-0001-8993-6400

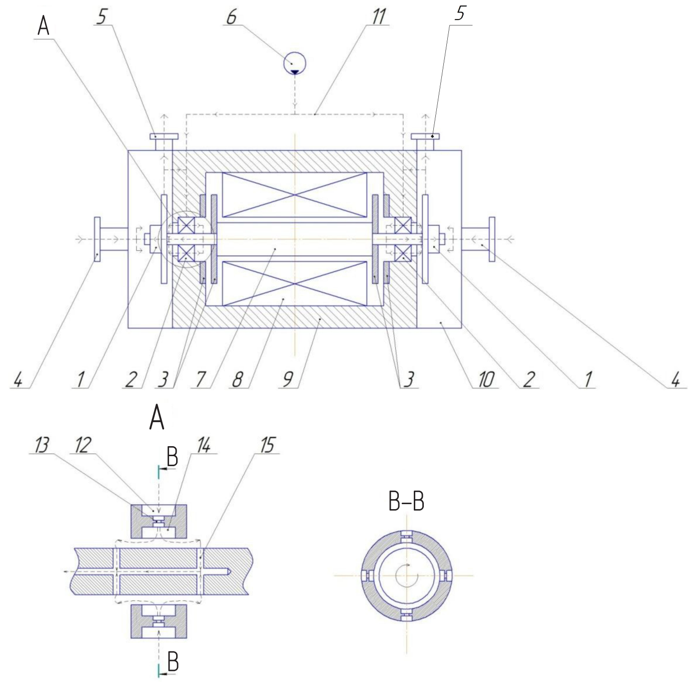

Fig. 1. Schematic diagram of a centrifugal pump

1. Mathematical model

Forces and moments acting on the rotor of a low-flow centrifugal pump with two symmetrical hydrostatic bearings are shown in Fig. 2, where mg is the weight of the rotor (in the figure this

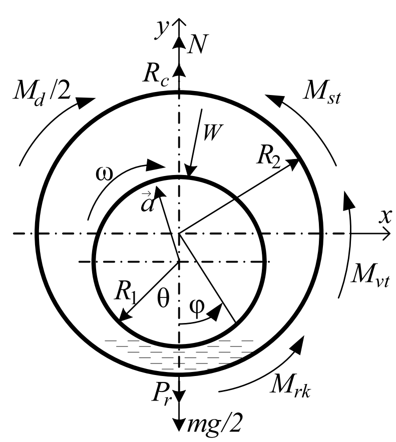

Fig. 2. Forces and moments acting on the rotor.

force is divided by two, since it is distributed over two bearings), N is the normal reaction of the support, R_c is the static reaction of the hydraulic bearing, P_r is the radial force, taking into account the fluid pressure on the impeller blades (its direction depends on the design features of the pump), M_{rk} is impeller moment, M_{vt} is viscous friction moment, M_{st} is dry friction moment, M_d is engine torque, R_1 and R_2 are the radii of the shaft and bearing housing, θ is the displacement of the center of mass of the rotor relative to the axis, W is the reaction of the liquid layer to the acceleration of the rotor axis.

The rotor dynamics equations are as follows:

$$\begin{cases} m\dfrac{d^2y}{dt^2} = 2R_{cy}(y,\omega) - 2P_r(\omega) - mg + 2N(y) - W_y(y, \dfrac{d^2y}{dt^2}), \\ I\dfrac{d\omega}{dt} = M_d(\omega) - 2M_{rk}(\omega) - 2M_{st}(y) - 2M_{vt}(y,\omega), \end{cases} \tag{1}$$

where I is the moment of inertia of the rotor about its axis, ω is the angular speed of the rotor, t is the time since the pump was started, $\Delta = R_2 - R_1$ is the average clearance. The values R_c, P_r, M_{rk}, M_{st}, M_{vt} are indicated with a factor of 2, since the pump has two bearings.

Oscillations of the rotor along the y axis are caused by two force reactions of the liquid layer, designated R_c and W. The expression of the force R_c, depending on the displacement of the rotor, is given in [10], in which the load was assumed to be applied strictly along the vertical axis y. The expression for the force W caused by the hydrodynamic reaction of the liquid layer to the acceleration of the rotor is obtained in Appendix 1. In case of strictly vertical loading, the component of the layer reaction can be written in the following form:

$$R_{cy} = l \cdot d \cdot \left[\frac{P_n \cdot \left(\mu_c \cdot \pi d_c^2/4\right)^2}{\left(\mu_c \cdot \pi d_c^2/4\right)^2 + \left(2\mu_t f(y)\right)^2} - \frac{P_n \cdot \left(\mu_c \cdot \pi d_c^2/4\right)^2}{\left(\mu_c \cdot \pi d_c^2/4\right)^2 + \left(2\mu_t f(-y)\right)^2} \right], \tag{2}$$

where l is the bearing width, d is the rotor diameter, μ_c is the nozzle flow rate, μ_t is the flow rate through the bearing ends, d_c nozzle diameter, P_n is the pump outlet pressure, $f(x)$ is the function given in [10] and characterizing the area of the gap sector

$$f(y) = l \cdot \Delta \cdot \int_0^{\pi/4} \left[\sin^2(\phi) + \left(\frac{y}{\Delta} + \cos(\phi) \right)^2 \right]^{1/2} d\phi.$$

The pressure at the pump outlet is found from the following equation [11]:

$$P_n = \rho\omega^2 R_2^2 \eta,$$

where η is the pump efficiency, ρ is the density of the working fluid.

When using formula (2), it is especially difficult to determine the coefficients μ_c and μ_t. In typical calculations, these coefficients are selected on the basis of tables obtained empirically for a certain range of diameters, as a result of which the calculation error increases. In addition, this formula assumes the average pressure, which creates a force directed strictly along the coordinate axes, which is an additional source of error. In reality, one must take into account the distribution of the pressure along the surface, at each point of which the elementary force vector is directed along the normal. Therefore, when finding the resulting force, it is necessary to integrate this vector along the surface. To eliminate these errors, a series of calculations was made for a hydrostatic bearing with different rotor eccentricities in the ANSYS Fluent package in order to determine the flow rates through the nozzle and the bearing ends, as well as the pressure correction function. Taking into account these coefficients, the modified formula (2) takes the following form:

$$R_{cy} = l \cdot d \cdot \left[\frac{P_n \cdot \left(\mu_c(y) \cdot \pi d_c^2/4\right)^2}{\left(\mu_c(y) \cdot \pi d_c^2/4\right)^2 + \left(2\mu_t(y) f(y)\right)^2} \chi(y) - \right. \\ \left. - \frac{P_n \cdot \left(\mu_c(-y) \cdot \pi d_c^2/4\right)^2}{\left(\mu_c(-y) \cdot \pi d_c^2/4\right)^2 + \left(2\mu_t(-y) f(-y)\right)^2} \chi(-y) \right]. \tag{3}$$

Here χ is a correction factor that takes into account the pressure distribution. Next, we pay a particular attention on a way to obtain these coefficients, depending on the rotor displacement, using the ANSYS Fluent package. To do this, in the software package, we simulate the bearing lubricant layer for a specific eccentricity. At the same time, inlets of the lubricating layer through the nozzles are created in the model. A model of a lubricating layer of finite thickness is shown in Fig. 3. Here, the inlets of the lubricating layer are labeled A, B, C, D.

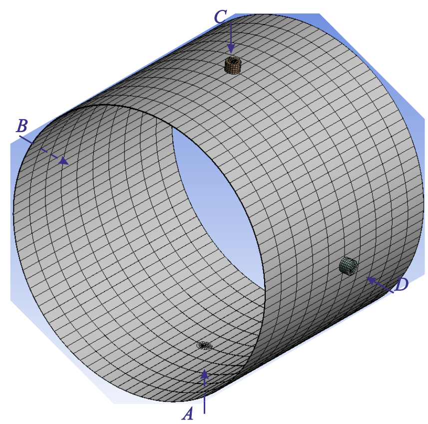

Fig. 3. Finite element model of the lubricating layer

To obtain a uniformly ordered mesh, it is important to split the lubricant layer model into five elements, i.e. a layer around the shaft and four lubricant inlets through the nozzles. We divide the layer around the shaft into 100 elements along the corner, 10 elements along the layer thickness and 10 elements along the length. In addition, we divide the grease inlet through the nozzle into 20 elements in angle, 5 elements in thickness and 5 elements in length. After building the model, we set the load and boundary conditions. Here, the pump pressure P_n is set at the nozzle inlet ends, atmospheric pressure is set at one bearing end, and at the other end zero liquid flow rate is assumed. Since the shaft rotates in a stationary housing, we fix the outer boundary between the housing and the lubricating layer. In this case, the rotation speed is set at the inner interface between the shaft and the lubricating layer. The resulting pressure distribution is shown in Fig. 4. According to Fig. 4, the liquid entering through the nozzles is distributed along the rotation of the shaft. In this case, the maximum pressure peak is observed at the liquid outlet from the lower nozzle. We also observe increased pressure along the end with the cuff, since there is nowhere for the liquid to exit.

Based on the pressure difference from below (in the vicinity of the point of minimum thickness of the lubricating layer) and from above (in the vicinity of the point of maximum layer thickness), we determine the lifting force R_c. Knowing the oil flow rate through the ends, we determine the functions $\mu_c(y)$ and $\mu_t(y)$ based on the balance of the fluid flow in the pump [12]:

$$\mu_c \cdot \frac{\pi \cdot d_c^2}{4} \cdot \sqrt{\frac{2(P_n - P)}{\rho}} = Q = 2\mu_t \cdot f\sqrt{\frac{2P}{\rho}},$$

where Q is the flow rate through the nozzle/ends. The found functions are shown in Fig. 5.

The found functions are used in the formula (3) to determine the lift of the rotor. Fig. 6 shows plots of the R_c functions corresponding to the analytical (2), hybrid (3) and numerical (based on the ANSYS package) models for comparison.

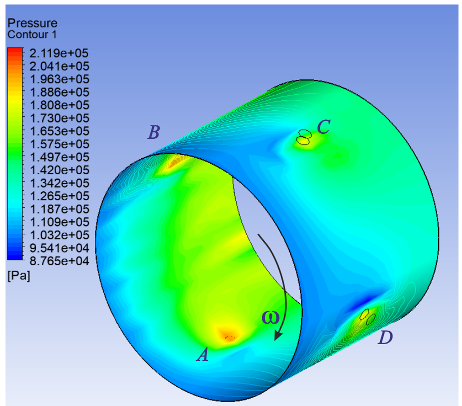

Fig. 4. Pressure distribution in the lubricating layer

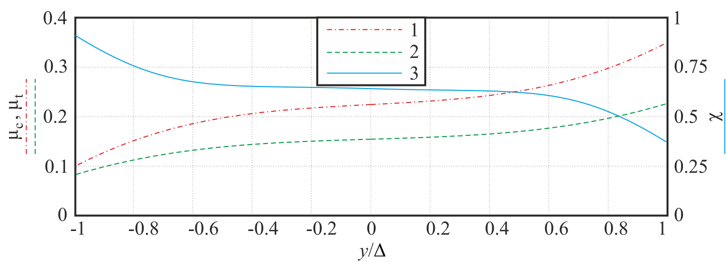

Fig. 5. Functions μ_c and μ_t, χ, depending on the shaft displacement. Curves 1 and 2 correspond to the flow rate coefficients μ_c and μ_t through the nozzles and bearing ends, respectively; curve 3 shows correction factor for pressure χ

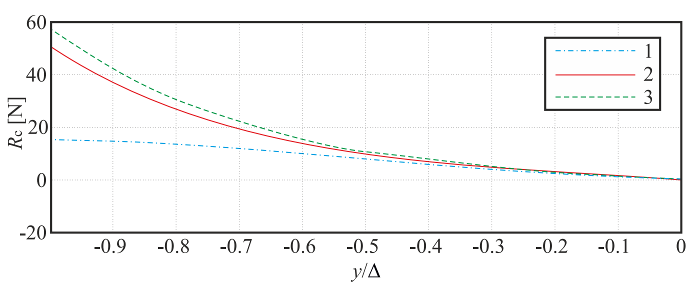

Fig. 6. Lifting force in the bearing. Curves 1, 2 correspond to the formulas (2) and (3), curve 3 is obtained from the ANSYS Fluent calculations.

Fig. 6 shows that at low eccentricities all curves are fairly close to each other. However, at eccentricities greater than 0.3, the curves obtained on the basis of the formula (3) and direct ANSYS calculation go up significantly parallel to each other. These curves have a particularly steep increase for the eccentricities larger than 0.6, which is associated with the transition from hydrostatic to hydrodynamic operating regime of the bearing. In this case, the curve corresponding to the formula (2) has a weak growth and remains almost parallel to the abscissa axis.

Next, we consider the additional force **W** caused by a dynamic reaction of the liquid layer on the rotor acceleration. This force is linearly dependent on the acceleration vector:

$$\mathbf{W} = \mathbf{K}\mathbf{a}, \quad \mathbf{a} = \left(\frac{d^2x}{dt^2} \quad , \quad \frac{d^2y}{dt^2} \right). \tag{4}$$

Components of the matrix coefficient $\mathbf{K}$ are derived in Appendix 1.

The expression for the radial force P_r acting on the impeller is given in [13]:

$$P_r = 0.1 \cdot \rho \cdot D_2^3 \cdot b_2 \cdot \eta \cdot \omega^2,$$

where D_2 is the diameter of the impeller outlet, b_2 is the width of the impeller at the outlet.

The normal support reaction is:

$$N = \begin{cases} P_r + \dfrac{mg}{2} - R_c, & y = -\Delta \\ 0, & y > -\Delta. \end{cases}$$

The dry friction moment is determined by the following expression:

$$M_{st} = \begin{cases} \dfrac{(2P_r + mg - R_c)df_{tr}}{4}, & y = -\Delta \\ 0, & y > -\Delta, \end{cases}$$

where f_{tr} is the dry friction coefficient.

The moment of viscous friction is determined from the following expression [10]:

$$M_{vt} = 0.25ld^3\mu\omega\frac{1}{\Delta}\int_0^{\pi} \frac{d\phi}{\sqrt{\sin^2(\phi) + \left(\frac{y}{\Delta} + \cos(\phi)\right)^2}}.$$

The torque generated by the engine is given by formula [14]:

$$M_d = J - J_1\omega,$$

where J and J_1 are dynamic and static coefficients of the torque-mechanical characteristics of the electric motor.

The moment on the impeller is determined by the expression:

$$M_{rk} = \frac{\omega\pi\mu R_2^4}{s} + \rho Q R_2^2\omega,$$

where s is the axial clearance between the impeller and the casing, μ is the dynamic viscosity of the oil, Q_p is the flow (fluid leakage from the impeller), determined by formula [15]:

$$Q_p = \mu_p \pi D_1 s\omega R_2\sqrt{2\eta},$$

where μ_p is the flow coefficient in the front axial clearance between the impeller and the pump casing [15], D_1 is the impeller diameter at the inlet.

2. Calculation results

For brevity, we use the following notation:

$$F_y = 2R_{cy} - 2P_r - mg + 2N.$$

Substituting all the determined force expressions into the equation (1) and taking into account the equation (3) and zero initial conditions, we write the system of equations in the Cauchy normal form:

$$\begin{cases} \dfrac{dV_y}{dt} = \dfrac{F_y\left(m - K_{11}\right) + F_x K_{21}}{\left(m - K_{11}\right)\left(m - K_{22}\right) - K_{12}K_{21}}, \\ \dfrac{dy}{dt} = V_y, \\ \dfrac{d\omega}{dt} = \dfrac{M_d - 2M_{rk} - 2M_{st} - 2M_{vt}}{I}, \\ V_y(0) = 0, \\ y(0) = -\Delta, \\ \omega(0) = 0. \end{cases} \tag{5}$$

Here $y(0) = -\Delta$, since the origin of coordinates is chosen in the center of the body, and the rotor at the initial moment is in the lowest position being in contact with the body. For comparison, we carry out two variants of calculation with different expressions of the lifting force R_c, determined by the formulas (2) and (3). Solving the system of differential equations (5) by the fourth order Runge-Kutta method, we obtain the angular velocity, the displacement and speeds of the rotation axis along the coordinate axes as functions of time (Figs. 7–9). The calculations were performed for the following input parameter: $\rho = 1000$ kg/m^3, $D_2 = 0.06$ m, $D_1 = 0.02$ m, $b_2 = 0.003$ m, $\eta = 0.5$, $R_2 = 0.03$ m, $l = 0.02$ m, $d = 0.01$ m, $\mu = 0.01$ Pa $\cdot$ s, $\Delta = 10^{-4}$ m, $f_{tr} = 0.1$ m, $J = 0.9$ H $\cdot$ m, $J_1 = 0.0015$ H $\cdot$ m $\cdot$ s, $m = 0.2$ kg, $I = 10^{-5}$ H $\cdot$ m $\cdot$ s^2, $d_c = 0.001$ m, $\mu_p = 0.2$, flow rates through nozzles and ends for analytical calculation using the formula (2): $\mu_c = 0.3$, $\mu_t = 0.2$ [15].

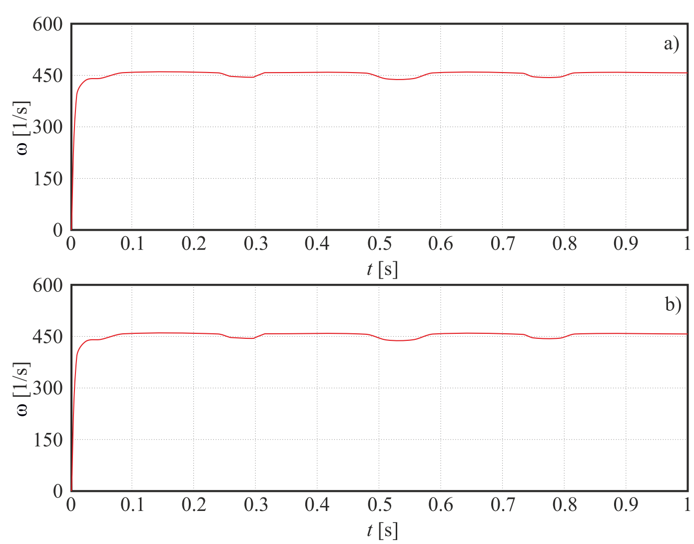

Fig. 7. The angular velocity in dependence on time

From Fig. 7 it can be seen that the rotor rotation reaches the operating angular speed rather quickly, in less than one second. At the same time, the angular velocity behaviours obtained on the basis of the expressions (2) and (3) are almost identical.

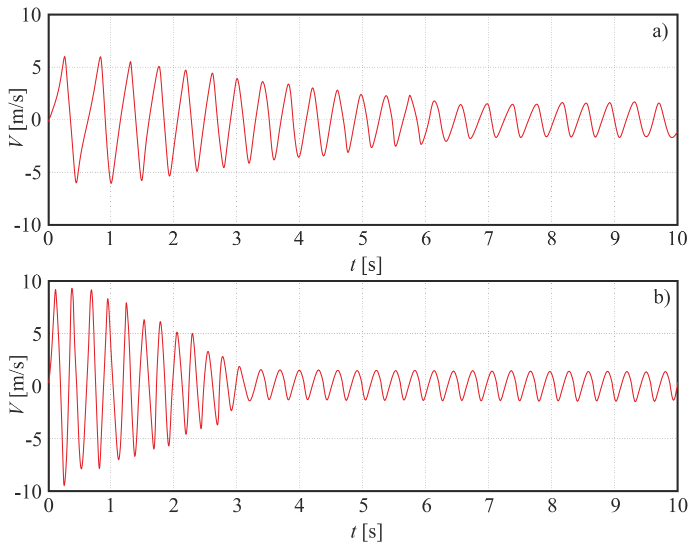

Fig. 8. The speed of the rotor displacement along the y axis: (a) and (b) correspond to formulas (2) and (3), respectively

Fig. 8 shows significant fluctuations in the displacement velocity of the rotor along the y axis. In this case, the calculation using the equation (2) shows a smaller initial amplitude of oscillations (Fig. 8a), as well as a longer and smoother damping when passing to a stationary value, compared to the calculation when using modified formulas (3) and (Fig. 8b).

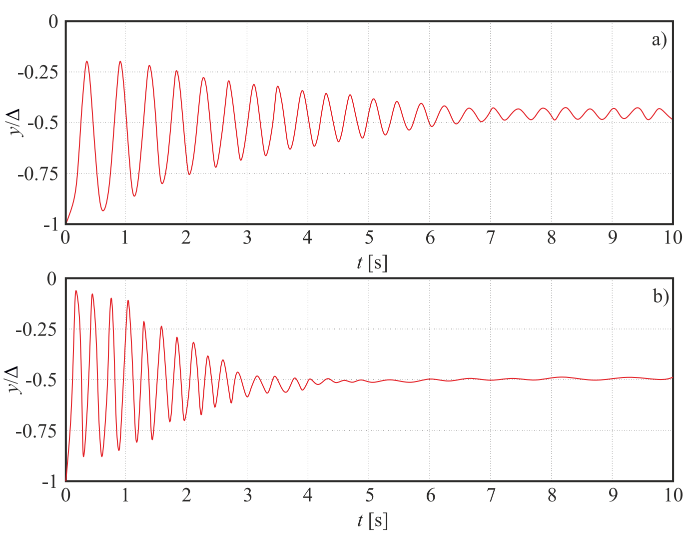

Fig. 9. Rotor displacement along the y axis: (a) and (b) correspond to (2) and (3), respectively

The results obtained on the basis of the equations (2) show gradual damping of the vertical oscillations (Fig. 9a). At the same time, the calculation using the modified equation (3) gives a faster decay of the oscillation amplitude along the y axis, as shown in Fig. 9b. Over time, the rotor asymptotically reaches the equilibrium rotation mode without oscillations.

Conclusion.

A mathematical model of the dynamics of a rotor in a low-flow centrifugal pump is built, taking into account the dynamic reaction of the liquid layer. Comparative characteristics of the "basic" calculation based on a purely analytical model and a "hybrid" calculation using the ANSYS Fluent package are given. Simulation of rotor dynamics with refined coefficients obtained on the basis of a single calculation in the ANSYS Fluent package shows a gradual, smooth transition from oscillations to a stationary operating mode. In this case, the calculation according to the approximate basic formulas shows a slow extinction of a non-stationary mode of operation, with an exit to constant small fluctuations. The resulting model can be used for preliminary calculation of pump operation modes, for optimal selection of design parameters in order to improve the dynamic properties of the rotor. At the same time, the proposed calculation method provides a sufficiently high accuracy of the results obtained without large computational costs.

Appendix 1. Dynamic layer response

Since the centrifugal pumps of spacecraft use low-viscosity fluids, we apply the Euler equation for the motion of an ideal fluid:

$$\rho\frac{\partial V}{\partial t} + \rho V\nabla V + \nabla P = 0. \tag{6}$$

Considering the effects associated with acceleration, we assume the velocity is small and neglect the convective term $\rho V\nabla V$. In this case, the equation (6) takes the following form:

$$\rho\frac{\partial V}{\partial t} + \nabla P = 0. \tag{7}$$

The equation (7) is supplemented with the continuity equation:

$$\nabla\cdot\mathbf{V} = 0.$$

From the Euler and continuity equations, we obtain the equation for the pressure in cylindrical coordinates:

$$\frac{1}{r}\frac{\partial}{\partial r}\left(r\frac{\partial P}{\partial r}\right) + \frac{1}{r^2}\frac{\partial^2 P}{\partial\phi^2} + \frac{\partial^2 P}{\partial y^2} = 0. \tag{8}$$

On the surface of the rotor at $r = R_1$ we have the boundary condition:

$$\rho\frac{\partial V_r}{\partial t} + \frac{\partial P}{\partial r} = 0. \tag{9}$$

On a fixed surface with $r = R_2$, the following condition is set:

$$\frac{\partial P}{\partial r} = 0.$$

If the rotor has acceleration a in an arbitrary direction, then its radial component has the form:

$$\left.\frac{\partial V_r}{\partial t}\right| = a_x\sin(\phi) - a_y\cos(\phi). \tag{10}$$

Substituting the equation (10) into the equation (9), we find the pressure gradient along the normal on the rotor surface:

$$\frac{\partial P}{\partial r} = \rho \left(a_y \cos(\phi) - a_x \sin(\phi) \right).$$

Integrating equation (8) along r and using the boundary conditions on the surfaces, we obtain the averaged equation:

$$\frac{1}{R^2} \frac{\partial^2 \bar{P} h}{\partial \phi^2} + \frac{\partial^2 \bar{P} h}{\partial y^2} = \rho \left(a_y \cos(\phi) - a_x \sin(\phi) \right), \tag{11}$$

where $\bar{P}$ is the mean pressure,

$$h = \Delta - x \sin(\phi) + y \cos(\phi).$$

For long bearings, we neglect the second term in equation (11):

$$\frac{\partial^2 \bar{P} h}{\partial \phi^2} = \rho R^2 \left(a_y \cos(\phi) - a_x \sin(\phi) \right). \tag{12}$$

By integrating equation (12) twice, we find the additional pressure associated with the acceleration of the rotor:

$$\bar{P} = -\frac{\rho R^2 \left(a_y \cos(\phi) - a_x \sin(\phi) \right)}{h}. \tag{13}$$

Next, integrating equation (13), we determine the components of the additional force acting on the rotor due to its acceleration:

$$W_x = \int_0^{2\pi} \bar{P} R \sin(\phi) d\phi = K_{11} a_x + K_{12} a_y,$$
$$W_y = \int_0^{2\pi} \bar{P} R \cos(\phi) d\phi = K_{21} a_x + K_{22} a_y,$$

where

$$K_{11} = -\frac{\rho l R^3}{\Delta} \int_0^{2\pi} \frac{\sin^2 \phi}{1 - \frac{x}{\Delta} \cos(\phi) + \frac{y}{\Delta} \cos \phi} d\phi,$$
$$K_{22} = -\frac{\rho l R^3}{\Delta} \int_0^{2\pi} \frac{\cos^2 \phi}{1 - \frac{x}{\Delta} \cos(\phi) + \frac{y}{\Delta} \cos \phi} d\phi,$$
$$K_{12} = K_{21} = -\frac{\rho l R^3}{\Delta} \int_0^{2\pi} \frac{\sin(\phi) \cos(\phi)}{1 - \frac{x}{\Delta} \cos(\phi) + \frac{y}{\Delta} \cos \phi} d\phi.$$

References

[1] E.V.Morozova, Optimization of a centrifugal pump by criteria dimensions and cavitation characteristics, *Gidravlika*, **2**(2018), 74–80 (in Russian).

[2] A.I.Petrov, N.Yu.Isaev, Hydrodynamic modeling of work centrifugal pump in the negative flow zone, *Gidravlika*, **3**(2017), 91–101 (in Russian).

[3] E.S.Menon, Liquid Pipeline Hydraulics, NY. Basel: SYSTEK Technologies, Inc. Marcel Dekker, Inc, 2004.

[4] B.G.Kuharenko, Limiting cycle of self-oscillations of the rotor blades of a centrifugal compressor, *Mechanical engineering and reliability problems*, **2**(2010), 10–14.

[5] D.S.Dolgin, A.E.Lebedev, I.S.Gudanov, Mathematical model of formation cavitation bubbles in a centrifugal pump, *Engineering vestnik of Don's*, **3**(2019), 7–13 (in Russian).

[6] V.A.Pyhliy, A.A.Juravlev, E.V.Glushkova, Semi-analytical solution method boundary and initial problems in relation to the calculation of the rotor blades of centrifugal open type pumps, *Power plants and technologies*, **1**(2019), 34–38.

[7] P.V.Pisarev, D.A.Ermakov, Yu.S.Kirova, O.A.Kashin, Numerical calculation of vibrating centrifugal pump blades loaded with fluid flow, *Nauchno tekhnicheskij vestnik Povolzh'ya*, **1**(2018), 90–93 (in Russian).

[8] P.V.Pisarev, Numerical analysis of oscillatory processes in two-stage centrifugal pumps of various shapes, *Mathematical modeling in natural sciences*, **1**(2017), 254–257.

[9] A.A.Lomakin, Centrifugal and axial pumps, Mashinostroenie, 1966 (in Russian).

[10] G.K.Borovin, A.I.Petrov, A.A.Protopopov, N.Yu.Isaev, Dynamics of rotors of oil-flow centrifugal pumps with hydrostatic bearings and driven by DC motors, *Preprinty IPM im. M. V. Keldysha*, (2016), no. 142 (in Russian).

[11] V.A.Voskresensiy, V.I.Diyakov, A.Z.Zile, Calculation and design of fluid friction supports: Handbook, Mashinostroenie, 1983 (in Russian).

[12] S.A.Chernavskiy, Plain bearings Mashgiz, 1963 (in Russian).

[13] V.M.Cherkasskiy, Pumps, fans, compressors, Energiya, 1977 (in Russian).

[14] V.O.Lomakin, A A.V.rtemov, A.I.Petrov, Determination of the influence of the main geometric parameters of the pump outlet NM 10000-210 on its characteristics, *Science and education: electronic scientific and technical publication*, (2012), no. 8, 71–83 (in Russian). DOI: 10.7463/0812.0445666

[15] G.K.Borovin, A.A.Protopopov, Calculation of the optimal axial clearance of a half-open impeller of a centrifugal low-flow pump of the thermal control system of a spacecraft, *Preprinty IPM im. M.V. Keldysha*, (2013), no. 086 (in Russian).

Численно-аналитическое моделирование работы центробежного насоса

Виктор А. Иванов
Сибирский федеральный университет
Красноярск, Российская Федерация
Николай В. Еркаев
Институт вычислительного моделирования СО РАН
Красноярск, Российская Федерация

Аннотация. Построена математическая модель нестационарных режимов вращения ротора центробежного насоса на основе предварительного расчета в ANSYS Fluent и последующего аналитического расчета с использованием уточненных параметров.

Ключевые слова: математическое моделирование, гидростатический подшипник, центробежный насос.

DOI: 10.17516/1997-1397-2021-14-2-224-229
УДК 538.958

Energy Gap Evaluation in Microcrystalline m-HfO_2 Powder

Artem O. Shilov*
Sergey S. Savchenko†
Alexander S. Vokhmintsev‡
Andrey V. Chukin§
Maksim S. Karabanalov¶
NANOTECH Centre, Ural Federal University
Yekaterinburg, Russian Federation

Maksim I. Vlasov
NANOTECH Centre, Ural Federal University
Yekaterinburg, Russian Federation
Institute of High-Temperature Electrochemistryof of the Ural Branch RAS
Yekaterinburg, Russian Federation

Ilya A. Weinstein‖
NANOTECH Centre, Ural Federal University
Yekaterinburg, Russian Federation
Institute of Metallurgy of the Ural Branch RAS
Yekaterinburg, Russian Federation

Received 10.11.2020, received in revised form 11.01.2021, accepted 20.01.2021

Abstract. In this paper optical properties of microcrystalline HfO_2 powder are investigated. X-ray diffraction and Raman spectroscopy were used to determine that the studied samples are in monoclinic phase. Based on the analysis of the diffuse reflectance spectra and applying Kubelka-Munk formalism we evaluated the indirect bandgap value $E_g = 5.34 \pm 0.05$ eV. The calculated value is in agreement with independent data for HfO_2 thin films synthesized by various methods. The paper is based on the materials of the report presented at the first Russian scientific confererence with the participation of the international community "YENISEI PHOTONICS – 2020".

Keywords: hafnium dioxide, diffuse reflectance, absorption edge

Citation: A.O. Shilov, S.S. Savchenko, A.S. Vokhmintsev, A.V. Chukin, M.S. Karabanalov, M.I. Vlasov, I.A. Weinstein, Energy Gap Evaluation in Microcrystalline m-HfO_2 Powder, J. Sib. Fed. Univ. Math. Phys., 2021, 14(2), 224–229. DOI: 10.17516/1997-1397-2021-14-2-224-229.

Introduction

Hafnium dioxide meets great interest of modern condensed matter physics as a wide-gap high-k material with superior thermal and chemical stability. Along with the other IVB metal oxides (ZrO_2, TiO_2) HfO_2 is considered to be a promising solid-state medium for creation of the

* https://orcid.org/0000-0001-8189-2431
† https://orcid.org/0000-0002-6256-5483
‡ https://orcid.org/0000-0003-2529-3770
§ https://orcid.org/0000-0001-7611-9591
¶ https://orcid.org/0000-0001-6619-2816
‖ i.a.weinstein@urfu.ru https://orcid.org/0000-0002-5573-7128

non-volatile memory cells because of its physical properties and favorable valence and conduction band alignments [1–5]. Due to wide energy gap and high refractive index hafnia is used as optical coatings [6]. As downscaling of field effect transistors has become difficult, HfO_2 could also be a candidate to replace SiO_2 as gate dielectric [7]. However, a deep understanding of the fundamental features in electronic structure and of the regularities in the functional characteristics formation is required to solve problems and to further develop the application principles of hafnium dioxide in opto- and nanoelectronic devices [2]. This work is devoted to the study of the structural and optical properties of nominally pure HfO_2 powder based on the sample characterization methods and analysis of diffuse reflectance spectra.

1. Experimental

In this paper the commercial hafnia powder of the HFO-1 grade (TU 48-4-201-72) was investigated. The purity of HfO_2 powder is 99.9 %, and the concentration of ZrO_2 does not exceed 0.1 %.

HfO_2 powder was characterized by AurigaCrossBeam (Carl Zeiss) scanning electron-ion microscope (SEM) with an accelerating voltage of 1 kV, coupled with an EDS device X-max 80 (Oxford Instruments) for analysis of chemical composition. The structural properties were studied by X-ray diffraction (XRD) measurements by X'Pert PRO MPD PANalytical diffractometer with CuKα radiation operating at 40 kV and 30 mA in the 2θ range from 10° to 90°, step size 0.05°.

Raman spectra were measured using Renishaw U1000 spectrometer under excitation by Cobolt Samba solid-state laser with a wavelength of 532 nm (5 mW power) and were recorded in the extended mode within the range of 50–850 cm^{-1} with spectral resolution of 1 cm^{-1}. The measurement of the diffuse reflectance spectra was performed using double beam SHIMADZU UV-2450 spectrophotometer and integrating sphere attachment ISR-2200 in range of 220–850 nm at room temperature and with barium sulfate used as the white reference plate.

2. Results

Fig.1 shows SEM-image of the investigated powder. According to the obtained images, the size of the particles is in range 1–40 μm. Analysis of the chemical composition revealed the presence of 83.8 ± 0.5 wt.% hafnium and 16.2 ± 0.5 wt.% oxygen in the sample. The obtained ratio is close to stoichiometric one. No impurities with noticeable concentration were found in the investigated powder.

XRD pattern of the HfO_2 powder is shown in Fig. 2a. The peaks correspond to m-HfO_2 – monoclinic, baddeleyite structure, group $P2_1/c$. This conclusion was confirmed by the analysis of the Raman spectrum (Fig. 2b). 17 peaks with the most intensive mode near 500 cm^{-1} is a characteristic set for m-HfO_2. In Fig. 2b the corresponding phonon modes are presented next to the peaks. It is noteworthy that the maximum near 135 cm^{-1} is the superposition of two active modes [8].

In Fig. 2c the diffuse reflectance spectrum is shown. A sharp decrease is observed for $\lambda <$ 250 nm. Also, for $\lambda = 240$ nm local maximum is present and the reflectance R > 95 % in range of $\lambda > 400$ nm.

3. Discussion

The measured diffuse reflectance spectrum was transformed into spectral dependence for optical absorption coefficient α using Kubelka-Munk function $F(R)$ (1) [5,9]:

$$\alpha \sim F(R) = \frac{(1-R)^2}{2R}. \tag{1}$$

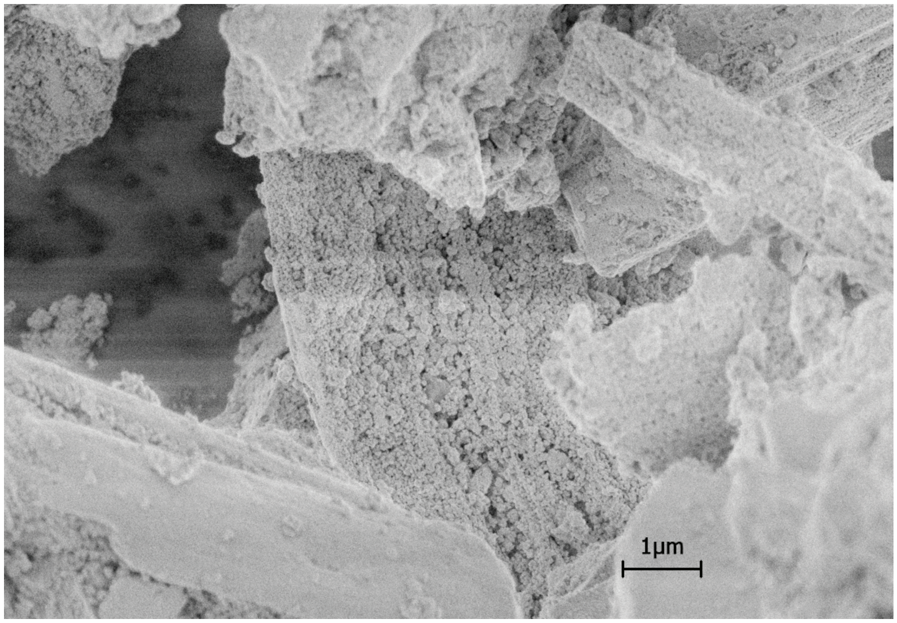

Fig. 1. SEM micrograph of HfO_2 powder under study

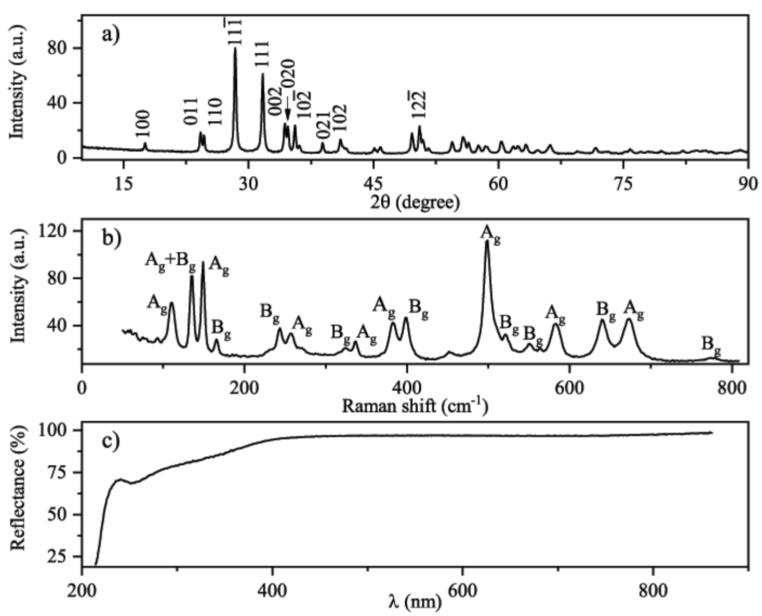

Fig. 2. Characterization of the investigated HfO_2 powder: a) XRD pattern, b) Raman-shift data, c) Diffuse reflectance spectrum

The obtained data is presented in Fig. 3. For the energy of incident photons $h\nu > 5.25$ eV the sharp increase due to optical transitions near intrinsic absorption edge is noted. A small broad band is observed in the energy range of 4.6–5.1 eV and an extended shoulder is present up to 3 eV. Considering the data on the absence of impurities in the studied powder we can conclude that the indicated spectral features have intrinsic origin in m-HfO_2 [10]. It is known that intrinsic absorption edge in m-HfO_2 is caused by indirect band-to-band transitions [7] and in this case should be applied (2) [11]:

$$\alpha h\nu = A(h\nu - E_g)^2, \tag{2}$$

where A is constant, $eV^{-1} \cdot cm^{-1}$.

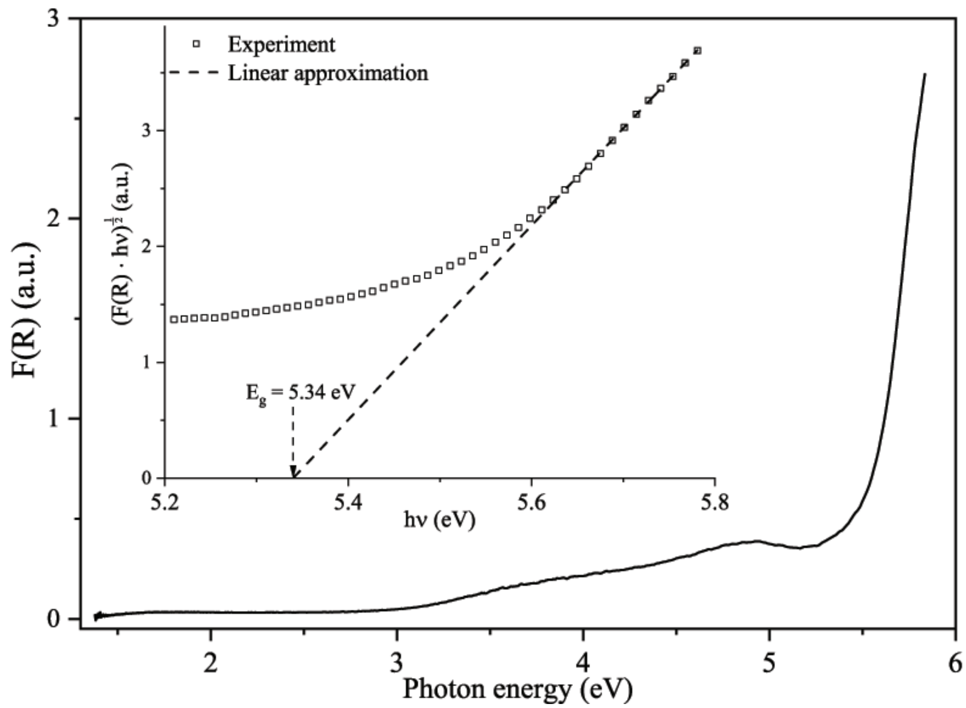

Fig. 3. Kubelka-Munk function, calculated for the diffuse reflectance spectrum. The inset shows optical bandgap evaluation

Bandgap value was evaluated using Tauc plot in coordinates $(F(R) \cdot h\nu)^{\frac{1}{2}}$. Linear part of the dependence was extrapolated in order to calculate the energy gap value $E_g = 5.34 \pm 0.05$ eV. It should be noted that this estimation was made up to emitted phonon energy $\hbar\omega$. Area of the intrinsic absorption edge $h\nu + \hbar\omega > E_g$ which corresponds to indirect transitions with absorption of vibrational modes is distorted by defect-induced processes in the band area of 4.9 eV. Nevertheless, the obtained E_g value is in agreement with other independent data. In particular, for HfO_2 thin films of produced by ion beam sputtering deposition method $E_g = 5.4 \pm 0.05$ eV [6]. For the films synthesized using atomic-layer deposition technique energy gap value is 5.55 eV [7].

Conclusion

In this paper structural and optical properties of pure HfO_2 powder were studied. XRD and Raman spectroscopy methods were used to identify that the sample is stabilized in monoclinic phase. SEM was used to determine that the size of the particles is in range 1–40 μm, impurities are absent. Based on the analysis of the diffuse reflectance spectra in the region of the intrinsic absorption edge at $\lambda <$250 nm, using the Kubelka-Munk function and the Tauc plot for indirect allowed transitions, the energy gap was evaluated as $E_g = 5.34 \pm 0.05$ eV. The results obtained are consistent with independent data for thin HfO_2 films.

The work was supported by Act 211 Government of the Russian Federation, contract no. 02. A03.21.0006 and by Minobrnauki research project FEUZ-2020-0059.

References

[1] J.T.Gaskins,P.E.Hopkins, D.R.Merrill, S.R.Bauers, E.Hadland, D.C.Johnson, D.Koh, J.H.Yum, S.Banerjee, B.J.Nordell, M.M.Paquette, A.N.Caruso, W.A.Lanford, P.Henry, L.Ross, H.Li, L.Li, M.French, A.M.Rudolph and S.W.King, Review—Investigation and Review of the Thermal, Mechanical, Electrical, Optical, and Structural Properties of Atomic Layer Deposited High-k Dielectrics: Beryllium Oxide, Aluminum Oxide, Hafnium Oxide, and Aluminum Nitride *ECS J. Solid State Sci. Technol.* **6** (2017), 189–207.

[2] V.A.Gritsenko, D.R.Islamov, T.V.Perevalov, V.Sh.Aliev, A.P.Yelisseyev, E.E.Lomonova, V.A.Pustovarov, A.Chin, *J. Phys. Chem. C*, **120**(2016), 19980–19986.

[3] A.S.Vokhmintsev, I.A.Weinstein, R.V.Kamalov, I.B.Dorosheva, Memristive effect in a nanotubular layer of anodized titanium dioxide, *Bull. Russ. Acad. Sci. Phys.*, **78**(2014), 932–935. DOI: 10.3103/S1062873814090317

[4] I.A.Petrenyov, A.S.Vokhmintsev, R.V.Kamalov, I.A.Weinstein, Conduction mechanisms in memristors based on nanotubular arrays of zirconium oxide, AIP Conference Proceedings, Vol. 2174, 2019, 020242.

[5] A. V. Kozhevina, A. S. Vokhmintsev, R. V. Kamalov, N. A. Martemyanov, A. V. Chukin, I. A. Weinstein Optical absorption edge parameters of zirconium dioxide nanotubular structures *J. Phys.: Conf. Ser.* **917**(2017), 062031.

[6] A.O.Shilov, S.S.Savchenko, A.S.Vokhmintsev, V.A.Gritsenko, I.A.Weinstein, Optical Parameters and Energy Gap Estimation in Hafnia Thin Film, AIP Conference Proceedings, Vol. 2313, 2020. DOI: 10.1063/5.0033176

[7] J. Aarik, H. Mandar, M. Kirm, L. Pung, Optical characterization of HfO_2 thin films grown by atomic layer deposition *Thin Solid Films* **466**(2004), 41–47.

[8] R.Wu, B. Zhou, Q. Li, Z. Jiang, W. Wang, W. Ma, X.Zhang, Elastic and vibrational properties of monoclinic HfO_2 from first-principles study. *Journal of Physics D: Applied Physics* **45(12)**(2012), 125304.

[9] P. Kubelka, F. Munk,Ein Beitrag zur Optik der Farbanstriche, *Z. Tech. Phys.* **11**(1931), 593–601.

[10] E. E. Hoppe, R. S. Sorbello, C. R. Aita Near-edge optical absorption behavior of sputter deposited hafnium dioxide *J. Appl. Phys.* **101**(2007), 123534.

[11] J. Tauc, Optical Properties of Amorphous Semiconductors, *Amorphous and Liquid Semiconductors* (1974), pp.159-220.

Оценка ширины запрещенной зоны в микрокристаллическом порошке m-HfO_2

Артём О. Шилов
Сергей С. Савченко
Александр С. Вохминцев
Андрей В. Чукин
Максим С. Карабаналов
НОЦ НАНОТЕХ, Уральский федеральный университет
Екатеринбург, Российская Федерация
Максим И. Власов
НОЦ НАНОТЕХ, Уральский федеральный университет
Екатеринбург, Российская Федерация
Институт высокотемпературной электрохимии УрО РАН
Екатеринбург, Российская Федерация
Илья А. Вайнштейн
НОЦ НАНОТЕХ, Уральский федеральный университет
Екатеринбург, Российская Федерация
Институт металлургии УрО РАН
Екатеринбург, Российская Федерация

Аннотация. В работе изучены оптические свойства микрокристаллического порошка диоксида гафния. Методами рентгеновской дифракции и рамановской спектроскопии установлено, что исследуемые образцы обладают моноклинной кристаллической решёткой. На основе анализа спектров диффузного отражения и применения формализма Кубелки-Мунка выполнена оценка ширины непрямой запрещённой зоны $E_g = 5.34 \pm 0.05$ эВ. Полученная величина согласуется с независимыми данными для пленок HfO_2, синтезированных различными методами. Статья подготовлена по материалам доклада на Первой Всероссийской научной конференции с международным участием «ЕНИСЕЙСКАЯ ФОТОНИКА — 2020.»

Ключевые слова: диоксид гафния, диффузное отражение, край поглощения.

DOI: 10.17516/1997-1397-2021-14-2-230-241
УДК 519.21

Joint Distribution of the Number of Vertices and the Area of Convex Hulls Generated by a Uniform Distribution in a Convex Polygon

Isakjan M. Khamdamov*
National University of Uzbekistan named after Mirzo Ulugbek
Tashkent, Uzbekistan
Zoya S. Chay†
Tashkent University of Information Technologies named after M. al-Khwarizmi
Tashkent, Uzbekistan

Received 05.07.2020, received in revised form 13.12.2020, accepted 20.01.2021

Abstract. A convex hull generated by a sample uniformly distributed on the plane is considered in the case when the support of a distribution is a convex polygon. A central limit theorem is proved for the joint distribution of the number of vertices and the area of a convex hull using the Poisson approximation of binomial point processes near the boundary of the support of distribution. Here we apply the results on the joint distribution of the number of vertices and the area of convex hulls generated by the Poisson distribution given in [6]. From the result obtained in the present paper, in particular, follow the results given in [3, 7], when the support is a convex polygon and the convex hull is generated by a homogeneous Poisson point process.

Keywords: convex hull, convex polygon, Poisson point process, binomial point process, central limit theorem.

Citation: I.M. Khamdamov, Z.S. Chay, Joint Distribution of the Number of Vertices and the Area of Convex Hulls Generated by a Uniform Distribution in a Convex Polygon, J. Sib. Fed. Univ. Math. Phys., 2021, 14(2), 230–241. DOI: 10.17516/1997-1397-2021-14-2-230-241.

Introduction

This paper is devoted to the study of properties of convex hulls generated by independent observations over a random vector that has a uniform distribution in a convex polygon. Convex hulls are very complex objects from the analytic point of view. Therefore, studying the properties of the simplest functionals of convex hulls, such as, the number of vertices or the area, is not an easy task. This explains the fact that, prior to obtaining the central limit theorem for the number of vertices of a convex hull by P. Groeneboom, the main achievement was considered to be the study of asymptotic expressions for the mean values of similar functionals (see, for example, [4, 5, 16]); the problems on asymptotic expressions for the variance remained unsolved until the appearance of the studies by C. Buchta [1, 2] and J. Pardon [14, 15].

It should be noted that P. Groeneboom, using the well-known property of homogeneous binomial point processes, which is that near the boundary of the support, it is almost indistinguishable

*khamdamov.isakjan@gmail.com
†chay1526@mail.ru

from a homogeneous Poisson point process, and using such powerful techniques as strongly mixing stationary processes and martingales, has proved the central limit theorems for the number of vertices of a convex hull in the case when the support of the original uniform distribution is either a convex polygon or a unit disk. The modified P. Groeneboom technique was applied in [3] to prove limit theorems for the area and perimeter of a convex hull in a polygon, and in [9], to prove a limit theorem for an area outside a convex hull in a disk.

Similar results were obtained later by J. Pardon [16, 17] without imposing any regularity conditions on the support boundary. In the present work, there is no need for using martingales, strongly mixing stationary processes, etc.; the approach used is a modification of the methods presented in [7, 10–13]. The results obtained by Sh. K. Formanov, I. M. Khamdamov in [6], are applied here; a joint limit distribution for the number of vertices and the area of the convex hull generated by a Poisson point process in a cone was obtained by elementary analytical and direct probabilistic methods.

1. Statement of problem and results

Let $\vec{x}_j,\ j = 1, 2, \ldots, n$ be the independent observations over a random vector having a uniform distribution in a convex polygon A with r sides. A matrix X_n is called a sample, the j-row of which is formed by the components of the vector $\vec{x}_j$. Let us denote the convex hull generated by vectors $\vec{x}_j,\ j = 1, 2, \ldots, n$ by $C_n = C_n(X_n)$.

We are interested in the joint limit distribution of the following functionals of C_n: the total number of vertices ν_n and the area S_n. It is clear that C_n, and, consequently, the indicated functionals, are uniquely determined by the set of vertices W_n. If the principle of vertex labeling is chosen, then it can be represented as a $\nu_n \times 2$ matrix. It is easy to show that this matrix has the property of sufficiency with respect to the boundary of the set A — the support of original distribution. The latter circumstance is of interest from the point of view of statistics of uniform distributions.

Before formulating the main results, we introduce some notation. Let S be the area of the polygon A. Then we assume that

$$D_n = S - S_n$$

and let

$$a_n = \frac{2r\log n}{3},\quad a'_n = \frac{Sa_n}{n},\quad b_n = \sqrt{\frac{27}{10r\log n}},\quad b'_n = n\sqrt{\frac{27}{28rS^2\log n}} = \frac{\sqrt{5}nb_n}{\sqrt{14}S}.$$

We denote by ω a vector having a two-dimensional normal distribution with a zero vector of mean values, unit variances and a correlation coefficient $\sqrt{5/14}$.

Let us state the main theorem.

Theorem 1. *Under our assumptions, a random vector with components $b_n(\nu_n - a_n)$ and $b'_n(D_n - a'_n)$ converges in distribution to ω.*

Let us make the necessary explanations of the notation. The symbols $\xrightarrow{d}$, $\xrightarrow{p}$, $\to a.s.$ denote convergence in distribution, in probability, and almost sure, respectively. $f(\varepsilon) \asymp g(\varepsilon)$ means that there are positive constants c_1, c_2, ε_0 such that $c_1 f(\varepsilon) \leqslant g(\varepsilon) \leqslant c_2 f(\varepsilon)$ for any $0 < \varepsilon < \varepsilon_0$. Generally $o_p(1)$ is used for a sequence of random variables converging in probability to zero. The notation $\xi_n = O_p(1)$ means that $\sup_{n\geqslant 1} P(|\xi_n| > t) \to 0$ as $t \to \infty$. Everywhere $c,\ c_1,\ c_2, \ldots$ are the positive constants whose values might be changed from line to line and $c(\beta),\ c_1(\beta),\ c_2(\beta)$

are the positive constants, depending on the specified arguments. Further, $\xi \overset{dis}{=} \zeta$ means that the random variables ξ and ζ have a common law of probability distribution.

2. The Poisson approximation

In this section, we present the key idea of [7] about the Poisson approximation of a homogeneous binomial point process (h.b.p.p) $B_n(A)$ generated by n independent observations of a random variable having a uniform distribution with support A in a slightly different way. Here we consider the more general case, assuming that A is an arbitrary bounded convex set in R^2.

Let Γ_A be the boundary of the set A. For each $z \in \Gamma_A$, consider an open sphere $S(z, \varepsilon)$ of radius ε centered in z. It is easy to see that the set $A_\varepsilon = A - \bigcup_{z \in \Gamma_A} S(z, \varepsilon)$ is a strip along the border Γ_A. Let us denote $B_\varepsilon = A - A_\varepsilon$ and assume that $\lambda(A) = 1$, where $\lambda(\cdot)$ is the Lebesgue measure.

Let W_n, as before, be the set of vertices of the convex hull C_n generated by $B_n(A)$. The next lemma is a simple modification of Lemma 2.1 and its Corollary 2.1 given in [7].

Lemma 1. *There is a sequence of positive numbers ε_n converging to zero such that the probability that at least one of the vertices C_n laying in B_ε, converges to zero in $\varepsilon > \varepsilon_n$.*

Proof. It is easy to see that the event $E = \{W_n \bigcap B_\varepsilon \neq \varnothing\}$ coincides with the event "there is a pair of neighboring vertices w_1 and w_2 such that $w_1 \in B_\varepsilon$ ". Let the straight line $(p, z - w_1) = 0$ pass through the point w_2. Since $w_1 \in B_\varepsilon$, then this line divides A into two parts, the measure of each is no less than some value of $c(\varepsilon) > 0$ such that $\lim_{\varepsilon \to 0} c(\varepsilon) = 0$. Therefore at $n > 2$

$$P(E) = \frac{n(n-1)}{2} \iint\limits_{w_1 \in B_\varepsilon, w_2 \in A} P^{n-2} \{n-2 \text{ the sample points } X_n \text{ lie on one side}$$

$$\text{of the straight line } (p, z - w_1) = 0\}\, dw_1 dw_2 \leqslant n^2 (1 - c(\varepsilon))^n .$$

It remains to assume that

$$\varepsilon_n = \inf \left\{ \varepsilon : c(\varepsilon) \geqslant \frac{3 \log n}{n} \right\}. \tag{1}$$

The lemma is proved. □

Note that the rate of decrease $c(\varepsilon)$ at $\varepsilon \to 0$ depends on the smoothness Γ_A. In particular, if A is a sphere, then $c(\varepsilon) \asymp \varepsilon^{\frac{3}{2}}$; if A is a polygon, then $c(\varepsilon) \asymp \varepsilon^2$ and etc.

Since we are not interested in the estimates of the rate of convergence in the theorems given below, we will not worry about optimizing the choice of the strip containing W_n.

Let now $\Pi_n(\cdot)$ be a homogeneous Poisson point process (h.p.p.p.), the intensity of which is equal to $n\lambda(\cdot)$.

Consider the narrowing $\Pi_n(A)$ of this process to the set A. We denote by C'_n the convex hull generated by it, and the set of its vertices we denote by W'_n.

Lemma 2. *The probability that at least one of the vertices C'_n laying in B_ε, converges to zero, as $n \to \infty$ uniformly in $\varepsilon > \varepsilon_n$, where ε_n, is determined by relation (1).*

Proof. We assume that

$$E' = \left\{ W'_n \bigcap B_\varepsilon \neq \varnothing \right\}$$

and let $\mu_n(\cdot)$ be the random counting measure corresponding to $\Pi_n(A)$. By the formula of total probability we have

$$P(E') = \sum_{k=0}^{\infty} P\left(\mu_n(A) = k\right) P\left(E' / \mu_n(A) = k\right). \tag{2}$$

Since the conditional distribution $\Pi_n(A)$ under the condition $\mu_n(A) = k$ coincides with $B_n(A)$, according to Lemma 1 for $k \geqslant 3$ we have

$$P\left(E' / \mu_n(A) = k\right) \leqslant k^2 \left(1 - c(\varepsilon)\right)^{k-2}. \tag{3}$$

Taking into account (2) and (3), we write

$$P(E') \leqslant \sum_{|k-n|<\frac{n}{4}} k^2 \left(1 - c(\varepsilon)\right)^{k-2} P\left(\mu_n(A) = k\right) + P\left(|\mu_n(A) - n| \geqslant \frac{n}{4}\right) = \Sigma_1 + \Sigma_2. \tag{4}$$

Using the Chebyshev inequality, we have

$$\Sigma_2 \leqslant 16n^{-1}. \tag{5}$$

Further on, for sufficiently small $\varepsilon > 0$

$$\Sigma_1 \leqslant \max_{|k-n|<\frac{n}{4}} k^2 \left(1 - c(\varepsilon)\right)^{k-2} \leqslant \left(\frac{3n}{4}\right)^2 \left(1 - c(\varepsilon)\right)^{\frac{3n}{4}-2}.$$

It is easy to see that

$$\sup_{\varepsilon \geqslant \varepsilon_n} \Sigma_1 = o(1). \tag{6}$$

Combining (4)–(6), we arrive at the assertion of the lemma being proved. The lemma is proved. □

Let C_ε be the convex hull constructed from the part of the sample X_n in A_ε.

Lemma 1 implies that

$$\sup_{\varepsilon \geqslant \varepsilon_n} P\left(C_n \neq C_\varepsilon\right) \to 0 \text{ as } n \to \infty. \tag{7}$$

Let $B_n(A_\varepsilon)$ be the narrowing of the h.b.p.p. $B_n(\cdot)$ on A_ε. According to Lemma 2.2 in [7], $\Pi_n(A_\varepsilon)$ and $B_n(A_\varepsilon)$ can be defined on one probability space in such a way that

$$P\left(\Pi_n(A_\varepsilon) \neq B_n(A_\varepsilon)\right) \leqslant 2\lambda(A_\varepsilon). \tag{8}$$

Let us denote the convex hull generated by $\Pi_n(A_\varepsilon)$ by C'_ε. Then from Lemma 2 it follows that

$$\lim_{n\to\infty} \sup_{\varepsilon \geqslant \varepsilon_n} P\left(C'_n \neq C'_\varepsilon\right) = 0. \tag{9}$$

From (7)–(9) it follows that as $n \to \infty$

$$P\left(C'_n \neq C'_\varepsilon\right) \to 0. \tag{10}$$

Remark. Let $f_i,\ i = 1, 2, \ldots, k$ be a certain finite number of functionals defined on the set of convex polygons. If the joint distribution of random variables $f_i\left(C_n\right),\ i = 1, 2, \ldots, k$ converges to some distribution G, then it follows from (10) that $f_i\left(C'_n\right),\ i = 1, 2, \ldots, k$ also has this property. Thus, the problem of the limit distribution of the functionals ν_n and S_n, introduced in Section 1, is reduced to the study of ν'_n and S'_n are the corresponding characteristics of convex hulls generated by the h.p.p.p.

3. Convex hulls generated by the h.p.p.p.

3.1. Some properties of the h.p.p.p. Let K be a cone formed by two rays $l_i = (z : z = te_i,\, t > 0)$, $i = 1, 2$, where e_1 and e_2 are the unit vectors. Without loss of generality, we assume that e_1 and e_2 are the orthonormal vectors

$$e_0 = \frac{e_1 + e_2}{2}. \tag{11}$$

Let further $\Pi(\cdot)$ be a h.p.p.p. with intensity $\lambda(\cdot)$. We denote the narrowing on K by $\Pi(K)$. Consider the convex hull C' generated by K by $\Pi(K)$ and the set of its vertices Z.

Let us denote the vertex by $z_0 \in Z$ for which $(e_0, z - z_0) \geqslant 0$ for all $z \in Z$.

It is obvious that z_0 is determined unambiguously almost sure.

The straight line

$$(e_0, z - z_0) = 0 \tag{12}$$

is the supporting line for C'.

Consider a triangle formed by rays $l_i,\ i = 1, 2$ and a supporting line (12). We denote the set of interior points of this triangle by δ_0, and the area is denoted by ξ_0. It is easy to see that

$$\xi_0 = \frac{x_0^2}{2}, \tag{13}$$

where $x_0 = y_0 = u_0 + v_0$ and $z_0 = (u_0, v_0)$. Assume that

$$\eta_0 = \frac{v_0}{x_0}. \tag{14}$$

Then from (13) and (14) it is easy to obtain

$$u_0 = (1 - \eta_0)\sqrt{2\xi_0}, \quad v_0 = \eta_0\sqrt{2\xi_0}. \tag{15}$$

Let us label the vertices C', going around the boundary counterclockwise. Since z_0 is defined, each of the vertices gets its own number $j,\ -\infty < j < \infty$. Let us choose on the ray l_1 a sequence of points $x_j,\ j \geqslant 1$, lying on the intersection of l_1 and the lines passing through the vertices z_{j-1} and z_j, respectively. Likewise, on the ray l_2, points $y_j,\ j \leqslant -1$, are obtained as a result of intersections of l_2 and the lines passing through $z_j,\ z_{j+1}$, respectively.

Let $\delta_j,\ j \neq 0$; the set of interior points of a triangle with vertices z_{j-1}, $(x_{j-1}, 0)$, $(x_j, 0)$, if $j \geqslant 1$, and vertices z_{j+1}, $(0, y_{j+1})$, $(0, y_j)$, if $j \leqslant -1$. We denote the vertices of the triangle by $(x_0, 0)$, $(0, y_0)$, the set of interior points by δ_0. The third vertex of this triangle is the point $(0, 0)$. The figures are taken from [6] (see Fig. 1).

We assume that

$$\xi_j = \lambda(\delta_j).$$

Then it is easy to obtain

$$\xi_j = \begin{cases} v_{j-1}(x_j - x_{j-1})/2, \text{ if } j \geqslant 1 \\ u_{j+1}(y_j - y_{j+1})/2, \text{ if } j \leqslant -1 \end{cases}, \tag{16}$$

where $z_j = (u_j, v_j)$. If we assume that

$$\rho_j = \frac{u_j - u_{j-1}}{v_{j-1} - v_j}, \tag{17}$$

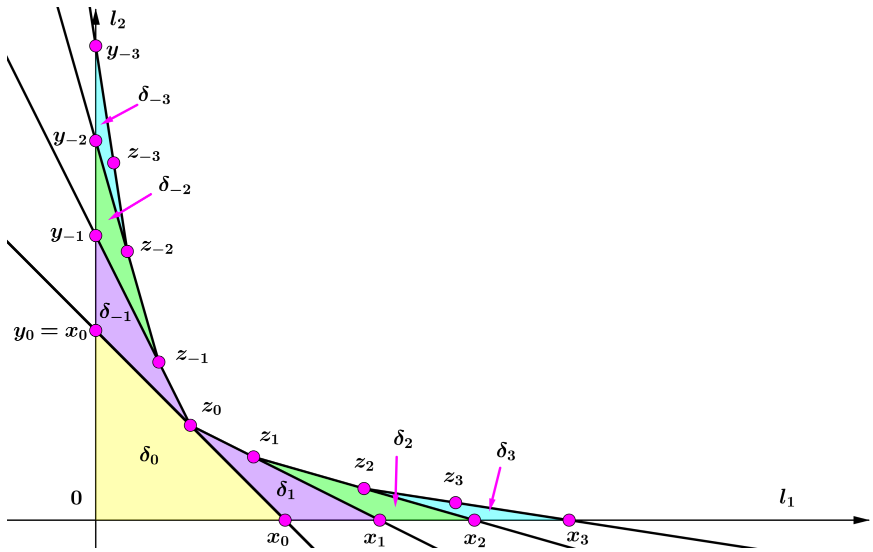

Fig. 1. Illustration of z_j and δ_j

then

$$\xi_j = \frac{v_{j-1}^2}{2}(\rho_j - \rho_{j-1}). \tag{18}$$

Now we define the boundary functionals

$$\theta_T = \inf\{j : x_j \geqslant T\} \quad \text{and} \quad \theta'_T = \inf\{-j : y_j \geqslant T\}, \tag{19}$$

where $T > 0$.

We assume that

$$\alpha(T) = \frac{2\log T}{3}, \quad \beta^2(t) = \frac{10\log t}{27}.$$

$$S_T = \begin{cases} \xi_1 + \xi_2 + \ldots + \xi_{\theta_T} & \text{if } \theta_T \geqslant 1 \\ 0 & \text{if } \theta_T = 0 \end{cases} \quad \text{and} \quad S'_T = \begin{cases} \xi_{-1} + \xi_{-2} + \ldots + \xi_{-\theta'_T} & \text{if } \theta'_T \geqslant 1 \\ 0 & \text{if } \theta'_T = 0 \end{cases}. \tag{20}$$

We present the following theorem with corollaries obtained in [6], which play the key role in this article (see Theorem 1, Corollaries 1, 2, 3 [6]).

Theorem 2 (Formanov and Khamdamov). *Under our assumptions, as $T \to \infty$, we have*

$$(\beta(T))^{-1}(\theta_T - \alpha(T), S_T - \alpha(T)) \stackrel{d}{\Rightarrow} N(0, B) \quad \textit{with} \quad B = \begin{pmatrix} 1 & 1 \\ 1 & 14/5 \end{pmatrix}.$$

Here $N(0, B)$ is a normally distributed random vector with a zero vector of mean values and a covariance matrix B.

Corollary 1 (Formanov and Khamdamov). *In our case $E\theta_T = \alpha(T) + o(\beta(T))$ and $Var\theta_T = \beta^2(T)(1 + o(1))$ as $T \to \infty$.*

Corollary 2 (Formanov and Khamdamov). *Let $0 < T_1 \leqslant T_2$ such that $c_1T_1 < T_2 < c_2T_1$ for some $c_1 > 0,\ c_2 > 0$. Then $\theta_{T_2} - \theta_{T_1} = o_p(\beta(T_1))$ as $T_1 \to \infty$.*

Corollary 3 (Formanov and Khamdamov). *Let $0 < T_1 \leqslant T_2$ such that $c_1T_1 < T_2 < c_2T_1$ for some $c_1 > 0,\ c_2 > 0$. Then $(S_{T_2} - S_{T_1})/\beta(T_1)$ converges in probability to zero as $T_1 \to \infty$.*

It is easy to see that at $\min\{T_1, T_2\} \to \infty$ the random vectors (θ_{T_1}, S_{T_1}) and $\left(\theta'_{T_2}, S'_{T_2}\right)$ are asymptotically independent. Moreover, the statements of Theorem 2 and its Corollaries 1–3 hold for $\left(\theta'_{T_2}, S'_{T_2}\right)$.

4. Proof of Theorem 1

The reasoning here is completely elementary. Generally, a verbal description of geometric objects is somewhat lengthy.

In accordance with the conclusions obtained at the end of Section 2 from Lemmas 1 and 2, it is sufficient to obtain the limit distribution for the number of vertices ν'_n and the area S'_n of the convex hull C'_n generated by the narrowing of the $\Pi_n(A)$ h.p.p.p. $\Pi_n(\cdot)$ on the set A. The scheme of further reasoning is as follows. First, we divide the boundary C'_n into $2r$ conditionally independent parts in such a way that each of the r angles of the polygon A corresponds to two elements of this partition. Thus, each of the functionals of interest to us ν'_n and S'_n is represented as a sum of $2r$ random variables. Then, using the properties of the h.p.p.p. stated in Section 3, the asymptotic independence and normality of these random variables are established.

Thus, the general principles for studying the problem are the same as in [7], although their implementation is completely different.

4.1. Dividing the boundary into conditionally independent parts. We denote the vertices of an r-gon of the support A of the initial uniform distribution by $a^{(i)},\ i = 1, 2, \ldots, r$. Let further, for some $\varepsilon > 0$

$$B_i = A \bigcap S\left(a^{(i)}, \varepsilon\right), \tag{21}$$

where $S(z, \varepsilon)$ is a disk of radius ε centered at z. Let us denote the narrowing $\Pi_n(\cdot)$ to a cone K_i with the vertex $a^{(i)}$ and generating rays l_{i1} and l_{i2} by $\Pi_{ni}(\cdot),\ i = 1, 2, \ldots, r$, passing through $a^{(i+1)}$ and $a^{(i-1)}$ respectively. It is clear that $a^{(-1)} = a^{(r)}$, $a^{(r+1)} = a^{(1)}$.

Let e_{0i} play the same role with respect to K_i as played by the vector with respect to K_i in Section 3. Note that e_0 is determined by the equality (11). More precisely,

$$e_{0i} = 2^{-1}\left(\frac{a^{(i+1)} - a^{(i)}}{\|a^{(i+1)} - a^{(i)}\|} + \frac{a^{(i-1)} - a^{(i)}}{\|a^{(i-1)} - a^{(i)}\|}\right).$$

We denote the convex hull as C_{ni} generated by $\Pi_{ni}(\cdot)$. Let us agree to denote the set of vertices C'_n by Z_{ni}. Recall that the set of vertices C'_n in Section 2 is denoted by W'_n. We select in Z_{ni} and W'_n the elements z_{0i} and w_{0i}, that possess the property that the straight lines $(e_{0i}, w - z_{0i}) = 0$ and $(e_{0i}, w - w_{0i}) = 0$ are the supporting lines for C_{ni} and C'_n, respectively.

Assume that

$$\Upsilon_1 = \{\pi : z_{0i} = w_{0i},\ i = 1, 2, \ldots, r\} \tag{22}$$

and

$$\Upsilon_2 = \{\pi : z_{0i} \in B_i,\ i = 1, 2, \ldots, r\}, \tag{23}$$

where π is the implementation of $\Pi_n(\cdot)$, and B_i is determined by equality (21).

It is easy to understand that as $n \to \infty$

$$P(\Upsilon_i) \to 1, \quad i = 1, 2. \tag{24}$$

As follows from (22)–(24), with probability close to 1, the boundary of each hull C_{ni} has a non-empty intersection with C'_n. Note that the points $w_{0i},\ i = 1, 2, \dots, r$ divide the boundary C'_n into r parts. We split each of them into two more parts. Let $w^{(i)}$ be the vertex $W'_n \subset C'_n$, for which the straight line $\left(p_i, w - w^{(i)}\right) = 0$, where $p_i \perp \left(a^{(i+1)} - a^{(i)}\right)$ is a supporting line to C'_n. It is easy to see that $w^{(i)}$ is the closest vertex to the ray l_{i1} from the vertices W'_n. Note that as the n vertex $w^{(i)}$ grows, it approaches this ray indefinitely, i.e., $\left(p_i, w^{(i)} - a^{(i)}\right) \to 0$. Since the conditional distribution on the section of the supporting line $\left(p_i, w - w^{(i)}\right) = 0$ lying in A, under the condition $\left(p_i, w^{(i)} - a^{(i)}\right) = t$ is uniform, we have

$$\lim_{\varepsilon \to 0} \lim_{n \to 0} \inf P\left(w^{(i)} \in \bigcap_{j=1}^{r} \overline{B}_j\right) = 1. \tag{25}$$

Hence it follows that

$$\lim_{\varepsilon \to 0} \lim_{n \to 0} \inf P\left(\overline{w}_i \in \bigcap_{j=1}^{r} \overline{B}_j\right) = 1, \tag{26}$$

where $\overline{w}_i$ is the base of the perpendicular drawn from w_i to l_{i1}.

Consider

$$\Upsilon_3 = \left\{\overline{w}_i \in \bigcap_{j=1}^{r} \overline{B}_j,\ i = 1, 2, \dots, r\right\}.$$

As follows from (25) and (26), for any $\varepsilon > 0$ one can find such $N > 0$ that, for all sufficiently large $n > N$, the following inequality holds

$$P\left(\Upsilon_3\right) \geqslant 1 - \varepsilon.$$

In what follows, without specifying, we consider only those implementations of $\Pi_n(\cdot)$ that are contained in $\bigcap_{j=1}^{3} \Upsilon_j$. For such implementations $w^{(i)},\ i = 1, 2, \dots, r$ lie between w_{0i} and $w_{0(i+1)}$. Thus, the boundary C'_n is divided into $2r$ parts. It is easy to see, that these parts are conditionally independent for the given $w_{0i},\ w^{(i)},\ i = 1, 2, \dots, r$.

4.2. Choice of approximating functionals. Let us consider the section of the boundary C'_n between the vertices w_{01} and $w^{(i)}$. The section between $w^{(r)}$ and w_{01} is studied in a similar way. Let us label the vertices C'_n, going around the boundary counterclockwise, starting from w_{01}. As a result, on the considered section of the boundary, we obtain $w_j,\ j = 0, 1, 2, \dots, \mu$, where $w_0 = w_{01},\ w_\mu = w^{(1)}$. We perform a similar operation with the vertices $z \in C'_{n1}$, obtaining $z_j,\ j = 0, 1, 2, \dots$, where, in view of (22) and (24) $z_0 = w_{01} = w_0$.

In order to use the h.p.p.p. properties described in Section 3, we need to proceed from $\Pi(\cdot)$ to $\Pi_n(\cdot)$. In such transition, the linear characteristics x_j, y_j, u_j, v_j, change to $x'_j = n^{-\frac{1}{2}} x_j$, $y'_j = n^{-\frac{1}{2}} y_j$, $u'_j = n^{-\frac{1}{2}} u_j$, $v'_j = n^{-\frac{1}{2}} v_j$ respectively, while the area ξ_j of the triangle δ_j becomes $\xi'_j = n^{-1} \xi_j$. Dimensionless quantities η_j, τ_j, ρ_j remain unchanged in such transition. We denote the images z_j of such a transformation by z'_j.

Let $T = \varepsilon \sqrt{n}$, $T_1 = h\sqrt{n}$ where h is the length of the side A connecting the vertices $a^{(1)}$ and $a^{(2)}$. In accordance with (19), we assume that

$$\theta = \theta_T \quad \text{and} \quad \chi = \theta_{T_1}.$$

It is clear that

$$\theta = \inf\left\{j : x'_j \geqslant \varepsilon\right\} \quad \text{and} \quad \chi = \inf\left\{j : x'_j \geqslant h\right\}.$$

Note that x_j and x'_j are constructed on the vertices z_{j-1}, z_j and z'_{j-1}, z'_j, respectively. Note that $w_j = z'_j$, at least for $0 \leqslant j \leqslant \chi - 1$.

Let further

$$p = \xi'_1 + \xi'_2 + \cdots + \xi'_\theta, \tag{27}$$

and

$$q = \xi'_1 + \xi'_2 + \cdots + \xi'_\chi. \tag{28}$$

Assume that

$$\theta^* = \frac{\theta - \alpha}{\beta_1}, \quad p^* = \frac{np - \alpha}{\beta_2}, \tag{29}$$

where

$$\alpha = \frac{1}{3}\log n, \quad \beta_1 = \sqrt{\frac{5\log n}{27}}, \quad \beta_2 = \sqrt{\frac{14\log n}{27}}. \tag{30}$$

From (20), (27), (28) and Theorem 2 it follows that

$$(\theta^*, p) \overset{d}{\Rightarrow} \omega, \tag{31}$$

where ω is determined from Theorem 1. Now we assume that

$$\chi^* = \frac{\chi - \alpha}{\beta_1}, \quad q^* = \frac{nq - \alpha}{\beta_2}. \tag{32}$$

According to Corollaries 1–3, in view of (28) and (30), we have

$$\frac{\theta - \chi}{\beta_1} \xrightarrow{p} 0, \quad \frac{n(p-q)}{\beta_1} \xrightarrow{p} 0. \tag{33}$$

From (29)–(33) follows that

$$(\chi^*, q^*) \overset{d}{\Rightarrow} \omega. \tag{34}$$

Similar characteristics θ', p' and χ', q' constructed along the section of the boundary C'_n between the vertices $w^{(r)}$ and $w_{01} = w$, also have properties (31) and (34). It is important that they are asymptotically independent of θ, χ, p and q. And no less important is the fact that θ, θ', p and p' are completely determined by the narrowing of $\Pi_n(\cdot)$ to B_1. It follows that similar characteristics θ_i, θ'_i, p_i, p'_i for the boundary sections corresponding to the angles with the vertices $a^{(i)}$, $i = 1, 2, \ldots, r$ are independent. By analogy with (29) and (32), we define

$$\Theta^* = \frac{\Theta - 2r\alpha}{\beta_1\sqrt{2r}} \quad \text{and} \quad P^* = \frac{nP - 2r\alpha}{\beta_2\sqrt{2r}}, \tag{35}$$

where

$$\Theta = \sum_{i=1}^{r} \left(\theta_i + \theta'_i\right), \quad P = \sum_{i=1}^{r} \left(p_i + p'_i\right).$$

Due to independence of $\left(\theta_i + \theta'_i, p_j + p'_j\right)$, $i, j - 1, 2, \ldots, r$, from (31) we obtain

$$(\Theta, P) \overset{d}{\Rightarrow} \omega.$$

Finally, by analogy with (35), we introduce

$$\mathbb{X}^* = \frac{\mathbb{X} - 2r\alpha}{\beta_1\sqrt{2r}}, \quad \mathbb{Q}^* = \frac{\mathbb{Q} - 2r\alpha}{\beta_2\sqrt{2r}}, \tag{36}$$

where (compare with (35))

$$\mathbb{X} = \sum_{i=1}^{r} (\chi_i + \chi_i'), \quad \mathbb{Q} = \sum_{i=1}^{r} (q_i + q_i').$$

Note that $(\chi_i + \chi_i', q_i + q_i')$, $i = 1, 2, \ldots, r$, generally speaking, are independent. However, in view of (33) and (34), we can assert that

$$(\mathbb{X}^*, \mathbb{Q}^*) \overset{d}{\Rightarrow} \omega. \tag{37}$$

It is the functionals $\mathbb{X}^*$ and $\mathbb{Q}^*$ that give us the required approximation for ν_n' and S_n'.

4.3. Estimation of the approximation accuracy. Let s be the area of the figure bounded by the section of the boundary C_n' between the vertices $w_0 = w_{01}$ and $w_\mu = w^{(1)}$, the segment of the ray l_{11} between the points $\overline{w}_1$ and $x_0' e_{11}$ and the supporting line $(e_{01}, w - w_{01}) = 0$. Here, the points $w_0, w_\mu, \overline{w}_1$ are defined in Sections 4.1 and 4.2,

$$e_{11} = \frac{a^{(2)} - a^{(1)}}{\|a^{(2)} - a^{(1)}\|}$$

and x_0' corresponds to x_0 when going from $\Pi(\cdot)$ to $\Pi_n(\cdot)$.

Let us construct similar left characteristics μ' and s' in the section of the boundary between the vertices $w^{(r)}$ and w_{01}.

In what follows, we denote μ_i, μ_i', s_i and s_i', the analogs of μ, μ', s and s', corresponding to the angle with the vertex $a^{(i)}$. It is easy to see that ν_n' is the total number of vertices C_n' and can be represented as

$$\nu_n' = \sum_{i=1}^{r} (\mu_i + \mu_i'). \tag{38}$$

And area $A - C_n'$ can be represented in the form

$$\lambda (A - C_n') = \sum_{i=1}^{r} (s_i + s_i') + \xi_{0i}', \tag{39}$$

where ξ_{0i}' is the area of the triangle cut by the supporting line $(e_{0i}, w - w_{0i}) = 0$.

Note that

$$n\xi_{01}' = \xi_0 = O(1), \tag{40}$$

where ξ_0 has an exponential distribution (see for example [6]). Similarly

$$n\xi_{0i}' = \xi_0 = O(1), \; i = 1, 2, \ldots, r. \tag{41}$$

As an approximation for μ_i, μ_i', s_i and s_i', we use χ_i, χ_i', q_i and q_i', introduced in Section 4.2. In this case, it is enough to evaluate the proximity of $(\mu_1, s_1) \overset{dis}{=} (\mu, s) + o_p(1)$ and $(\chi_1, q_1) \overset{dis}{=} (\chi, q)$. The remaining pairs of vectors are matched similarly.

To complete the proof of the theorem, it suffices to show the proximity of s and q, i.e.

$$\frac{n(s - q)}{\sqrt{\log n}} \xrightarrow{p} 0 \text{ at } n \to \infty \tag{42}$$

and proximity of μ and χ , i.e.

$$\frac{\mu - \chi}{\sqrt{\log n}} \xrightarrow{p} 0 \text{ at } n \to \infty. \tag{43}$$

We obtain the relation (42) from Corollary 3, and relation (43) from Corollary 2. The obtained relations (42) and (43) with the relations (36), (37)–(41) allow us to assert that a random vector with components $\dfrac{\nu_n' - 2r\alpha}{\beta_1\sqrt{2r}}$ and $\dfrac{n(1 - S_n' - 2r\alpha}{\beta_2\sqrt{2r}}$ converges in distribution to ω. Taking into account Remark given at the end of Section 3, we obtain the assertion of the theorem. The theorem is proved.

References

[1] C.Buchta, On the distribution of the number of vertices of a random polygon, *Anz. Osterreich. Akad. Wiss. Math. Natur. K1*, **139**(2003), 17–19.

[2] C.Buchta, Exact formulae for variances of functionals of convex hulls, *Advances in Applied Probability*, **45**(2013), no. 4, 917–924. DOI: 10.1239/aap/1386857850

[3] A.J.Cabo, P.Groeneboom, Limit theorems for functiohals of convex hulls, *Probab. Theory Relat. Fields*, **100**(1994), 31–55.

[4] H.Carnal, Die konvexe Hulle von n rotations symmetrisch verteilten Punkten, *Z. Wahrscheinlichkeits theorie verw. Geb.*, (1970), no. 15, 168–176.

[5] B.Efron, The convex hull of a random set of points. Biometrika, **52**(1965), 331–343.

[6] Sh.K.Formanov, I.M.Khamdamov, On joint probability distribution of the number of vertices and area of the convex hulls generated by a Poisson point process, *Statistics and Probability Letters*, **169**(2021), 108966, 1–7.

[7] P.Groeneboom, Limit theorems for convex hulls, *Probab. Theory Related Fields*, **79**(1988), 327–368.

[8] P.Groeneboom, Convex hulls of uniform samples from a convex polygon, *Adv. Appl. Prob. (SGSA)*, **44**(2012), 330–342. DOI: 10.1239/aap/1339878714

[9] T.Hsing, On the asymptotic distribution of the area outside a random convex hull in a disk, *The Annals of Applied Probability*, **4**(1994), no. 2, 478–493.

[10] I.M.Khamdamov, On Limit Theorem for the Number of Vertices of the Convex Hulls in a Unit Disk, *Journal of Siberian Federal University. Mathematics and Physics*, **13**(2020), no. 3, 275–284. DOI: 10.17516/1997-1397-2020-13-3-275-284

[11] I.M.Khamdamov, Properties of convex hull generated by inhomogeneous Poisson point process, *Ufa Mathematical Journal*, **12**(2020), no. 3, 81–96. DOI: 10.13108/2020-12-3-81

[12] A.V.Nagaev, Some properties of convex hulls generated by homogeneous Poisson point processes in an unbounded convex domain, *Ann. Inst. Statist. Math.*, **47**(1995), no. 1, 21–29.

[13] A.V.Nagaev, I.M.Khamdamov, Limit theorems for functionals of random convex hulls. Preprint of Institute of Mathematics, Academy of Sciences of Uzbekistan, Tashkent, 1991 (in Russian.)

[14] J.Pardon, Central limit theorems for random polygons in an arbitrary convex set, *The Annals of Probability*, **1**(2011), no. 3, 881–903.

[15] J.Pardon, Central Limit Theorems for Uniform Model Random Polygons, *J. Theor. Probab,* **25**(2012), 823–833.

[16] A.Reny, R.Sulanke, Uber diekovexe Hulle von zufalling gewahlten Punkte, *Z. Wahrscheinlichkeits theorie verw. Geb.*, **2**(1963), 75–84.

Совместное распределение числа вершин и площади выпуклых оболочек, порожденных равномерным распределением в выпуклом многоугольнике

Исакжан М. Хамдамов
Национальный университет Узбекистана им. Мирзо Улугбека
Ташкент, Узбекистан
Зоя С. Чай
Ташкентский университет информационных технологий
Ташкент, Узбекистан

Аннотация. Рассматривается выпуклая оболочка, порожденная выборкой, равномерно распределенной на плоскости для случая, когда носитель распределения представляет собой выпуклый многоугольник. Доказывается центральная предельная теорема для совместного распределения числа вершин и площади выпуклой оболочки с использованием пуассоновской аппроксимации биномиальных точечных процессов вблизи границы носителя распределения. Здесь применяются результаты [6] совместного распределения числа вершин и площади выпуклых оболочек, порожденных пуассоновским распределением. Из результатов, полученных в настоящей статье, в частности, следуют результаты [3, 7], когда носитель представляет собой выпуклый многоугольник, а выпуклая оболочка порождается однородным пуассоновским точечным процессом.

Ключевые слова: выпуклая оболочка, выпуклый многоугольник, пуассоновский точечный процесс, биномиальный точечный процесс, центральная предельная теорема.

DOI: 10.17516/1997-1397-2021-14-2-242-248
УДК 531.259.1

Steel 110G13L. Thermomagnetic and Galvanomagnetic Effects in its Films

Timur V. Fadeev*
Siberian Federal University
Krasnoyarsk, Russian Federation
Mikhail V. Dorokhin†
Iurii M. Kuznetsov
National Research State University named after N. I. Lobachevsky
Nizhnij Novgorod, Russian Federation
Lyudmila I. Kveglis‡
Vladimir V. Shevchuk§
Siberian Federal University
Krasnoyarsk, Russian Federation

Received 10.08.2020, received in revised form 10.09.2020, accepted 20.11.2020

Abstract. The article shows the ability to control magnetic properties due to modulation of phases in the film with varying temperature of growth. So, at low growth temperatures, a film is formed with an axis of easy magnetization in plane. An increase in temperature leads to a change in the phase composition of the film. It is shown that the presence of even a small component of the magnetization vector in the perpendicular direction leads to the appearance of a thermomagnetic effect of a large magnitude with respect to thermal noise.

Keywords: Hadfield steel, films, thermomagnetic effect, magnetization, semiconductor properties, Hall resistances, Nernst-Ettingshausen stresses.

Citation: T.V. Fadeev, M.V. Dorokhin, Iu.M. Kuznetsov, L.I. Kveglis, V.V. Shevchuk, Steel 110G13L. Thermomagnetic and Galvanomagnetic Effects in its Films, J. Sib. Fed. Univ. Math. Phys., 2021, 14(2), 242–248. DOI: 10.17516/1997-1397-2021-14-2-242-248.

Environmental problems associated primarily with the inefficient use of fuel resources, the question of the development of alternative sources of electric energy, in particular, autonomous low-power energy sources. It is interesting to consider magnetic materials as transformers of thermomagnetic energy [1]. The principle of operation of thermomagnetic converters is based on the Nernst-Ettingshausen effect [2]. By analogy with the Hall effect [3], in which the transverse voltage arises when an electric current passes through the antenna, the voltage between two components: ordinary, different "hot" and "cold" carriers, and abnormal ones associated with spin-dependent carrier scattering in magnetic centers in [4]. This may be due to the large mobility of charge carriers due to intersections in electronic bands. To improve the thermoelectric characteristics of a particular material (power factor), it is necessary to increase the electrical

*timur.fadeev.96@mail.ru
†dorokhin@nifti.unn.ru
‡kveglis@list.ru
§vova_bob13@mail.ru

conductivity and reduce the thermal conductivity $\lambda = \lambda_e + \lambda_{ph}$ (λ_e and λ_{ph} mean electronic and background inlays in λ, respectively) [5], it has been theoretically and experimentally shown that steel from Hadfield has metal and semiconductor properties. This combination allows us to expect large values of thermoelectric figure of merit in such materials [6].

The mathematical expressions describing the effects of Hall and Nernst-Ettingshausen in magnetic systems have the following form:

$$\begin{aligned} U_{NE} &= Q_0 B\Delta T + Q_M M(B)\Delta T, \\ U_H &= R_0 BI + R_M M(B)I, \end{aligned} \tag{1}$$

where Q_0 is the ordinary Nernst-Ettingshausen constant, Q_M is the anomalous Nernst-Ettingshausen constant, ΔT is the temperature gradient, M is the magnetization of the structure, B is the induction of an external magnetic field, I is the induction of an external magnetic field, I is the electric current passing through sample, R_0 is the ordinary Hall constant, R_M is the anomalous Hall constant. The constants R_0 and Q_0 do not have magnetic properties and mobile vehicles (mobility, concentration, resistance, scattering coefficient, etc.). Anomalous constant oscillations in the magnetic system.

The magnitude of the ordinary Nernst-Ettingshausen component is small and amounts to several tens of microvolts, while the anomalous component can reach gigantic values in compared to the usual effect due to strong spin-dependent scattering. Thin-film thermomagnetic, in which the magnetization is oriented perpendicular to a flat film, are of the greatest practical interest. A similar situation can be realized in a system with strong magnetic anisotropy, for example, in [7].

Hadfield steel is a composition having a mixture of magnetic and non-magnetic phases. As objects of study, we used two-layer films formed on sapphire substrates as a result of pulsed laser deposition in a vacuum of 10–6 Torr. Dimensions 1×1 cm and a thickness of 2 mm. Structures 1 and 2 differ in substrate temperatures during spraying of 250 and 400°C, respectively. The spraying time was 60 minutes, which corresponds to a thickness of 50 nm.

Perhaps this is due to the fact that the alloy is an antiferromagnetic invar, in which the appearance of localized magnetization in the sample occurs under shock loading. The latter is due to the fact that the structural features of $Fe_{86}Mn_{13}C$ are different types of magnetic ordering in the same sample. In Fig. 1, you can see the image of the surface of a bulk $Fe_{86}Mn_{13}C$ sample after shock loading obtained by scanning electron microscopy. Individual grains are visible. Dark bands in some grains turn into dark bands of neighboring grains. X-ray diffraction studies take place after the appearance of martensite deformation. This phase is localized in the shear strain bands of austenitic grains [10].

According to the Zhurkov equation [12]:

$$\tau = \tau_0 \cdot e^{\frac{u_0 - \gamma \cdot \sigma}{k \cdot T}}, \tag{2}$$

where τ is durability at a given voltage (s); τ_0 is period of thermal fluctuations of vibrations (s); u_0 is the activation energy of destruction (kJ/mol); γ is the structurally sensitive coefficient (cm^3/mol); σ is the stress in the localized volume equal to γ, (MPa); k is the gas constant (kJ/mol. $\cdot$ deg. K); T is the temperature (degree K).

Fig. 2 shows an image of the structure of a thinned foil based on Hadfield steel. Comparing Fig. 1 and Fig. 2, we can conclude that the structure of bulk samples of Hadfield steel is large-scale, which indicates the alternation of the bands of ferrimagnetic deformation martensite and non-magnetic austenite.

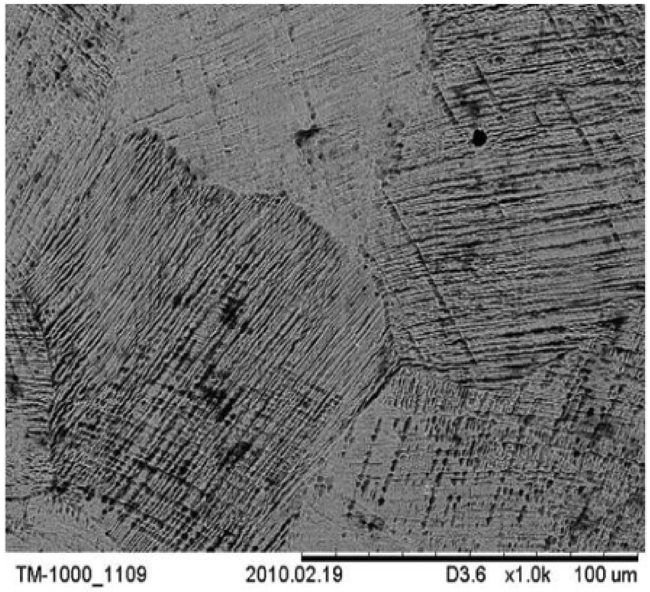

Fig. 1. Image of the structure of Hadfield steel samples of the surface of a massive sample in a scanning microscope

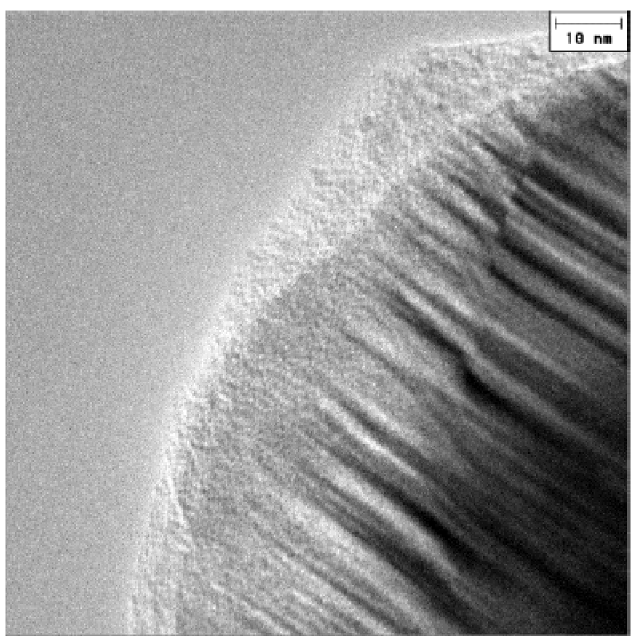

Fig. 2. Image of the structure of a thinned foil of a Hadfield steel sample in a transmission electron microscope

Thus, it can be assumed that it is precisely the different state of the magnetic structure that can determine the sign of the thermo-EMF in experiments. The thermo-EMF observed in the experiment may be due to the longitudinal or transverse Nernst-Ettingshausen (NE) effects —

these are the thermomagnetic effects observed when a semiconductor with a temperature gradient is placed in an external magnetic field [11].

The research methods consisted in measuring the dependence of the Hall and planar Hall resistances on the magnetic field, the Nernst-Ettingshausen voltage, the Seebeck effect, and registration of the structure magnetization in the planar direction using magnetometry with a variable gradient field.

To record the dependences of the Hall resistance and Nernst-Ettingshausen voltage on the magnetic field, 6 ohmic contacts were formed on the surface of the structure. The sample was mounted on a holder, the schematic diagram of which is shown in Fig. 3. The holder is equipped with a resistor-heater and radiator, which provides heat removal from one of the faces of the structure to form a temperature gradient.

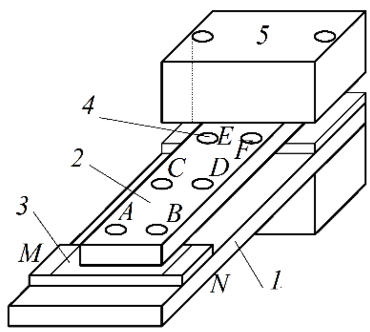

Fig. 3. Schematic representation of the installation of the sample on six contact holders for recording thermal effects, as well as the Hall effect. Heat flow spreads along the structure. 1 — substrate holder, 2 — sample, 3 — resistor-heater, 4 — contact pads, 5 — radiator

The technique allows us to consistently conduct experiments to study the effects of Hall (RH) and Nernst-Ettingshausen (Q):

$$(I_{MN}U_{CD}) - Q. \tag{3}$$

Fig. 4 shows the experimentally obtained dependences of the Hall resistances of the magnetic fields of the structures under study according to the method described above:

It can be seen from the obtained experimental curves that structure 1, formed at a temperature of 250°C, has a linear dependence of the Hall resistance on the magnetic field, which indicates that the magnetization vector lies in the plane of the structure, which does not allow magnetizing the structure in this region of the magnetic field. An increase in the sputtering temperature (structure 2) leads to the formation of a magnetic structure with a small perpendicular component of the magnetization vector, which is expressed in the appearance of nonlinearity in the dependence of the Hall resistance on the magnetic field (Fig. 4, black curve). The presence of oriented magnetization in the plane for both films is confirmed by an analysis of the nature of the magnetic field dependences of the magnetization vector, recorded by magnetometry with a variable field gradient. The obtained experimental curves are shown in Fig. 5.

The obtained curves show that the dependence of magnetization on the magnetic field has the form of a hysteresis loop, which indicates the presence of a ferromagnetic order in the structures under study. It is important to note that the loop width of structure 2 is smaller than that of structure 1, which further confirms the thesis that the second structure has a perpendicular component of magnetization.

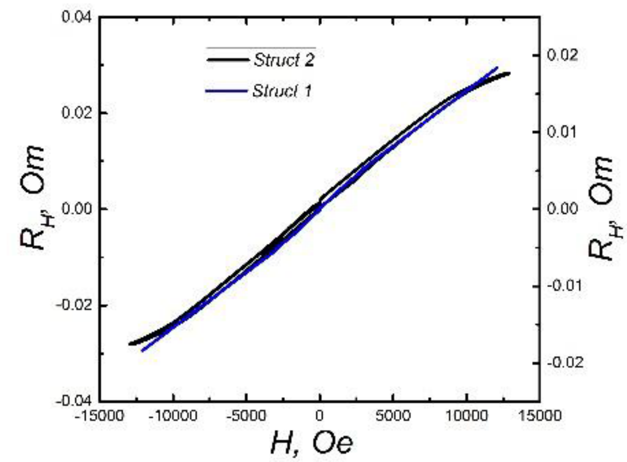

Fig. 4. Dependences of the Hall resistances of the magnetic fields of the structures under study: blue curve — structure 1, black curve — structure 2

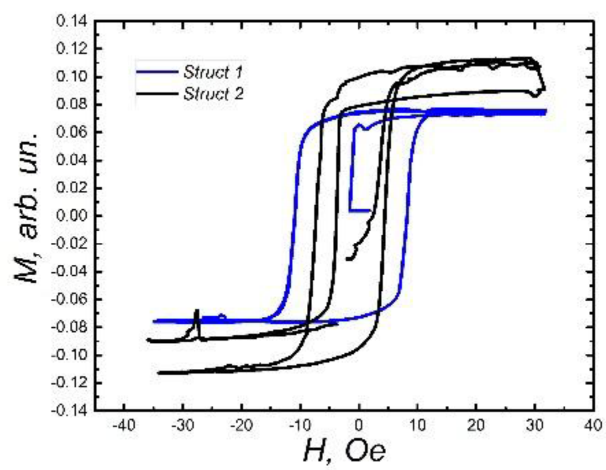

Fig. 5. Dependences of the magnetization of the studied structures on the magnetic field: blue curve — structure 1, black curve — structure 2

The absence of a perpendicular component of magnetization in structure 1 leads to the absence of the Nernst-Ettingshausen effect, while in structure 2 the effect was more than 40 μV with a temperature gradient of 10 degrees (Fig. 6).

It is important to note the presence of anisotropic magnetoresistance in the studied structures, expressed in the characteristic form of the dependence of the magnetic field on the plane Hall resistance (Fig. 7).

The paper shows the ability to control magnetic properties due to modulation of phases in the film at various rising temperatures. Thus, at low growth temperatures, a film with a flat axis of easy magnetization is formed. An increase in temperature leads to a change in the phase composition of the film, which is probably the reason for the rotation of the easy magnetization axis by an angle relative to the plane. This is manifested in the appearance of a hysteresis loop in the magnetic field dependences of the magnetization, the Hall effect, and the Nernst-Ettingshausen effect, and also leads to an increase in the thermomagnetic properties.

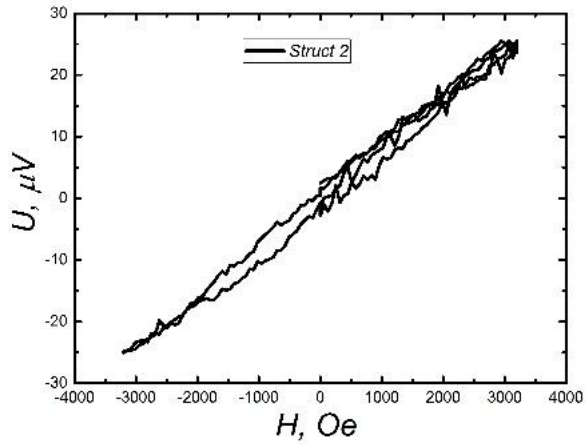

Fig. 6. Magnetic field dependence of the Nernst-Ettingshausen voltage of structure 2

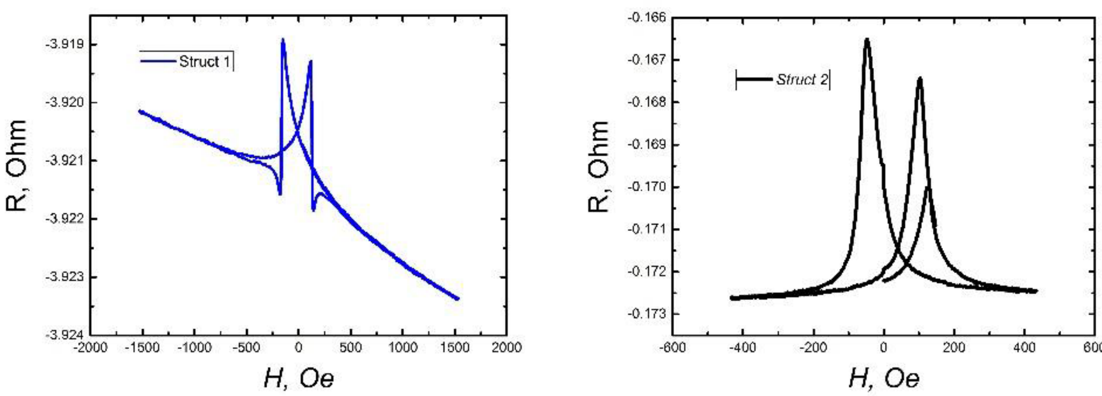

a) б)

Fig. 7. Dependences of the magnetic field on the flat Hall resistance of structures: a – 1, b – 2

References

[1] V.I.Bochegov, *Tech. Phys. Lett.*, **41**(2015), 595–598. DOI: 10.1134/S1063785015060188

[2] V.E.Gasumyants, *Phys. Sol. State*, **61**(2019), 1370–1378. DOI: 10.1134/S1063783419080134

[3] A.V.Kudrin, *JMMM*, **485**(2019), 236–243. DOI: 10.1016/j.jmmm.2019.04.088

[4] A.D.Arsenyeva, *Physics of the solid state*, **33**(1991), no. 5, 1443–1446 (in Russian).

[5] B.Hinterleitner, *Nature*, **576**(2019), 85–90. DOI: 10.1038/s41586-019-1751-9

[6] L.I.Kveglis, Moscow International Symposium on Magnetism, 2008.

[7] A.V.Zdoroveyshchev, *Phys. Sol. State*, **61**(2019), no. 9, 1577–1582. DOI: 10.1134/S1063783419090294

[8] L.I.Kveglis, *Journal of Engineering & Technologies*, **8**(2015), no. 1, 48–56.

[9] L.I.Kveglis, *Superlattices and Microstructures*, **46**(2009), no. 2, 114–120.

[10] I.M.Tsidilkovskiy, Thermomagnetic phenomena in semiconductors, Moscow, Fizmatgiz, Series "Physics of semiconductors and semiconductor devices", 1960.

[11] R.Abylkalykova, A.Dzhes, L.Kveglis, F.Noskov, M.Volochaev, A.Cherkov, Investigating deformation martensite in thinned samples and films of $Fe_{86}Mn_{13}C$ alloy, *Bulletin of the Russian Academy of Sciences: Physics*, **78**(2014), 330–332. DOI: 10.3103/S1062873814040030

[12] A.G.Gurevich, Fizika tverdogo tela : ucheb. posobiye dlya studentov fiz. spetsial'nostey un-tov i tekhn. un-tov, SPb.: Nev. Dialect, 2004 (Akad. typ. Nauka RAN) (in Russian).

Сталь 110Г13Л. Термомагнитные и гальваномагнитные эффекты в ее пленках

Тимур В. Фадеев
Сибирский федеральный университет
Красноярск, Российская Федерация
Михаил В. Дорохин
Юрий М. Кузнецов
Национальный исследовательский государственный университет им. Н. И. Лобачевского
Нижний Новгород, Российская Федерация
Людмила И. Квеглис
Владимир В. Шевчук
Сибирский федеральный университет
Красноярск, Российская Федерация

Аннотация. В статье показана возможность управления магнитными свойствами за счет модуляции фаз в пленке при варьировании температуры роста структуры. Так, при низких температурах формируется пленка с осью легкого намагничивания в плоскости. Повышение температуры приводит к изменению фазового состава пленки. Показано, что наличие даже небольшой компоненты вектора намагниченности в перпендикулярном направлении приводит к возникновению термомагнитного эффекта большой относительно тепловых шумов величины.

Ключевые слова: сталь Гадфильда, пленки, термомагнитный эффект, намагниченность, полупроводниковые свойства, сопротивление Холла, напряжение Нернста-Эттингсгаузена.

DOI: 10.17516/1997-1397-2021-14-2-249-257
УДК 535.247.1

Photostability of CdTe Quantum Dots and Graphene Quantum Dots under their Continuous Visible and UV Irradiation

Melina A. Goryunova*
Aleksei S. Tsipotan†
Vitaliy V. Slabko‡
Siberian Federal University
Krasnoyarsk, Russian Federation

Received 10.08.2020, received in revised form 11.01.2021, accepted 20.02.2021

Abstract. In the last decade, ultraviolet detectors have received significant attention due to their widespread use in civil and military fields. In this work, we have studied the effect of radiation of different ranges (UV and visible) on the spectral properties of CdTe quantum dots and wide-gap graphene QDs. The results obtained can be used to create an integrated UV radiation detector based on new physical principles.

Keywords: UV detectors, quantum dots, photostability.

Citation: M.A. Goryunova, A.S. Tsipotan, V.V. Slabko, Photostability of CdTe Quantum Dots and Graphene Quantum Dots under their Continuous Visible and UV Irradiation, J. Sib. Fed. Univ. Math. Phys., 2021, 14(2), 249–257. DOI: 10.17516/1997-1397-2021-14-2-249-257.

Introduction

Radiation sensors in the UV spectral range have been of great scientific and practical interest for a long time. This is due not only to new scientific data on the effect of UV radiation on human life and health, but also to the awareness of the fact that a number of tasks of an industrial, medical, environmental, security nature can be solved with the help of such sensors [1–4].

At present, the search for new materials for sensors that record the ultraviolet radiation dose is being actively pursued. Thus, the authors of [5] proposed methylammonium lead chloride (MAPbCl3) as a material for a UV sensor, on the basis of which a relatively fast detector insensitive in the visible region was obtained. The possibility of detecting ultraviolet radiation was found in a metal-insulator-metal (MIM) structure with carbon-boron nitride [6]. One of the promising materials for UV detection is nanostructured ZnO, in the form of nanodisks [7], nanowires [8] and colloidal quantum dots [9].

The study of the quantum dots (QDs) optical properties is becoming increasingly important in connection with the possible application of semiconductor nanostructures in science and technology, namely in UV sensors. Quantum dots are semiconductor nanoparticles, the electronic properties of which differ significantly from the properties of a bulk material. Quantum dots have

*goryunova7816@gmail.com
†acipotan@sfu-kras.ru
‡VSlabko@sfu-kras.ru

found applications in photovoltaic systems such as light emitting diodes and flat light emitting panels, lasers, solar cells and photovoltaic converters, as biological markers, i.e. wherever variable, wavelength-tunable optical properties are required. Their properties are useful for medical technologies, optoelectronic devices [10–14], etc.

A number of works performed in recent years are devoted to the study of the stability of quantum dots and ways to increase it. The photostability of CdSe / ZnS quantum dots and multilayer graphene was studied in the work [15]. A correlation was established between the quantum yield of QD luminescence and their photoelectric properties in hybrid structures. It is shown that a decrease in the quantum yield of QD luminescence as a result of the adsorption of azo dye molecules 1- (2-pyridylazo) -2-naphthol on the QD surface and a photoinduced increase in the quantum yield of QD luminescence is accompanied by a symbatic change in the photoconductivity of the structures.

The spectral properties of mixtures of colloidal CdS quantum dots with an average diameter of 2.5 nm and methylene blue molecules dispersed in gelatin are studied. The study by the authors of the works [16] established the manifestations of their hybrid association. An increase in the intensity of methylene blue luminescence in the presence of CdS quantum dots is found. A model of this effect is proposed, based on the transfer of the electronic excitation energy from the luminescence centers of the CdS quantum dot to methylene blue molecules.

The paper proposes a [17] technique for the successful replacement of the organic shell of colloidal QDs of cadmium selenide of various sizes. It was found that the spectral parameters of QD samples depend on the type of organic shell. It is shown that the morphology of structures does not depend on the size of QDs, but is determined by the chemical composition of the organic shell. A spectral analysis of the luminescence of QD-based superstructures showed that the position and intensity of the luminescence band strongly depends on the quality of the QD surface passivation. Previously, the photostability of CdTe colloidal quantum dots was considered in the work [18]. These objects were sensitive to UV radiation, however, their physical properties change significantly, which probably will not allow their use as a material for a UV radiation detector.

The aim of this work is to study the comparative characteristics of the photostability of colloidal CdTe quantum dots and wide-gap graphene quantum dots when they are irradiated with continuous radiation in the visible and UV ranges.

1. Materials

We studied water-soluble CdTe quantum dots stabilized with thioglycolic acid with a fluorescence maximum at 550 nm (PlasmaChem) and graphene colloidal quantum dots (CQD) quantum dots (Sigma Aldrich). The molar concentration of CdTe quantum dots in the solution was $C = 3 \cdot 10^{-6}\, M$, the concentration of graphene dots was $C = 1 \cdot 10^{-5}\, M$ [19]. The structure and local elemental composition of the samples were examined on a JEM-2100 (JEOL), high-resolution transmission electron microscope equipped with an Oxford Inca x-sight energy dispersive spectrometer at an accelerating voltage of 200 kV (Fig. 1).

2. Experimental setup

Solutions for studying the photostability of quantum dots were placed in quartz fluorimetric cells 10x10 mm in size. A DRSh-250-3M lamp operating in a glow mode was used as a light

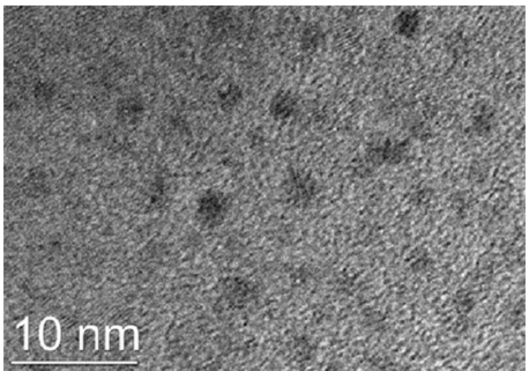

a)

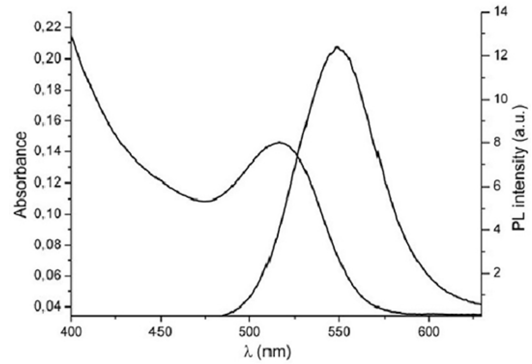

b)

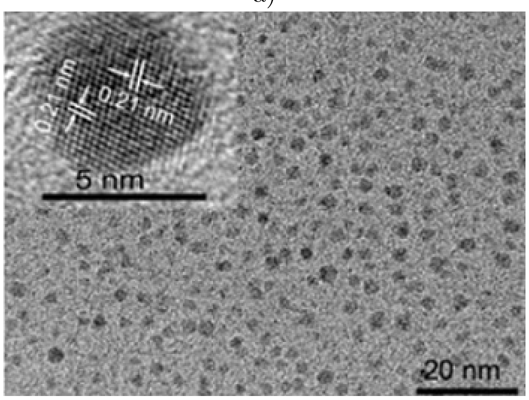

c)

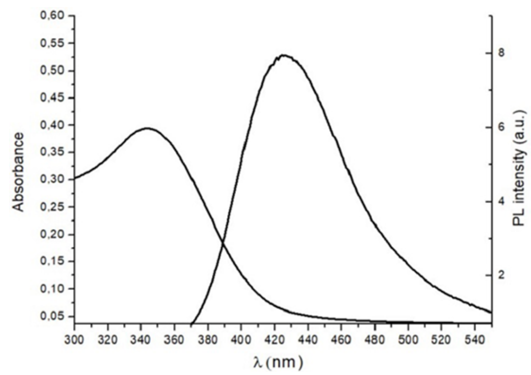

d)

Fig. 1. Physical properties of nanoparticles: electronic photographs of HR TEM CdTe (a), optical properties: absorption and photoluminescence spectra (b) and HR TEM CQD (c) and (d), respectively

source for irradiating the cuvettes. The emission spectrum of the DRSh-250-3M lamp is shown in Fig. 2a. It is a series of bright lines lying in the range from 275 to 600 nm. The selection of ultraviolet and visible ranges was carried out using an appropriate set of light filters, respectively (Fig. 2b and Fig. 2c).

The power was measured using an IMO-2N average power and laser radiation energy meter, and was equal to $P = 0,067\,W$. The same intensity in all experiments equal to $I = 379,3\,W/cm^2$.

The absorption spectra of the solutions were investigated using a Lambda 35 spectrophotometer (PerkinElmer), and fluorescence spectra using a Fluorolog 3 fluorometer (Horiba Jobin Yvon) at room temperature.

3. Experimental results

Irradiation with UV and visible ranges of the studied quantum dots was carried out for 60 minutes for each of the samples. The luminescence and absorption spectra were recorded before the beginning of irradiation, during the course with an interval of 10 min, and after irradiation. The evolution of the absorption and luminescence spectra is shown in Figs. 3 and 4.

As can be seen from the figures, the effect of ultraviolet radiation on CdTe quantum dots

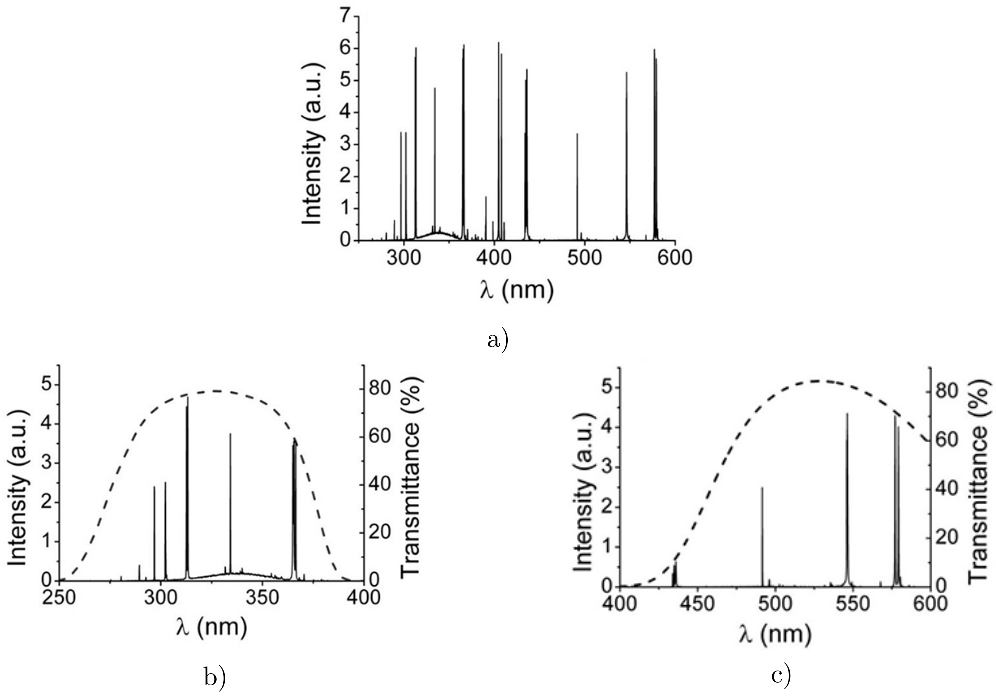

Fig. 2. The dependence of the radiation intensity on the wavelength for the DRSh-250-3M lamp and the spectral ranges of irradiation, taking into account the transmission of light filters

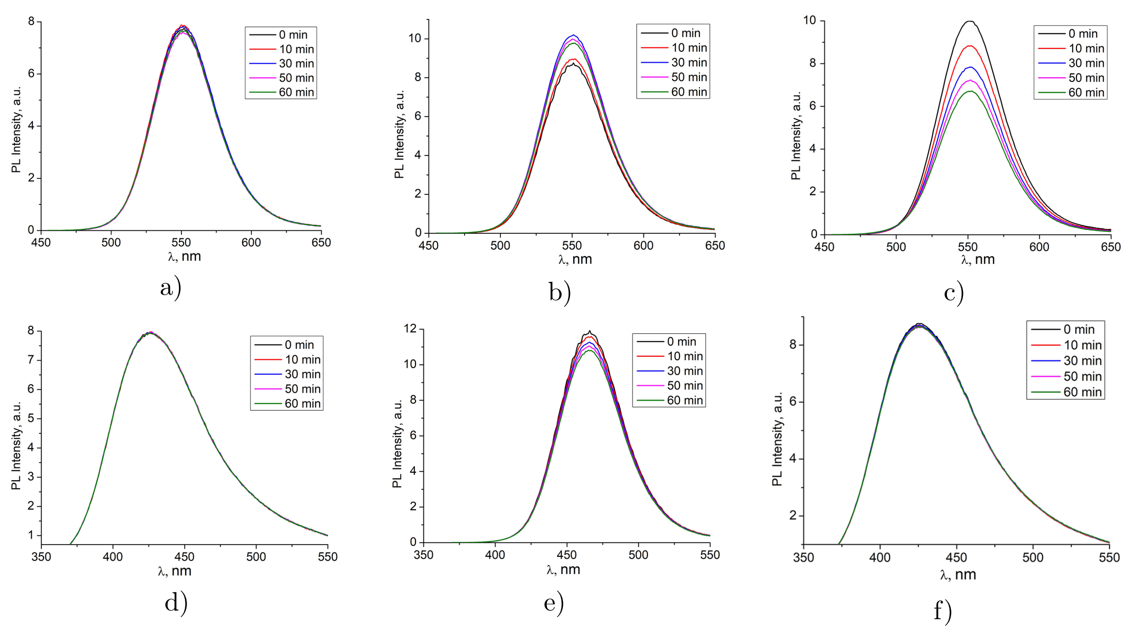

Fig. 3. Evolution of luminescence spectra of samples a) CdTe control, b) CdTe visible irradiation, c) CdTe UV irradiation, d) CQD control, e) CQD visible irradiation, f) CQD UV irradiation

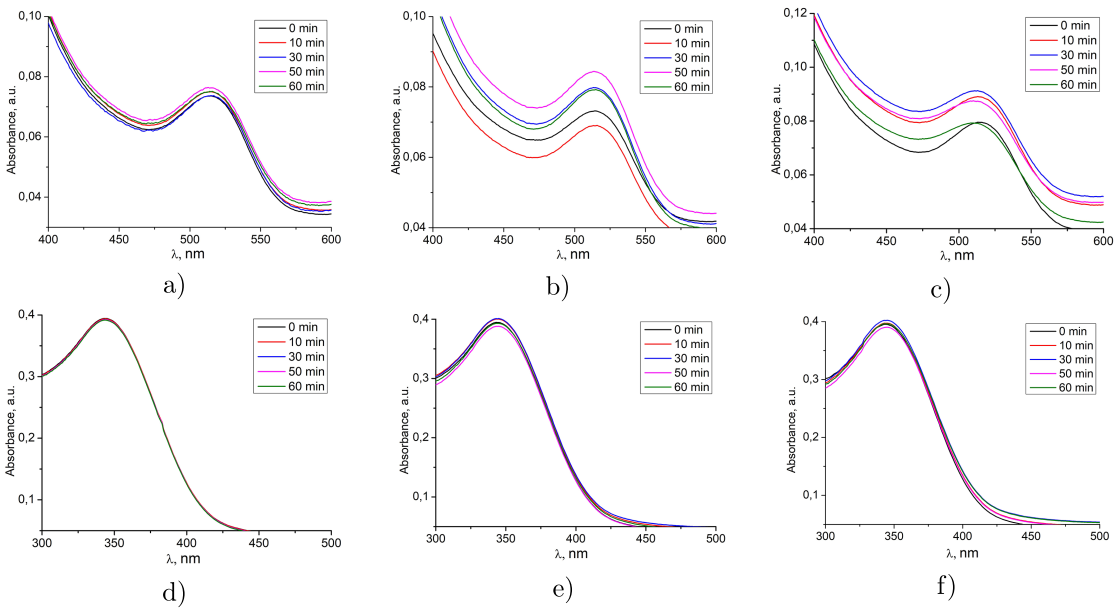

Fig. 4. Evolution of absorption spectra of samples a) CdTe control, b) CdTe visible irradiation, c) CdTe UV irradiation, d) CQD control, e) CQD visible irradiation, f) CQD UV irradiation

leads to a significant decrease in both absorption and luminescence depending on the exposure time. In this case, exposure to radiation in the visible range leads to a significantly smaller change in these characteristics. In the case of graphene quantum dots, irradiation in both the visible and UV ranges has a smaller effect on the absorption and luminescence spectra.

For further analysis of the data obtained, the dependences of the magnitude of the maximum of the luminescence intensity and absorption were plotted, normalized to the magnitude of the maxima before the start of irradiation (Fig. 5).

As can be seen from Fig. 5, irradiation of the CdTe quantum dot solution with the UV range of the spectrum leads to a decrease in the maximum intensity of both absorption and luminescence. The initial increase in the maximum absorption intensity is associated with an increase in scattering by large agglomerates of particles formed during irradiation with ultraviolet light. The mechanism of the effect of UV radiation on quantum dots is considered in detail in the work [18]. At the same time, the maximum intensity for the control sample and the sample irradiated in the visible range practically does not change within the measurement error.

The behavior of graphene quantum dots is different. The luminescence intensity remains for all 3 samples within the measurement error. In the absorption spectra of graphene quantum dots, a decrease in intensity is observed upon irradiation with UV light. In contrast to CdTe quantum dots, no increase in the absorption intensity is observed at the initial stage, which suggests that these quantum dots do not form, at least at the initial stage, aggregates.

Fig. 6 shows the change in the luminescence and absorption wavelength maxima of quantum dots with the time of irradiation in different ranges.

Fig. 6a shows that the change in the maximum of the luminescence wavelength with the time of irradiation practically does not occur in all three CdTe samples. Note that the wavelength of the absorption maximum shifts to the region of shorter wavelengths, when irradiated with UV light, which is associated with a decrease in the size of individual particles, and the spectral

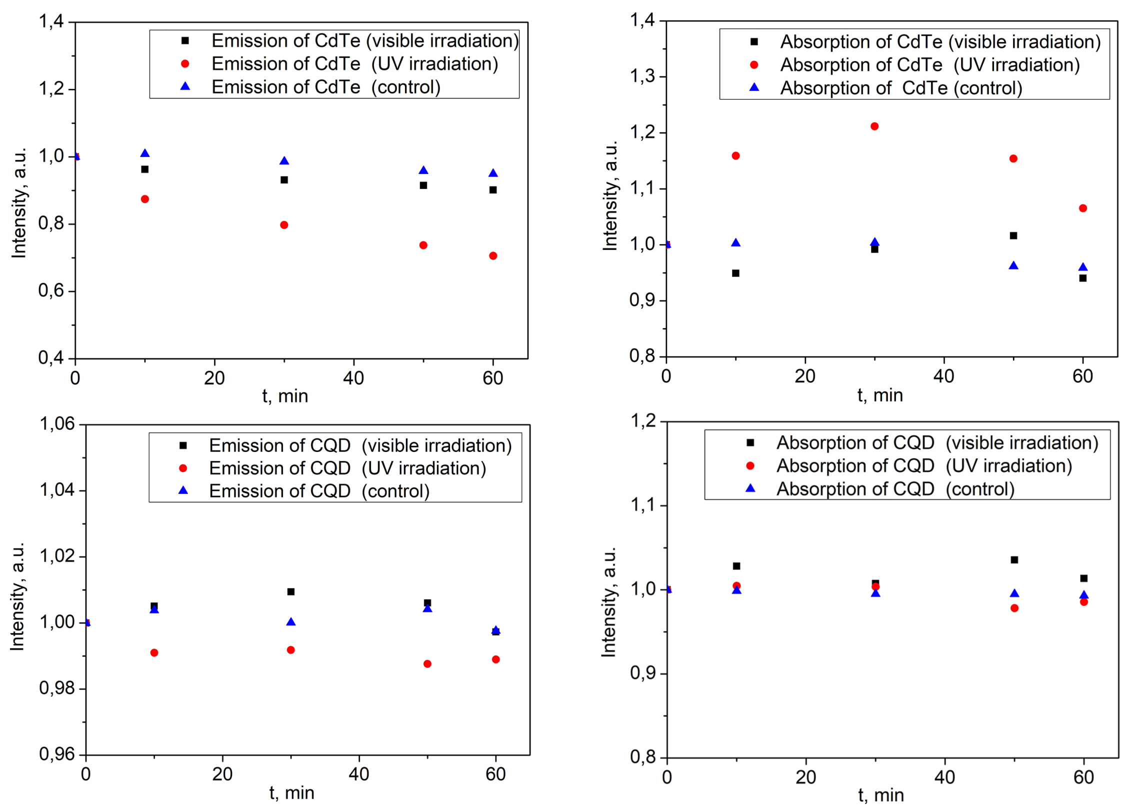

a) b)

Fig. 5. a) Normalized change in the maximum of the luminescence intensity from the exposure time, b) Normalized change in the maximum absorption intensity from the exposure time

position of the absorption maxima of samples numbered 1 and 2 (control and irradiated in the visible range) is practically match.

At the same time, the position of the absorption and luminescence maxima of graphene quantum dots practically does not undergo any changes, which suggests that the sizes of individual particles remain constant.

Conclusion

Colloidal graphene quantum dots and CdTe investigated in this work retain their optical and structural properties when exposed to radiation in the visible range, which is important for a number of their applications, for example, as solar cells. At the same time, their optical properties change when exposed to UV radiation. The latter allows them to be used as detectors that allow determining the dose of the radiation received. At the same time, the effect of UV radiation on CdTe quantum dots manifests itself in the form of a shift in the absorption maxima and an increase in optical density in the region of the first exciton transition due to particle aggregation and light scattering by large conglomerates, which leads to the need for additional processing of spectra. In the case of graphene quantum dots, the effect of UV radiation manifests itself in a decrease in the absorption maximum, which directly makes it possible to judge the received radiation dose.

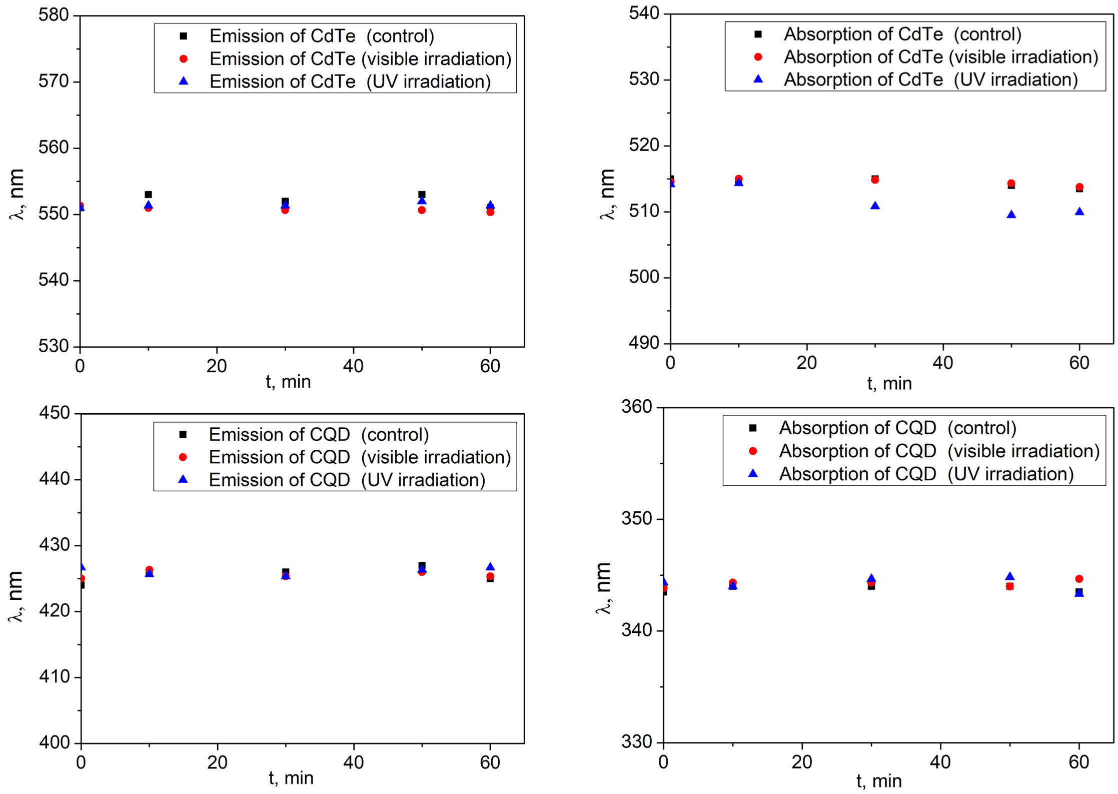

a)   b)

Fig. 6. a) Changes in the maximum of the luminescence wavelength from the time of irradiation, b) Changes in the maximum of the absorption wavelength from the time of irradiation

This research was supported by the Ministry of Science and Higher Education of the Russian Federation (Grant MK–1355.2019.2).

References

[1] E.D.Arama, V.F.Zhitar', T.D.Shemyakova, UV Sensors, *Electronic Materials Processing*, **42**(2006), no. 5, 72–76 (in Russian).

[2] I.Artyukov, Ultraviolet Radiation Detectors, *Photonics*, **5**(2008), 26-33 (in Russian).

[3] Y.Zheng, L.Cheng, M.Yuan, Z.Wang, L.Zhang, Y.Qin, T.Jing, An electrospun nanowire-based triboelectric nanogenerator and its application in a fully self-powered UV detector, *Nanoscale*, **6**(2014), no. 14, 7842–7846. DOI: 10.1039/c4nr01934b

[4] D.Li, X.Sun, H.Song, Z.Li, Y.Chen, H.Jiang, G.Miao, Realization of a high-performance GaN UV detector by nanoplasmonic enhancement, *Adv. Mater.*, **24**(2012), no. 6, 845–849. DOI: 10.1002/adma.201102585

[5] V.Adinolfi, O.Ouellette, M.I.Saidaminov, G.Walters, A.L.Abdelhady, O.M.Bakr, E.H.Sargent, Fast and Sensitive Solution-Processed Visible-Blind Perovskite UV Photodetectors, *Adv. Mater.*, **28**(2016), no. 33, 7264–7268. DOI: 10.1002/adma.201601196

[6] A.Prakash, S.D.Nehate, K.B.Sundaram, Boron carbon nitride based metal-insulator-metal UV detectors for harsh environment applications, *Optics Letters* **41**(2016), no. 18, 4249–4252. DOI: 10.1364/ol.41.004249

[7] M.R.Alenezi, A.S.Alshammari, T.H.Alzanki, P.Jarowski, S.J.Henley, S.R.P.Silva, ZnO Nanodisk Based UV Detectors with Printed Electrodes, *Langmuir*, **30**(2014), no. 13, 3913–3921. DOI: 10.1021/la500143w

[8] M.R.Alenezi, S.J.Henley, S.R.P.Silva, On-chip Fabrication of High Performance Nanostructured ZnO UV Detectors, *Sci. Rep*, **5**(2015), no. 1, 8516. DOI: 10.1038/srep08516

[9] M.Gong, Q.Liu, B.Cook, B.Kattel, T.Wang, W.-L.Chan, et.al., All-Printable ZnO Quantum Dots/Graphene van der Waals Heterostructures for Ultrasensitive Detection of Ultraviolet Light, *ACS Nano*, **11**(2017), no. 4, 4114-4123. DOI: 10.1021/acsnano.7b00805

[10] S.Buhbut, S.Itzhakov, D.Oron, A.Zaban, Quantum Dot Antennas for Photoelectrochemical Solar Cells, *Phys. Chem. Lett. J.*, **2**(2011), no. 15, 1917–1924. DOI: 10.1021/jz200518q

[11] P.V.Kamat, Quantum Dot Solar Cells. The Next Big Thing in Photovoltaics, *Phys. Chem. Lett. J.*, **4**(2013), no. 6, 908-918. DOI: 10.1021/jz400052e

[12] K.-E.Kim, T.G.Kim, Y.-M.Sung, Fluorescent cholesterol sensing using enzyme-modified CdSe/ZnS quantum dots, *Nanopart. Res. J.*, **14**(2012), no. 10, 1–9. DOI: 10.1007/s11051-012-1179-8

[13] N.Tessler, V.Medvedev, M.Kazes, S.Kan, U.Banin, Efficient near-infrared polymer nanocrystal light-emitting diodes, *Science*, **295**(2002), no. 5559, 1506–1508. DOI: 10.1126/science.1068153

[14] D.C.Oertel, M.G.Bawendi, A.C.Arango, V.Bulovic, Photodetectors based on treated CdSe quantum-dot films, *Appl. Phys. Lett.*, **87**(2005), no. 21, 213505. DOI: 10.1063/1.2136227

[15] I.A.Reznik, Y.A.Gromova, A.S.Zlatov, M.A.Baranov, A.O.Orlova, S.A.Moshkalev, V.G.Maslov, A.V.Baranov, A.V.Fedorov, Hybrid structures based on quantum dots and graphene nanobelts, *Optics and Spectroscopy*, **122**(2017), no. 1, 114–119. DOI: 10.1134/s0030400x17010258

[16] O.V.Ovchinnikov, M.S.Smirnov, B.I.Shapiro, T.S.Shatskikh, A.N.Latyshev, P.T.H.Mien, V.Y.Khokhlov, Spectral manifestations of hybrid association of CdS colloidal quantum dots with methylene blue molecules, *Optics and Spectroscopy*, **115**(2013), no. 3, 340–348. DOI: 10.1134/s0030400x1309018x

[17] E.V.Ushakova, T.K.Kormilina, M.A.Burkova, S.A.Cherevkov, V.V.Zakharov, V.K.Turkov, A.V.Fedorov, A.V.Baranov, The influence of ligand type on self-organization and optical properties of cadmium selenide quantum dots, *Optics and Spectroscopy*, **122**(2017), no. 1, 25–29. DOI: 10.1134/s0030400x17010301

[18] A.S.Tsipotan, M.A.Gerasimova, A.S.Aleksandrovsky, S.M.Zharkov, V.V.Slabko, Effect of visible and UV irradiation on the aggregation stability of CdTe quantum dots, *Nanopart. Res. J.*, **18**(2016), no. 11, 324. DOI: 10.1007/s11051-016-3638-0

[19] J.Ge, M.Lan, B.Zhou, W.Liu, L.Guo, H.Wang,et.al., A graphene quantum dot photodynamic therapy agent with high singlet oxygen generation, *Nature Communications*, **5**(2014), no. 1, 4596. DOI: 10.1038/ncomms5596

Фотостабильность коллоидных квантовых точек CdTe и графеновых квантовых точек при их облучении непрерывным излучением в видимом и УФ-диапазонах

Мелина А. Горюнова
Алексей С. Ципотан
Виталий В. Слабко
Сибирский федеральный университет
Красноярск, Российская Федерация

Аннотация. В последнее десятилетие ультрафиолетовые детекторы привлекли значительное внимание из-за их широкого применения в гражданской и военной областях. В настоящей работе исследовано влияние излучения разных диапазонов (УФ- и видимого) на спектральные свойства квантовых точек CdTe и широкозонных графеновых КТ. Полученные результаты могут быть использованы для создания интегрального детектора УФ-излучения на новых физических принципах.

Ключевые слова: детекторы УФ-излучения, квантовые точки, фотостабильность.

Journal of Siberian Federal University. Mathematics & Physics 2021, 14(2), 258–260

DOI: 10.17516/1997-1397-2021-14-2-258-260
УДК 512.54

A Short Essay towards if P not equal NP

Vladimir V. Rybakov*
Siberian Federal University
Krasnoyarsk, Russian Federation
A. P. Ershov Institute of Informatics Systems
Novosibirsk, Russian Federation

Received 10.12.2020, received in revised form 10.01.2021, accepted 12.02.2020

Abstract. We find a computational algorithmic task and prove that it is solvable in polynomial time by a non-deterministic Turing machine and cannot be solved in polynomial time by any deterministic Turing machine. The point is that our task does not look as very canonical one and if it may be classified as computational problem in standard terms.

Keywords: deterministic computations, non-deterministic computations.

Citation: V.V. Rybakov, A Short Essay towards if P not equal NP, J. Sib. Fed. Univ. Math. Phys., 2021, 14(2), 258–260. DOI: 10.17516/1997-1397-2021-14-2-258-260.

1. Definitions and Formulations

To recall notation, P is the class of all computational tasks (problems) which may be solved by deterministic TMs in polynomial time, NP is the class of all computational tasks (problems) which may be solved by none-deterministic TMs in a polynomial time. Terminology and definitions concerning Turing Machines (TMs) and basics of mathematical theory of computation are supposed to be known for the reader.

What is a computational algorithmic task (problem)? Recall first what is a computable function? That is a function which may be computed by a TM. So, what is a solvable computable algorithmic task (Problem)?

That is a task which may be solved by a TM by an algorithm written in its program. That is — being passed by input data on the tape, TM works in accordance with its program and stops giving required output data (or just answer - yes - no -, if the task is a recognition of the input data).

We start by definition of the computational problem Pr. Consider the following computational task. It is a precise formal version of the Problem of Braking Coded Lock.

We model it by a Turing machine with the alphabet containing 0 and 1, an amount of marks for internal states $q_j, j \in J$, etc., as standard for a deterministic Turing machine etc. For any given set $(a_1, a_2, \ldots, a_n)$, where $a_i = 0$ or $a_i = 1$ we consider it as the code for our codded lock. We wish to open it. We describe below a TM solving this task.

(1) We put first $(a_1, a_2, \ldots, a_n)$ in the tape of TM and isolate in the final its part putting before first symbol a_1 a mark c showing that here we put the code. The machine cannot enter this part for any state before TM comes to comparison state. The tape cannot be extended after a_n. The part $a_1, a_2, \ldots, a_n$ cannot be edited.

(2) We then first put in the input of our TM any trial code $(c_1, c_2, \ldots, c_n)$, $(c_i = 0, 1)$ extending the tape to the left and compare it with $(a_1, a_2, \ldots, a_n)$. If we get total coincidence we put $(a_1, a_2, \ldots, a_n)$ outside and answer YES.

*Vladimir_Rybakov@mail.ru

(3) If $(c_1, c_2, \ldots, c_n)$ does not coinside with $(a_1, a_2, \ldots, a_n)$ at first met convergence we delete immediately from the tape of TM all $(c_1, c_2, \ldots, c_n)$ and only after this we get internal state of TM which only allow to move to the beginning of the tape.

(4) Then we start an early chosen, fixed and written in program of our TM algorithm A generating new trial code $(c_1, c_2, \ldots, c_n)$ and continue the comparison as in (2).

2. Results

We assume the algorithm A to be fixed, written in the instructions of our TM and might be applied for any given code $(a_1, a_2, \ldots, a_n)$. So our TM models both sides – codded lock owner, and code lock cracker.

Lemma 1. *Pr is a computational algorithmic computational task (problem) which is solvable in exponential time for some algorithm A for any given code.*

Proof. There are many known algorithms A doing this task in exponential time. The problem is algorithmic since we (may use) are using distinct algorithms A, computational as we use computations by TM.

It is time to emphasise here that the solution of the problem Pr consist of ONLY search (invention) and construction the algorithm A and writing it in the memory in commands of TM. Nothing else to do is prohibited. We cannot change the conditions, demands of the task. We are only allowed to find and construct algorithms A.

Lemma 2. *Pr is a computational algorithmic task (problem) which is solvable in polynomial time by a non-deterministic Turing machine.*

Proof is again evident. Just to take non-deterministic instructions in A while generating the input $I = \{c_1, \ldots, c_n\}$ (we need only n steps and $2n$ instructions to do it), and then we need only polynomial time to make comparison. □

All is fine, but the question is: where the proof that Pr cannot be solved in polynomial time with deterministic machine is? Here is the proof.

Lemma 3. *Pr cannot be solved in polynomial time by a non-deterministic Turing machine.*

Proof. Assume that there is a deterministic algorithm A solving this problem in polynomial time for any code $(a_1, \ldots, a_n)$ (working in accordance with the conditions (formulation) of the problem Pr as description above). Since the task does not allow to use the internal results of comparison trial inputs $(c_1, \ldots, c_n)$ with the code of the lock $(a_1, \ldots a_n)$, after rejecting the trial input $c_1, \ldots, c_n$ the machine TM again comes to generating new example $c_1, \ldots, c_n$, and then new one and so on, without any additional information about reason of rejecting - which symbols do not coincide.

The point here is that for any very initial trial input $(c_1, \ldots, c_n)$ the sequence of these new trial inputs $c_1, \ldots, c_n$ will be exactly the same as for any another given very first trial input (before finding (accepting) $(a_1, \ldots, a_n)$ and stopping). Why so? Because the algorithm A **is deterministic** — the sequence of steps and generated trial inputs $c_1, \ldots, c_n$ from A is predefined and does not depend on real value rejected trials $c_1, \ldots, c_n$, only it knows — if the trial does not coincide with the code $(a_1, \ldots, a_n)$ — we continue, generate a new one.

So, in any k-th step of applying A it generates at most k different trials $c_1, \ldots, c_n$. Let then $a_1, \ldots, a_n$ be the tuple which does not belong to trials which may be generated by A in its $2^n - 1$ consequent applications. Then if $a_1, \ldots, a_n$ is taken as the code our TM will require at least 2^n steps before crack $a_1, \ldots, a_n$. □

Thus as the result we have

Theorem 4. *$PR \in NP$ and $PR \notin P$, so $P \neq NP$.*

Clearly that the interest to non-deterministic computation comes (primarily?) from famous Cook-Levin theorem, cf. [1]. There is a big amount of papers towards if $P = NP$ or $P \neq NP$, cf. [1–4].

We do not touch in this short notice complexity theory and the problem satisfiability in Boolean logic and hence the famous Cook-Levin theorem. Just we would like to emphasize that if not to fix very precisely the meaning what is a computational algorithmic problem — it may confuse the researchers and put efforts aside. So, if we use general — and very plausible and even rather convincing interpretation — as in this paper — we shortly obtain the negative answer on if $P = NP$. Though questions about behaviour of Turing machines and how algorithms work on them in accordance with their programs and precisely specified tasks are definitely computational algorithmic problems (maybe internal ones — but nonetheless). Therefore the question of what is a computational algorithmic problem definitely needs clarification.

This research is supported by High Schools of Economics (HSE) Moscow; supported by the Krasnoyarsk Mathematical Center and financed by the Ministry of Science and Higher Education of the Russian Federation (Grant No. 075-02-2020-1534/1).

References

[1] S.A.Cook, The complexity of theorem proving procedures, Proceedings of the Third Annual ACM Symposium on Theory of Computing, 1971, 151–158. DOI: 10.1145/800157.805047.

[2] https://en.wikipedia.org/wiki/P_versus_NP_problem

[3] Javier A.Arroyo-Figueroa, The Existence of the Tau One-Way Functions Class as a Proof that P != NP, 2016. https://arxiv.org/abs/1604.03758

[4] Mathias Hauptmann, On Alternation and the Union Theorem, Mathematics, Computer Science, 2016. https://arxiv.org/abs/1602.04781

Заметка о проблеме равенства P и NP

Владимир В. Рыбаков
Сибирский федеральный университет
Красноярск, Российская Федерация
Институт систем информатики им. А. П. Ершова
Новосибирск, Российская Федерация

Аннотация. В статье вводится алгоритмическая проблема и доказывается, что она разрешима за полиномиальное время на недетерминированных машинах Тьюринга и не решается за полиномиальное время на детерминированных машинах Тьюринга. В то же время, введенная проблема не выглядит как стандартная в общепринятом понимании и не самоочевидно может ли она быть классифицирована как каноническая.

Ключевые слова: детерминированные вычисления, недетерминированные вычисления.